

**ELECTRONIC AND MAGNETIC  
STRUCTURES OF  
ANTIFERROMAGNETIC THIN FILMS**

By

**JAYANTA DAS**

**PHYS05200804001**

**Saha Institute Of Nuclear Physics, Kolkata**

A thesis submitted to the  
Board of Studies in Physical Sciences  
In partial fulfillment of requirements  
For the Degree of

**DOCTOR OF PHILOSOPHY**

of

**HOMI BHABHA NATIONAL INSTITUTE**



**May, 2015**

# Homi Bhabha National Institute<sup>1</sup>

## Recommendations of the Viva Voce Committee

As members of the Viva Voce Committee, we certify that we have read the dissertation prepared by Jayanta Das entitled "Electronic and magnetic structures of antiferromagnetic thin films" and recommend that it may be accepted as fulfilling the thesis requirement for the award of Degree of Doctor of Philosophy.

---

Chairman - <Name> *D. Ghose*  
Prof. Debabrata Ghose  
SPMS Div, SINP, Kolkata-64 **Date:** 24/09/2015

---

Guide / Convener - <Name> *[Signature]*  
Prof. Krishnakumar S R Menon **Date:** 24/09/2015  
SPM Div, SINP, Kolkata-64

---

Co-guide - <Name> (if any) **Date:**

---

Examiner - <Name> *Kalobaran Maiti*  
Prof. Kalobaran Maiti  
TIFR, Mumbai 5 **Date:** 24/09/2015

---

Member 1- <Name> *[Signature]*  
Prof. P M G Nambissan **Date:** 24/09/2015  
ANP Div, SINP, Kolkata-64

---

Member 2- <Name> *R. Ranganathan*  
Prof. R Ranganathan **Date:** 24/09/2015  
ECMP Div, SINP, Kolkata-64

---

Final approval and acceptance of this thesis is contingent upon the candidate's submission of the final copies of the thesis to HBNI.

I/We hereby certify that I/we have read this thesis prepared under my/our direction and recommend that it may be accepted as fulfilling the thesis requirement.

**Date:** 24/09/2015

**Place:** Kolkata

<Signature>

Co-guide (if applicable)

*[Signature]*  
Prof. Krishnakumar S R Menon  
Associate professor F, SPMS Div.  
Saha Institute of Nuclear Physics  
1/AF, Bidhannagar, Kolkata-64

<Signature>

Guide

## STATEMENT BY AUTHOR

This dissertation has been submitted in partial fulfillment of requirements for an advanced degree at Homi Bhabha National Institute (HBNI) and is deposited in the Library to be made available to borrowers under rules of the HBNI.

Brief quotations from this dissertation are allowable without special permission, provided that accurate acknowledgement of source is made. Requests for permission for extended quotation from or reproduction of this manuscript in whole or in part may be granted by the Competent Authority of HBNI when in his or her judgment the proposed use of the material is in the interests of scholarship. In all other instances, however, permission must be obtained from the author.

*Jayanta Das*

<Signature>

<Candidate Name>

JAYANTA DAS

## DECLARATION

I, hereby declare that the investigation presented in the thesis has been carried out by me. The work is original and has not been submitted earlier as a whole or in part for a degree / diploma at this or any other Institution / University.

*Jayanta Das*

<Signature>

<Candidate Name>

JAYANTA DAS

## List of Publications

### Journals

1. "Surface antiferromagnetic domain imaging using low-energy unpolarized electrons", < Krishnakumar S. R. Menon, Suman Mandal, Jayanta Das, Tevfik Onur Montes, Miguel Angel Niño Andrea Locatelli, and Rachid Belkhou >, Physical Review B, **2011**, 84, 132402, 1-5.
2. "Growth of antiferromagnetically ordered Cr monolayer on Ag(100)", < Jayanta Das, Asish K. Kundu and Krishnakumar S.R. Menon>, Vacuum, **2015**, 112, 5-11.
3. "Structure of Cr monolayer on Ag(001): A buried two-dimensional  $c(2 \times 2)$  antiferromagnet", < Jayanta Das, Sananda Biswas, Asish K. Kundu, Shobhana Narasimhan and Krishnakumar S. R. Menon >, Physical Review B, **2015**, 91, 125435, 1-8.

### Conference Proceedings

1. "A high resolution microscopic approach for imaging antiferromagnetic nanodomains of NiO thin film", < Jayanta Das, Krishnakumar S R Menon >, AIP Conference Proceedings, **2013**, 1536, 175.

*Jayanta Das*

<Signature>

<Candidate Name>

JAYANTA DAS

**Dedicated to my beloved parents**

## Acknowledgements

This thesis took more than five years to take shape and it would never been possible without the help, support and encouragement of many people.

I would like to express my heartfelt gratitude to Prof. Krishnakumar S. R. Menon, my thesis supervisor, for introducing me to the Angle-resolved Photoemission Spectroscopy techniques and the interesting field of Low Energy Electron Microscopy and Photoemission Electron Microscopy. I have been benefited from his valuable advice and scientific discussions.

I am grateful to Andrea Locatelli, Tevfik Onur Montes, Miguel Angel Niño, beamline scientist of Nanospectroscopy beamline in Sincrotrone Trieste, Italy. I am also thankful to Dr. Rachid Belkhou of Synchrotron SOLEIL, France for his scientific collaboration. I am acknowledge the Department of Science and Technology (DST), Government of India, for financial support.

I sincerely acknowledge the engineering and technical staffs at PREVAC sp. zoo. (Ltd.), Poland and VG SCIENTA, Sweden for all technical helps in troubleshooting instrumental problems. I thank Prof. Shovana Narasimhan and her student Dr. Sananda Biswas, Jawaharlal Nehru Centre for Advanced Scientific Research, India for theoretical collaborations. Special thanks to all my lab-mates for creating a friendly and working atmosphere in our group. It is worthwhile to remember Asish Kumar Kundu whose valuable efforts led many experiments to success. It's my pleasure to acknowledge all the teaching and non-teaching members, my seniors and juniors in SPMS division, SINP.

Few words are not sufficient to express the unconditional and endless love, support, encouragement of my family.

Kolkata

April, 2015

Jayanta Das

# Contents

Synopsis	xii
List of Figures	xxxii
List of Tables	xlvi
<b>1 Antiferromagnetism in lower dimension: Surfaces and 2D systems</b>	<b>1</b>
1.1 Introduction . . . . .	1
1.2 Magnetism in low dimension . . . . .	4
1.2.1 Magnetic moment at surfaces and in ultrathin films . . . . .	7
1.2.2 Finite-Size Effects on the Magnetic Ordering Temperature . . . . .	8
1.3 Scope of the thesis: antiferromagnetic systems . . . . .	10
1.3.1 1 ML Cr/Ag(001) . . . . .	10
1.3.2 NiO/Ag(001) . . . . .	11
<b>2 Experimental techniques and methods</b>	<b>14</b>
2.1 Introduction . . . . .	14
2.2 What is Epitaxial Growth? . . . . .	16
2.2.1 Interfacial strain: Pseudomorphic growth . . . . .	16
2.2.2 Different parameters of MBE growth . . . . .	18

2.3	Deposition of epitaxial films . . . . .	19
2.4	Low Energy Electron Diffraction (LEED) . . . . .	20
2.4.1	Theory . . . . .	20
2.4.1.1	Kinematic theory: Single scattering . . . . .	21
2.4.1.2	Dynamical theory: Multiple scattering . . . . .	22
2.4.2	LEED: Instrumental configurations . . . . .	23
2.4.2.1	Calibration . . . . .	25
2.4.3	Superstructure in LEED pattern . . . . .	27
2.4.3.1	LEED half-order spots: Surface antiferromagnetic order . . . . .	28
2.5	Photoemission spectroscopy . . . . .	32
2.5.1	Theory . . . . .	36
2.5.2	Angle Resolved Photoemission Spectroscopy (ARPES) . . . . .	39
2.5.3	X-ray Photoemission Spectroscopy (XPS) . . . . .	40
2.6	ARPES facility at SINP . . . . .	41
2.6.1	Load lock . . . . .	42
2.6.2	Preparation chamber . . . . .	42
2.6.3	Analysis chamber . . . . .	45
2.6.4	Electron Energy Analyzer . . . . .	48
2.7	Modes of photoemission data collection . . . . .	51
2.8	X-ray absorption techniques . . . . .	53
2.8.1	Synchrotron radiation . . . . .	56
2.8.2	Linear dichroism . . . . .	56
2.8.3	The XMLD effect . . . . .	58
2.9	Magnetic imaging techniques . . . . .	59
2.9.1	Low energy electron microscopy (LEEM) . . . . .	60
2.9.2	Imaging modes in low energy electron microscope . . . . .	61
2.9.3	Photoemission electron microscopy . . . . .	64
2.10	Summary . . . . .	65

<b>3</b>	<b>Growth of monolayer Cr film on Ag(001)</b>	<b>67</b>
3.1	Introduction . . . . .	67
3.2	Background works . . . . .	69
3.3	The Cr/Ag(001) system . . . . .	72
3.4	Experimental details . . . . .	75
3.4.1	Growth . . . . .	75
3.4.2	Low Energy Electron Diffraction studies . . . . .	76
3.4.3	Temperature dependence of half-order spots: interfacial inter- mixing . . . . .	82
3.4.4	Optimization of the growth temperature . . . . .	84
3.4.5	Valence band photoemission studies . . . . .	87
3.4.6	Direct <i>vs.</i> step deposition of Cr . . . . .	90
3.4.7	Optimizing Cr deposition rate . . . . .	93
3.4.8	Importance of a smooth substrate surface . . . . .	94
3.5	Summary . . . . .	96
<b>4</b>	<b>Structure of antiferromagnetic Cr monolayer on Ag(001)</b>	<b>97</b>
4.1	Introduction . . . . .	97
4.2	Earlier studies . . . . .	99
4.3	Cr Coverage dependence: LEED studies . . . . .	103
4.4	Cr Coverage dependence: ARPES studies . . . . .	106
4.5	Segregation of Ag on Cr monolayer . . . . .	110
4.6	Theoretical calculations . . . . .	113
4.7	Conclusion . . . . .	118
<b>5</b>	<b>Electronic structure and magnetism of monolayer Cr film</b>	<b>120</b>
5.1	Introduction . . . . .	120
5.2	Valence band: ARPES studies . . . . .	123
5.2.1	Surface brillouin zone and symmetry directions . . . . .	123

5.2.2	Valence band of flat Cr monolayer . . . . .	125
5.2.2.1	Evidence of 2D antiferromagnetism . . . . .	131
5.2.3	Valence band: Cr coverage dependence . . . . .	137
5.2.4	Valence band: Growth temperature dependence . . . . .	140
5.3	Core levels : X-ray photoemission studies . . . . .	142
5.4	Magnetism of Cr monolayer: Ising behavior of $c(2\times 2)$ 2D antiferromagnet	144
5.5	Summary . . . . .	148
<b>6</b>	<b>Growth of NiO film on Ag(001): characterization of electronic structure</b>	<b>149</b>
6.1	Introduction . . . . .	149
6.2	Background works on NiO thin film growth . . . . .	152
6.3	Experimental Details: . . . . .	156
6.3.1	Choice and preparation of the substrate . . . . .	156
6.3.2	Calibration of Ni effusion cell . . . . .	158
6.3.3	Oxidizing Ni/Ag(001): LEED and XPS studies . . . . .	159
6.3.4	Epitaxial growth of NiO at different growth conditions . . . . .	162
6.3.4.1	LEED studies . . . . .	163
6.3.4.2	Ni to O stoichiometry . . . . .	165
6.3.5	XPS: Thickness dependence of NiO film . . . . .	166
6.3.6	Valence band structure of NiO/Ag(001) . . . . .	170
6.3.6.1	Earlier works . . . . .	170
6.3.6.2	ARPES studies . . . . .	173
6.3.6.3	ARPES: Thickness dependence . . . . .	175
6.3.6.4	ARPES: Temperature dependence . . . . .	179
6.3.6.5	ARPES: Photon energy dependence . . . . .	181
6.4	Conclusion . . . . .	183

<b>7</b>	<b>Magnetic structure of epitaxial NiO film</b>	<b>184</b>
7.1	Introduction . . . . .	184
7.2	Background works . . . . .	187
7.3	Magnetic structure of NiO . . . . .	190
7.3.1	Twin and Spin domains . . . . .	190
7.3.2	The real and reciprocal lattice . . . . .	191
7.4	Technical Details: . . . . .	192
7.5	Experimental Details . . . . .	193
7.5.1	Antiferromagnetic Low Energy Electron Microscopy (AFM-LEEM) . . . . .	194
7.5.1.1	AFM-LEEM: Thickness dependence . . . . .	200
7.5.1.2	Beam energy dependence of Twin domains . . . . .	202
7.5.1.3	Thickness dependence of Néel temperature ( $T_N$ ) . . . . .	204
7.5.1.4	XMLD at different film thickness . . . . .	206
7.5.2	XMLD-PEEM: Spectromicroscopy . . . . .	209
7.5.2.1	XMLD-PEEM: polarization dependency . . . . .	209
7.5.2.2	XMLD-PEEM: thickness dependent AFM domains . . . . .	210
7.5.3	Comparison between AFM-LEEM and XMLD-PEEM . . . . .	212
7.6	Summary . . . . .	214
<b>8</b>	<b>Effect of oxygen vacancy defects on the electronic structure and magnetism of NiO film</b>	<b>215</b>
8.1	Introduction . . . . .	215
8.2	Experimental details . . . . .	217
8.2.1	Effect on electronic structures . . . . .	217
8.2.1.1	Modification of core levels . . . . .	217
8.2.1.2	Modification of valence band . . . . .	219
8.2.1.3	Angle dependent XPS studies: Core levels . . . . .	220

8.2.1.4	Angle dependent XPS studies: Valence band . . . . .	222
8.2.1.5	Effect of vacuum and oxygen annealing . . . . .	223
8.2.1.6	Discussion . . . . .	224
8.2.2	Effect the oxygen vacancies on magnetism . . . . .	227
8.3	Conclusion . . . . .	229
	<b>Bibliography</b> . . . . .	<b>231</b>

# Synopsis

**Antiferromagnetism in lower dimension - Surfaces and 2D systems:** Magnetism of thin films, specially the surface magnetism of metal and metal oxide films are one of the most attractive topics of surface science research now-a-days. Surprising properties of two-dimensional magnetisms and their vast applications in device synthesis and in different fields of material research have made the study of 2D magnetism more interesting. Techniques like magnetic force microscopy (MFM), spin polarized low energy electron microscopy (SP-LEEM), spin polarised photoemission (SP-PES), Magneto Optical Kerr Effect (MOKE) microscopy, Spin Polarized Scanning Tunneling Microscopy (SP-STM) and x-ray magnetic circular dichroism (XMCD) are well established for their capability to probe surface ferromagnetism of bulk materials and thin films. On the other hand, probing surface antiferromagnetism is quite challenging due to their lack of net magnetic moment. It is also important and interesting to study the details of surface electronic structure of antiferromagnetic materials and correlate them to their surface magnetism. When discussing about surface magnetism i.e. low dimensional magnetism the following points are important. First of all, any change in the electronic state occupation results in a change of surface magnetic moment. Lower atomic coordination results in band narrowing leading to a further modification in surface moments. From atomic perspective one expects these moments to increase at the surface since the dimensionality of the surface atomic layer is in between bulk and isolated atoms. Secondly, from statistical mechanics perspective, the average surface moment at non-zero temperature is expected to decrease. For surfaces a loss of magnetic neighbor represents weakening of exchange interaction, which results in a significant decrement in magnetic order with temperature, a changed ordering temperature and a change in critical behavior compared to bulk. Third, the broken translational symmetry along the normal direction to the surface makes the orbital momentum along this direction less quenched and making the spin

orbit coupling stronger leading to large magnetic anisotropy at surfaces. This can dominate over the system's magnetic anisotropy and force the easy magnetic direction of the sample to be oriented towards perpendicular to the sample surface. Fourth, the surface antiferromagnetism is strongly dependent on the physical structure of the film surface; the flat or multilayer growth mode, surface alloying, defects, step and step-edges, terraces formation *etc.* These interesting aspects provoke deeper studies in surface antiferromagnetism in their reduced dimension. As case studies, two types of model antiferromagnetic thin film systems, A) an insulating transition-metal oxide, Nickel oxide (NiO) thin films and B) an elemental transition metal Cr monolayer film. NiO is a prototype bulk antiferromagnet, well known as a wide band gap insulator. This mono-oxide has simple crystallographic structure, its magnetic structure is not simple though and hence it attracted many research studies on its magnetic and electronic structures since decades. Cr, on the other hand, is known as spin density wave (SDW) antiferromagnet having quite complex magnetic structure in its bulk format [1]. When deposited as one monolayer overlayer its magnetic structure becomes commensurate with giant enhancement of magnetic moments [2,3]. The electronic structure (mainly the  $3d$  valence band) shows a drastic change at reduced dimension of the film. Both these systems, the first one, a 3D antiferromagnet (when deposited as ultrathin film one may consider as a quassi-3D system) and the second one, a purely 2D antiferromagnet are two extremely interesting prototypical systems and their growth, structure, electronic and magnetic structures are the main focus of this thesis. The general discussion of surface antiferromagnetism will be discussed in thesis chapter 1.

**Experimental techniques and methods:** The electronic structure measurements have been performed using the photoemission technique in the ARPES (Angle Resolved PhotoEmission Spectroscopy) laboratory at Saha Institute of Nuclear Physics, Kolkata [4]. The valence band and the core levels are excited by ultraviolet and x-ray photons respectively resulting in UPS (Ultraviolet Photoemission

Spectroscopy) and XPS (X-ray Photoemission Spectroscopy). The ARPES set-up is made of mainly three vacuum chambers, (1) Load Lock chamber, the entrance chamber for any sample from atmospheric ambient pressure to high vacuum (HV),  $1 \times 10^{-9}$  mbar. (2) Preparation chamber, where the sample can be cleaved, sputtered, annealed at required temperatures, thin films are deposited on chosen substrates; this chamber consists of a four-grid Low Energy Electron Diffraction (LEED) instrument which helps in determining the crystalline quality of the sample as well as their crystalline directions. (3) Analysis chamber, which is composed of monochromatic Al  $K_{\alpha}$  x-ray source (photon energy: 1486.7 eV) and ultraviolet photon sources He  $I_{\alpha}$  (21.2 eV) and He  $II_{\alpha}$  (40.8 eV). The VG SCIENTA-R4000WAL electron energy analyzer with 2D-CCD detector is there attached to the analysis chamber which resolves the photoelectrons according to their kinetic energy ( $E_k$ ) and emission angles ( $\theta_e$ ). Imaging the antiferromagnetic nanodomains of NiO films were performed by using mainly two techniques: (1) the well established, X-ray Magnetic Linear Dichroism-PhotoEmission Electron Microscopy (XMLD-PEEM), where plane polarized x-ray is used to probe the surface antiferromagnetic domains; (2) the new approach, Antiferromagnetic Low Energy Electron Microscopy (AFM-LEEM), where low energy electrons are used to probe the surface antiferromagnetism of the sample. These magnetic imaging experiments were performed at Nanospectroscopy beamline of Elettra synchrotron, Italy [5]. Some of the magnetic studies e.g. the intensity variation of the antiferromagnetic half-order spots in Low Energy Electron Diffraction (LEED) with sample temperature in both cases of NiO and Cr film at different film thickness are performed by regular four-grid LEED apparatus in the ARPES laboratory with high sensitive CCD camera in order to study thickness dependence of the magnetic ordering Néel temperature ( $T_N$ ). The detail of the techniques used for different measurements has been discussed in chapter 2 of this thesis.

**Growth of monolayer Cr film on Ag(001):** This chapter discusses the details of the growth of antiferromagnetic Cr film and its strong dependence on growth

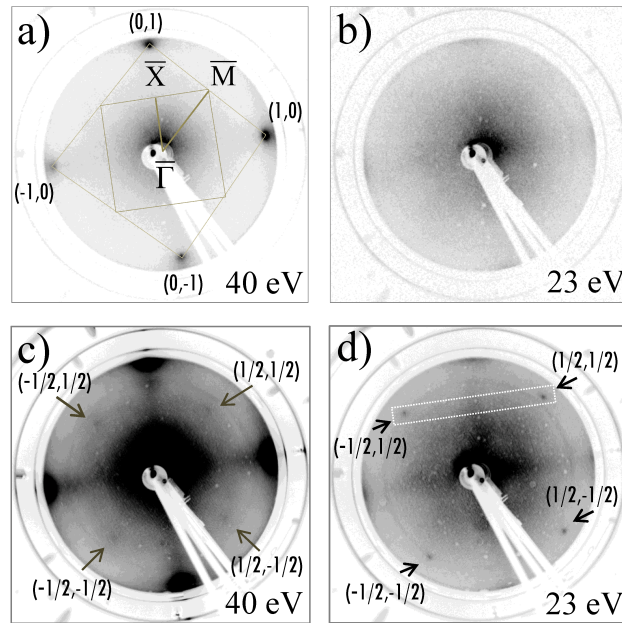


**Figure 1:** LEED of Cr 1 ML film grown on Ag(100). Growth temperature RT; at beam energy (a) 40 eV (b) 23 eV. Growth temperature 428 K; at beam energy (c) 40 eV (d) 23 eV.

conditions. In case of the growth of 1 ML antiferromagnetic Cr film on Ag(001), the substrate surface quality is a vital parameter since the stability of the overlayer's physical structure and magnetism strongly depends on the growth mechanism of the film. BCC (body centered cubic) Cr with its lattice parameter  $2.88 \text{ \AA}$  grows on Ag(001) pseudomorphically [6] with lattice mismatch less than 0.3%. At room temperature deposition Cr grows in multilayer structure from the early stage [7]. On the other hand, at higher temperature deposition an increased surface mobility helps in flat growth of Cr film on Ag(001) [8]. At very high temperature there occurs alloy formation destroying epitaxial quality. Rigorous studies have been performed to optimize the best growth condition for a flat 1 ML Cr film. How different growth parameters like growth temperature, deposition rate, direct and step wise growth and substrate surface quality affects the growth procedure have been discussed in this chapter in detail [9]. The segregation of Ag atoms on Cr monolayer film under high

temperature deposition [6,10,11], the interlayer intermixing under thermal treatment has also been focussed [12]. In figure 1(a) and (b), the LEED of 1 ML Cr film grown on Ag(001) at RT has been shown for 40 and 23 eV respectively where no half-order spots are visible. Whereas in figure 1(c) and (d)  $c(2\times 2)$  half orders are visible for flat 1 ML Cr film grown at 428 K at same beam energies. Appearance of these half orders is trace of 2D antiferromagnetism persistent in the film. This chapter deals with standardizing various growth parameters to prepare the flat antiferromagnetic monolayer Cr film over Ag substrate in correlation with the physical structure of the film. In chapter 3, the details on the flat monolayer growth of antiferromagnetic Cr layer has been discussed.

**Structure of antiferromagnetic Cr monolayer on Ag(001):** The surface energy of Cr ( $= 2400 \text{ mJ/m}^2$ ) is much higher than that of the Ag substrate ( $= 1250 \text{ mJ/m}^2$ ). According to Bauer's criterion [13], a flat growth mode (surface wetting) is favored when the surface free energy of the deposited metal is sufficiently lower than the free energy of the substrate, under thermodynamic equilibrium. For this reason, instead of the growth of a flat Cr overlayer, one may have the growth of multilayer domains or islands, or even a flat layer of Cr buried under one or more Ag layers, if the kinetic barriers can be overcome. It is crucial to have a detailed idea about the structure of Cr film at its ultrathin (sub-monolayer) film thickness range is as we find that its magnetic properties have intimate correlations with its physical structure. The structure of the film depends on different growth modes which can be achieved at various deposition conditions. Chapter 4 consists of experimental proof of the antiferromagnetic Cr monolayer being sandwiched between  $p(1\times 1)$  monolayer Ag on top and Ag(001) crystal at bottom, which is supported by theoretical calculations.

**Electronic structure and magnetism of monolayer Cr film:** At reduced dimension, in the form of monolayer flat film, the giant enhancement of magnetic moments of Cr sites stabilizes a  $c(2\times 2)$  structure with commensurate surface antiferromagnetism. The  $3d$  valence electrons which manipulate the magnetic behavior of Cr

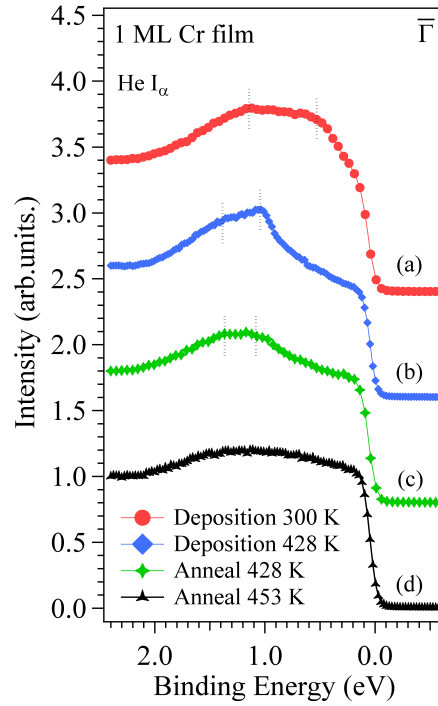


**Figure 2:** ARPES line spectra of 1 ML Cr/Ag(100) at position (a) deposited at RT(300 K) (b) deposited at 428 K (c) After post deposition anneal at 428 K for 30 min. (d) After post-deposition anneal at 453 K for 30 min.

film have binding energy that lies within the 0-2 eV mainly where there exist no other Ag bands except the *sp* bands. Cr *d* bands have negligible electronic hybridization with Ag bands and hence they are almost unaffected by the substrate electronic structure. As per LEED study Cr monolayer shows antiferromagnetic half orders in the sub monolayer film thickness range and vanishes with increasing film thickness close to 2 ML. The valence band structure of flat 1 ML antiferromagnetic Cr film is completely different compared to its paramagnetic phase in thicker films [14]. In figure 2, the ARPES line profile of valence band structure at  $\bar{\Gamma}$  position for different growth and post deposition annealing temperatures. The room temperature prepared film [spectra (a)] consists of mostly multilayer islands and few small monolayer terraces. The valence band electronic structure is a mixture of both paramagnetic and antiferromagnetic phases. A band crossing the Fermi level implies metallicity of

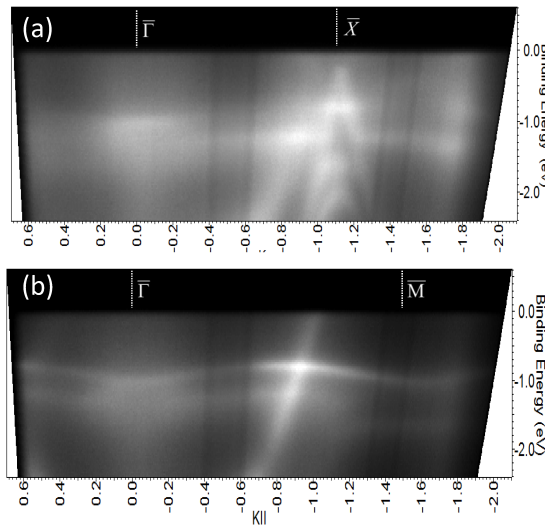


**Figure 3:** Cr  $3d$  valence band along (a)  $\bar{\Gamma}$  to  $\bar{X}$ . (b)  $\bar{\Gamma}$  to  $\bar{M}$  symmetry points. Source He  $I_{\alpha}$  (21.2 eV).

the film [dispersion not shown here]. The film grown at 428 K on the other hand [spectra (b)] shows two well resolved antiferromagnetic  $3d$  bands  $\bar{\Gamma}_5$  and  $\bar{\Gamma}_1$  at 1.1 and 1.4 eV binding energy positions [15]. When this film is annealed at 428 K for 30 min [spectra (c)] the intensity of these antiferromagnetic bands decreases. The  $c(2 \times 2)$  half-order spots disappear in LEED. Annealing at further higher temperature (453 K) [spectra (d)] results in almost uniform intensity within the 0-2 eV binding energy which indicates complete destruction of antiferromagnetic phase. This is a result of Cr-Ag intermixing/alloying at the top surface which destroys the crystalline quality as well as the electronic structure of the film. A thickness dependent study of valence band electronic structure of Cr film was also performed, where we observed maximum half-order intensity at 1.2 ML. In figure 3(a) and (b) the VB of Cr  $3d$  probed by ARPES using He  $I_{\alpha}$  source are shown for two different symmetry directions. The symmetry of the band dispersions indicates to the  $c(2 \times 2)$  phase inherent in the 1.2 ML Cr film. A rigorous XPS study on the Cr  $2p$  core level electronic structure was performed at different film thickness.

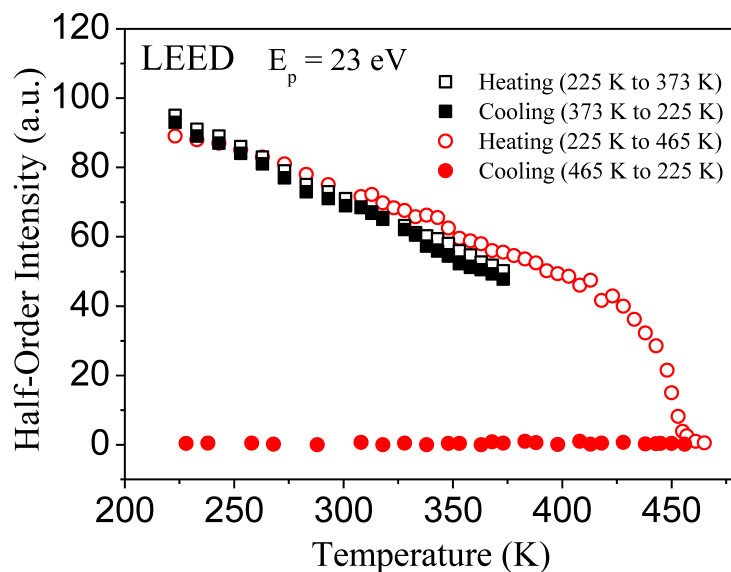


**Figure 4:** Temperature variation of  $c(2 \times 2)$  half-order average intensity of 1 ML Cr film showing an irreversible phase transition above 455 K.

It was theoretically predicted and experimentally demonstrated that there occurs huge enhancement of magnetic moments (500-600%) at the surface of bulk Cr and in reduced dimension as monolayer over a suitable substrate. Our experimental results, as mentioned before, show appearance of very low intensity  $c(2 \times 2)$  magnetic superstructure in LEED whose intensity at 23 eV beam energy is only 2% with respect to the integer order (1,0) spots (at 55 eV) while measured at RT [16]. These half-order  $(1/2, 1/2)$  spots are visible distinctly within very low beam energy range of 20-40 eV with a high exposure and high gain parameter of the 12-bit camera associated with our LEED instrument. These magnetic spots originate from the exchange interaction between the in plane Cr moments and the electron spin moments; hence much weaker than the integer order spot intensities which are the results of coulomb interactions. In figure 4, the temperature variation of LEED half-order average intensities are shown for a 1.2 ML Cr film thickness at which we find the maximum half-order intensity. Experimental data shows that when sample temperature is increased from 225 K to 373 K intensity falls down linearly but it recovers back to its initial value

when film is cooled back to low temperature. On the other hand, increasing the sample temperature upto 455 K leads to complete disappearance of the half-order spots which is an irreversible process upon cooling down the sample. The Cr-Ag intermixing procedure destroys the structural quality of the film completely which results in rupturing the in-plane commensurate antiferromagnetic ordering of the Cr moments above the critical phase transition temperature 455 K. The magnetic as well as electronic structure of 1 ML AF Cr overlayer is discussed in chapter 5 of this thesis.

**Growth of NiO film on Ag(001): characterization of electronic structure:** NiO has simple rocksalt structure with stable ionic bonding between Ni and O atoms. Hence its surface free energy is lower compared to any noble metal surface. Therefore, as per Bauer's criterion, it is expected that NiO will wet the metal surface to stabilize surface free energy. The face centred cubic Ag(001) crystal has a surface lattice constant of 4.089 Å whereas NiO with its inter-penetrating fcc structure has a lattice parameter of 4.17 Å [17], so there is a lattice mismatch of 2% only, which helps NiO to grow on top of Ag(001) in layer by layer fashion with small amount of interfacial strain. Before the deposition of NiO film the preparation of highest quality substrate is an important parameter for MBE growth and also to minimize the number of terraces, domains and step-like structures on the substrate surface. The Ag(001) crystal substrate is prepared by repeated cycles of Ar<sup>+</sup> ion sputtering for 15 min followed by annealing at 823 K for 30 min. The sputtering and annealing procedure is repeated until a bright and sharp  $p(1 \times 1)$  four-fold LEED pattern is observed. The Ar<sup>+</sup> sputtering digs out layers from the surface of the Ag(001) single crystal exposing fresh layer at the top. Sputtering ruptures soft metal surface degrading the surface crystalline quality. A high temperature annealing recovers the crystalline quality *via* lattice vibration. Nickel is evaporated from an effusion cell at a rate of 0.2 ML/min holding the crystal at 473 K in oxygen environment (pressure:  $7 \times 10^{-6}$  mbar). The deposited film is then annealed at 573 K for 30 min in the same oxygen pressure.

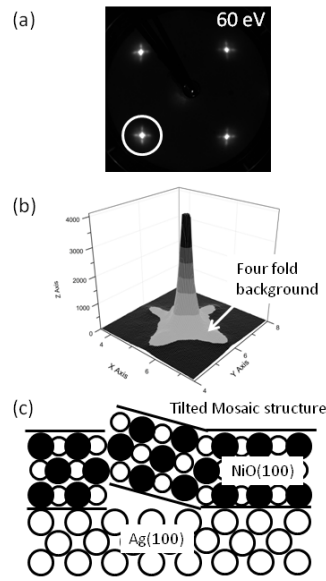


**Figure 5:** (a) LEED of 10ML NiO/Ag(100), beam energy: 60 eV. (b) 3D intensity profile of the (-1,0) LEED spot. (c) the mosaic structure formation in NiO film due to misfit dislocation is shown.

This improves the crystalline quality of the film better as confirmed from LEED. A good quality NiO film produces sharp  $p(1 \times 1)$  four-fold LEED pattern following the Ag(001) substrate. The crystalline structure and quality of the film can be well controlled by varying the nickel to oxygen stoichiometry by controlling the oxygen pressure while the film is deposited. Higher temperature growth helps to improve the crystalline quality of the deposited film reducing number of defect sites. However the sticking coefficient of oxygen decreases at sufficiently high temperature (above 623 K) resulting in the growth of a NiO film with sufficient amount of un-reacted metallic nickel left in the film as per earlier reports [18]. However, our experimental observation reveals that RT grown films shows four extra satellite spots along  $\langle 001 \rangle$  directions surrounding each LEED spot [shown in figure 5(a) and (b)] which signifies formation of mosaic structures [19] [shown in figure 5(c)] on Ag(001) surface. A post deposition anneal reduces the four fold background making the surface quality better. Therefore it is important to find out an optimum growth condition for smooth and

defect free growth of the film. Under mild  $\text{Ar}^+$  ion sputtering oxygen vacancy defects are created mainly on the surface of the film which creates circular ‘halo’s surrounding each LEED spots [not shown here]. Under vacuum annealing the film at 573 K for 30 min the oxygen vacancy defects at the film surface are partially compensated by oxygen atoms diffusing out the bulk of the film which results in reduction of halo region and FWHM of each spot. Under annealing treatment in oxygen environment almost all the defect sites are removed from the film surface resulting in smoother defect free surface as evident from sharper LEED spots. LEED IV calculation in accordance with experimental results can predict the detailed surface structural information. This thesis contains elaborative description on the growth and structure of NiO film.

Being well-known as a prototype strongly correlated insulating system the electronic structure of NiO has always been an interesting research topic. There is strong on-site  $d$ - $d$  coulomb interaction between the nickel  $3d$  electrons ( $U_{dd}$ ). This prompts electronic localization in this system resulting in the insulating behaviour of this transition metal mono-oxide. The electronic ground state of NiO is  $\text{Ni } 3d^8 \text{ O } 2p^6$  at its purely ionic picture. The Ni  $3d$  orbitals are strongly localized and well hybridized with O  $2p$  orbital. The on-site Coulomb interaction ( $U_{dd}$ ) is defined as the energy needed for transition from  $d^8 d^8$  to  $d^7 d^9$  state, i.e. the energy required for hopping of one electron from one Ni site to another. The charge transfer energy ( $\Delta$ ) is the energy required for  $d^8$  to  $d^9 L$  transition, i.e. the energy needed for an electron transfer from oxygen  $2p$  orbital to transition metal  $3d$  orbital. Here ‘ $L$ ’ stands for a ligand (oxygen) hole. The one electron band theory can not explain the insulating nature of this material since it does not consider the on-site Coulomb term  $U$ . The local density approximation of density functional theory taking into account of the coulomb potential (LDA+ $U$ ) reveals that there is 4 eV band gap in NiO. Since long time NiO was believed to be a Mott insulator [20], but later it was well established that the charge transfer energy  $\Delta$  in NiO being smaller than  $U$

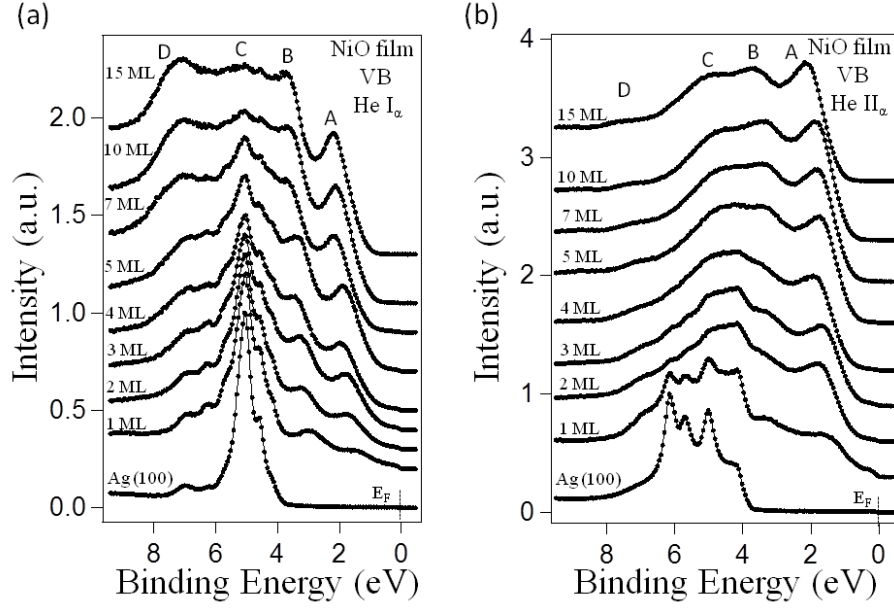


**Figure 6:** ARPES line spectra at  $\bar{\Gamma}$  position for NiO film of different thickness probed by (a) He  $I_{\alpha}$  and (b) He  $II_{\alpha}$ .

it should be called a charge transfer insulator. In figure 6(a) and (b) the ARPES valence band line profile at  $\bar{\Gamma}$  position of NiO films for various thicknesses are shown alongwith the Ag(001) valence band line profile probed by He  $I_{\alpha}$  and He  $II_{\alpha}$  photon sources respectively. In case of bare Ag substrate the d bands are prominent from 4 to 8 eV binding energy range. The Ni  $3d$  bands appears close to 2 eV binding energy which lies within the binding energy window where no Ag band exists at  $\bar{\Gamma}$  position, and hence these bands are visible starting from the lowest NiO film thickness shown in the data. On the other hand, the O  $2p$  bands appear close to 5 eV binding energy and hence become prominent when thicker oxide films are deposited [21]. The Ni  $2p$  and O  $1s$  core level photoemission data are shown in figure 7(a) and (b) respectively for different film thickness. The core hole created by the photoemission process repels the holes of the partially filled  $3d$  orbital; electrons are contributed by the surrounding oxygen ligands to the Ni atoms in octahedral symmetry. The photoemission final states created are hence mixed states  $|\phi_f\rangle = |c^{-1}d^9L^{-1}\rangle +$

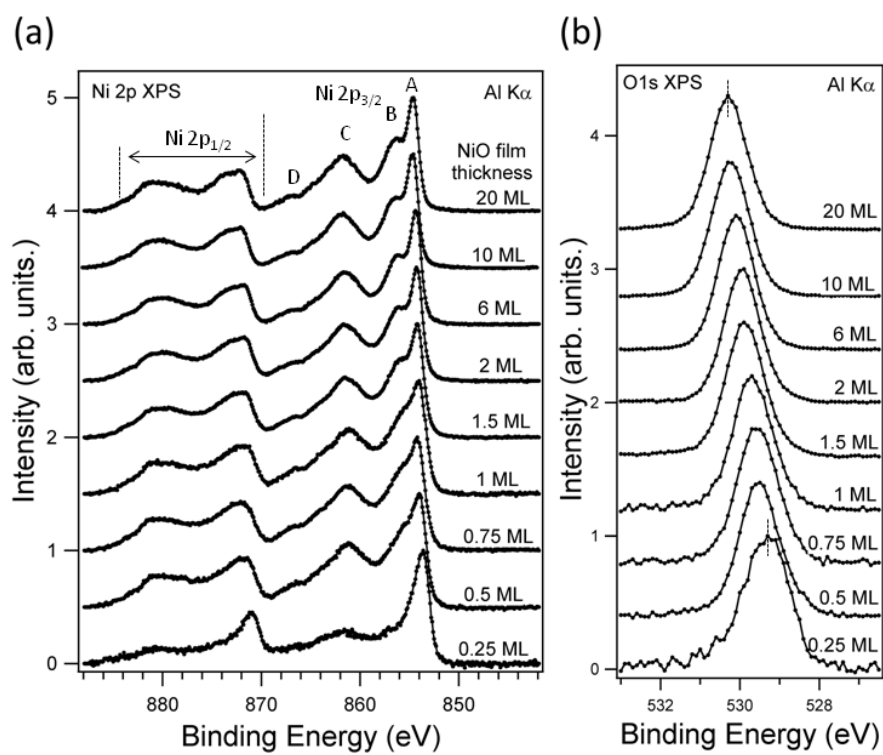


**Figure 7:** XPS of NiO at different film thickness (a) Ni 2p. (b) O 1s.

$|c^{-1}d^{10}L^{-2}\rangle + |c^{-1}d^8\rangle$ , where  $L^{-1}$  represents a hole created in ligand orbital and  $c^{-1}$  is a core hole created in photoemission process [22]. Different peaks are denoted for Ni  $2p$  and O  $1s$  spectra. The growth and thickness dependence of the electronic structures and their temperature dependence are narrated in chapter 6 of the thesis.

**Magnetic structure of epitaxial NiO film:** The moments associated with the nickel atoms are arranged in such an order that along the  $\langle 111 \rangle$  direction the spin-up and spin-down nickel layers are separated by oxygen atomic layers in a perfect NiO single crystal. Having a cubic structure NiO has four symmetric  $\langle 111 \rangle$  antiferromagnetic directions. There exists four Twin (T) domains in NiO single crystal called  $T_1$ ,  $T_2$ ,  $T_3$  and  $T_4$  labeled by four different directions  $(111)$ ,  $(\bar{1}\bar{1}1)$ ,  $(11\bar{1})$  and  $(\bar{1}11)$  respectively normal to those planes. In each T domain there are three possible directions along which the Ni moments are antiferromagnetically aligned forming Spin (S) domains [23]. In case of NiO, thin films the twin as well as spin domain sizes are dominated by the physical grain size. Having zero net magnetic moment ( $\vec{M}=0$ ) there are only few techniques available for probing the domains of antiferromagnetic materials. We have used two dedicated techniques for imaging the antiferromagnetic domains of NiO thin film deposited on top of Ag(001) substrate. First one, X-ray Absorption Spectroscopy (XAS) performed with plane polarized x-ray at Ni  $L_2$  edges, called XMLD (X-ray Magnetic Linear Dichroism) where the absorption cross-section between different multiplet peaks depends on the angle between the magnetic moments with the light polarization vector as well as with the lattice planes. The ratio between the multiplet peak intensity values i.e.  $I_{XMLD} = |I_{L2a}/I_{L2b}|$  is the resultant XMLD signal. XMLD directly probes the magnetic anisotropy or the measure of expectation value  $\langle \vec{M}^2 \rangle$ . The dependency of the XMLD intensity on the angle between the plane of polarization and the expectation value  $\langle \vec{M}^2 \rangle$  can be expressed by:  $I_L = I_0 - C \langle \vec{M}^2 \rangle (3\cos^2\theta - 1)$  where  $\theta$  is the angle between  $\langle \vec{M}^2 \rangle$  and  $\vec{E}$  (the plane of polarization). Microscopic images of the magnetic domains were collected using photoemission electron microscopy (PEEM) using the XMLD

contrast to generate the images [24,25]. The magnetic unit cell in NiO is double than that of its chemical unit cell because of its antiferromagnetic spin arrangement. Low energy electrons are exchange scattered from the Ni moments in the sample which produces four-fold  $p(2\times 2)$  weak intensity (2% compared to integer orders) half-order spots in the LEED pattern. The second technique, Antiferromagnetic low energy electron microscopy (AFM-LEEM), where the dark field imaging technique using the half-order electrons probes the antiferromagnetic domains with quite better resolution and thus is more efficient in probing the tiny magnetic nanodomains of NiO thin film [26,27]. The antiferromagnetic origin of the half-order spots becomes evident as their intensity decreases with increasing sample temperature eventually vanishing near 523 K which is the Neel temperature ( $T_N$ ) of NiO single crystal. The antiferromagnetic strength and hence  $T_N$  of the sample varies with film thickness. Selecting a single half-order spot by a contrast aperture electron microscopy was performed in LEEM instrument which probes one set of antiferromagnetic twin domains. In figure 8, the AF domains of NiO film at its different film thickness (6, 18, 40 and 60 ML) are shown where domain evolution can be understood with increasing film thickness. The domains probed by x-ray are shown in the top row in comparison with the same domains probed by unpolarized electrons at the bottom. In chapter 7, a rigorous study on the magnetic structure of NiO film and its thickness dependence, the Néel temperature variation with film thickness and the effect of vacancy defect on magnetic strength of the film are discussed.

**Effect of oxygen vacancy defects on the electronic structure and magnetism of NiO film:** In chapter 8, the creation of oxygen vacancies and metallic nickel states at the NiO/Ag(001) film surface and its effect on the valence band and core level electronic structure have been studied. While the oxygen vacancies in NiO films can be produced by UHV annealing at high temperature as well as mild  $\text{Ar}^+$  sputtering; metallic NiO states are only produced in the film by severe sputtering process. Angle dependent photoemission studies provide an idea about

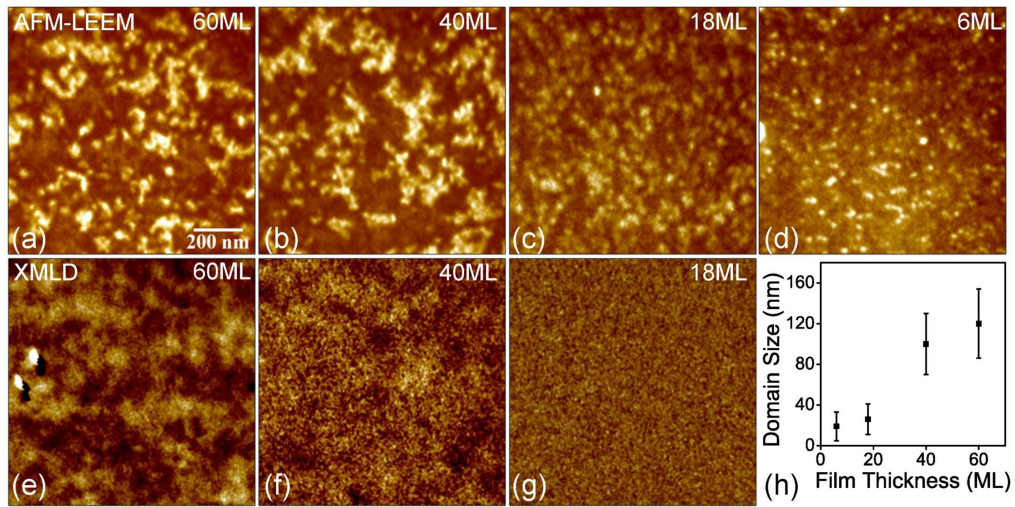


**Figure 8:** Top row shows AFM-LEEM images of the antiferromagnetic twin domains of NiO films of thickness (a) 60 ML (b) 40 ML (c) 19 ML and (d) 6 ML. Bottom row shows the XMLD-PEEM images of (e) 60 ML (f) 40 ML (g) 18 ML NiO film. Figure (h) represents the thickness dependence of domain size.

the distribution of defect densities at various depths of the oxide film. The effect of UHV and oxygen annealing on the electronic structure of the film has also been reinvestigated.

Removal of oxygen atom affect the superexchange interaction between the up-spin and down-spin Ni atoms in the crystalline NiO film and thus decreasing the antiferromagnetic order and strength of the film which is reflected in the Néel temperature decrement. The temperature dependency of the LEED half-order intensity shows consistent decrement of  $T_N$  value with increased oxygen vacancy concentration at the NiO film surface.

### References:

- [1] H. Zabel, J. Phys. Cond. Matt., 11, 9303 (1999).
- [2] A. J. Freeman and C. L. Fu, J. App. Phys. , 61, 3356 (1987).
- [3] S. Blügel, M. Weinert, P. H. Dederichs, Phys. Rev. Lett., 60, 1077 (1988).
- [4] S. K. Mahatha, K. S. R. Menon, Current Science, 98, 759 (2010).

- [5] A. Locatelli, L. Aballe, T. O. Mendes, M. Kiskinova and E. Bauer, Surf. Interface Anal., 38, 1554 (2006).
- [6] P. Steadman, C. Norris, C. L. Nicklin, N. Jones and J. S. G. Taylor, Phys. Rev. B., 64, 245412 (2001).
- [7] C. Krembel, M. C. Hanf, J.C. Peruchetti, D. Bolmont and G. Gewinner, Surf. Sci., 269/270, 748 (1992).
- [8] C. Krembel, M. C. Hanf, J.C. Peruchetti, D. Bolmont and G. Gewinner, Phys. Rev. B, 44, 8407 (1991).
- [9] J. Das, A. K. Kundu and K. S. R. Menon, Vacuum, 112, 5 (2015).
- [10] C. Krembel, M. C. Hanf, J.C. Peruchetti, D. Bolmont and G. Gewinner, Journ. of Vac. Sci. and Tech. A, 10, 3325 (1992).
- [11] J. F. Lawler, R.G. P. Van der Kraan, H. Van. Kempen, A. J. Quinn, 165, 195 (1997).
- [12] M.C. Hanf, C. Krembel and G. Gewinner, Surf. Sci., 519, 1 (2002).
- [13] Bauer E. Z Kristallogr 110, 372 (1958).
- [14] C. Krembel, M. C. Hanf, J.C. Peruchetti, D. Bolmont and G. Gewinner, Phys. Rev. B., 44, 11472 (1991).
- [15] G. Allan, Phys. Rev. B., 44, 13641 (1991).
- [16] M. C. Hanf, C. Krembel, D. Bolmont and G. Gewinner, Phys. Rev. B., 68, 144419 (2003).
- [17] S. Altieri, L. H. Tjeng, and G. A. Sawatzky, Phys. Rev. B, 61, 16948 (2000).
- [18] C. M. Cheng, C. C. Wang, H. T. Jeng, C.S. Hsue, B.Y. Hsua, D. J. Huang, K. D. Tsueia, 403, 1539 (2008). [19] M. Schluze, R. Reissner, Surf. Sci., 482, 285 (2001).
- [20] B. H. Brandow, Advances in Physics, 26, 651 (1977).
- [21] Seolun Yang, Shijin Seong and J.-S. Kim, Journal of Korean Physical Society, 57, 1312 (2010).
- [22] M. A. Van Veenendaal, G. A. Sawatzky, Phys. Rev. Lett, 70, 2459 (1993).
- [23] H. Ohldag, PhD Thesis, *Exchange coupling of Co and Fe on antiferromagnetic*

*NiO investigated by dichroism x-ray absorption spectromicroscopy*, Universitäts und Landbibliothek Düsseldorf, (2003).

[24] Y. Z. Wu, Y. Zhao, E. Arenholz, A. T. Young, B. Sinkovic, C. Won, and Z. Q. Qiu, *Phys. Rev. B.*, 78, 064413 (2008).

[25] J. Sthr, A. Scholl, T. J. Regan, S. Anders, J. Lüning, M. R. Scheinfein, H. A. Padmore, and R. L. White, *Phys. Rev. Lett.*, 83, 1862 (1999).

[26] J. Das and K. S. R. Menon, *AIP Conf. Proc.*, 1536, 175 (2013).

[27] K.S.R. Menon, S. Mandal, J. Das, T. O. Menten, M. A. Nino, A. Locatelli and R. Belkhou, *Phys. Rev. B.*, 84, 132402 (2011).

## List of Figures

- 1 LEED of Cr 1 ML film grown on Ag(100). Growth temperature RT; at beam energy (a) 40 eV (b) 23 eV. Growth temperature 428 K; at beam energy (c) 40 eV (d) 23 eV. . . . . xvi
- 2 ARPES line spectra of 1 ML Cr/Ag(100) at position (a) deposited at RT(300 K) (b) deposited at 428 K (c) After post deposition anneal at 428 K for 30 min. (d) After post-deposition anneal at 453 K for 30 min. xviii
- 3 Cr *3d* valence band along (a)  $\bar{\Gamma}$  to  $\bar{X}$ . (b)  $\bar{\Gamma}$  to  $\bar{M}$  symmetry points. Source He  $I_{\alpha}$  (21.2 eV). . . . . xix
- 4 Temperature variation of  $c(2\times 2)$  half-order average intensity of 1 ML Cr film showing an irreversible phase transition above 455 K. . . . . xx
- 5 (a) LEED of 10ML NiO/Ag(100), beam energy: 60 eV. (b) 3D intensity profile of the (-1,0) LEED spot. (c) the mosaic structure formation in NiO film due to misfit dislocation is shown. . . . . xxii
- 6 ARPES line spectra at  $\Gamma$  position for NiO film of different thickness probed by (a) He  $I_{\alpha}$  and (b) He  $II_{\alpha}$ . . . . . xxiv
- 7 XPS of NiO at different film thickness (a) Ni 2p. (b) O 1s. . . . . xxv

8	Top row shows AFM-LEEM images of the antiferromagnetic twin domains of NiO films of thickness (a) 60 ML (b) 40 ML (c) 19 ML and (d) 6 ML. Bottom row shows the XMLD-PEEM images of (e) 60 ML (f) 40 ML (g) 18 ML NiO film. Figure (h) represents the thickness dependence of domain size. . . . .	xxviii
1.1	Schematic representation of band narrowing and resulting increased magnetic moments at surfaces and in ultrathin films. . . . .	8
2.1	(a) In-plane tensile strain, (b) Out-of-plane compressive strain (c) Lattice parameter relaxation at a critical thickness $d_c$ . . . . .	17
2.2	Universal curve of mean free path for the inelastic scattering of electrons in a solid [28]. . . . .	21
2.3	Schematic of a conventional rear-view LEED setup. . . . .	23
2.4	For a fixed sample distance $z=18$ mm from the LEED instrument, average radial profile plots of LEED spots have been shown as a function of focus voltage. . . . .	26
2.5	For a focus voltage of 53 volt, average radial profile plots of LEED spots have been shown as a function of sample distance. . . . .	27
2.6	Our LEED IV data for (0,1) spots of Ag(001) single crystal has been compared with the IV data of earlier reported data by Schindler <i>et al.</i> [33]. . . . .	28
2.7	Adlayer superstructure(a) $p(1\times 1)$ (b) $p(2\times 2)$ configuration. . . . .	29
2.8	Adlayer superstructure a) $p(1\times 1)$ (b) $c(2\times 2)$ configuration. . . . .	29

2.9	(a) The antiferromagnetic order of Ni spins in NiO crystal shows that the magnetic unit cell is double than the chemical unit cell. Existence of the oxygen atoms has been neglected for simplification. (b) Antiferromagnetic arrangement of the Cr moments in monolayer film over Ag(001) single crystal. (c) $p(2\times 2)$ LEED half-order spots, in case of NiO, corresponding to figure (a). (d) $c(2\times 2)$ LEED half-order spots, in case of Cr, corresponding to figure (b). . . . .	30
2.10	Sketch of a modern photoemission experiment. . . . .	34
2.11	Schematic view of the photoemission process depicting relation between energy levels in solid and the electron energy distribution produced by photon of energy $h\nu$ . [39,40] . . . . .	35
2.12	The schematic diagram showing different chambers and components of the ARPES system at SINP. . . . .	42
2.13	Photograph of SINP-ARPES laboratory. . . . .	43
2.14	The schematic diagram (from Ref [42]) of the Monochromatic UV lamp used in the ARPES setup. . . . .	46
2.15	Experimental energy resolution measurement on Xe $5p_{3/2}$ . . . . .	47
2.16	Schematic of a concentric hemispherical electron energy analyzer. Taken from [32] . . . . .	50
2.17	Schematic of the Scienta electron energy analyzer with 2D detector. [32]	51
2.18	Schematic representation of energy balance (top) and typical spectra (bottom) for a) an EDC experiment and b) a CIS experiment [55]. . .	52
2.19	Schematics describing different modes of measurements in x-ray absorption spectroscopy (see text for details). . . . .	53
2.20	The x-ray absorption, creation of photoelectrons and Auger electrons. Number of emitted electrons has been plotted against electron kinetic energy. . . . .	55

2.21	(a) The absorption of plane polarized x-ray by the NiO sample. The plane of polarization of the incident x-ray may be parallel or perpendicular to the sample surface. (b) The x-ray absorption spectra at Ni $L$ is shown. (c) The multiplet splitting of the Ni $L_2$ peak is shown. . . . .	57
2.22	Schematics of HP and VP x-ray incidence on NiO film. . . . .	59
2.23	Simplified sketch illustrating basic components of a low energy (or photoemission) electron microscope. . . . .	61
2.24	LEED pattern of 60 ML NiO/Ag(001) (a) 60 eV. (b) 30 eV, the half order (1/2,0) spots are indicated by A, B, C and D. . . . .	62
2.25	(a) Bright-field and (b) dark-field LEEM images (30 eV beam energy) of (the same region of) NiO/Ag(100) surface. . . . .	63
2.26	Schematics of a PhotoEmission Electron Microscope (PEEM). . . . .	65
3.1	(a) Top surface of Ag(001) fcc crystal; the surface non-primitive unit cell is shown which has lattice constant 4.09 Å (b) 1 ML Cr with its surface unit cell having lattice constant 2.88 Å (c) bcc Cr grows on fcc Ag(001) crystal epitaxially with its <100> crystallographic direction 45° rotated. . . . .	74
3.2	$p(1 \times 1)$ LEED pattern showing the four fold integer order spots in case of (a) clean Ag(001) substrate (b) 1 ML Cr deposited on Ag(001) at 300 K (RT). (c) 1 ML Cr deposited on Ag(001) at 428 K. (d) Enhanced contrast of figure (c); four extra low intensity spots are visible at (1/2, 1/2) positions. . . . .	77
3.3	(a) The average intensity plot of the $c(2 \times 2)$ half orders (LEED IV) is shown against electron beam energy range 20-45 eV. . . . .	78

- 3.4 (a) LEED pattern of monolayer Cr film deposited at 428 K; existence of distinguishable four-fold half-order  $(1/2, 1/2)$  spots. Integer order  $(1,0)$  spots do not enter into the field-of-view of LEED screen at this low beam energy. (b) LEED pattern of monolayer Cr film deposited at 300 K; no existence of  $(1/2, 1/2)$  spots. (c) Line profile drawn over half-order spots at different sample temperatures: 300 K, 380 K and 460 K; showing intensity variation of half orders at different temperatures. (d) Schematic of antiferromagnetic spin arrangement in monolayer Cr film over Ag(001). . . . . 80
- 3.5 Temperature variation of LEED  $(1/2, 1/2)$  spots. Once their intensity vanishes to zero they do not reappear back upon cooling down the sample. . . . . 82
- 3.6 LEED of 1 ML Cr film deposited on Ag(001) at various growth temperatures : (a) 300 K (b) 373 K (c) 406 K (d) 417 K (e) 428 K (f) 455 K. All the LEED data are presented for 23 eV electron beam energy with enhanced contrast to show the half-order  $(1/2, 1/2)$  spots. Location of the  $c(2\times 2)$  half-order spots are indicated by small arrows. The integer order spots do not enter into the field of view of screen at this low beam energy. Position of the half orders appear to be rotated in different images due to mounting of Ag(001) crystal substrate on the sample holder. Maximum half-order intensity is visible at 428 K growth temperature. . . . . 85
- 3.7 Average intensity of  $c(2\times 2)$  half-order spots of 1 ML Cr film deposited on Ag(001) at different substrate temperatures. Inset I: Line profile over LEED half-order spots of 1 ML Cr film deposited at different temperatures. Inset II: FWHM values (in pixels) of the half-order line profiles of 1 ML Cr film deposited at various temperatures. . . . . 86

- 3.8 Figure (a): ARPES spectra from 1 ML Cr film at  $\bar{\Gamma}$  using He I $_{\alpha}$  photons for different cases; spectra (a) film deposited at RT (300 K), spectra (b) deposited at 428 K, spectra (c) deposited at 428 K and further annealed at 428 K, spectra (d) deposited at 428 K and annealed at 453 K are shown. Figure (b): ARPES spectra from 1 ML Cr film at  $\bar{\Gamma}$  using He II $_{\alpha}$ ; spectra (a) film deposited at RT (300 K), spectra b) deposited at 428 K. All measurements have been performed at RT. . . . . 88
- 3.9 Line profiles over LEED half-order spots for Cr film coverages 0.2, 0.4 and 1 ML respectively; (a) deposition in step of 0.2 ML coverage (b) deposition of desired thickness in single shot. ARPES line scan of these Cr coverages at  $\bar{\Gamma}$ ; (c) deposition in step of 0.2 ML (d) direct deposition. . . . . 91
- 3.10 (a) Line profiles over LEED  $c(2 \times 2)$  half-order spots for 1 ML Cr films grown with deposition rates 0.2 Å/min and 0.06 Å/min. (b) Line profile scan at the  $\bar{\Gamma}$  position of ARPES data for bare Ag(100) substrate, 1 ML Cr grown at 428 K. . . . . 94
- 3.11 (a) LEED line profiles drawn over half orders for 1 ML Cr film deposited on Ag(001) substrate annealed at 823 and 773 K. (b) corresponding ARPES line profiles drawn at  $\bar{\Gamma}$ . . . . . 95

- 4.1 LEED pattern at beam energy 23 eV for different Cr coverages on Ag(001): (a) 0.2 ML, no  $c(2 \times 2)$  reconstruction visible (b) 0.5 ML, faint and broad half orders (c) 1 ML,  $(1/2, 1/2)$  spots are distinctly visible (d) 1.2 ML, maximum intensity of the half-order spots (e) 1.5 ML, half orders visible with lower intensity (f) 2 ML, half orders almost invisible. (g) Line profile scan over LEED half-order spots for different Cr coverage. All the line profiles are drawn along the same direction as shown in the rectangular box enclosing the  $(1/2, 1/2)$  spots in figure (d). 104
- 4.2  $c(2 \times 2)$  half-order spot intensity variation with Cr coverage. Beam energy 23 eV. . . . . 105
- 4.3 (a) Antiferromagnetic Cr  $3d$  valence band at  $\bar{M}$  symmetry point for different film coverages probed by He  $I_{\alpha}$ . (b) Band intensity vs. Cr coverage plot corresponding to figure (a). (c) Cr  $3d$  valence band at  $\bar{M}$  symmetry point for different film coverages probed by He  $II_{\alpha}$ . (d) Band intensity plot vs. Cr coverage corresponding to figure (c). . . . . 108
- 4.4 ARPES data at  $\bar{M}$  symmetry point (a) clean Ag(001). (b) 1 ML Cr deposited on Ag(001) at 428 K. Photon energy: 21.2 eV (He  $I_{\alpha}$ ) (c) ARPES line profile spectra drawn at  $\bar{M}$  position for 1 ML Cr deposited on Ag(001) at 300 K (RT) and 428 K. Data are displayed for a broader binding energy range 0-8 eV. Intensity variation of Ag Tamm surface state upon deposition of monolayer Cr is shown. . . . . 111

- 4.5 Geometry of the energetically most favored structure AFM 1Ag/Cr/Ag(001). (a) top view, (b) side view of the system. light gray and dark gray (green online) spheres represent the Ag and Cr atoms, respectively. The red arrows indicate the directions of spins. Note that in the absence of spin-orbit interactions, in-plane and out-of-plane spin directions are equivalent. (c) shows  $\Delta_{ij}$ , the percentage change in interlayer separations, for the first few surface layers. See the text for the definition of  $\Delta_{ij}$  and figure (b) for the convention used in numbering layers. . . . . 116
- 4.6 Theoretically calculated results for the spin-polarized projected densities of states (PDOS) of 1Ag/Cr/Ag(001) in the AFM configuration. The dashed line, solid line and the filled curve indicate the PDOS from first layer Ag  $4d$  states, second layer Cr  $3d$  states and third layer Ag  $4d$  states, respectively. . . . . 117
- 5.1 (a) Schematic diagram of an face centered cubic (fcc) lattice. (b) fcc bulk brillouin zone (BBZ) and its projection to  $\langle 001 \rangle$  direction showing the surface brillouin zone (SBZ) is depicted. (c)  $p(1 \times 1)$  LEED pattern of Ag(001) surface showing the first integer order (1,0) spots; the Wigner-Seitz (WS) cell drawn in the reciprocal space, which is actually the surface brillouin zone is indicated in red square. The  $\bar{\Gamma}$ ,  $\bar{M}$  and  $\bar{X}$  high symmetry points are shown. (d) Schematic diagram of an body centered cubic (bcc) lattice. (e) Bulk brillouin zone of bcc lattice and its surface projection along  $[001]$  direction. (f) Surface brillouin zone and symmetry directions of bcc and fcc lattice. . . . . 124

- 5.2 Comparison of LEED at beam energy 23 eV: (a) clean Ag(001) (b) 1 ML Cr grown on Ag(001) at 428 K; antiferromagnetic (1/2, 1/2) spots visible. ARPES data probing the valence bands along  $\bar{\Gamma}$ - $\bar{M}$  (c) Bare Ag(001) (d) 1 ML Cr/Ag(001). (e) Second derivative of figure (c). (f) Second derivative of figure (d). ARPES data probing the valence bands along  $\bar{\Gamma}$ - $\bar{X}$  (g) Bare Ag(001) (h) 1 ML Cr/Ag(001). (i) Second derivative of figure (g). (j) Second derivative of figure (h). Photon source monochromatic He I $_{\alpha}$  (21.2 eV). . . . . 126
- 5.3 (a) Line profile drawn over the ARPES data at different emission angles; at 0 $^{\circ}$  ( $\bar{\Gamma}$ ), 57 $^{\circ}$  ( $\bar{M}$ ) and 35 $^{\circ}$ . (b) Line profile drawn over the ARPES data at different emission angles; at 0 $^{\circ}$  ( $\bar{\Gamma}$ ) and 30 $^{\circ}$  ( $\bar{X}$ ). Photon source monochromatic He I $_{\alpha}$  (21.2 eV). . . . . 128
- 5.4 ARPES data probing the valence bands along  $\bar{\Gamma}$ - $\bar{M}$  (a) Bare Ag(001) (b) 1 ML Cr/Ag(001). (c) Second derivative of figure (a). (d) Second derivative of figure (b). ARPES data probing the valence bands along  $\bar{\Gamma}$ - $\bar{X}$  (e) Bare Ag(001) (f) 1 ML Cr/Ag(001). (g) Second derivative of figure (e). (h) Second derivative of figure (f). Photon source monochromatic He II $_{\alpha}$  (40.8 eV). . . . . 129
- 5.5 (a) Calculated band structure for a paramagnetic transition metal on a square lattice by Wang [129]. (b) Tight binding calculations of electronic structure of Cr layer adsorbed on Ag(001) surface by G. Allan [133]. . . . . 132
- 5.6 (a) Calculated band structure of bare Ag(001) at the high symmetry point  $\bar{X}$  performed by the group of Prof. Shobhana Narasimhan *et al.* [120] (b) Corresponding experimental ARPES data from our measurements on Ag(001) surface. . . . . 134

5.7	(a) Calculated band structure for 1 Ag/1 Cr/Ag(001) performed by the group of Prof. Shobhana Narasimhan <i>et al.</i> [120] (b) Experimental band structure along $\bar{\Gamma}$ - $\bar{X}$ . . . . .	135
5.8	Second derivative of experimental ARPES data at different Cr coverage: (a) 0.1 ML. (b) 0.2 ML. (c) 0.5 ML. (d) 0.8 ML. (e) 1.2 ML. (f) 1.4 ML. (g) 1.6 ML. (h) 2 ML. (i) 2.5 ML. (j) 5 ML. Each film was deposited directly on Ag(001) crystal kept at 428 K. Band structure along $\bar{\Gamma}$ - $\bar{M}$ . Photon source He I $_{\alpha}$ . ( $\hbar\omega = 21.2$ eV). The antiferromagnetic Cr $3d$ valence band structure is visible from 0.1 ML; Intensity of the AF bands is highest at 1.2 ML. The band structure changes from antiferromagnetic to paramagnetic from coverage greater than 2 ML. . . . .	138
5.9	ARPES data along $\bar{\Gamma}$ - $\bar{M}$ for 1 ML Cr film deposited at (a) 300 K (b) 428 K. Along $\bar{\Gamma}$ - $\bar{X}$ for 1 ML Cr film deposited at (c) 300 K (d) 428 K. Photon source He I $_{\alpha}$ . . . . .	142
5.10	(a) X-ray photoemission spectral data of Cr $2p$ peaks for different Cr coverages. (b) Binding energy shift of Cr $2p_{1/2}$ at submonolayer coverage for deposition temperature 300 K and 428 K. . . . .	143
5.11	(a) Temperature dependence of (1/2, 1/2) spot intensity in LEED at beam energy 23 eV (raw data). (b) Data normalized by Debye-waller factor and fitted by Onsager-Yang equation. . . . .	145
5.12	LEED (1/2, 1/2) spots of monolayer Cr film at beam energy 23 eV for sample temperature (a) 223 K (b) 455 K. ARPES data at $\bar{\Gamma}$ position, sample temperature (c) 223 K, high intensity antiferromagnetic Cr $3d$ bands visible. (d) 455 K, antiferromagnetic bands vanished. . . . .	147
6.1	superexchange interaction in NiO. . . . .	151

- 6.2 (a) XPS Ni  $2p_{3/2}$  peak intensity for deposition of different Ni thickness (in monolayers). (b) Intensity of Ag  $3d$  under deposition of various Ni film thickness. (c) The exponentially increasing Ni  $2p_{3/2}$  intensity and exponentially decaying Ag  $3d_{5/2}$  intensity are plotted against Ni monolayers. . . . . 160
- 6.3 Low Energy Electron Diffraction pattern of (a) clean Ag(001) (b) 0.5 ML Ni/Ag(001) (c) 1 ML Ni/Ag(001), the spots have been encircled to indicate their positions (d) 2 ML Ni/Ag(001). Electron energy 55 eV. 161
- 6.4 XPS Ni  $2p_{3/2}$  peaks for Ni and NiO film are shown. There is 1.7 eV chemical shift in the main line due to oxidation. Photon source: Mg  $K_{\alpha}$  (1253.7 eV) . . . . . 162
- 6.5  $p(1\times 1)$  LEED pattern of 10 ML NiO films deposited on Ag(001) at various growth conditions. Beam energy 57 eV. Rows stand for three different growth temperatures. Columns stand for two different oxygen pressure during growth. . . . . 163
- 6.6 The  $p(1\times 1)$  LEED pattern with a zoomed in view of (1,0) spot has been shown. The mosaic formation due to misfit dislocation has been schematically represented. . . . . 164
- 6.7 O 1s to Ni 2p XPS intensity ratio for different growth conditions of NiO. 166
- 6.8 XPS Ni 2p and O 1s peak intensity plotted for different film thickness. X-ray source: monochromatic Al  $K_{\alpha}$  (1486.6 eV). . . . . 168
- 6.9 (Top) Two metal ion sites with a core hole on one site. (Middle) Screening of an electron from the surrounding oxygen ligands. (Bottom) Nonlocal screening from an electron from a neighboring unit. . . . . 169
- 6.10 The binding energy position shown for different thickness of NiO film. (a) Ni  $2p_{3/2}$  (b) O 1s. Binding energy increases with film thickness for both cases. . . . . 170

6.11	The valence band structure of 20 ML NiO film deposited over Ag(001). Photon source (a) He I $_{\alpha}$ (b) He II $_{\alpha}$ . Bands are shown along $\bar{\Gamma}$ to $\bar{M}$ direction. . . . .	173
6.12	LDA band calculations and experimental data of bulk NiO by Shen <i>et al.</i> [184] along [100] direction. (a) Non-magnetic calculations. (b) Antiferromagnetic calculations. . . . .	174
6.13	The valence band structures of NiO film deposited over Ag(001) for different film thicknesses. Photon source: He I $_{\alpha}$ . Bands are shown at $\bar{\Gamma}$ position along $\bar{M}$ - $\bar{\Gamma}$ - $\bar{M}$ direction. . . . .	176
6.14	The valence band structures of NiO film deposited over Ag(001) for different film thicknesses. Photon source: He II $_{\alpha}$ . Bands are shown at $\bar{\Gamma}$ position along $\bar{M}$ - $\bar{\Gamma}$ - $\bar{M}$ direction. . . . .	178
6.15	Line profiles drawn at $\bar{\Gamma}$ position for bare Ag(001) and different thickness of NiO film. Photon energy: (a) He I $_{\alpha}$ (b) He II $_{\alpha}$ . . . . .	179
6.16	ARPES line profiles drawn at $\bar{\Gamma}$ position for NiO(001)/Ag(001) film at different sample temperatures. Photon energy: He I $_{\alpha}$ . Film thickness 20 ML . . . . .	180
6.17	UPS and XPS to probe the valence band electronic structure of 20 ML NiO film. He I $_{\alpha}$ and He II $_{\alpha}$ photon sources are used as UV sources and Al K $_{\alpha}$ is used as x-ray photon source. . . . .	182
7.1	Collinear arrangement of magnetic cations in a rocksalt monoxide. A domain with (111) ferromagnetic sheets and moments parallel or antiparallel with the $(\bar{2}11)$ direction is shown. . . . .	186
7.2	(a) The antiferromagnetically ordered (111) planes are shown. (b) The T1 and T3 planes. (c) The T2 and T4 planes. (d) Three spin directions that give rise to spin domains within a single twin domain.	191

- 7.3 (a) The antiferromagnetically ordered (111) planes in real lattice. (b) Appearance of extra spots in reciprocal lattice. . . . . 192
- 7.4 Schematics of the AFM-LEEM method for imaging AFM domains of NiO/Ag(001). Unpolarized electrons from the electron gun are elastically backscattered by the ordered AFM surface lattice producing half-order diffraction beams. The dark-field images, formed by the electrons originating from the half-order beams, display contrast due to the surface AFM domains. Three different colors (yellow, green and blue) represent different types of domains. . . . . 194
- 7.5 The LEED pattern of 60 ML NiO/Ag(001) film at 31 eV beam energy has been displayed at the center. Four  $p(2\times 2)$  half-order spots are visible. Their coordinates are denoted as  $(0,1/2)$ ,  $(1/2,0)$ ,  $(-1/2,0)$  and  $(0,-1/2)$ . The AFM-LEEM images corresponding to each half-order spot are displayed in figure (a), (b), (c) and (d) respectively. . . . . 196
- 7.6 The LEED pattern of 60 ML NiO/Ag(001) film at 31 eV beam energy has been displayed at the center. Four  $p(2\times 2)$  half-order spots are visible. Their coordinates are denoted as  $(0,1/2)$ ,  $(1/2,0)$ ,  $(-1/2,0)$  and  $(0,-1/2)$ . A feature has been encircled by blue boundary to its contrast in different images when viewed through different half-order spots. . . 197
- 7.7 (a) The T1 and T3 domains/planes, (c) The T2 and T4 domains/planes, in real lattice. (b) The reciprocal lattice of figure (a) showing the T1 and T3 axes, (d) The reciprocal lattice of figure (c) showing the T2 and T4 axes, on which the 3D half-order lattice points are shown at exact middle of two integer order lattice points. . . . . 198

7.8	(a) AFM-LEEM image of the magnetic nanodomains of a 6 ML NiO film. (b) Line profile plot drawn over the domains shows average domain size to be 20 nm. (c), (d), (e) and (f) are same zoomed in portion of figure (a) viewed through (0,1/2), (0,-1/2), (1/2,0) and (-1/2,0). (g) Addition of image (c) and (d). (h) Addition of image (e) and (f). (i) Addition of image (c), (d), (e) and (f). (j) Bright field image viewed through the (0,0) spot. . . . .	200
7.9	The magnetic (Twin) domains of NiO films of different thickness (6, 18, 40 and 60 ML) probed <i>via</i> AFM-LEEM technique. The same half-order spot (1/2,0) has been used for all the cases. All the images are collected at RT. . . . .	201
7.10	The area vs. perimeter plot for the fractal domains probed by AFM-LEEM in case of 6 ML and 60 ML NiO film. . . . .	202
7.11	AFM-LEEM image of a 60 ML NiO film viewed through the (0,1/2) spot. (a) Beam energy 23.5 eV. (b) Beam energy 30.5 eV. (c) Intensity of different (T)win domains encircled by red, blue and black borders have been plotted at different beam energies. (d) The contrast of the bright and grey domains with respect to the dark domains (encircled by black) has been plotted. . . . .	203
7.12	Average intensity variation of $p(2\times 2)$ half-order spots. (a) Lower thickness range, Film thickness 0.5, 0.75, 1, 1.5 and 2 ML. (b) Higher thickness range, Film thickness 2, 6, 10 and 15 ML. Electron beam energy of 24 eV is used. . . . .	205
7.13	Higher XMLD signal for VP x-ray absorption indicating in-plane distribution of the Ni moments. . . . .	207
7.14	XAS at Ni L edge with vertically polarized (VP) x-ray beam. Film thickness 6, 18, 40 and 60 ML. . . . .	208

7.15	(a) XAS at Ni $L_2$ edge in case of a 60 ML NiO film. Both the cases of VP and HP are shown. (b) XMLD-PEEM image for VP beam. (c) XMLD-PEEM image for HP beam. . . . .	210
7.16	XMLD-PEEM image at vertically polarized x-ray beam. NiO film of different thickness (a) 60 ML (b) 40 ML (c) 18 ML (d) 6 ML. . . . .	211
7.17	The zoomed in AFM-LEEM images of NiO films of various thickness. (a) 60 ML (b) 40 ML (c) 18 ML and (d) 6 ML. The corresponding XMLD-PEEM images at Ni $L_2$ edge shown at the same region (e) 60 ML (f) 40 ML (g) 18 ML. (h) Film thickness vs. average domain size plot. . . . .	213
8.1	XPS core levels (a) Ni $2p$ (b) O $1s$ of 20 ML NiO film probed by Al $K_\alpha$ under different Ar <sup>+</sup> sputter time. . . . .	218
8.2	Valence band spectra of 20 ML NiO film under different Ar sputter duration probed by (a) Al $K_\alpha$ (1486.6 eV) x-ray source (b) He II $\alpha$ (40.8 eV) ultraviolet photon source. . . . .	219
8.3	Angle dependent XPS study for two different electron emission angles; normal emission ( $\theta = 0^\circ$ ); grazing emission ( $\theta = 70^\circ$ ); core levels (a) Ni $2p$ . (b) O $1s$ . NiO film thickness 20 ML. . . . .	221
8.4	(a) Angle dependent XPS valence band study of 20 ML NiO film for electron emission angles; normal emission ( $\theta = 0^\circ$ ); grazing emission ( $\theta = 70^\circ$ ) for Ar sputtered, vacuum annealed and oxygen annealed film. $p(1 \times 1)$ LEED pattern of 20 ML NiO film at 53 eV (b) Ar sputtered (c) UHV annealed (d) Oxygen annealed. . . . .	222
8.5	UPS valence band of NiO film at different conditions; As prepared, vacuum annealed and oxygen annealed case. (a) 20 ML NiO/Ag(100). (b) 1 ML NiO/Ag(100). Inset: appearance of defect state near Fermi level after vacuum annealing the film. . . . .	223

- 8.6 LEED  $p(2\times 2)$  half-order spot intensity (a) 300 K (RT) (b) 523 K (above  $T_N$ ). (c) Temperature dependence of half-order intensity of the 'as prepared' 20 ML NiO film grown on Ag(001). Néel temperature variation of the film after passing through various number of sputter and anneal cycles are also shown. . . . . 228

## List of Tables

4.1	Results from DFT calculations for the energetics of various ferromagnetic (FM) and antiferromagnetic (AFM) configurations of Cr on Ag(001) systems studied here. $\Delta E$ denotes the energy of a given configuration with respect to the lowest energy configuration, i.e., the AFM configuration of 1Ag/Cr/Ag(001). $m_{Cr}$ is the magnetic moment per Cr atom in the given system. . . . .	114
6.1	Ni evaporation rate at various temperatures of Knudsen cell . . . . .	158
7.1	The possible (T)win and (S)pin domains in NiO . . . . .	191

# **Antiferromagnetism in lower dimension: Surfaces and 2D systems**

## **1.1 Introduction**

The topic of magnetic properties of surfaces, thin films, multilayers and superlattices is of tremendous scientific and economic importance, not only for the well-known data storage devices but also for the future electronics, which may utilize the spin of electrons in addition to their charge. Surfaces, interfaces, thin films and nano-structures often display magnetic properties fundamentally different from the properties of bulk crystals, which are thus important to understand principles of magnetism at reduced dimensions. Recent experiments probed local magnetic moments (and their temperature dependencies) of films at their surfaces/interfaces, small clusters, as well as nanowires, nanodots, and single atoms deposited on solid surfaces [1, 2].

Surface magnetism is inseparably connected to the magnetism in ultrathin films. Even the surface of a paramagnet can become magnetic after growing a ferromagnetic thin film on top of it. Our initial knowledge of magnetic surfaces comes from the theoretical analysis of ultrathin film slabs, which are being used by theorists in band structure calculations [3–5], and also from experiments with ultrathin magnetic films [6–9].

When discussing surface magnetism (or, more generally, low-dimensional magnetism) several phenomena should be considered. First of all, any change in the electronic states occupation at the surface results in a change of the surface magnetic moment. Lower atomic coordination results in band narrowing, leading to further changes of the surface magnetic moment. From an atomic perspective, one expects these moments to increase at the surface, which has dimensionality somewhere between bulk (nonmagnetic for most materials), monolayer, and isolated atoms (most of which possess a net spin). Second, from a statistical mechanics perspective, the average moment at nonzero temperature is expected to decrease. For magnetic surfaces, the loss of magnetic neighbors represents a weakening of the exchange interaction, which results in a stronger decrease of magnetic order with temperature, a changed Curie temperature, and a changed critical behavior if compared to that of a bulk material. Third, at the surface, the translational symmetry along the axis perpendicular to the sample surface is broken. Thus the orbital moment is less quenched than in the sample volume. Consequently, the spin-orbit interaction becomes significant, leading to a large surface magnetic anisotropy that can dominate the system magnetic anisotropy and forces the easy magnetization axis to be oriented perpendicular to the sample in the case of ultrathin films.

However, before starting to discuss surface magnetism we should answer a fundamental question: what does surface mean and how thick is it? As per analogy, if someone wants to carry out experiments on two-dimensional ferromagnets, the first and most important question is how thin must the film be before its magnetic properties are two dimensional in nature? A commonly accepted criterion of magnetic two dimensionality comes from the spin wave theory: the thermodynamic properties of a film are those of a two-dimensional ferromagnet only if the lowest spin wave branch is thermally populated. Following this argument, Mills [10] defined the ‘critical thickness’  $N_c$  and stated: the monolayer is a true two-dimensional magnet, and one makes the transition to three-dimensional magnetism in only a few monolayers. In

our discussion, we limit ourselves to surface phenomena that correspond to only the very surface atomic layers.

The changes of magnetic properties at surfaces can be investigated by a variety of experimental and theoretical techniques. Comparing experiment with theory, however, is not an easy task. First, the local measurements of the magnetic quantities (like magnetic moment or magnetic anisotropy) are quite difficult, and very often the information cannot be obtained directly. Second, calculations usually refer to simple model systems and therefore differ from real structures that are obtained experimentally.

The spin of the electron is at the heart of magnetic and other electron correlation phenomena in condensed matter physics. There is a multitude of experimental techniques that probe the collective behavior of spins in solids and the interaction of spins with other degrees of freedom. They all project out some observable of electronic states but measures an ensemble average for others. Magnetic resonance techniques operate directly in spin space and provide detailed information about the magnetic moments and spin dynamics. Magnetic x-ray and neutron scattering are highly sensitive to the magnetic ordering phenomena and spin structures in real space. Sometimes, the persistent magnetism in a sample (surface or bulk) strongly affects its electronic structure. Angle Resolved Photoemission (ARPES) then becomes an useful tool which offers unique information especially for different magnetic systems. It measures the energy and momentum of different magnetic states and therefore sensitive to the spin structures in reciprocal space. In this thesis, ARPES has been used rigorously for probing the band-dispersions of the valence levels in case of antiferromagnetic thin films.

## 1.2 Magnetism in low dimension

In last few decades, the availability of experimental techniques endowed with high sensitivity with respect to the magnetic properties of ferromagnetic (FM) materials has motivated a large amount of studies dedicated to the investigation of low-dimensional FM systems consisting of small particles or films deposited onto either nonmagnetic or antiferromagnetic (AFM) substrates. There are many techniques available for the characterization of ferromagnetic materials, specially the surface ferromagnetism such as MOKE, MFM, XMCD, SP-STM, SP-PES, SEMPA *etc.* The net non-zero polarization present in ferromagnetic samples makes them easier to be characterized both from microscopic and spectroscopic point of view. On the other hand, in case of antiferromagnetic samples the lack of net moment and hence less availability of useful techniques for their characterizations, left them neglected and many of their interesting properties unexplored.

The interest in the surface AFM systems started due to the interesting properties such as exchange-bias and interfacial exchange-coupling where the AFM surface/thin films play a crucial role. Still, the studies were very much limited due to the lack of experimental methods to study the surface AFM order. The difficulty is due to the fact that the AFM systems do not possess any net magnetic moment and is difficult to detect. You may mention that the classical methods to study the bulk AFM systems such as SQUID, VSM *etc* could not be used effectively to study surface/thin film AFM as the methods are bulk sensitive. Similarly, the Neutron diffraction is also bulk sensitive and for ultra thin films, the sample volumes are much smaller to give any measurable diffraction signals. There are a few experimental methods based on scanning probe microscopy such as SP-STM and Magnetic exchange force microscopy. However, these are very specialized techniques and have not been widely used for the study of AFM materials. The most widely used experimental technique to study the surface AFM is the x-ray magnetic linear dichroism (XMLD) technique

where the x-ray absorption of the sample at a particular elemental edge is studied with linear polarized x-rays. The XMLD technique, with the help of photoemission electron microscopy, can be more useful for magnetic imaging of the antiferromagnetic surfaces. This method is discussed in chapter 2 in detail.

Similar to the well-known FM materials, confined surface AFM systems are in fact characterized by magnetic properties that, because of interface or size effects, can be considerably different from the ones observed in the bulk [11]. Examples range from the stabilization of exotic AFM ordering to the onset of uniaxial anisotropy in low-dimensional AFM samples. Moreover, systems comprising AFM-FM interfaces represent a world of their own, thanks to their rich phenomenology related to interface exchange coupling. Finite-size effects in both FM and AFM materials reflect deviations from bulk properties associated with the reduction of the sample dimensions. So-called intrinsic effects occur in material systems for which one or more sample dimensions, for example, the thickness of a layer or diameter of a particle, is comparable with the intrinsic correlation length scale of the property being considered. Strongly correlated systems such as AFM oxides are characterized by very short correlation lengths, so intrinsic finite-size effects can be observed only in ultrathin films or nanoparticles. In addition, surface-related finite-size effects might be caused by the competition between the properties of atoms in the core of a particle or layer and those at the surface, possibly originating from the reduced coordination number. As an example, surface spins often possess higher magnetocrystalline anisotropy than the ones in the sample volume because of the reduced symmetry. Chemical or structural effects may also arise due to phenomena such as surface segregation, relaxation, or reconstruction. Of course, the environment (the material surrounding the particle or the film substrate) can also dramatically alter the properties of interface atoms through hybridization, strain, or chemical interdiffusion, not to mention the crucial role of exchange in determining the magnetism of systems where an AFM material interacts with a FM partner.

The high degree of correlation between the electronic, magnetic, chemical, structural, and morphologic features obviously makes the preparation and the characterization of high-quality samples a crucial point in any study involving low-dimensional systems. In this respect, AFM transition-metal (TM) monoxides are often regarded as a privileged reference. The reasons for this choice are manifold. First, these oxides can be grown as high-quality thin films on appropriate substrates and are characterized by a high chemical and mechanical stability. Second, their AFM ordering temperature (Néel temperature  $T_N$ ) is relatively high: to cite two relevant cases,  $T_N = 523$  K for bulk NiO and  $T_N = 291$  K for bulk CoO. Another important feature of TM oxides is their insulating nature resulting from strong inter- and intra-atomic electronic correlations. Their magnetic properties arise as a consequence of the short-range super-exchange interaction mediated by the oxygen bonds [208]. Because of the absence of itinerant magnetism associated with conduction electrons, the only long-range magnetic interaction is represented by the dipole-dipole interaction, which can be neglected in many cases. Therefore, from the magnetic point of view, TM oxides can be described within the frame of the Heisenberg or Ising formalism as ensembles of well-localized spins with near-neighbor interactions. Finally, we would like to mention that AFM TM oxides are also considered as model systems for the AFM parent compounds of high  $T_c$  cuprates since, in the latter, the interplay between charge and magnetic ordering is described by the Anderson's super-exchange theory, which also governs the magnetic properties of AFM insulators such as NiO or CoO. The surface electronic and magnetic structure of transition metal oxides have not been studied in detail by many groups, since most of the studies are concerned with the bulk properties of these materials. Such studies could be interesting, since it may correlate the surface antiferromagnetism with the surface electronic structure, specifically, the valence band electronic structure.

The case of Cr is even more interesting. Cr, in its bulk format, is a spin density wave (SDW) antiferromagnet, having Néel temperature close to room temperature

(311 K). Here, the SDW wave vector is incommensurate with the lattice. The magnitude of Cr moment in bulk is  $0.58 \mu_B$ . Having half-filled  $3d$  shell, the magnetic moment of Cr atom is strongly modulated by the presence of neighbors. The magnetic moments of Cr enhances dramatically (almost 500-600%) in reduced dimension. In a flat monolayer Cr, the enhanced moments are arranged in order to form commensurate AFM phase. The property of this purely two-dimensional magnetism is drastically different from its bulk AFM phase. The Néel temperature of this lower dimensional strong antiferromagnet (455 K) is quite higher than its bulk counterpart. Thus, monolayer Cr is an example of an elemental commensurate antiferromagnet.

### 1.2.1 Magnetic moment at surfaces and in ultrathin films

Reduced dimensionality affects the ground-state magnetization, resulting in an increased magnetic moment and an increased DOS near the Fermi level,  $D(E_F)$  [13]. The increased DOS near the Fermi level in a reduced dimensional system can result in ferromagnetic behavior even for elements that are nonmagnetic in the bulk. This concerns elements very close to satisfying the Stoner criterion, that is, what is required by the Stoner-Wohlfarth model for the existence of ferromagnetism.

The ground-state magnetic properties can be modified by varying the DOS at the Fermi level. The lower atomic coordination associated with atoms at the surface (or in the monolayer films) can lead to a reduced overlap of the  $d$  electron wave functions and to a resulting reduction in bandwidth. At the surface of  $3d$  metals, the  $3d$  band narrows, and the states are more localized than bulk ones. This leads to the increase in  $D(E_F)$ . Then the reduced overlap and relatively narrow bands can lead to an enhanced magnetic moment [figure 1.1]. The surface layer is expected to exhibit a weaker magnetic enhancement than a free-standing monolayer because of its atomic coordination number. The enhancement of the magnetic moment is

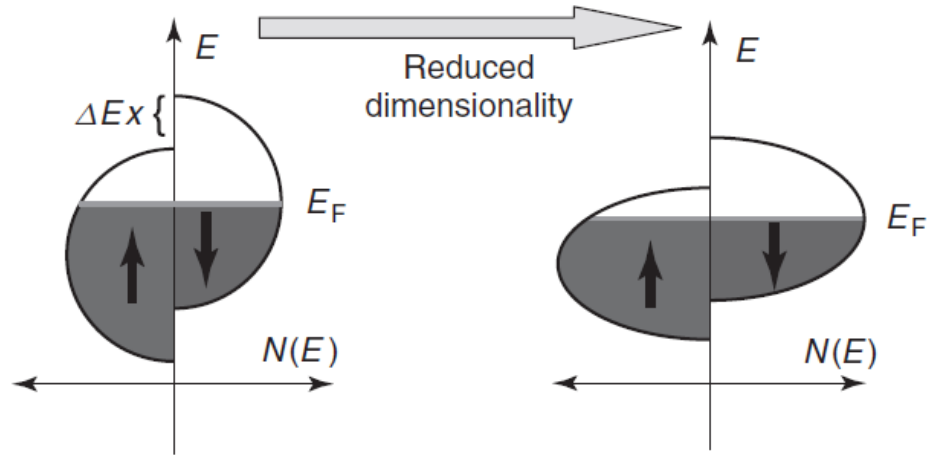


**Figure 1.1:** Schematic representation of band narrowing and resulting increased magnetic moments at surfaces and in ultrathin films.

related to the increase in the average exchange splitting  $\Delta E_{ex}$ . Recently, it was realized that not only the spin moment but also the orbital magnetic moment can be strongly enhanced with reduced dimensions, for example, at surfaces. In the presence of spin-orbit coupling, for reasons of symmetry, almost no orbital magnetic moment remains in the bulk ferromagnet. There are two qualitative arguments to explain the enhancement of the orbital moment at the surface. First, the spin-orbit interaction couples the orbit to the spin moment, so that the orbital magnetic moment increases with the increasing spin magnetic moment [14]. Second, the quenching of the orbital moment, which occurs in high lattice symmetries, can be removed by the symmetry reduction at the surface.

### 1.2.2 Finite-Size Effects on the Magnetic Ordering Temperature

The reduction of the critical magnetic ordering temperature  $T_{order}$  is a typical finite-size effect in both FM ( $T_{order} = T_c = \text{Curie temperature}$ ) and AFM ( $T_{order} = T_N$ ) low-dimensional systems. It can be seen as a consequence of the sample

asymptotically approaching the conditions at which the Mermin-Wagner theorem applies as its size is progressively reduced. This theorem states that, because of fluctuations, continuous symmetry cannot be spontaneously broken (i.e., the sample cannot develop long-range FM or AFM order) at finite temperature in systems with short-range interactions in dimensions  $d \leq 2$  [15]. Experiments have evidenced drastic reductions in the magnetic transition temperature  $T_N$  for a variety of AFM oxides in low-dimensional geometries such as nanoparticles [16, 17], thin films [18, 19], nanoparticles [20] and nanoparticles [21–23], nanotubes [24] and nanowires [25].

In a simple mean-field approach, which assumes  $T_{order}$  to be proportional to the exchange energy density of the particle or thin film, the reduction of the magnetic transition temperature is due to the decrease in the total exchange energy associated with the reduced number of neighboring atoms. In this picture, the system environment is not passive and might contribute to defining the total exchange energy, for instance, by inducing surface magnetic anisotropy through a strain field or by modifying the magnitude of the interface moments and the strength of their mutual coupling through hybridization or other interactions. According to the mean-field model, the variation of  $T_{order}$  with respect to the bulk value  $T_{order}(\infty)$  is expected to be proportional to the inverse of the particle size or of the film thickness  $D$ . However, this prediction is not consistent with the experimental results, and the reduction in the ordering temperature  $T_{order}$  with size is better described in terms of scaling theories [26], according to which the correlation length of the fluctuations of the AFM order parameter diverges logarithmically with the reduced temperature  $(T - T_{order})/T_{order}$  as the temperature  $T$  approaches the magnetic ordering transition  $T_{order}$ . For a system with size  $D$  much larger than a characteristic length  $\xi$  describing the spatial extent of the spin-spin coupling, this yields a fractional decrease of  $T_{order}$  that follows a power-law curve [27]:

$$\frac{T_{order}(\infty) - T_{order}(D)}{T_{order}(\infty)} = \left(\frac{\xi + a}{2D}\right)^\lambda \quad (1.1)$$

where  $\lambda$  is the shift exponent and  $a$  is the lattice spacing. For  $D \ll \xi$ ,  $T_{order}$  is expected to vary linearly with respect to  $D$ . Hence the ordering temperature should vary with film thickness. This part has been studied in chapter 7 in this thesis where we observe a gradual increment of the magnetic ordering temperature with increasing NiO film thickness.

### 1.3 Scope of the thesis: antiferromagnetic systems

In this thesis, two different antiferromagnetic thin film systems have been chosen as case studies. The first one, Cr, is an early transition metal. A flat monolayer of Cr is a purely two-dimensional antiferromagnetic system, with enhanced magnetic moments compared to bulk Cr. The second one, NiO, is a late transition metal oxide, well-known bulk (three-dimensional) antiferromagnet. For both cases, Ag(001) substrate has been chosen as an appropriate substrate due to lattice matching as well as other thermodynamic advantages.

#### 1.3.1 1 ML Cr/Ag(001)

Having half-filled  $3d$  shell, Cr is ultra-sensitive to its coordination. Therefore, in reduced dimension its magnetic moment enhances dramatically (upto 500-600%). In a flat Cr monolayer (grown on top of Ag(001) crystal), these enhanced magnetic moments are arranged antiferromagnetically in a commensurate phase. Whereas bulk Cr shows an SDW (spin density wave) incommensurate antiferromagnetic structure.

The growth of flat Cr monolayer on Ag(001) is a crucial part. The commensurate antiferromagnetic phase which is the cause behind the evolution of  $c(2 \times 2)$  half order spots are visible only in an atomically flat Cr monolayer. Formation of bi- or multi-layer Cr island on Ag(001) destroys this antiferromagnetic phase resulting from decrease in the first NN distance. The flat growth of Cr on Ag(001) substrate depends

on few vital growth conditions, therefore, optimizing those growth parameters are very important. In chapter 3, in this thesis, we present the optimization of these different parameters in detail.

The structure of flat monolayer Cr on Ag(001) is complicated. We find that the formation of 1 ML Cr/Ag(001) is thermodynamically unfavorable, due to the higher surface energy involved. Our studies found that monolayer Cr is covered by 1 atomic layer of Ag and is a stable phase. So, the  $c(2\times 2)$  antiferromagnetic Cr monolayer is sandwiched between 1 layer of Ag on top and Ag(001) substrate at bottom. The stability of this sandwiched magnetic structure, where monolayer Ag segregates over Cr layer, has been tested via both experiment and DFT calculations which are in agreement with each other. In chapter 4, we discuss the details of physical structure of this system.

The most interesting aspect of a monolayer Cr film in antiferromagnetic phase is its valence band structure. The antiferromagnetic valence band of monolayer Cr is completely different from the paramagnetic band structure observed at higher film thickness. The valence band dispersions of monolayer Cr has been probed by monochromatic He  $I_\alpha$  and He  $II_\alpha$  ultraviolet photon sources using Angle resolved photoemission spectroscopy (ARPES). The details of the valence band structure of antiferromagnetic Cr monolayer is the focus of chapter 5.

### 1.3.2 NiO/Ag(001)

NiO is a bulk antiferromagnet with Néel temperature of 523 K. In spite of having a simple rocksalt structure, the magnetic structure of NiO is rather complex. The magnetic Twin and Spin domains construct the magnetic structure in an ordered NiO lattice. Moreover, being a strongly correlated insulating transition metal oxide, its electronic structure also has been drawn many scientific attentions till now. Even though sophisticated band structure calculations such as LDA+DMFT are able

to successfully explain the bulk electronic structure of NiO, though the effect of antiferromagnetism in the valence band electronic structure is not still clear from experimental point of view. The electronic structure have been studied on single crystal systems which are often plagued by the different issues such as charging effects etc. However, there are only a few studies on the electronic structure of epitaxially grown NiO. So, in this thesis, we focus on the electronic and magnetic structure of epitaxially grown NiO ultrathin films.

The details of valence band as well as core level electronic structure of NiO thin films have been discussed in chapter 6 of this thesis. The thickness dependence of NiO valence band and core levels e.g., Ni  $2p$  and O  $1s$  has been shown. The effect of the vicinity of non-magnetic noble metal substrate, Ag, is also illustrated at low thickness regime.

In chapter 7, imaging of the antiferromagnetic domains, performed using two different electron microscopic techniques, namely the Low Energy Electron Microscopy (LEEM) and PhotoEmission Electron Microscopy (PEEM) using the X-ray magnetic linear dichroism (XMLD), has been focussed. The evolution of magnetic domains with film thickness has been demonstrated using these two complementary techniques. The advantage of each technique over the another has been discussed. Variation of Néel temperature ( $T_N$ ) and XMLD signal with NiO film thickness has also been discussed.

Mild sputtering of the oxide surface with  $\text{Ar}^+$  ions as well as high temperature vacuum annealing produces oxygen vacancies in the sample surface. Sputtering removes predominantly oxygen atoms from the top surface of NiO film, leaving the Ni atoms, which form clusters on the oxide surface. The elemental core level spectra as well as the valence bands of NiO get affected by the creation of oxygen vacancies in the sample. Néel temperature of the sample also reduces with creation of more oxygen vacancies as the antiferromagnetic strength of the sample weakens. Chapter

8 discusses the effect of oxygen vacancies on the electronic structure and magnetism of NiO film elaborately.

## Experimental techniques and methods

### 2.1 Introduction

This chapter focuses on the details of various experimental techniques used to perform experiments described in this thesis. As already mentioned in chapter 1, aim of this thesis is to explore the electronic as well as magnetic structure of two different antiferromagnetic thin film, namely Cr monolayer and NiO thin films on Ag(001) substrate. Since the focus is to study on thin films, hence surface-sensitive techniques are used. For studying the electronic and magnetic structure of solid surfaces, the surface must be clean in atomic scale requiring ultrahigh vacuum (UHV) [less than  $10^{-9}$  mbar] during the experiments. UHV is important for surface studies mainly for two reasons: 1) Within UHV environment a sample surface may be maintained in a contamination-free state for long enough duration to perform experiments on them. 2) It is also essential to perform low energy electron and ion based experiments without undue interference from gas phase scattering. After obtaining the UHV condition, thin films can be grown *in situ* on a suitable substrate in the growth chamber.

To make structural characterization of the deposited films, we need a Low Energy Electron Diffraction (LEED) set-up. After confirming the sample crystallinity, cleanliness, and symmetry direction using LEED, the sample is ready to be transferred

to the analysis chamber for further photoemission experiments. LEED may also indicate the presence of surface antiferromagnetic order in the deposited film, as we shall describe in case of Cr and NiO films, which will be discussed in different chapters of this thesis. A rigorous LEED IV study, which is the electron beam energy (V) *vs.* diffraction spot intensity (I) measurements, gives a detailed idea of the physical structure of the surface/film when compared to theoretically calculated IV curves.

The elemental analysis of the given sample and tracing their chemical (oxidation) changes can be performed using X-ray Photoemission Spectroscopy (XPS). However for investigating surface electronic valence band structure with high energy and momentum resolution, one needs to perform the Angle Resolved PhotoEmission Spectroscopy (ARPES) measurements using suitable (ultra-violet or soft x-ray) sources ultra-violet sources. In photoemission experiments, the most important part is to measure the kinetic energy of emitted electrons, for which the most common electron analyzers are of hemispherical type which will be discussed later in this chapter.

For surface antiferromagnetic domain imaging studies we have used two different techniques in this thesis. The first technique, based on the plane polarized x-ray absorption, uses the dichroism signal from the sample to image the antiferromagnetic domains utilizing the photoelectron in a PhotoEmission Electron Microscope (PEEM) system. This technique, called XMLD-PEEM, is well-established as an useful tool to image the magnetic domains of the antiferromagnetic sample. The second one, based on electron diffraction phenomena, called Low Energy Electron Microscopy (LEEM). Looking at the sample surface through the magnetic ‘half-order’ spots in LEED, it is possible to visualize the enlightened parts of the sample which are basically the magnetic twin domains. Since LEEM is being used to probe antiferromagnetic (AFM) domains, we specify the name of this method as AFM-LEEM. Besides the magnetic imaging, the intensity variation of LEED half-order spots are used to

determine the surface Néel temperature ( $T_N$ ) of the sample. The effect of thickness dependence and creation of defect states on  $T_N$  may also be estimated from these studies. Therefore, we demonstrate that LEED is a vital tool for preliminary magnetic studies on such epitaxial antiferromagnetic films.

## 2.2 What is Epitaxial Growth?

The term epitaxy comes from the Greek word ‘epi’, meaning ‘above’, and ‘taxis’, meaning ‘an ordered manner’. It can be translated as ‘arranging upon’. In general scientific language, epitaxy means the growth of a single crystal film on top of a crystalline substrate. There are mainly two different types of epitaxy, known as ‘homoepitaxy’ and ‘heteroepitaxy’. In case of homoepitaxy, the film and the substrate are of the same material, e.g. Si layers of different doping (impurity) content are grown on Si single crystal substrate for technical purposes. On the other hand, in heteroepitaxy, the film and substrate materials are different; hence are mostly used in thin film technology and engineering. In this thesis, I have discussed the heteroepitaxial growth of two different films, Cr and NiO, on Ag(001) single crystal substrate.

### 2.2.1 Interfacial strain: Pseudomorphic growth

In heteroepitaxy, for the growth of epitaxial film over a substrate with good crystalline quality, matching of the lattice parameter between the overlayer material and the substrate is essential. Where significant lattice mismatch persists, trying to grow a layer of a different material on top of a substrate may lead to interfacial strain strong enough to destroy the crystalline order of the film. Pseudomorphic growth means that layers in the heterostructure have the same lattice parameters due to the deformations. So, pseudomorphic layer is fully stressed by their neighbors. Small lattice mismatch

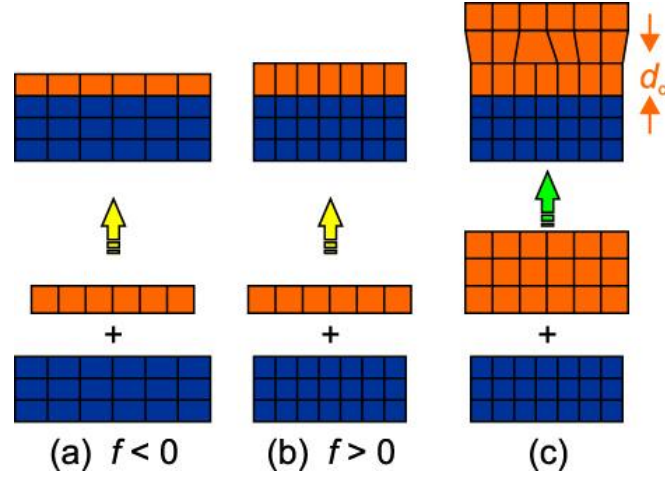


**Figure 2.1:** (a) In-plane tensile strain, (b) Out-of-plane compressive strain (c) Lattice parameter relaxation at a critical thickness  $d_c$ .

creates interfacial defects like misfit dislocations in the film, whereas higher mismatch may lead to formation of faceted structures. Such deviations from normal ‘layer by layer growth’ would lead to change in optical, thermal, mechanical, electronic and surface magnetic properties in the system. In many cases, the interfacial strain relaxes with increase of film thickness, enabling and stabilizing the layered growth. The lattice misfit is defined as:

$$f = [a(s) - a(f)]/a(f) \quad (2.1)$$

where  $a(s/f)$  are the lattice constants of the substrate and the film, respectively in their bulk format. In figure 2.1, pseudomorphic growth under different type of strain are represented schematically. For example, in our case, Ag(001) has a lattice parameter of 4.09 Å while bulk NiO(001) has lattice constant of 4.18 Å. The calculated lattice mismatch between these two materials is only 2%, hence NiO(001) film can be grown pseudomorphically on Ag(001) in layer by layer fashion. Above a critical thickness  $d_c$  [which is about 10 ML for NiO(001) growth on Ag(001)] the interfacial strain relaxes *via* the creation of misfit dislocations. On the other hand,

in case of Cr (bulk lattice parameter 2.88 Å) the mismatch with Ag(001) substrate is only 0.3%. But, in this case, the epitaxial growth is only possible if the Cr <001> crystalline direction rotates  $45^\circ$  with respect to the substrate; hence there occurs a rotated pseudomorphic growth. The details will be discussed at suitable places in different chapters of this thesis.

### 2.2.2 Different parameters of MBE growth

The term 'MBE' stands for 'Molecular Beam Epitaxy', a method where epitaxial metal and metal oxide films are grown on single crystal substrate in layer by layer manner deposition inside an UHV growth chamber. Though having a good lattice matching is one essential parameter for epitaxial growth, it is not sufficient condition. The miscibility gap of the deposited and substrate material is another important parameter for MBE growth. If the deposited material is easily dissolved in the substrate forming intermetallic alloy, the probability of epitaxial growth is less. Similarly, there should not occur any chemical reaction between these two materials. Another important factor is the surface energy of these two materials, which determines whether the deposited material will wet the substrate forming smooth film or discrete islands. For reactive deposition of oxide films, e.g., the case of NiO where Ni is evaporated on Ag(001) in oxygen environment, the oxygen pressure plays an important role in determining the quality as well as the stoichiometry of the deposited film. Temperature is another vital parameter as it controls the mobility of the adatoms on substrate surface. This determines how much the surface of the substrate will be covered by the deposited material. Therefore it is a mandatory part of MBE, to optimize all important parameters for growth in order to obtain best quality epitaxial film.

## 2.3 Deposition of epitaxial films

The study of surface electronic structure and magnetism requires a sample with clean surface in the atomic scale. Since the electronic as well as magnetic structure depends on the film thickness and the studies involves their band dispersion, atomically uniform and flat films are mandatory. This demands that the substrates must also be highly polished single crystals or cleaved surfaces with large terrace width and low step density. Moreover, clean conditions also imply an *in situ* preparation of the sample and the experimental chamber should have an attached facility for depositing the samples in good UHV conditions. As will be discussed in chapter 3 and 4, we observed antiferromagnetic order in a flat Cr monolayer film; the corresponding antiferromagnetic band structure of the film is visible flat two-dimensional Cr monolayers with high degree of order. The presence of bi or multilayer domains destroys the in-plane antiferromagnetic ordering in the sample. In case of NiO, growth of a flat, defect-free, highly epitaxial film is necessary, as will be discussed in chapter 6. Both Cr and NiO films are grown using MBE technique. As we are interested in investigating the surface electronic and magnetic structure of these films and hence high crystalline quality and smoothness of the film surfaces is a crucial parameter. Considering the lattice matching and surface energy, Ag(001) single crystal was chosen to be the most appropriate substrate for both cases. For higher epitaxial quality of the overlayer film, it is always essential to have an atomically flat substrate surface. The well-polished Ag(001) crystal (from MaTeck GmbH, Germany) was passed through repeated sputtering and annealing cycles.  $\text{Ar}^+$  beam was used to sputter the sample [ $P_{\text{Ar}} = 7 \times 10^{-6}$  mbar,  $1 \mu\text{A}$ ] typically for 15 min for bare Ag(001) crystals and higher duration for film covered surfaces. The energy of the  $\text{Ar}^+$  beam used also depends on the Ag crystal conditions; typically 500 or 700 eV for bare substrate and higher energies are used for film covered surfaces. Sputtering was followed by annealing the Ag crystal at 823 K for 30 min. To recover the thermodynamically

stable crystal structure, it is necessary to anneal the substrate in order to provide mobility to atoms. Different annealing temperatures can be used depending on the sample and the final structure required. In some cases, when a thermodynamically stable surface is not desired, the sample is quenched from a certain temperature to freeze the stable structure at that temperature. The annealing can be applied in several ways, depending on the setup: direct Joule heating by passing some current through the sample, radiation heating from a filament near the sample, and electron bombardment by accelerating electrons coming out of a filament onto the back of the sample. The annealing temperature is measured with a thermocouple inserted in the manipulator, in contact with the sample holder. The cooling of the sample can be performed, when needed, by contact of a sapphire ball on a copper block containing a liquid nitrogen capillary circuit. All the materials in this thesis were evaporated from water-cooled electron-beam evaporator and resistive heating Knudsen cell. The standard thickness calibration was performed by a quartz crystal microbalance.

## 2.4 Low Energy Electron Diffraction (LEED)

### 2.4.1 Theory

The basic reason for the high surface sensitivity of LEED is the fact that for low-energy electrons, the interaction between the solid and electrons is strong. Upon penetrating the crystal, primary electrons will lose kinetic energy due to inelastic scattering processes such as plasmon and phonon excitations as well as electron-electron interactions. In cases where the detailed nature of the inelastic processes is unimportant, they are commonly treated by assuming an exponential decay of the primary electron beam intensity,  $I_0$ , in the direction of propagation:

$$I(d) = I_0 e^{-d/\lambda(E)} \quad (2.2)$$

Here 'd' is the penetration depth and  $\lambda(E)$  denotes the inelastic mean free path, defined as the distance an electron can travel before its intensity has decreased by the factor  $1/e$ . While the inelastic scattering processes and consequently the electronic mean free path depend on the energy, it is relatively independent of the material [figure 2.2]. The mean free path turns out to be minimal (5-10 Å) in the energy range of low-energy electrons (20 - 200 eV). This effective attenuation means that only a few atomic layers are sampled by the electron beam and as a consequence the contribution of deeper atoms to the diffraction progressively decreases.

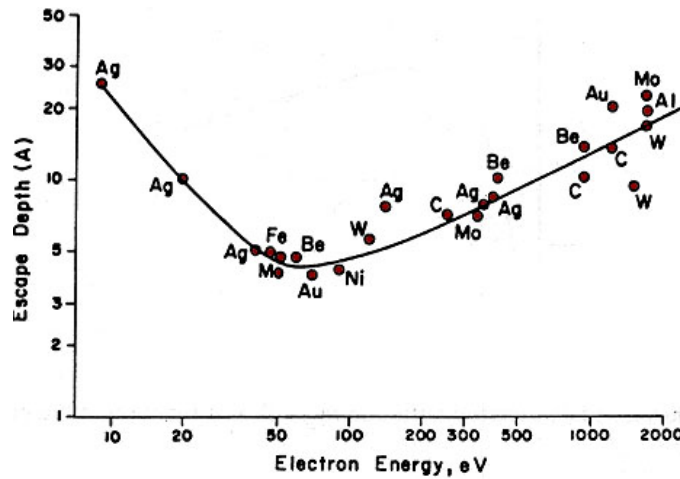


**Figure 2.2:** Universal curve of mean free path for the inelastic scattering of electrons in a solid [28].

#### 2.4.1.1 Kinematic theory: Single scattering

Kinematic diffraction is defined as the situation where electrons impinging on a well-ordered crystal surface are elastically scattered only once by that surface. In the theory, the electron beam is represented by a plane wave with a wavelength in accordance to the de Broglie hypothesis:

$$\lambda = h/\sqrt{(2mE)} \quad (2.3)$$

Let us consider a monoenergetic electron beam impinging on a surface. The beam is represented by a plane wave which is described by [29]

$$A_i = A_0 \exp(i \vec{k}_0 \cdot \vec{r}) \quad (2.4)$$

where  $A_i$  is the amplitude of the incident wave,  $A_0$  is a constant,  $\vec{k}_0$  is the incident wave vector, and  $\vec{r}$  is a space vector. If multiple scattering is neglected, the amplitude of a diffracted beam is represented by:

$$A_s = A_0 \left[ \sum \alpha f_n(\vec{s}) \exp(i \vec{s} \cdot \vec{r}_n) \right] \exp(i \vec{k}_{out} \cdot \vec{r}) \quad (2.5)$$

where  $f_n(\vec{s})$  is the atomic scattering factor for the  $n$ th atom located at position  $\vec{r}_n$ ,  $\vec{s} = \vec{k}_{out} - \vec{k}_0$  is the momentum transfer, and  $\vec{k}_{out}$  is the wave vector of the scattered wave ( $\alpha$  is a constant). However, the kinematic theory, which is based on single scattering phenomena, is inadequate. In real electron diffraction experiments, the electron pass through multiple scattering and therefore a detailed idea of surface structure can not be obtained from the kinematic model of LEED.

#### 2.4.1.2 Dynamical theory: Multiple scattering

Dynamical theory, based on multiple scattering formalism, has had its most profound impact in the area of surface-structure determination, and, consequently, LEED has been used to determine a large number of surface structures for a wide variety of materials. The energy dependence of the LEED spots can theoretically be calculated for given structure and its comparison with experimental LEED I-V data gives idea of the detailed structure of the material [29].

### 2.4.2 LEED: Instrumental configurations

Low energy electron diffraction (LEED) [30] from well-ordered surface can be used to determine structural information of the surface. Typical examples of well-ordered surfaces are prepared Ag(001) crystal surface or *in situ* grown epitaxial thin films on it. LEED is surface sensitive technique as the inelastic mean free path of electron is small (5-10 Å) in the energy region of 20-200 eV, as shown in figure 2.2 [28,31,32].

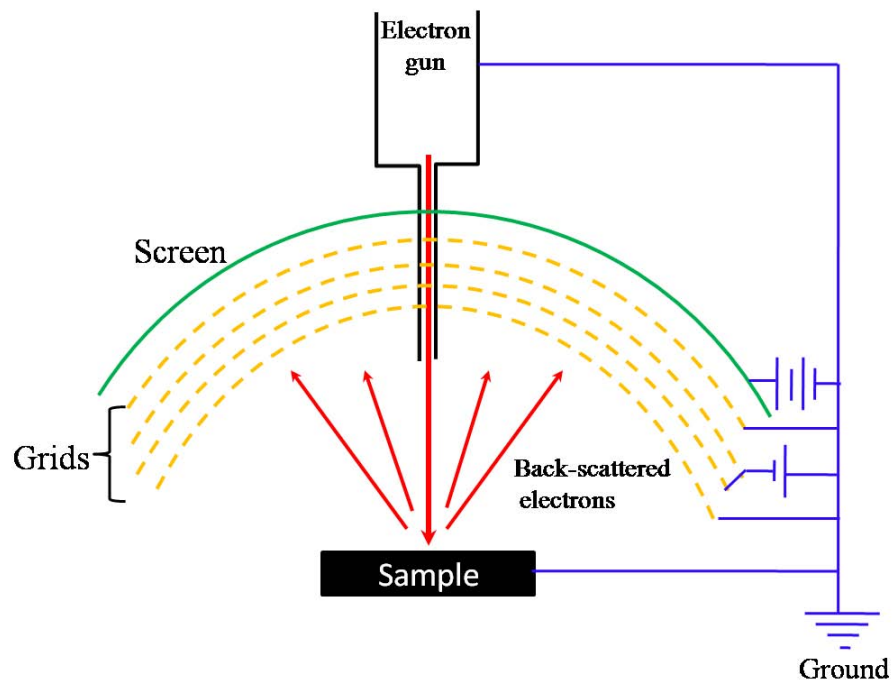


**Figure 2.3:** Schematic of a conventional rear-view LEED setup.

The operating principle of a standard LEED setup is schematically illustrated in figure 2.3. In a LEED experiment, monochromatic electrons (commonly within 20-200 eV) are accelerated from an electron gun and focused with a lens system, which falls normally on the sample surface. The electron gun for LEED has been designed in such a way that minimum light from the electron gun cathode will come out of the electron beam housing. A thoriated tungsten filament has been used as cathode, which is heated and therefore emits electrons. These electrons are accelerated by a variable voltage and focused on the sample surface, where they are

diffracted and traverse in the vacuum toward the fluorescent screen. The Wehnelt cylinder in the lens system acts as an electrostatic aperture between the cathode and the anode. It is on the same or on negative potential w.r.t. the cathode and regulates the penetration of the anode potential into the direction of the cathode. An increase of the Wehnelt voltage leads to a narrowing of the electron beam and the sharpness of the diffraction spots can be improved. In order to obtain a sharp focus over a broad range of energies, the lens voltages have to be varied as a function of energy. The secondary electrons and electrons which are inelastically scattered by the sample surface can be kept away from the fluorescent screen by applying a negative voltage to the suppressor grids. A set of four gold coated molybdenum grids at different places in front of the fluorescent screen serves as energy filter. These grids prevent access of low energy secondary electrons to the detection area, where the diffraction pattern of the Bragg's diffraction spots can be observed. The first grid from the sample side is at ground potential to ensure a field-free region between the sample and the first grid. The next two grids is set at the so called retarding voltage to minimize the contribution from inelastically backscattered electrons. This voltage is slightly lower than the kinetic energy of the electrons produced by the gun. Two grids have been used at the same retarding voltage, so that it repels almost all the inelastically scattered electrons. The elastically scattered electrons pass through the next grid, which is set to the ground potential again and are then accelerated toward the fluorescent screen that is generally set to a high positive voltage between 4 to 5 kV. This causes the screen to glow with an intensity at each point on the screen proportional to the incident electron flux and thus producing a visual map of the electron diffraction pattern. Thus, the elastically backscattered electrons give rise to the diffraction spots that are imaged on a phosphorous screen yielding reciprocal lattice of the surface. Behind the screen, there is a transparent window so that the LEED pattern can be directly observed or recorded with a 12-bit Peltier cooled charge coupled device (CCD) camera which is interfaced with a computer in order

to acquire frames of diffraction patterns with different exposure, acquisition time and gain parameters. The typical beam sizes are of the order of  $\sim 1 \text{ mm}^2$ , and has a coherence length of several hundreds of Å. Apart from well-ordered surface, LEED experiments also require UHV and extremely clean surface (free from any surface contamination). For this reason, surface preparation is generally performed *in situ* by sputtering and annealing or by other methods like flashing, cleaving *etc.* We can directly map the surface reciprocal space with LEED. It is interesting to note that, not only the bulk termination of the crystal structure but any surface reconstruction like atomic step arrays or adsorbate induced structures can be studied using LEED.

#### 2.4.2.1 Calibration

The LEED apparatus in our laboratory is a basic four-grid LEED [from OCI vacuum Microengineering, Canada. model: BDL800IR] with linear motion facility upto 100 mm retraction from sample. The optics of the LEED apparatus demands an optimized position for the sample; which means the sample has to be placed at the center of the hemispherical phosphor screen. It will be discussed in later chapters of this thesis, that the antiferromagnetic order present in the sample is at the origin of half-order spots that we observe in LEED for low electron beam energies. Intensity of magnetic half-order spots is much weaker (only 1-2%) compared to the integer order spots. Obviously, it is quite difficult to experimentally visualize their existence. It is therefore essential to optimize different LEED parameters such as Wehnelt voltage, grid voltage, focus voltage, retarding voltage, filament current, beam current and sample position *etc.* for the best LEED spots, i.e. the brightest spots with minimum FWHM. Among all these parameters, the focus voltage and the sample position are the two crucial ones which mostly affect the sharpness of the spots.

In figure 2.4, the average radial profile of first integer order LEED spots (1,0) have been displayed as a function of focus voltage, for a fixed sample position where

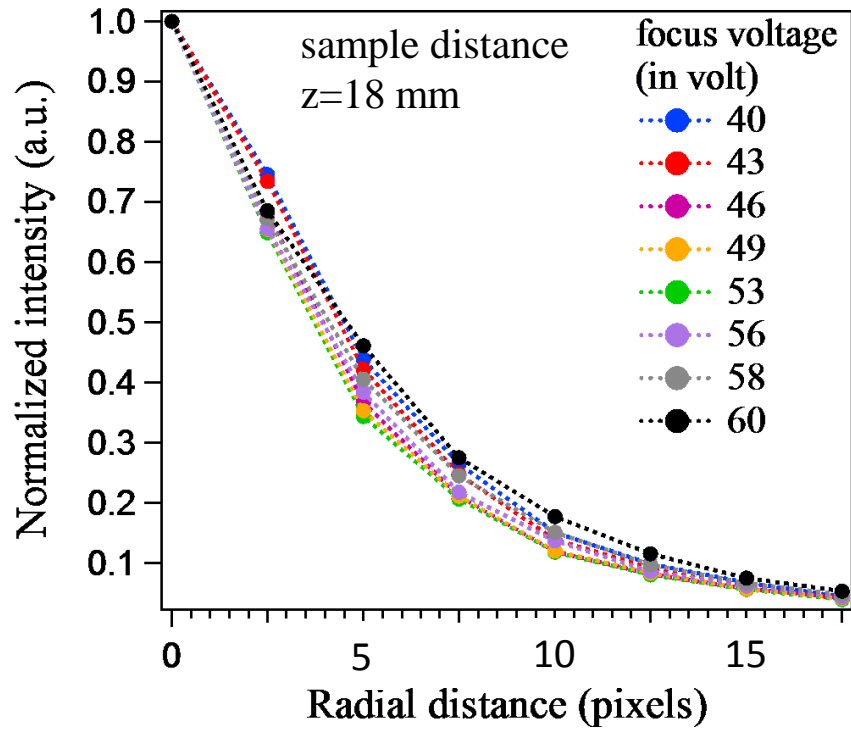


**Figure 2.4:** For a fixed sample distance  $z=18$  mm from the LEED instrument, average radial profile plots of LEED spots have been shown as a function of focus voltage.

distance of the sample surface from LEED instrument was 18 mm. The standard Ag(001) single crystal sample and 55 eV beam energy was used to optimize these LEED parameters. This plot shows that the sharpest LEED spots appear at 53 Volt focus voltage. This behavior of the LEED spots were also determined for few other sample positions. The second important parameter, the optimum sample distance, was determined fixing the focus voltage to 53 eV and varying sample position. Figure 2.5 shows the average radial profile plot of the LEED spots for different sample positions.

This plot shows that for sample distance 18 cm from the LEED apparatus, the LEED spots have minimum FWHM. Therefore this was chosen to be the optimum position for the sample.

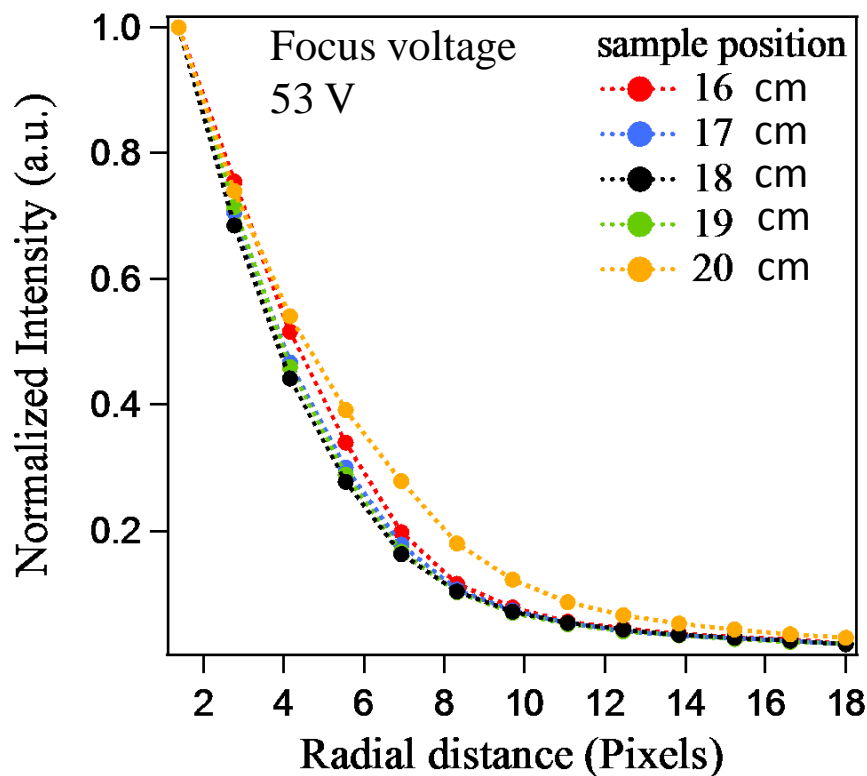


**Figure 2.5:** For a focus voltage of 53 volt, average radial profile plots of LEED spots have been shown as a function of sample distance.

A LEED IV study was also performed on cleaned and well ordered Ag(001) single crystal surface and our experimental data was compared with previously reported IV data by K.M. Schindler *et al.* [33]. They have invented a new method to extract improved IV data using LEED spot background subtraction technique. Figure 2.6 shows that our experimental data matches quite well with the earlier reported IV curve, which demonstrates the reliability of our LEED data.

### 2.4.3 Superstructure in LEED pattern

The schematics of a  $p(1 \times 1)$  atomic arrangement is shown in figure 2.7 (a). The adsorption of a  $p(2 \times 2)$  overlayer has been shown in figure 2.7 (b). Due to the atomic coordinations of the adsorbed layer ‘extra spots’ with four-fold symmetry will appear

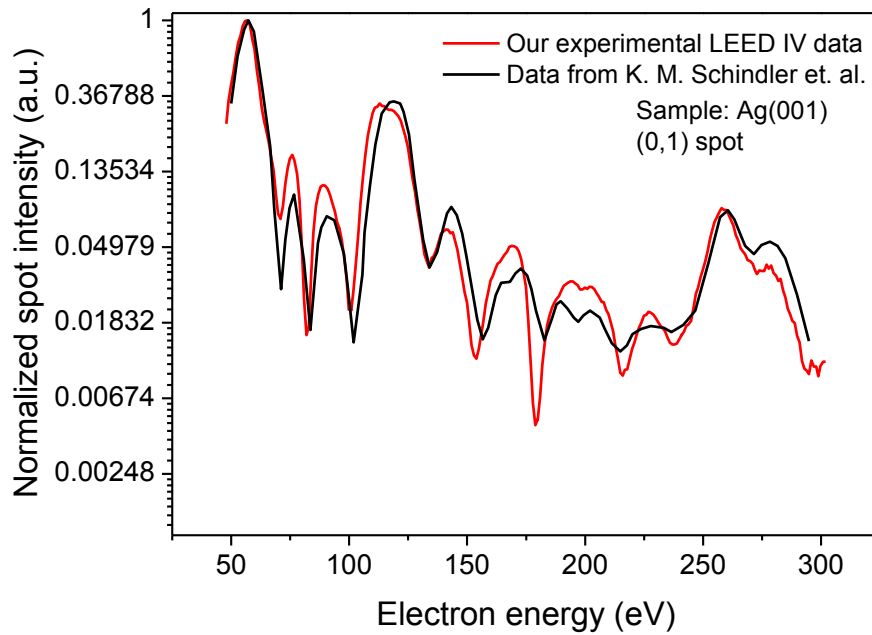


**Figure 2.6:** Our LEED IV data for (0,1) spots of Ag(001) single crystal has been compared with the IV data of earlier reported data by Schindler *et al.* [33].

in LEED, resulting in a  $p(2\times 2)$  constructed LEED pattern. Similarly, a  $c(2\times 2)$  adsorption in real space has been shown in figure 2.8 (b).

#### 2.4.3.1 LEED half-order spots: Surface antiferromagnetic order

Electron scattering from antiferromagnetic crystal arises due to mainly four principal interactions: coulomb, exchange, dipole and spin-orbit. The spin-orbit interaction has two contributions, one from a magnetic term involving the spins of the magnetic electrons of the host ion and another from a nonmagnetic term involving only the spin of the incident electron. The exchange, dipole and magnetic spin-orbit interactions are magnetic in origin and therefore will display the structure of the magnetic unit cell, while the coulomb and non-magnetic spin-orbit interactions will display the structure of the chemical cell. To probe the magnetic origin of the half-order spots Palmberg *et al.* [34] has estimated the ratio of exchange to coulomb scattering. Using dynamical LEED calculations, Tamura *et al.* [35] has shown LEED IV profiles of the

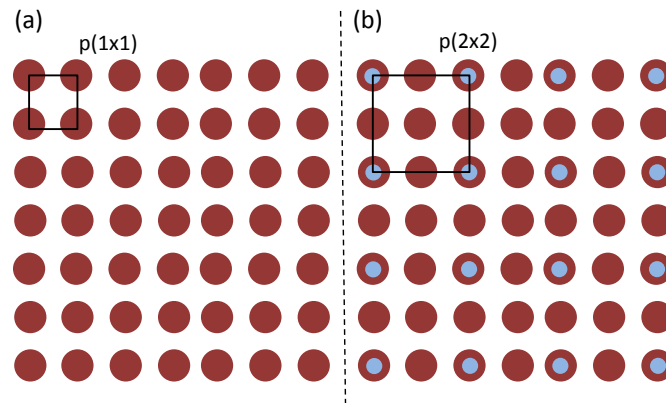


**Figure 2.7:** Adlayer superstructure (a)  $p(1 \times 1)$  (b)  $p(2 \times 2)$  configuration.

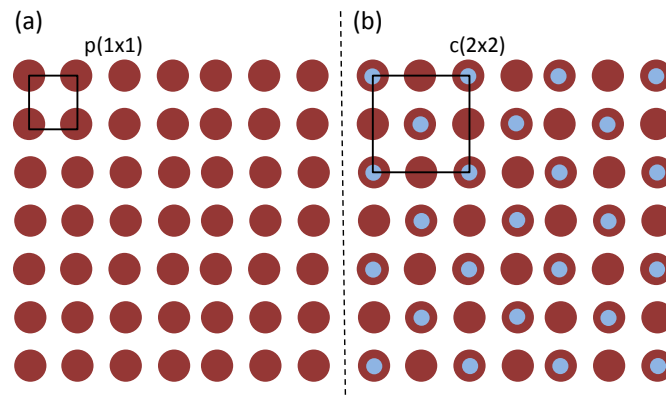


**Figure 2.8:** Adlayer superstructure (a)  $p(1 \times 1)$  (b)  $c(2 \times 2)$  configuration.

‘extra-spots’ [ $c(2 \times 2)$  half orders]. Their theoretical studies demanded the magnetic origin of the half-order spot in both NiO and Cr systems.

Spin ordering in antiferromagnetic NiO leads to a magnetic unit cell having dimensions twice that of the chemical cell. The arrangement of spins as determined by neutron diffraction [36,37], is represented in figure 2.9 (a). At the NiO (001) surface, the arrangement of Ni moments have a  $p(1 \times 2)$  or  $p(2 \times 1)$  configurations depending on the presence of different twin domains present [38]. In the case of NiO(001) single crystal or thin film surfaces, usually these two types of magnetic ordering is present, yielding an average  $p(2 \times 2)$  magnetic configuration. Coherent exchange-scattering of the incident electrons by the ordered spin system like NiO produces half-order beams

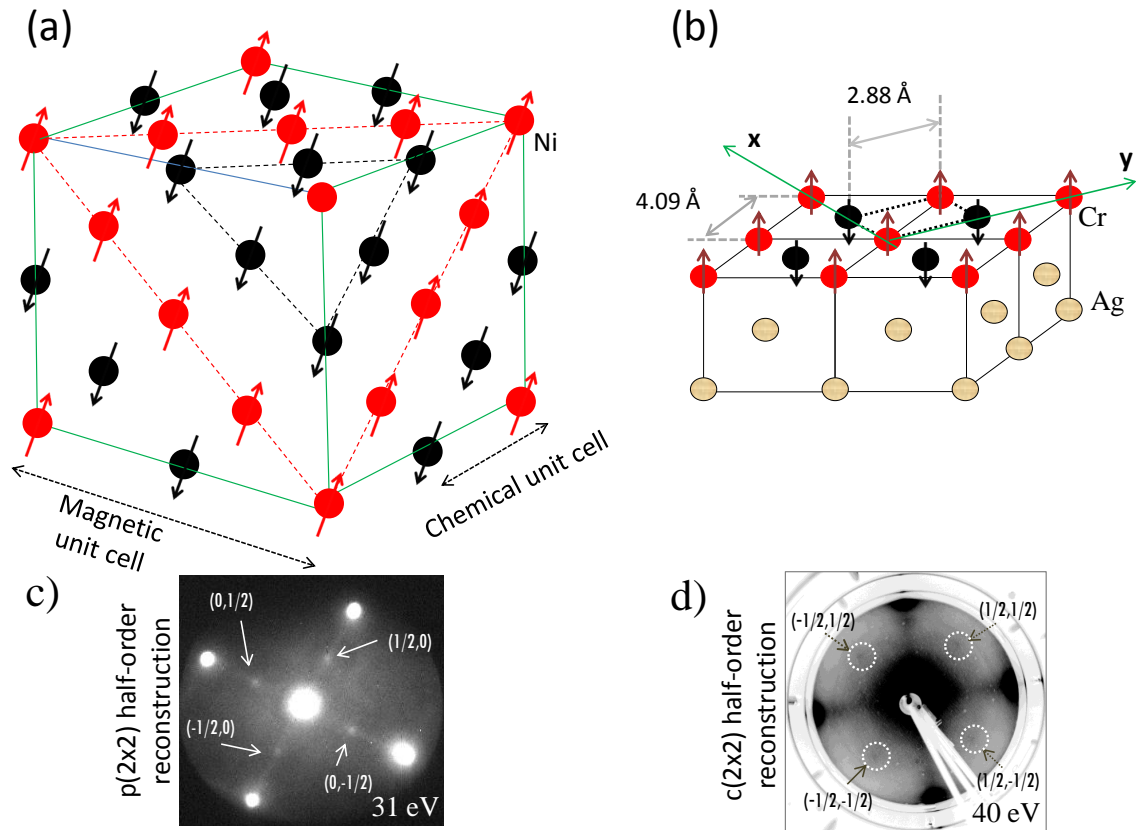


**Figure 2.9:** (a) The antiferromagnetic order of Ni spins in NiO crystal shows that the magnetic unit cell is double than the chemical unit cell. Existence of the oxygen atoms has been neglected for simplification. (b) Antiferromagnetic arrangement of the Cr moments in monolayer film over Ag(001) single crystal. (c)  $p(2 \times 2)$  LEED half-order spots, in case of NiO, corresponding to figure (a). (d)  $c(2 \times 2)$  LEED half-order spots, in case of Cr, corresponding to figure (b).

in electron diffraction. In figure 2.9 (c), a  $p(2 \times 2)$  superstructure is visible in the LEED data of NiO(001) surface collected at 31 eV, which is in fact a superposition of  $p(1 \times 2)$  and  $p(2 \times 1)$  types of superstructures arising from different magnetic domains.

In case of 1 ML Cr overlayer, the antiferromagnetic arrangement of Cr magnetic moments are of  $c(2 \times 2)$  pattern. The doubling of the magnetic lattice constant occurs along x and y axes as indicated in the figure. The magnetic superstructure, which is of  $c(2 \times 2)$  pattern, is visible in the LEED data collected at 40 eV as shown in figure 2.9 (d).

How to confirm that these fractional-ordered spots in LEED is due to magnetic origin? Reconstruction in LEED may also appear due to adsorption of gases or atomic rearrangement at the surface. None of these possibilities may occurs in our case, since all the experiments are performed in good UHV and at stable temperatures. The purity of the samples have been tested by XPS elemental scans, and no adsorption at surface were confirmed. The half-order spots in LEED originate due to exchange interaction of the low energy electrons with ordered Ni/Cr moments. The magnitude of exchange interaction is quite small, so is the intensity of the fractional ordered spots. The integer-order spots are the result of coulomb interaction which is comparatively higher by many orders of magnitude. The intensity of the half-order spots, which appear to be 2-4% of the integer order spots, is another proof in support of the magnetic origin of half-order spots. Moreover, the half-order spots appear with significant intensity at beam energies below 30 eV, where the magnitude of exchange interaction becomes significant. Also, the temperature dependence of the half-order intensities speaks for their antiferromagnetic origin, as discussed in respective chapters. Apart from LEED studies, the persistent antiferromagnetism in both films have also been confirmed by photoemission studies, which will be discussed in appropriate chapters later.

*Coherence length in LEED:* The practical LEED experiments deviate from the theoretical ideal of a perfectly monochromatic, perfectly collimated beam of electrons incident on the surface. There are two contributions; the finite energy spread of the electrons (of the order of 0.5 eV) and the finite angular spread of the electron beam. The joint effect is that, the electrons arriving at the surface are coherent only over a certain characteristic length, the coherence length. Only surface atoms within the coherence length can be considered to be illuminated by a simple plane wave. Electrons scattered from regions of the surface separated by more than a coherence length cannot interfere to produce a diffraction pattern (because the

incoming electrons are not coherent). Therefore, no surface structure with a length scale larger than the coherence length can form a diffraction pattern.

Thus in case of antiferromagnetic surfaces, magnetic half-order spots will only be visible in LEED if the antiferromagnetic correlation length is larger than the coherence length of the incident electron beam. Otherwise, the half-order intensity will significantly decrease. In our laboratory LEED instrument, the beam size is adjustable by the potential of the Wehnelt cylinder from 1 mm to 250  $\mu\text{m}$ . Whereas the electron coherence length is much lower (about 30 nm). After deposition of a film, if the physical domains formed on the substrate are of significantly smaller in size, naturally it also restricts the magnetic domain size as well as the magnetic correlation length. Then, there is a finite probability that the magnetic correlation length will be shorter than the electron coherence length. Under this situation, a significant reduction in the half-order intensity will be observed. In our experiments, we could not observe any  $c(2\times 2)$  half-order spots for the case of 0.1 and 0.2 ML Cr films deposited on Ag(001), where tiny nanodomains are expected to form, though the antiferromagnetic nature of both film coverages were proved from the photoemission studies. This will be discussed further in chapter 3 in appropriate context.

LEED from antiferromagnetic crystals provides an opportunity to probe magnetic structure within the laboratory. Also, it gives most direct means for studying the role of exchange in electron scattering.

## 2.5 Photoemission spectroscopy

Photoemission is widely used in the study of electronic structure of solids, surfaces, electron spectroscopy for chemical analysis (ESCA) and for catalytic studies *etc.* [39–43]. It utilizes the photoelectric effect in which an electron is ejected from occupied electronic level of the sample after being exposed to sufficiently energetic light or photon beam whose energy is analyzed by the electron energy analyzer.

The photoelectric effect which was first discovered by Hertz [44] in 1887 and later explained by Einstein [45] in 1905 by invoking the concept of quantum nature of light. However, it took a long time for photoelectric effect to get established as a technique to extract interesting and valuable information regarding the states of an electron inside a solid. Kai Siegbahn [46, 47] was awarded the Nobel Prize in Physics in 1981 for his development of electron spectroscopy. In photoemission experiment, the kinetic energy of the detected photoelectrons usually varies from few eV upto few hundred eV, depending on the photon energy used. This results in surface sensitivity of the technique, as the electron mean free path of the typical photoelectron in solid ranges from 5-30 Å [28] as shown in figure 2.1. The photon source is either a gas discharge lamp, X-ray gun or a synchrotron radiation source. The light impinges on the sample, and the electrons excited by the photoelectric effect are then analyzed with respect to the kinetic energy  $E_{kin}$  and their momentum  $k$  in electrostatic analyzer. The energy of the incoming photon can be in ultraviolet regime (5 to 100 eV, UPS), soft x-ray regime (100 to 1000 eV, SXPS), x-ray regime (>1000 eV, XPS) or in the hard x-ray regime (>3000 eV, HAXPS). In this simple picture, PES measures electron states of the sample under consideration. From the momentum and energy distribution of the electron, and with some reasonable assumptions, one can determine the electron dispersion curves  $E(k)$  in the solid. Using XPS, one can observe the photo-ionization of core levels where energies depend on the chemical state of the sample. Therefore, the spectroscopy of core levels can often be used for chemical analysis. Whereas using ultra-violet photoemission spectroscopy, one can have an idea about the valence bands of the sample.

Photoemission spectroscopy measures the density of states (DOS) of the sample under consideration. DOS is the number of states available in energy range  $E$  to  $E+\Delta E$  per unit volume. Photoemission intensity is directly proportional to DOS of the sample. There are several techniques to study the electronic structure of solids, but most of them are indirect and integrated techniques, such as the

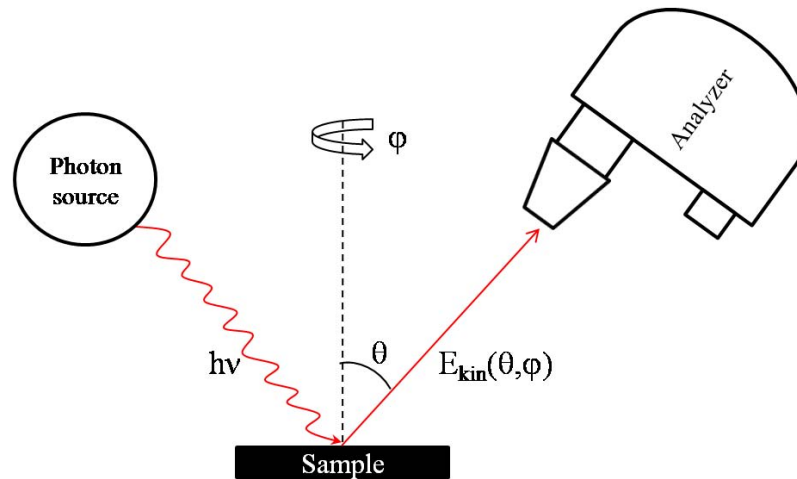


**Figure 2.10:** Sketch of a modern photoemission experiment.

optical experiments to study the absorption and dielectric constant, or the resistivity measurements. Here the quantum numbers of individual electrons are not sampled. PES can directly measure the DOS, but it is still integrating in angle and therefore information about the electron momentum is lost. In order to obtain the full set of electronic quantum numbers (except the spin), one has to turn to ARPES (details in next section).

The important parameters to be measured then are kinetic energy  $E_{kin}$  of photoemitted electron and its angle to surface normal as shown in figure 2.10. Knowing the energy of the photon ( $h\nu$ ) and the work function of the sample surface ( $\Phi$ ) one can determine the binding energy  $E_B$  of the electron in sample from the following equation

$$E_{kin} = h\nu - \Phi - E_B. \quad (2.6)$$

Figure 2.11 shows how energy level diagram and the energy distribution of photoemitted electron relate to each other. The Fermi energy  $E_F$  is the top of the valence band and has a separation  $\Phi$  from the vacuum level  $E_{vac}$ .

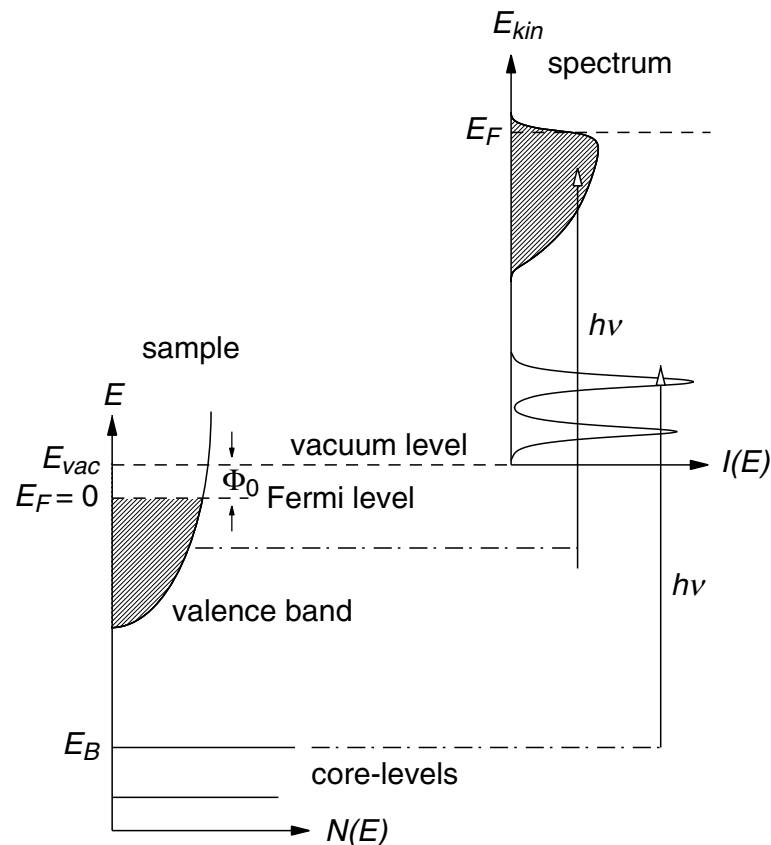


**Figure 2.11:** Schematic view of the photoemission process depicting relation between energy levels in solid and the electron energy distribution produced by photon of energy  $h\nu$ . [39,40]

There are some advantages in using electrons for surface spectroscopy as compared to photons, ions and atoms.

- a) The escape depth of electron is few Å, electrons are therefore suited to probe electronic states within the surface region of the sample (e.g., electronic states of thin films and surface states).
- b) Electrons are easily focused and their energy is easily tunable by electric field.
- c) Electrons are easy to detect and to count.
- d) Using electrostatic field, it is easy to analyze the energy and angle of electron.
- e) Electrons vanish after they have been detected. This is an appreciable advantage compared to, for instance, to ions or atoms which are used in surface physics too.

Electron mean free path for metals is of the order of few Å [see figure 2.2]. This means that any spectroscopy of solid surfaces involving electron samples only very thin layer of sample. Thus, if one wishes to learn about the surface properties of solids, one has to work with atomically clean surfaces. The investigation of surface states or electronic states of thin films requires UHV condition to prevent interference from adsorbed contamination. In order to get photoemission spectra from clean surfaces of reactive metals (such as alkali or rare earth metals), the residual gas pressure should be better than  $10^{-10}$  mbar.

### 2.5.1 Theory

The most commonly used model for interpretation of photoemission spectra in solids is so called three-step model, developed by Berglund and Spicer [48]. According to this very successful model, photoemission process can be separated in three steps:

- a) absorption of a photon and consequent excitation of electron into a crystal final state
- b) propagation of the photo-excited electron to the surface
- c) finally, escape of the photoelectron from the solid into the vacuum.

For a given kinetic energy  $E_{kin}$ , the parallel momentum outside the crystal  $k_{||}$  is determined by the emission angle of the photoelectron. The geometry of an ARPES experiment is schematically shown in figure 2.10. Usually one fixes a surface axis to the emission azimuthal direction obtaining the simplified form of eq. (2.13). Since translation symmetry along the surface is still present in the vacuum-solid interface, parallel momentum conservation of a periodic medium gives  $k_{||} = k_{f||} + g$ . Where  $k_{f||}$  is the parallel momentum of the final state inside the crystal and  $g$  is a reciprocal surface lattice vector. In addition, since the momentum of the photon is negligible for  $h\nu < 10$  keV, translational symmetry in bulk leads again to momentum conservation in a periodic medium, i.e.,  $k_f = k_i + G$ ,  $G$  being a reciprocal bulk lattice vector, and  $k_i$

the initial state momentum. In the reduced zone scheme of the crystal, where all reciprocal lattice vectors are included, this expression simplifies to  $k_f=k_i$ , leading to the following relation:

$$k_{||} = k_{f||} + g = k_{i||} + g \quad (2.7)$$

The determination of the momentum component perpendicular to the surface is unfortunately not so direct. The breaking of translational symmetry along this direction leads to a relaxation of  $k_{\perp}$  conservation, so that  $k_{i\perp}$  cannot be directly obtained. However, knowing the dispersion of the final state bands perpendicular to the surface, the initial state perpendicular momentum  $k_{i\perp}$  can be derived from energy conservation. As a first approach, we can suppose free-electron-like final state bands, shifted from the vacuum reference  $E_{vac}$  by the inner potential  $V_0$ . Then energy conservation leads to the following expression:

$$k_{f\perp} = \sqrt{\frac{2m}{\hbar^2}(E_{kin} + V_0) - k_{f||}^2} \quad (2.8)$$

Once we know  $k_{f\perp}$ ,  $k_{i\perp}$  is directly obtained from momentum conservation inside the crystal, i.e.,  $k_{f\perp}=k_{i\perp}+G$ . A more precise derivation of Eq. (2.8) requires a better approximation to the real dispersion relation  $E(k_{f\perp})$ . For the photon energies used in this thesis, the approximation of free-electron-like final bands is valid except in energy gap regions, where free-electron behavior is no longer the case of final states.

The most general and widely applied theoretical description of photoemission spectrum is based on using Fermi's Golden Rule [39] as a result of perturbation theory in first order. In this approach, the photocurrent  $j$  is the result of a photon induced excitation of a system from initial state  $|i\rangle$  into a final state  $|f\rangle$  resulting

in a photoelectron with momentum  $k$  and kinetic energy  $E_{kin}$  and remaining  $(N - 1)$  electron system:

$$j(E_{kin}, k_{||}, h\nu) \propto \sum T_f |M_{fi}|^2 \delta(E_f - E_i - h\nu) \delta(k_f - k_i) \quad (2.9)$$

where  $T_f$  accounts for the transmission probability of the final Bloch state into the vacuum and  $|M_{fi}|^2 = |\langle f | \delta H | i \rangle|^2$  is the transition rate between two states inside the crystal. The  $\delta$ -Dirac terms account for the energy and momentum conservations.

The perturbation operator  $\delta H$  describes the interaction of a (spin-less) electron in the system with the electromagnetic field  $\mathbf{A}$ . For sufficiently low electromagnetic field the Hamiltonian of the system can be written as,

$$H = H_0 + \delta H = H_0 + \frac{e}{2mc} (\mathbf{A} \cdot \mathbf{p} + \mathbf{p} \cdot \mathbf{A}) \quad (2.10)$$

where  $H_0 = (\mathbf{p}^2/2m) + V$  is the unperturbed Hamiltonian,  $\mathbf{p}$  is the momentum operator  $\mathbf{p} = -i\hbar\nabla$ ,  $m$  and  $c$  are mass of electron and speed of light respectively.

For photon energies below 1 keV (standard laboratory photon sources),  $\mathbf{A}$  varies slowly in the mean free path scale of the electron. Further,  $\delta H$  can be approximated as,

$$\delta H \propto \frac{e}{2mc} \mathbf{A} \cdot \mathbf{p} \quad (2.11)$$

using the commutator relation  $\mathbf{A} \cdot \mathbf{p} + \mathbf{p} \cdot \mathbf{A} = 2\mathbf{A} \cdot \mathbf{p} - i\hbar(\nabla \cdot \mathbf{A})$  and the dipole approximation  $\nabla \cdot \mathbf{A} = 0$ , i.e.,  $\mathbf{A}$  is constant over atomic dimensions compared to the wavelength of light used. In the ultra-violet photon energy range  $\mathbf{A}$  can be taken as constant. By using the commutation relation between  $H_0$  and  $\mathbf{p}$ , we can write the matrix element  $M_{fi}$  as  $M_{fi} \propto \mathbf{A} \cdot \langle f | \nabla V | i \rangle$ , where  $V$  is the crystal potential. According to this equation the origin of the photoemission intensity is the potential gradient.

### 2.5.2 Angle Resolved Photoemission Spectroscopy (ARPES)

Angle-resolved Photoemission Spectroscopy (ARPES) is possibly the simplest and most direct method for the study of the electronic band structure of surfaces and have been quite extensively used for the study of metal, semiconductor and oxide surfaces [41, 49]. It has been used to study simple one-dimensional (1D) and two-dimensional (2D) systems to more complex three-dimensional (3D) systems and have been quite successful in establishing the electronic structure of these materials; many detailed reviews on this subject are available in the literature [42, 43]. For 2D nature of the crystalline surface, there is a periodicity in the surface (x-y) plane but periodicity breaks along the surface normal (z) direction. Apart from energy conservation, the momentum of out-going electrons is also conserved; however, only the parallel component is conserved while the perpendicular component is not conserved due to loss of translational symmetry along the surface normal. For a given kinetic energy  $E_{kin}$  the parallel component of the electron crystal momentum  $k_{||}$  is given by,

$$(k_{||x}, k_{||y}) = \sqrt{\frac{2mE_{kin}}{\hbar^2}} \cdot (\sin \theta \cos \phi, \sin \theta \sin \phi) \quad (2.12)$$

where  $k_{||}$  is the out-going photoelectron momentum,  $m$  is mass of the electron and  $\theta$  and  $\phi$  are polar and azimuthal emission angles respectively. The geometry of an ARPES experiment is schematically shown in figure 2.10. Usually one fixes a surface axis to the emission azimuthal direction obtaining the simplified form:

$$k_{||} = \sqrt{\frac{2mE_{kin}}{\hbar^2}} \sin \theta. \quad (2.13)$$

From the energy and angular distribution of the emitted electrons, the energy *vs.* momentum information of the crystal (band dispersion) can be determined. This process of “band mapping” is a powerful probe of electronic structure of the crystalline materials. The theoretical band structure calculations are also important in studying

electronic structure of solids. The angle-resolved measurements can be compared directly with the calculated band structure, which enhances the understanding of the experimentally obtained electronic structure of the solids.

Several reasons that confirm the ability of this technique to determine the electronic structure are listed below,

a) It allows a direct determination of the quantum numbers of the electron system, such as those for electron momentum and energy, so that a complete analysis of the electronic structure can be obtained.

b) The short escape depth of photoelectrons (5-15 Å for the photon energy range of 10-1000 eV) make this technique surface sensitive, hence both bulk and surface contribute to the photoemission intensity. This point is of crucial importance for analyzing the surface electronic structure, such as surface, adsorbate or thin film states.

c) The transition time between electronic states and the escape time of the photoelectrons are of the order of  $\sim 1$  fs, thus the atoms do not have time to rearrange and therefore change the electronic state during the photoemission process. In solid state, this approximation of static atomic arrangement is often referred to as the adiabatic or Born-Oppenheimer approximation, and simplifies very much the interpretation of the data and the calculation of the electronic structure.

### 2.5.3 X-ray Photoemission Spectroscopy (XPS)

Instead of using light with energies in the ultraviolet range as described above, it is also possible to perform photoelectron spectroscopy with higher excitation energies in the X-ray regime. The photon energy is then high enough (e.g. 1486.7 eV) to excite electrons from core levels which is usually referred to as XPS or core-level photoemission spectroscopy. The simplest application of XPS is the determination of the chemical composition of the investigated sample known as ESCA, as the

binding energies are characteristic for the elements in the periodic table. Still more information can be obtained by taking energy shifts and line shapes into account and analyzing them carefully. The exact peak positions may be capable of indicating the chemical state of the component elements of the sample. From line shapes it is possible to draw conclusions about detailed electronic structure parameters, interactions and even about valence band properties because valence band electrons are generally involved in relaxation processes that follow the core electron excitation. An asymmetry in core level peak indicates for example the metallic behavior of the respective sample [50]. A detailed description for other many-body effects arise from the participation of more than one electron during the photoemission process can be found in Ref. [51].

## 2.6 ARPES facility at SINP

In this section, I will describe the ARPES facility [52] that has been established at SINP for detailed surface electronic structure characterization of crystalline materials. This state-of-the-art facility provides high energy and angular resolutions for modern day ARPES measurements and allows different measurements such as Band-Structure Mapping, Fermi-Surface Mapping and Photoelectron Diffraction *etc.*

The ARPES system was designed at SINP and custom fabricated by PREVAC Sp. z o.o., Poland, integrating different brands of components. The schematic diagram and photograph of the ARPES system is shown in figure 2.12 and 2.13 respectively. The ARPES system consist of three different chambers namely, Load-lock, Preparation and Analysis chambers with easy transfer mechanism of samples between the chambers. The description of each chamber with its components will provide a general idea about the system.

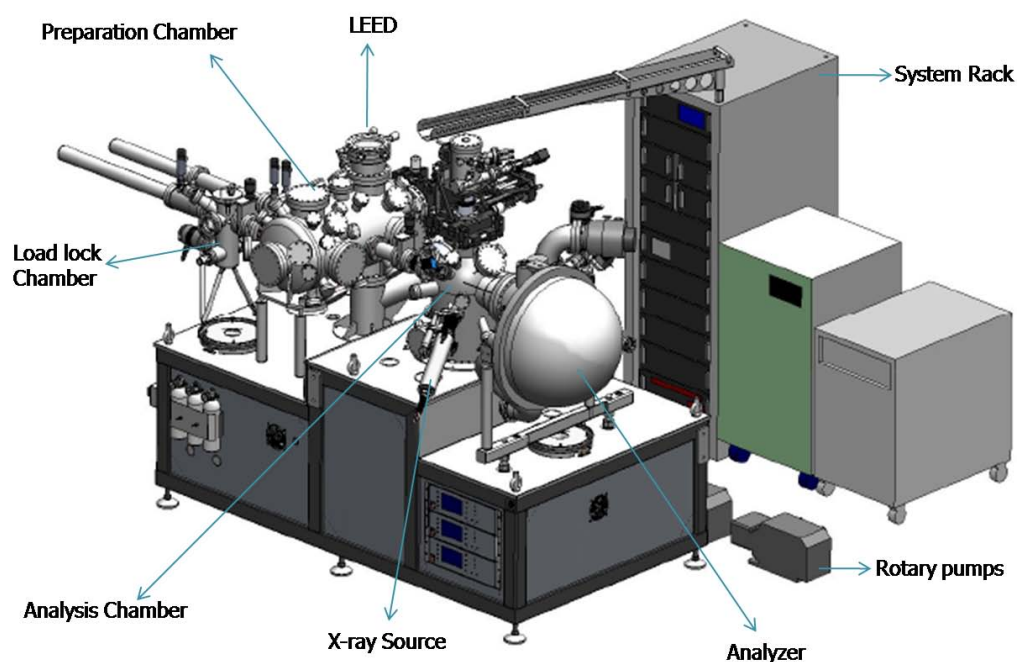


**Figure 2.12:** The schematic diagram showing different chambers and components of the ARPES system at SINP.

### 2.6.1 Load lock

The load-lock or fast entry chamber is to put the sample from atmospheric pressure to high vacuum ( $< 5 \times 10^{-8}$  mbar) where the samples can be left for initial degas. This is facilitated with a halogen lamp which can be used to heat samples up to  $200^\circ\text{C}$ . A vacuum suitcase can be readily attached to the load-lock to transfer the sample to other UHV systems.

### 2.6.2 Preparation chamber

Apart from the standard surface preparation requirements, the preparation chamber is also equipped to perform growth of metal and metal-oxide ultra-thin film and multilayers. The base pressure of the preparation chamber is  $< 2 \times 10^{-10}$  mbar and is achieved by 1000 litre/sec Turbo Molecular Pump (TMP) (Leybold Vacuum GmbH) backed by another TMP of capacity 70 litre/sec backed by a rotary pump, and is

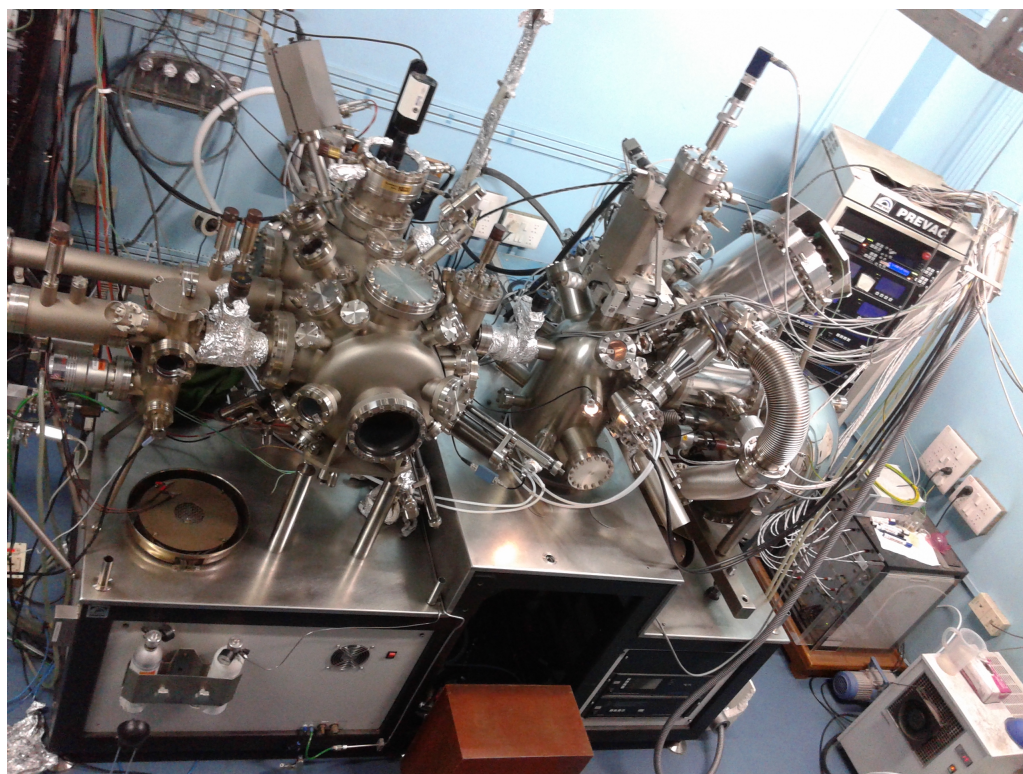


**Figure 2.13:** Photograph of SINP-ARPES laboratory.

also pumped by an ion pump with a capacity of 300 litre/sec. This chamber consists of a Titanium Sublimation Pump (TSP) also. Some of the important components of the preparation chamber are described below.

**a. 4-axis Sample Manipulator:** For the sample manipulation, the preparation chamber is equipped with a 4-axis (X, Y, Z, polar rotation ( $\theta$ )) manipulator with heating and liquid nitrogen cooling facility. In this manipulator we can heat the sample up to 1200°C in the continuous mode and 2000°C in the flash mode and can cool the sample up to -170°C. The sample temperature is measured by K and C type thermocouples depending on the measured temperature range. The Z motion as well as theta rotation of the manipulator is motorized and controlled by computer to make appropriate movements for sample transfers and for growing films of different thickness on the same substrate at different locations with the help of a mask.

**b. Sputtering gun:** Ar sputter gun is used to clean the top surface of the sample. The energy of the  $\text{Ar}^+$  ions produced from the sputter gun can be controlled (200-5000 eV) depending on the requirement. Usually after sputtering, one needs to anneal the sample so that the surface atoms can re-order and take their equilibrium positions.

**c. UHV cleaver:** The preparation chamber is also equipped with a UHV cleaver and can be used to cleave insulating and semiconducting crystals *in situ*. Using the same crystal, multiple cleaves can be made and samples can be heated up to  $600^\circ\text{C}$ .

**d. Parking chamber:** The parking chamber can store up to 6 samples at a time. We can avoid surface contamination of crystals by storing them in-situ and helps to speed up the surface preparation process.

**e. Evaporator:** For the growth of ultra-thin metal films, we use a water-cooled e-beam evaporator. Here, the metal rod/ingot in crucible is evaporated by electron beam bombardment heating. The flux of the ions ejected from the evaporator is monitored and is calibrated to the rate of evaporation. The preparation chamber also has a Knudsen cell that can heat up the evaporating materials to reach higher temperature as 2173 K. It consists of some home-made resistive heating as well as e-beam evaporators.

**f. Quartz microbalance:** The rate of evaporation of materials at the sample position can be monitored by the quartz microbalance. The shift in the resonant frequency of the quartz crystal due to the excess material deposited on top is calibrated to the rate of deposition. The microbalance is mounted on a Z-shift which enables its linear motion. The calibration of the evaporation rate is performed after placing the quartz crystal at the growth position.

**g. Low energy electron diffraction (LEED):** LEED is the standard technique to study the surface crystalline order. The surface cleanliness, crystal orientation at the surface and crystalline order can be deduced from the LEED pattern in a

quantitative way. We have a LEED system from OCI vacuum Microengineering, Inc. Canada. The details of the LEED has already been discussed earlier in this chapter.

**h. Sample holders:** Two different types of sample holders are used for all the experiments mentioned in this thesis. The first one, PTS 1000, is capable of resistive heating the sample slowly upto  $1000^{\circ}\text{C}$ . Here, the Ag(001) single crystal sample is heated by a heating coil mounted at the bottom of the sample holder. The second one, PTS 1200, can heat the sample upto  $1200^{\circ}\text{C}$ . This sample holder is composed of electron beam heating and therefore can heat up the sample with comparatively faster ramp. The crystal is grounded in both sample holders and the temperature is measured by a K type thermocouple. Perfect mounting of the single crystal on the sample holder is important. The flatness of the crystal is checked by a laser beam reflection from the sample top surface. The crystalline direction of the sample is checked from LEED measurements.

### 2.6.3 Analysis chamber

The analysis chamber is dedicated for performing the photoemission experiments. The base pressure of this chamber is better than  $8 \times 10^{-11}$  mbar which is achieved by a 600 litre/sec TMP backed by 70 litre/sec TMP and a rotary pump. The chamber is also pumped by a titanium sublimation pump (TSP) integrated with a liquid nitrogen cryo shroud. As the ARPES measurements are very sensitive to the stray magnetic field around the sample region, the analysis chamber is made out of mu-metal so that on the sample region we have less than 0.5 micro Tesla field. The analysis chamber is equipped with the following components.

**a. 5-axis Sample Manipulator:** For the sample handling in analysis chamber, we have another 5-axis manipulator (X,Y,Z translation and  $\theta$ ,  $\phi$  rotation) with heating and cooling facilities as described before. The polar as well as azimuthal

rotation of the manipulator is computer controlled so that ARPES spectra can be collected at different polar and azimuthal angles in an automated way.

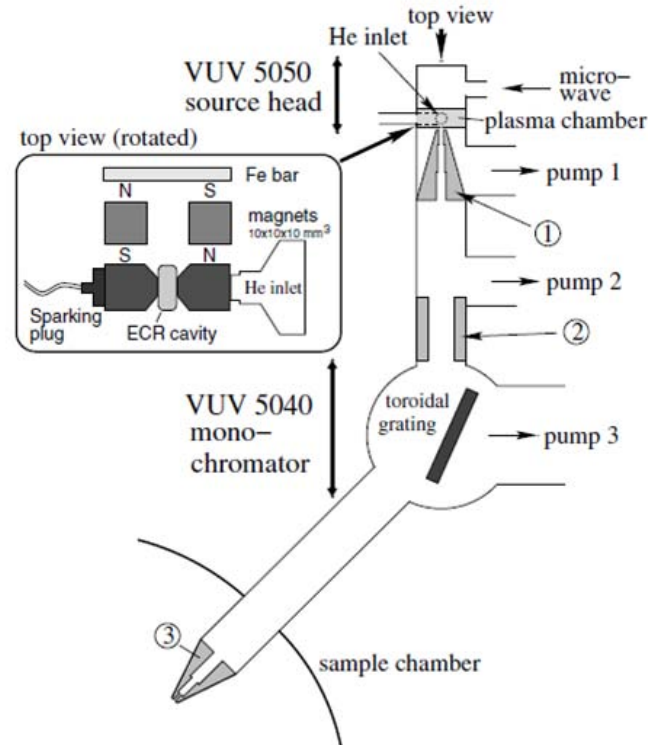


**Figure 2.14:** The schematic diagram (from Ref [42]) of the Monochromatic UV lamp used in the ARPES setup.

**b. Monochromatic X-ray source:** The analysis chamber is equipped with a single-anode monochromatic x-ray source (Model: MX 650, from VG-Scienta) for performing XPS and Photoelectron Diffraction. The Scienta MX 650 X-ray source produces high intensity monochromatic Al  $K_{\alpha}$  radiation. It contains an aluminium anode and a quartz crystal monochromator. It yields an excitation energy of 1486.7 eV in a narrow band of 0.4 eV.

**c. Monochromatized High Intensity UV lamp:** For the high-resolution ARPES measurements, it is required to have a high intensity UV lamp which is monochromatized to remove the higher order satellites of the radiations. In the analysis chamber, we are equipped with such a high-intensity lamp (VG Scienta

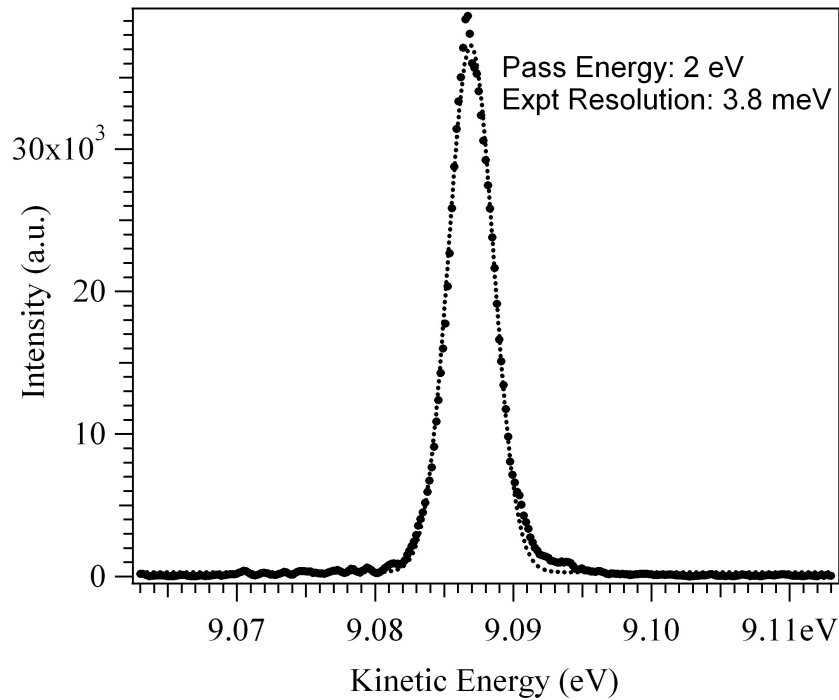


**Figure 2.15:** Experimental energy resolution measurement on Xe  $5p_{3/2}$ .

VUV5000) which is a microwave driven Electron Cyclotron Resonance (ECR) based He lamp and is coupled with VUV5040 monochromator. The exit stage of the monochromator can house different diameter capillaries to have a reduced spot size on the sample as the angular resolution of the ARPES critically depends on the photon beam spot size. This capillary also restricts the flow of the Helium into the experimental chamber and thus maintaining a good vacuum during experiments. We use a capillary of inner diameter 0.8 mm and obtain a spot size of  $\sim 1.2$  mm of the photon beam at the sample position. Moreover, it helps to maintain the chamber pressure to the base pressure even during the ARPES experiments. For the ease of operation, the whole UV lamp is mounted on a special manipulator so that the lamp can be inserted very close to the sample (about 10 mm) and can be retracted after the experiments. The UV lamp primarily gives He  $I_{\alpha}$  (21.22 eV) and He  $II_{\alpha}$  (40.81 eV) with energy resolution better than 1 meV. The schematic diagram of the UV lamp assembly is shown in figure 2.14. As can be seen, the whole assembly is

pumped by various pumping stages to reduce the flow of helium into the analysis chamber.

**d. Hemispherical Electron Analyzer:** The heart of the ARPES experiment is to measure the kinetic energy of the outgoing electrons at different emission angles. In the analysis chamber, we have a 200 mm concentric hemispherical analyzer (VG Scienta R 4000-WAL) with wide-angle lens for high-resolution and fast ARPES measurements. This is the state-of-the-art 2D analyzer with Multi-channel Plate (MCP)-CCD detector which can map the emission angle of the electrons with their kinetic energy and obtain a direct dispersion images on the screen. The widest angular range possible is  $\pm 15^\circ$  with an angular resolution  $\sim 1^\circ$ ; there are other angular ranges  $\pm 7^\circ$  and  $\pm 3^\circ$  with angular resolutions  $\sim 0.4^\circ$  and  $\sim 0.1^\circ$ , respectively. The energy and angular resolution have been tested at the laboratory with values matching near the specified values. The angular dispersions of the analyzer have been tested with a special angular device mounted on the sample manipulator. The gas cell measurements on the  $5p_{3/2}$  core level of Xenon (at binding energy  $\sim 12.1$  eV), gives the energy resolution matching to the expected performance of the analyzer as shown in figure 2.15. However, the experimental energy resolution on solid samples depends on the sample temperature.

#### 2.6.4 Electron Energy Analyzer

In photoemission process, the most important part is measuring kinetic energy of the photoelectrons. The photoelectrons drifting in the vacuum are pulled toward and focused into the energy analyzer by an electric field generated by an electrostatic lens. Though energy analyzers come in different configurations, the most common type is the Concentric Hemispherical Analyzer (CHA) [53]. A CHA consists of two hemispheres of radius  $R_1$  and  $R_2$  (figure 2.16) of slightly different sizes having the same center point. A voltage is placed across the two hemispheres such that the inner

one is positively charged relative to the outer one, hence creating a radial electric field. The electrostatic lens directs the photoelectrons into the space between the two hemispheres. Subsequently, all the photoelectrons will experience a centripetal force and hence undergo uniform circular motion. Thus, the radius of curvature of this motion for a given potential difference between the two hemispheres is determined by the electron's kinetic energy. The kinetic energy of the electron traveling on the central path  $R_0=(R_1+R_2)/2$  is given by

$$E_p = \frac{eV}{R_2/R_1 - R_1/R_2} \quad (2.14)$$

This energy is called the pass energy of the analyzer, and it is determined by the radii of the hemispheres and the voltage applied between them. Photoelectrons that have a kinetic energy greater than the pass energy will have a larger radius of curvature and will therefore collide with the outer hemisphere. Whereas photoelectrons that possess a kinetic energy less than the pass energy will have a smaller radius of curvature and will coincidentally collide with the inner hemisphere. Note that the pass energy actually has a small range of energies associated with it, since the space between the hemispheres is not infinitesimally small. When a photoelectron survives to come out the other side of the space between the hemispheres, it strikes an electron multiplier in order to increase the signal to a more discernible amount. Electron multipliers consist of material with electrons in a low binding energy state such that the energy of the photoelectron is capable of dislodging multiple electrons from their atoms, which in turn will dislodge even more electrons. This cascade effect increases the number of electrons striking the detector, thus improving the signal since the current contribution of a single electron would be difficult to detect. Note that the kinetic energy of these detected electrons is not important since the kinetic energy of the electron that started the cascade has already been determined.

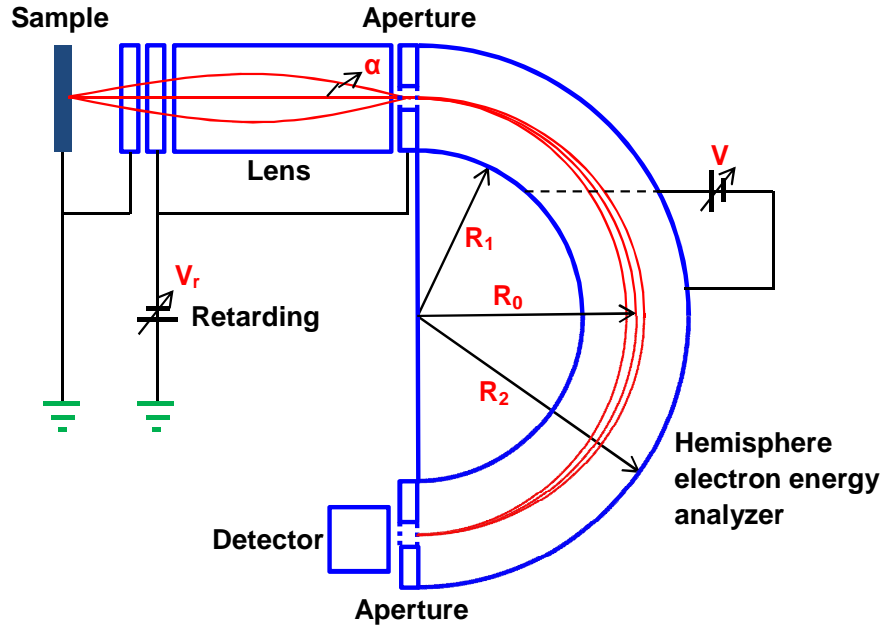


**Figure 2.16:** Schematic of a concentric hemispherical electron energy analyzer. Taken from [32]

The energy resolution of a CHA is calculated as [54]

$$\Delta E = E_p \left( \frac{x_1 + x_2}{2R_0} + \alpha^2 \right) \quad (2.15)$$

where  $x_1$  and  $x_2$  are width of the entrance and exit apertures,  $\alpha$  is the angular acceptance of the electron beam at the entrance slit. From the above relation, it is evident that the radii of the hemisphere and the slit width are relevant in determining the resolution of an energy analyzer. Hence, a large hemisphere is inherently favored because of a better resolution. In reality, the pass energy and the aperture sizes are set to achieve a good compromise between signal intensity and energy resolution.

A modern Scienta electron energy analyzer with 2D detector is shown below in figure 2.17, which is widely used in modern ARPES experiments for improved data acquisition efficiency, improved energy resolution and improved momentum resolution.

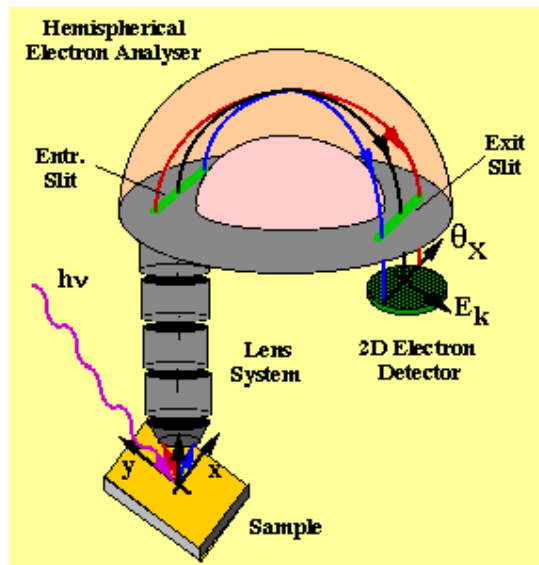


**Figure 2.17:** Schematic of the Scienta electron energy analyzer with 2D detector. [32]

## 2.7 Modes of photoemission data collection

Photoemission experiments can be performed in different modes. The most common mode is called Energy Distribution Curve (EDC) and consists on measuring the kinetic energy of the photoelectrons for a fixed photon energy, as can be seen in figure 2.18(a). Since the total energy must be conserved, different kinetic energy implies different initial energy. A typical EDC spectra is shown in bottom of figure 2.18(a). The peaks correspond to elastically scattered photoelectrons, while the inelastic electrons spread in a smooth background. The cut-off at high kinetic energies indicates the Fermi level. In general, EDC curves are used to investigate the dispersion of the initial states, as well as the lifetime of the initial hole and the final electron. By taking EDC curves for different emission angles at the same photon energy we are selecting different parallel momenta and therefore the dispersion of the initial states parallel to the surface can be mapped. This is what is usually done in a laboratory.

Another type of experimental mode is the Constant Initial State (CIS). Here one can fix the initial energy by simultaneously varying both the photon and the measuring kinetic energy, as can be seen in figure 2.18(b). thereby measuring the initial state photoemission cross section as a function of photon energy. In the CIS spectra shown below we see that the photoemission cross section of the initial state oscillates as we vary the photon energy. We can obtain information about the spectral function of the initial and final momentum perpendicular to the surface from CIS experiments. In this thesis all the photoemission data were collected in EDC mode, hence CIS mode is beyond the scope of this thesis.

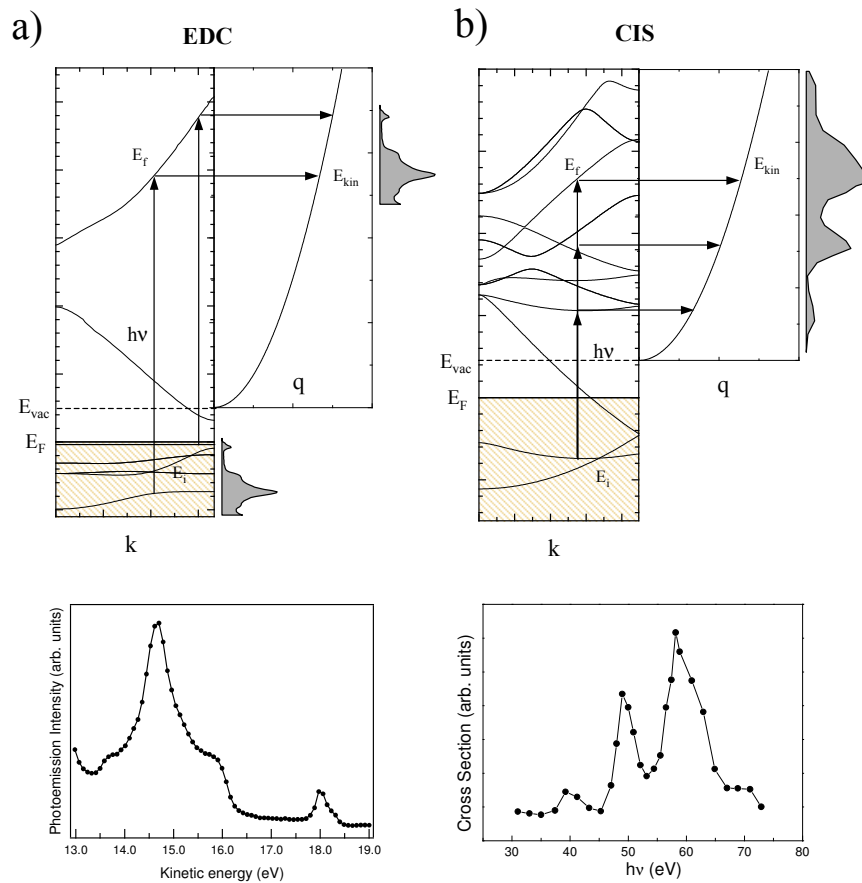


**Figure 2.18:** Schematic representation of energy balance (top) and typical spectra (bottom) for a) an EDC experiment and b) a CIS experiment [55].

## 2.8 X-ray absorption techniques

X-ray absorption spectroscopy is a very powerful tool for material characterization in view of its chemical specificity and is used particularly for local structure and electronic structure characterization [56, 57]. Moreover the polarization (of incident x-ray) dependence of spectral shape also allows us to study magnetic properties at surfaces and buried interfaces [58]. Hard x-ray (with x-ray energy of few keV)

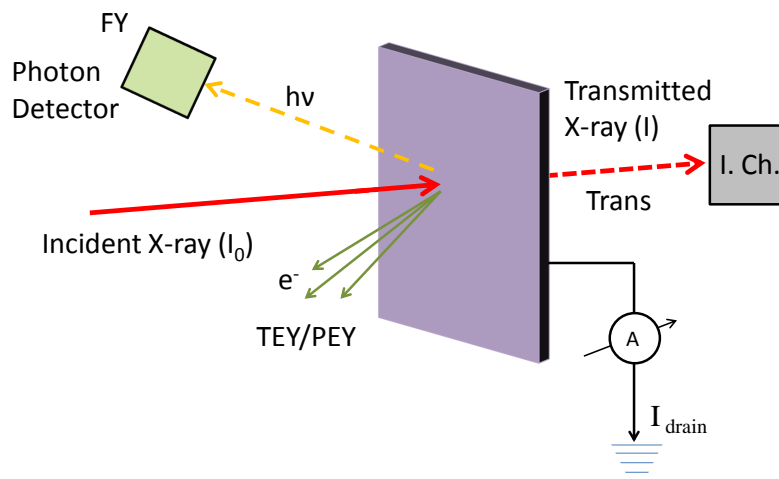


**Figure 2.19:** Schematics describing different modes of measurements in x-ray absorption spectroscopy (see text for details).

absorption spectra are usually collected in transmission mode, schematically presented in figure 2.19. X-ray absorption coefficient  $\mu$  is calculated by detecting the intensity of incident x-ray ( $I_0$ ) and the transmitted ( $I$ ) x-ray using the Lambert-Beer law:

$$I = I_0 e^{-\mu x} \quad (2.16)$$

where ' $x$ ' is the sample thickness passed by the incident x-ray. Absorption coefficient is a smooth function of x-ray energy ( $\mu \simeq Z^4 E^{-3}$ ), unless  $E$  matches with an excitation energy. When it happens, one observe a sharp rise (known as an absorption edge) in the absorption spectrum due to the excitation of core-level electrons to unoccupied band above Fermi energy. Absorption spectra are collected by tuning x-ray energy from few tens of eV below the absorption edge to sufficiently above and monitoring transmitted x-ray intensity as a function of energy. Since the binding energy of core-level electrons is material characteristic, one can perform chemical specific experiments by tuning x-ray energy at corresponding edge of the material. The incident and transmitted x-ray intensities can be measured by ionization chambers.

For soft x-ray (energy range few tens to hundreds of eV), however, transmission detection mode is not suitable as the sample thickness must be very thin (typically less than  $0.1 \mu\text{m}$ ) to detect transmitted x-ray signal, which is practically not possible for various experimental situations. The experiments with soft x-ray have to be performed in ultra-high vacuum (UHV) to avoid absorption from air. When a core electron is excited by incident x-ray with proper energy, a core hole is also created which can be reoccupied by energetically higher state, causing the emission of either Auger electron or photon. If the Auger electron arise from sub-surface region, they can set off series of inelastic collisions that produce a bunch of secondary electrons with lower energy than Auger electrons. One can measure the intensity of all electrons emitted from the surface, which is assumed to be proportional to absorption cross-section. This mode of detection is commonly known as total electron yield (TEY). Emission of electrons may be compensated by using positively biased electrodes near sample-surface. Emission of electrons from grounded sample sets off a current (known as drain current), which can be measured as a very close approximation to absorption coefficient in TEY mode. As the electron emits from the near surface region of the sample (due to limited inelastic mean free path), this mode of detection is sub-surface sensitive. However, the surface sensitivity varies from material to material and

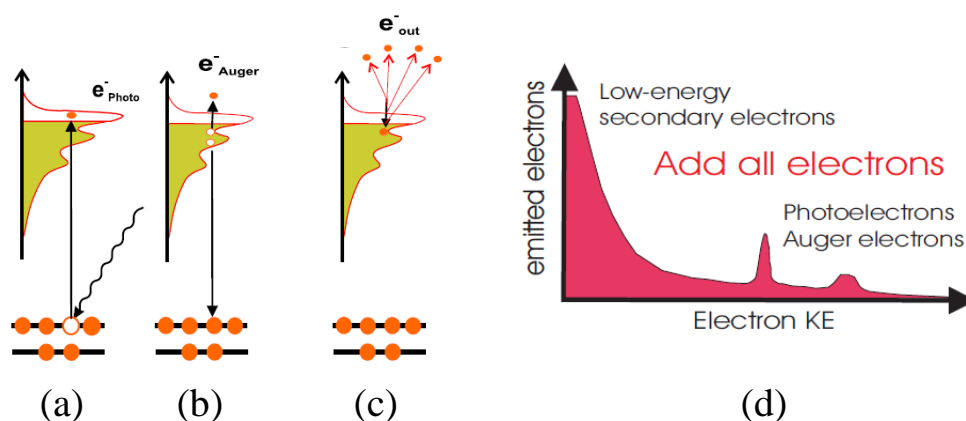


**Figure 2.20:** The x-ray absorption, creation of photoelectrons and Auger electrons. Number of emitted electrons has been plotted against electron kinetic energy.

typically lies between 2-10 nm range. One can also detect the radiation resulting from the core-hole decay and this mode of detection is called fluorescent yield (FY). FY mode is more bulk sensitive (probing depth is typically  $> 20$  nm) compared to TEY mode. Better surface sensitivity can be achieved in partial electron yield (PEY) mode. In PEY mode, an electron energy analyzer is used to select the emitted electrons within particular energy range. However, TEY mode is immensely used in soft x-ray absorption because of its surface sensitivity and technical sensitivity.

Incident x-ray is absorbed by a core level electron and the recombination processes cause the electron yield emitted from the sample. The incoming photon produces a photoelectron and the resulting core recombines by emitting an Auger electron. The photo electron and the Auger electron may now either be emitted into the vacuum or due to their limited mean free path lose their energy by inelastic scattering. In this case a larger number of low energy secondary electrons per initial photo electron is generated. Due to their larger mean free path the secondary electrons will eventually be emitted into the vacuum. If the sample is grounded the ground current which is necessary to compensate for the emitted charge can finally be measured, which is the total electron yield. The procedure is depicted in figure 2.20.

The XAS lineshape of transition metals and oxides is dominated by the large (10 eV)  $2p$  core-hole spin-orbit coupling, which splits the  $L$  ( $2p$  to  $3d$ ) absorption spectrum into two portions. The lower-energy  $L_3$  region is associated with transitions to a  $2P_{3/2}$  final state; the higher-energy  $L_2$  region is associated with transitions to a  $2P_{1/2}$  final state. Unfortunately, this is the only spectral feature that is easy to understand in the general case. Two of the most important phenomena related to transition metal oxides are crystal field and multiplet effects. These effects split the relatively simple peaks of the metal spectrum into several smaller sub-peaks. The Ni  $L_2$  peak is subdivided into two parts due to multiplet splitting.

### 2.8.1 Synchrotron radiation

In x-ray absorption measurements, one needs to tune (or vary) x-ray energy and also requires x-ray with sufficiently high intensity. State-of-the-art synchrotron sources, which provide intense and tunable radiation, are essential for performing x-ray absorption experiments. Synchrotron radiation is produced when energetic charge particles (electrons) undergo an accelerated motion. As the velocity of electrons is very near to the speed of light, radiation is emitted with very small opening angle (in a narrow cone, due to relativistic effects) in the forward direction at a tangent to the electron's path. Apart from high intensity with tunable energy, one can also select the polarization of radiation, which is particularly useful for dichroism measurements [58]. Many microscopic and spectroscopic studies for characterization of magnetic structure of NiO films, like XAS, XMLD, PEEM and LEEM has been performed at Nanospectroscopy beamline of Elettra synchrotron, Italy.

### 2.8.2 Linear dichroism

A linear dichroism spectrum is the difference between spectra taken with the incident x-ray electric field vector perpendicular and parallel to a system axis of interest. This

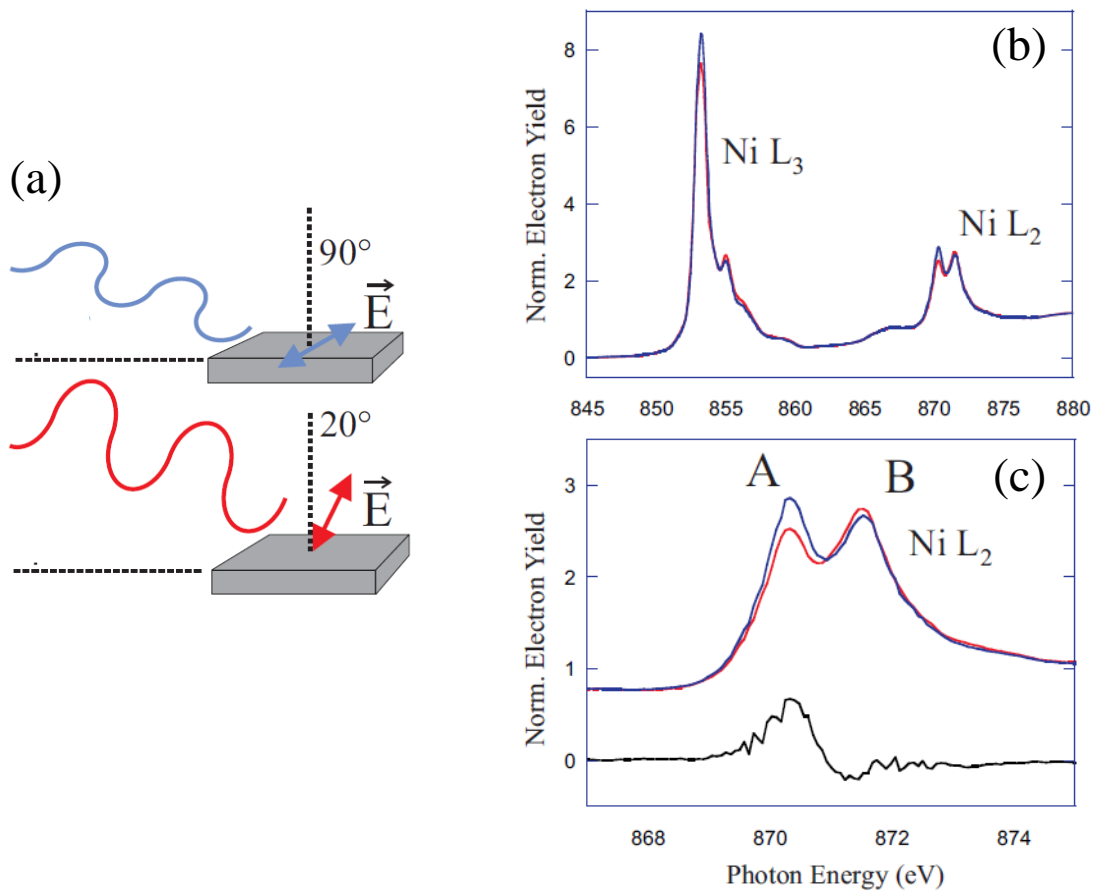


**Figure 2.21:** (a) The absorption of plane polarized x-ray by the NiO sample. The plane of polarization of the incident x-ray may be parallel or perpendicular to the sample surface. (b) The x-ray absorption spectra at Ni  $L$  is shown. (c) The multiplet splitting of the Ni  $L_2$  peak is shown.

thesis considers linear dichroism of a magnetic origin, specifically, the distortion of electron orbitals accompanying antiferromagnetic ordering. In this case, the axis of interest is  $\vec{A}$ , the antiferromagnetic spin axis. Linear dichroism measures the projection  $M^2$  of the magnetization vector  $\vec{M}$  on  $\vec{A}$ .

In figure 2.21 (a), incidence of plane polarized x-ray on the sample surface has been shown. The plane of polarization may lie on the plane of sample surface or perpendicular to the surface. Figure (b) shows the x-ray absorption spectra at Ni  $L$  edge. For a metallic Ni sample both the  $L_3$  and  $L_2$  are single peak. For oxide

sample, i.e. NiO, these peaks divides into multipeaks. Division of  $L_2$  edge into two distinct peaks, A and B are prominent in figure (c).

For antiferromagnets XMLD is currently the only technique to quantify the orientation of the AFM axis at surfaces. An XMLD intensity will be defined as the x-ray absorption ratio between the low and the high energy absorption fraction within an absorption resonance, for example A and B as noted on figure 2.21 (c). One finds for the dependence of the XMLD intensity on the angle between the incident electromagnetic field  $\vec{E}$  and the thermodynamic expectation value of  $\langle M^2 \rangle$ .

$$I_L = I_0 - C \langle M^2 \rangle (3 \cos^2(\vec{E}, \langle \vec{M}^2 \rangle) - 1) \quad (2.17)$$

$I_L$  is the electron yield intensity originating from a particular absorption and  $I_0$  represents the isotropic absorption intensity. The XMLD intensity shows a maxima for parallel alignment between the sample AFM axis and electric field vector of the polarized beam.

### 2.8.3 The XMLD effect

In XMLD experiments [59], x-ray absorption spectra are collected (at Ni  $L_2$  edge) with different (linear) orientations of polarization axes of incident x-ray with different orientations of the sample with respect to incident x-ray to achieve angular dependent spectral shape. Variation of spectral shape with angular orientation of linear polarization-axis is known as x-ray magnetic linear dichroism (XMLD). This arises from charge-anisotropy induced by the exchange and spin-orbit interactions. Here we present our discussion with a typical example of spin configuration in NiO(001) thin films grown on nonmagnetic substrate Ag(001). In figure 2.22, both the vertical and horizontal polarization of incident x-ray beam on sample, has been displayed. The resultant XAS spectra of a 60 ML NiO film at Ni  $L_2$  edge has been shown later in chapter 7. In order to determine the surface spin-axes ( $\mathbf{A}$ ) from experimental

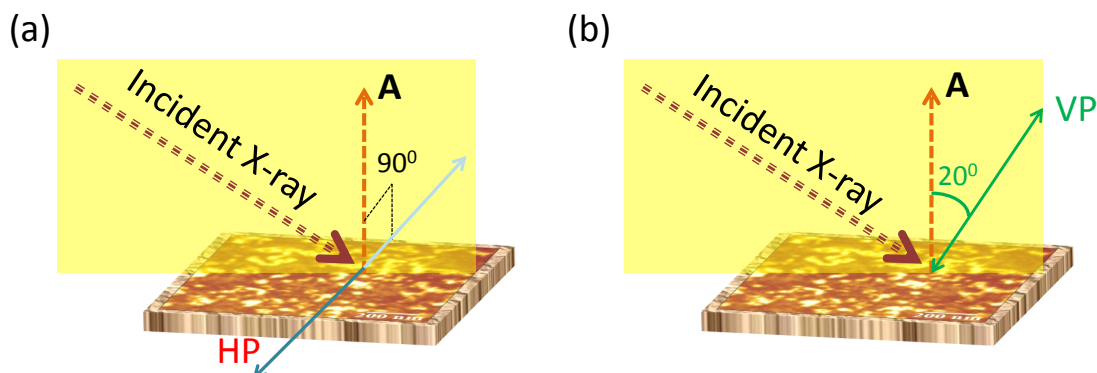


**Figure 2.22:** Schematics of HP and VP x-ray incidence on NiO film.

spectra, one needs to have an angular expression which relates the x-ray absorption spectral shape to the orientation of  $\mathbf{A}$  and the incident light polarization axis ( $\mathbf{E}$ ), as the effect is polarization dependent. The traditional approach to this problem within the isotropic formalism is given by the following angle dependent expression

$$I(\theta, T) = \alpha + \beta(3\cos^2\theta - 1) \quad (2.18)$$

where the first term on the right hand side is a constant at particular temperature and the angular dependence comes in the second term.  $\theta$  is the angle between  $\mathbf{E}$  and  $\mathbf{A}$  and  $\beta$  contains a term  $\langle M^2 \rangle_T$ , which is the domain average of the antiferromagnetic moments that vanishes above Néel temperature.

## 2.9 Magnetic imaging techniques

In order to obtain spatially resolved information of different structural aspects and surface magnetic order, two different imaging techniques are employed. Microscopy using low energy unpolarized electrons was frequently performed. In addition to low energy electron microscopy, local surface magnetic order has been investigated using photoemission electron microscopy with XMLD contrast mechanism.

### 2.9.1 Low energy electron microscopy (LEEM)

In LEED, the diffracted beams from sample surface are collected on the screen, however, they can also be used to image the surface in a low energy electron microscope with very high lateral resolution (typically less than 10 nm). In figure 2.23, we schematically describe different components of such a microscope. The sample, mounted on a manipulator facing the objective lens, is also a part of the microscope optics and kept at  $-20$  keV. The illumination column, containing an electron gun and few lenses (condenser), provides monochromatic electron beam for the experiments. A 20 keV electron beam is produced and focused in the illumination column, which can be varied in a range of few eV with respect to  $-20$  keV. Electron beam from illumination column can be deflected by the beam separator and can be transferred through the objective lens to the sample. The separator uses magnetic field, where electron beam passing through the field will be deflected by the Lorentz force. Energetic incident electron beam is slowed down by retarding field between objective lens (at ground) and sample-surface (at  $-20$  keV) to an energy of few eV. Near zero (or slight negative) electron energy is used for performing some specialized experiments such as mirror electron microscopy (MEM), that will be discussed later. Approximately  $80 \mu\text{m}$  region of sample-surface can be illuminated by electron beam, which can be reduced further using apertures. Elastically backscattered electrons from sample-surface are then accelerated by the same strong electric field between sample-surface and objective lens. The imaging electron beam (emitted from sample-surface) is separated from the illumination electron beam again by the beam separator and deflected into the image column. A magnified image of sample-surface is produced by the objective lens, which is further magnified in the image column of the microscope. Image column consists of field, intermediate and projector lenses and through this, the electrons are projected onto the channel plate. Finally, image from the screen is acquired by a CCD camera.

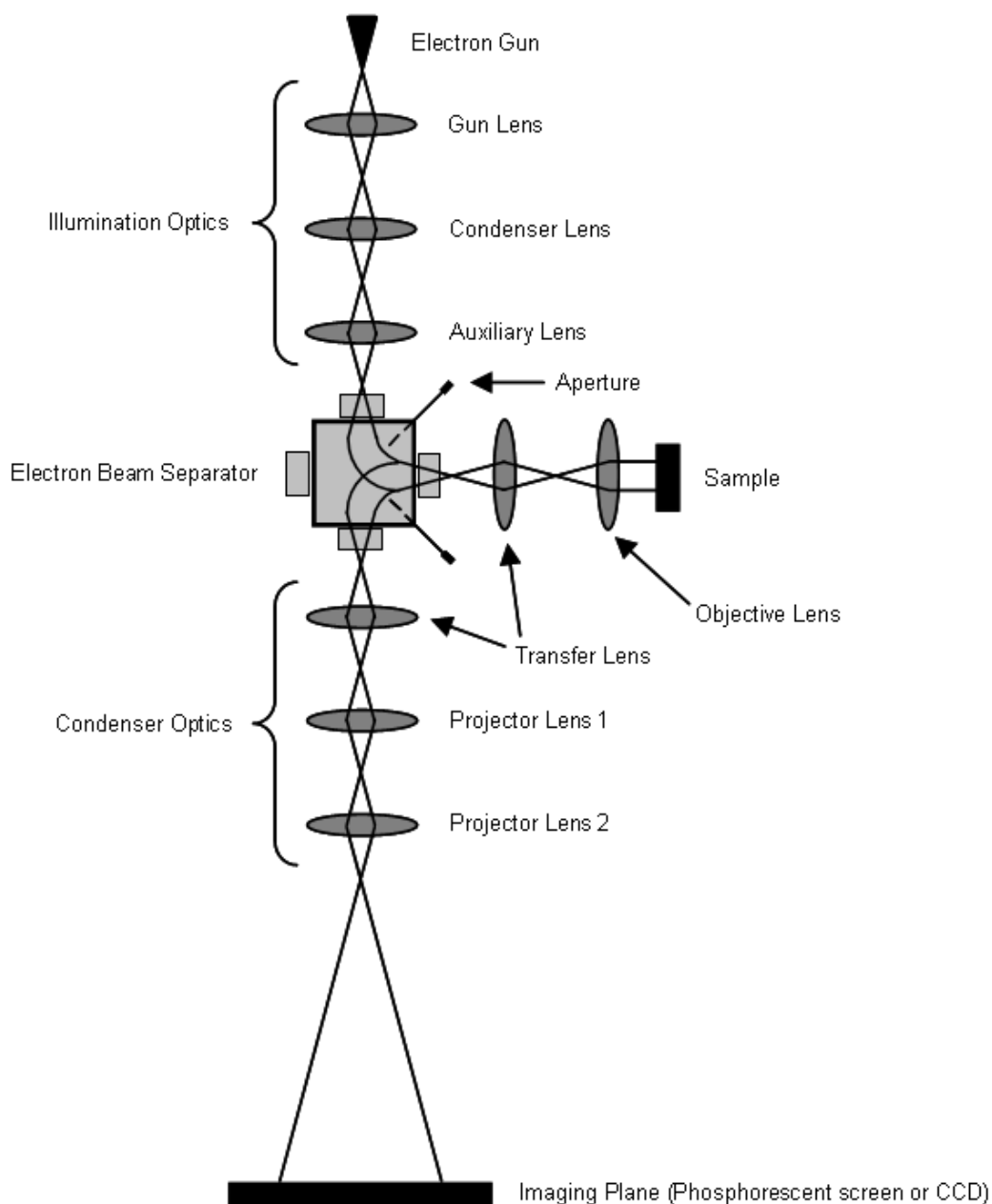


**Figure 2.23:** Simplified sketch illustrating basic components of a low energy (or photoemission) electron microscope.

### 2.9.2 Imaging modes in low energy electron microscope

In low energy electron microscope, surface of the sample can be imaged using different electron primary energies or selecting particular diffracted beam, which

define different imaging modes. In mirror electron microscopy (MEM) mode, incident electron beam energy (near zero or slight negative) is such that electrons interact weakly with the surface or get reflected just before reaching the sample-surface. The image contrast arises due to surface morphology and local variation in surface potential. As there is no scattering condition, MEM also allows to study non-crystalline surfaces. On the other hand, LEEM mode uses elastically backscattered electrons from the sample-surface to image a crystalline surface. In the LEEM mode, incident electron beam energy is sufficient (few eV) to interact with sample-surface with preferred primary energy ( $E_p$ ). The probed area of the specimen for micro-LEED

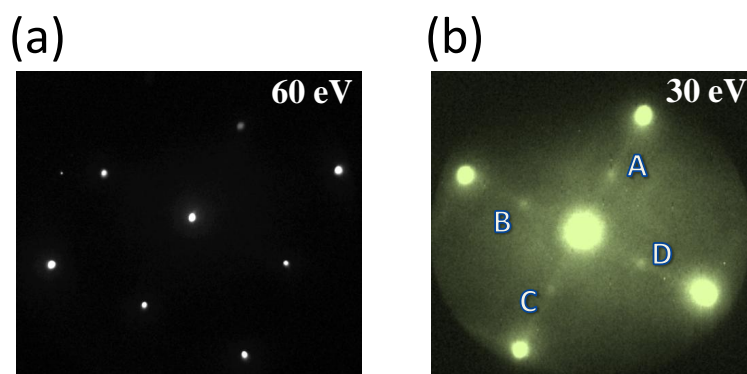


**Figure 2.24:** LEED pattern of 60 ML NiO/Ag(001) (a) 60 eV. (b) 30 eV, the half order (1/2,0) spots are indicated by A, B, C and D.

experiments is selected using field-limiting aperture in the image plane after objective lens. Diffraction pattern produced from this selected region in the back-focal plane of objective lens is reproduced in the viewing screen by adjusting the lenses in image column. Typical LEED patterns as observed for a 60 ML NiO/Ag(001) film surface are presented in figure 2.24. For imaging, an aperture can be put in the diffraction plane in order to select particular scattered electron beam for imaging. When the ‘00’ beam is selected, one performs bright-field imaging. A bright-field image of 60 ML NiO/Ag(001) surface is presented in figure 2.25 (a). In the dark-field operation mode,

a diffracted (other than '00') beam is selected for imaging. The sample region that contributes to that particular beam used for imaging appears bright in the image, while other regions remain dark. A typical dark-field image obtained using  $(1/2, 0)$  half-order beam [figure 2.24(b)] is presented in figure 2.25 (b) for the same sample region. Both the images in fig. 2.25 contain common morphological features, however, contrast pattern is completely different depending on the imaging modes. A phase difference in the backscattered waves can be introduced by a surface step (from the height difference), which can be imaged in the de-focused condition. Wave length of electron is comparable to single atomic height at low energy. In this situation, phase shift varies greatly at small change in incident energy and gives rise to different interference conditions. This is known as phase contrast mechanism. The Italian

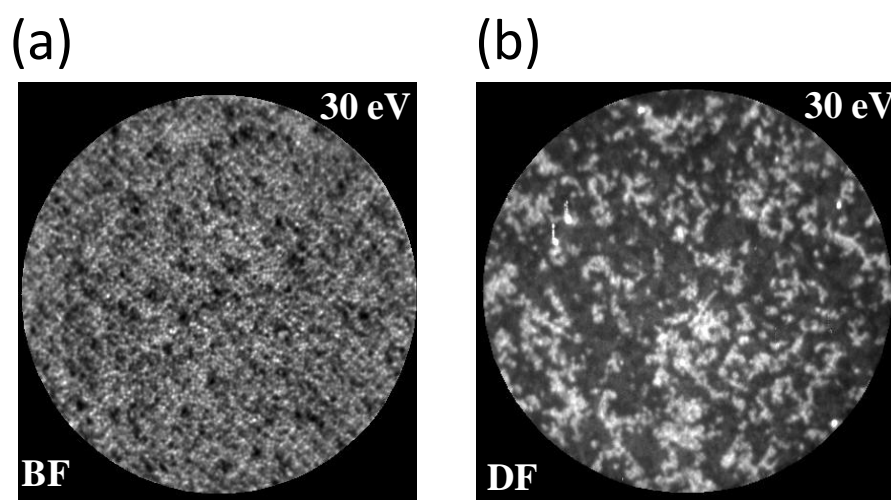


**Figure 2.25:** (a) Bright-field and (b) dark-field LEEM images (30 eV beam energy) of (the same region of) NiO/Ag(100) surface.

branch-line of the Nanospectroscopy beamline hosts the spectroscopic photoemission and low energy electron microscope (SPELEEM III, Elmitec GmbH) has been used for all the magnetic microscopic measurements. The SPELEEM consists of a LEEM

and an energy filtered x-ray PEEM. Typical spatial resolution obtained with such microscope was about 40 nm in PEEM mode and about 10 nm in LEEM mode.

### 2.9.3 Photoemission electron microscopy

#### *Imaging with XMLD, XLD or XMCD as contrast mechanism*

The XMLD spectroscopy to determine surface antiferromagnetic order is discussed in section 2.11, which provides only an average information of the probed volume. This is exemplified with NiO(001) thin films grown on nonmagnetic substrates. It is obvious that measurements in a laterally resolved way will yield local information that allows more finer studies such as domain structure, domain wall and their evolution. Such studies are possible using photoemission electron microscopy (PEEM) [60, 61] utilizing the local variation of absorption coefficient over the sample-surface. In PEEM, surface-images with concerned contrast mechanism are acquired using the electrons that are emitted from the sample-surface by x-ray irradiation. The schematic of a PEEM system is shown in figure 2.26]. In the PEEM mode of operation, the sample-surface is illuminated by x-ray (at a grazing incidence of about  $16^\circ$ ), normally tuned at particular absorption edge. Emitted photoelectrons are accelerated by a strong electric field between sample-surface and objective lens and subsequently used for imaging by the image column. Local absorption coefficient of sample-surface may vary in different ways and can give rise to contrast in the PEEM images, which may be of chemical, magnetic or structural origin [62].

In order to obtain antiferromagnetic domain pattern of NiO(001) film surface, we first measure an absorption spectrum at the Ni  $L_2$  edge with linearly polarized x-ray. The x-ray energy is tuned to the first peak of the Ni  $L_2$  multiplet structure [shown as peak A in figure 2.23 (c)] and PEEM images are collected. Similarly another PEEM image is collected at the second peak of Ni  $L_2$  edge [peak B in figure 2.23 (c)]. In these images, we observe small magnetic contrast (with XMLD as contrast

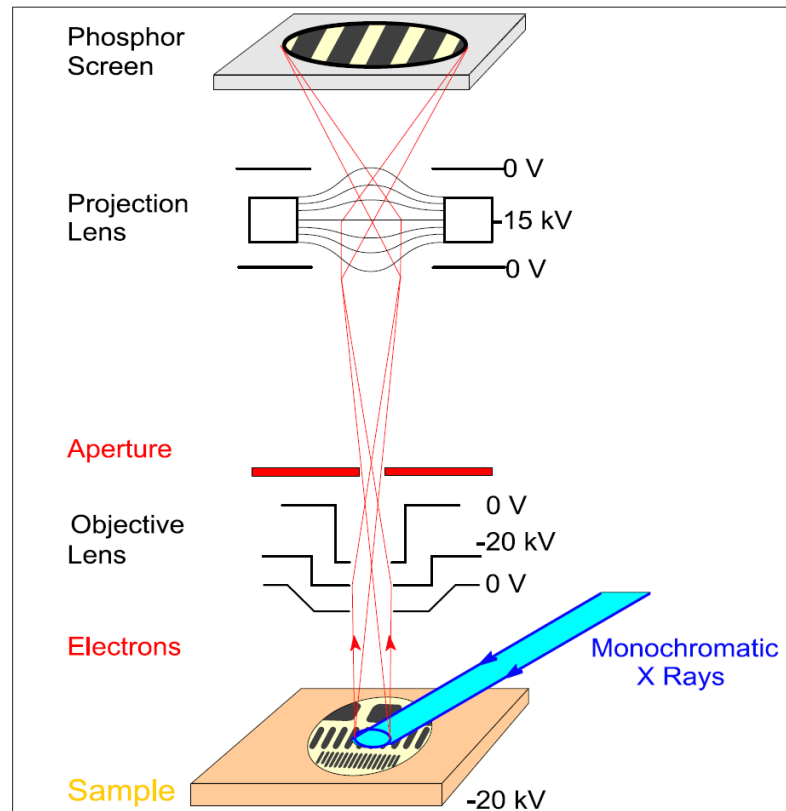


**Figure 2.26:** Schematics of a PhotoEmission Electron Microscope (PEEM).

mechanism) on large morphological background. To enhance the antiferromagnetic contrast and to reduce the morphological contrast, we further divide first image by second image. The  $I_1/I_2$ -image representing the antiferromagnetic domain pattern of NiO(001) surface and cancels off the morphological part of the contrast. The details of this phenomena are described in a later chapter in this thesis. It is also possible to determine surface antiferromagnetic spin-axis locally from the PEEM images by performing angular dependent experiments.

## 2.10 Summary

This chapter provides a brief introduction to different experimental techniques used in this thesis. To probe the valence band electronic structure of the crystalline thin

films, ARPES has been satisfactorily used. On the other hand, XPS probes the core levels of the elemental components. The in-plane surface antiferromagnetic order has been probed by LEED (using the presence of half-order spots). For detailed studies of magnetic domain structures of the films, imaging techniques like LEEM (within the dark-field mode) and XMLD-PEEM have been employed.

## Growth of monolayer Cr film on Ag(001)

### 3.1 Introduction

The first suggestion that bulk Cr might be an antiferromagnet was proposed by Louis Néel in 1936. The negative exchange coupling between the Cr atoms was also invented by him *via* experimental measurement of magnetic susceptibility. Gradually Cr became an interesting material for further scientific investigations and discontinuous changes in different physical properties like Young modulus, internal friction, thermal expansivity and electrical resistivity *etc.* has been found out near Néel temperature ( $T_N$ ). The modern phase of magnetic studies began with the use of neutron diffraction [64–66] to explore magnetic structures. Body centered cubic (bcc) Cr is found to have static incommensurate spin density wave (SDW) antiferromagnetic structure with Néel temperature ( $T_N$ ) 311 K.

The question arises is, how the magnetic structure of Cr is altered in thin films and superlattices either due to dimensionality reduction or due to proximity with ferromagnetic or paramagnetic boundary layers? However, study of magnetic structure in low-dimension using usual experimental techniques is not easy. Neutron and x-ray

---

*The work, presented in this chapter, has been published in Vacuum, 112, 5-11 (2015).*

scattering are not suitable because of small scattering volume. Early tight binding calculations of Allan [67] showed for the first time that Cr(001) surface would exhibit a magnetic moment of  $2.8 \mu_B$ , which is more than five times larger than bulk Cr moment ( $0.59 \mu_B$ ). In case of bulk Cr(001), the surface is made of ferromagnetic terraces where terraces separated by single surface steps are antiferromagnetically coupled to each other [68,69]. The case of monolayer Cr on Ag(001) is completely different from the Cr(001) surface where the overlayer is characterized by commensurate antiferromagnetic phase with an expected large enhancement in magnetic moments of each Cr atom.

Monolayer of transition metals supported by noble metal substrates (i.e. Au, Ag, Cu etc.) have considerably interesting magnetic properties. Reduced symmetry at lower dimension results in phenomena like giant enhancement of magnetic moments [70], giant spin polarization [71] and perpendicular magnetic anisotropy [72] etc. in these ultrathin film systems. As Cr is having half filled  $3d$  ( $3d^5 4s^1$ ) shell its electronic properties should be extraordinarily sensitive to changes in the coordination and symmetry. In case of monolayer Cr film, there will be less electronic overlap from neighboring Cr sites which helps in forming giant moments associated with each site. Hence it is important to form atomically flat monolayer Cr film on suitable substrate, because a monolayer film is a purely two-dimensional (2D) system. A better understanding of magnetic structure of the film demands the detailed knowledge of physical structure as well as a high control on the growth technique. This chapter focus on the growth of an antiferromagnetic Cr monolayer on Ag(001) single crystal substrate. The physical structure of Cr film plays a major role in determining the magnetic and electronic properties and in case of Cr/Ag(001) system, the physical structure of the film strongly depends upon different growth parameters. The major growth parameters such as the growth temperature, effect of post-deposition annealing, the Cr evaporation rate, smoothness of the substrate surface etc. have

also been optimized for the best growth of flat monolayer Cr film on an Ag(001) single crystal substrate.

## 3.2 Background works

Two-dimensional (2D) magnetism of ultrathin transition metal films has drawn the attention of many earlier research works because of their exciting magnetic properties at reduced dimensions [73–82]. The Ising-like magnetic behavior of these films have made them fascinating due to the presence of long range 2D magnetic order that exists at finite temperature contradicting the Heisenberg model. Freeman *et al.* [74] has demonstrated from theoretical point of view that surface antiferromagnetic properties are completely different from bulk antiferromagnetic properties. A full potential linearized augmented plane wave (FLAPW) method calculation has shown that transition metals V, Cr, Fe, Ni and Co shows enhanced magnetic moment at surface, compared to their bulk counterpart. According to their calculation, the magnitude of magnetic moment at Cr(001) surface is  $2.49 \mu_B$ ; much higher than the bulk magnetic moment of  $0.59 \mu_B$ . However their calculations predicted existence of a ferromagnetic Cr(001) surface [75]. Angle resolved photoemission studies by Klebanoff *et al.* [80] predicted a ferromagnetic Cr(001) surface with an associated surface magnetic moment  $(2.4 \pm 0.3) \mu_B$ , quite close to the theoretical predicted value. According to the total energy calculation of Blügel *et al.*, [77] transition metal Fe, Co and Ni favors ferromagnetic  $p(1 \times 1)$  configuration whereas V, Mn and Cr favors antiferromagnetic  $c(2 \times 2)$  configuration as a monolayer overlayer on top of Pd(100). In spite of the interesting physics, access to the surface antiferromagnetism has been limited due to the experimental difficulties in detecting them. Newstead *et al.* [84] performed electron spectroscopy experiments on Cr ultrathin film deposited on Ag(001). They confirmed epitaxial growth upto two monolayers where the second layer start to grow before the completion of first layer. The maximum thickness

upto which monolayer Cr forms on the substrate is 0.33 ML coverage as per their report. Photoemission measurements of Cr  $3s$  multiplet splitting showed a rapid reduction of magnetic moment with coverage, according to their studies. Polarized neutron reflection measurements performed by Johnson *et al.* [81] reported long range ferromagnetic order with enhanced magnetic moments in 0.33 ML Cr film, whereas no ferromagnetic order was detected in a 3.3 ML film. Using inverse photoemission technique, Ortega and Himpsel [85] has found that in case of Cr monolayer grown on Ag(001) at 440 K a magnetic exchange splitting of 2.7 eV for majority spin state is observed, which is 20 times larger than bulk Cr, suggesting a strong enhancement of local magnetic moment in monolayer Cr. Another inverse photoemission report by Haugan *et al.* [86] has shown collapse of magnetic splitting caused by lateral compression of the Cr film on Cu(001) compared to Ag(001) and Au(001).

Supporting the theoretical prediction of Blügel *et al.* [77] the existence of antiferromagnetic phase was first experimentally reported by Gewinner's group [87]. Interestingly, it was observed by them that it was possible to grow flat monolayer of Cr on Ag(100) when deposited at higher substrate temperatures (430-450 K). Their x-ray photoelectron diffraction (XPD) and photoemission studies proved the growth of flat monolayer under certain deposition conditions. Further, they also observed a weak but distinct  $c(2\times 2)$  superstructure spots attributed to the 2D antiferromagnetic order in the LEED pattern [87,88]. This was a significant step towards experimentally studying the 2D antiferromagnetism. Even though many further experiments were performed by the group of G. Gewinner, attempts by other groups to repeat these experiments and observe the magnetic  $c(2\times 2)$  superstructure spots were not successful. STM studies [89,90] on the growth of Cr submonolayers at elevated temperatures have reported Ag segregation/agglomeration, however have failed to observe the magnetic  $c(2\times 2)$  superstructure spots in LEED and concluded that flat Cr film on Ag(100) is not formed. Similarly, monolayer growth of Cr was noted from the Inverse Photoemission studies [85] with enhanced magnetic moments, however

failed to observe the  $c(2 \times 2)$  LEED superstructure spots. The physical structure of monolayer Cr on Ag(001) substrate is another interesting topic to investigate, since the electronic as well as magnetic structure of monolayer Cr are strongly dependent on it. An *in situ* surface x-ray diffraction study by Steadman *et al.* [91] has shown the sensitivity of Cr growth on Ag(100) at different temperatures. They observed the growth of flat Cr monolayer on Ag(100) at higher substrate temperatures, however could not confirm the magnetic ordering. Moreover, their results are in agreement with the STM studies where segregation of Ag on top of sub-monolayer Cr was confirmed for growth at 430 K. Photoelectron diffraction experiments were performed by the group of Gewinner [92–95] to answer the questions regarding the structure of monolayer Cr deposited on noble metal substrates and they came to interesting conclusions.

The reported contradictory observations among different research groups opened up scope for further investigation on this system. It is a matter of substantial interest to scrutinize why only one research group (that of Gewinner at Laboratoire de Physique et de Spectroscopie Electronique, France) has reported repeated observation of LEED  $c(2 \times 2)$  half-order  $(1/2, 1/2)$  spots so far whereas many other groups were unable to observe them. Hence here, we have undertaken a detailed growth study of Cr monolayer on Ag(001) substrate at elevated temperatures and confirm their antiferromagnetic ordering. However, it is worthwhile to mention that observation of half-order spots in monolayer Cr film was successful only after many failed attempts and over a period of two months. A detailed knowledge of different growth parameters are very important in obtaining reproducible experimental results and for better understanding the properties of the grown film. Thus, we have carried out the Cr monolayer growth at different substrate temperatures, direct/step-wise growth condition, different growth rates and at different sample/substrate annealing temperatures and are characterized using LEED and photoemission studies. We have optimized the best growth conditions for obtaining flat Cr monolayer on Ag(001) with highest degree of antiferromagnetic ordering along with largest domain sizes.

Different aspects of the growth, formation of  $c(2\times 2)$  monolayer domains and their structural stability with temperature and possible interfacial alloy formation are discussed in detail in this chapter.

### 3.3 The Cr/Ag(001) system

The order and strength of 2D magnetism in a monolayer Cr film strongly depends on its physical structure. When deposited on a noble metal substrate, the magnetic structure of the film is governed by different effects like film thickness, interfacial strain due to lattice mismatch, intermixing or alloying at film-substrate interface *etc.* The electronic structure of the film is expected to be moderated by the hybridization between the transition metal  $d$ -bands and noble metal states. However, it is found that the 2D electronic property of a free monolayer is essentially retained when the monolayer is deposited onto the noble metal substrate as there is very little overlap (hybridization) between the noble metal  $d$  bands and Cr  $3d$  states, leading to the electronic isolation. Hence, Ag(001) can be chosen as an appropriate substrate for the growth of Cr overlayer on it. Within the binding energy window of 3 eV below  $E_F$  there are only dispersive Ag  $sp$  bands; the higher intensity Ag  $4d$  bands lie at higher binding energy (3-6 eV) range from  $E_F$ . The Cr  $3d$  bands appear within the binding energy range of 0-2 eV and they do not intermix with the Ag  $4d$  bands. This is an advantage of choosing noble metal substrates over other substrates.

For the epitaxial growth, a deciding factor is whether the deposited film alloys with the substrate either in the bulk or at the interface. Energy calculations of Fu and Freeman [74] has shown stable Cr overlayers on Au(001). However, Hanf *et al.* [97] reported that Cr diffuses inward Au(001) and replaces Au lattice sites forming interfacial alloy. This alloy formation process is diffusion limited temperature dependent phenomena; it also depends on the total amount of Cr involved in this procedure. They observed interfacial alloy exists upto 4 ML or even more for Cr

deposition at 400 K. On the other hand, there is a large miscibility gap between Cr and Ag in the bulk above their melting point [83] which implies no bulk alloying or intermixing between Cr and Ag, unlike in the case of Cr and Au. This also raises the possibility of layer by layer growth of Cr over Ag(001). In fact, a small amount of Cr-Ag intermixing was detected in our experiment and this alloying was found to be very critically depending on the growth/annealing temperatures. For higher temperature, the alloying was found to be the main reason for destroying the magnetism of the flat monolayer Cr film. Steadman and his group [91] concluded, from their in-situ x-ray diffraction experiments, that about  $22 \pm 13$  % exchange of Cr sites with Ag occurs for the antiferromagnetic Cr monolayer deposited at 430 K; even though the monolayer structure was found to be generally stable with this small intermixing.

Lattice matching between the deposited film and the substrate is another important factor for the growth of any epitaxial film. Growth of Cr has already been tested on various substrates like Cu(001) [86, 98, 99], Au(001) [97, 100, 101], Pd(001) [77] *etc.* No surface alloying is reported in case of Cu(001); however, bi or multilayer growth of Cr was observed on it. On top of Au(001), formation of interfacial alloy at room temperature (RT) does not let the Cr overlayer become stable though there is a good matching in lattice parameters. Blügel *et al.* [77, 78] has theoretically considered the stability of transition metal overlayers on top of Pd(001). Strong enhancement of magnetic moments of overlayer material was reported by them. Significant lattice mismatch of overlayer with Pd(001) leads to intra atomic electronic isolation in the overlayer as well as with the substrate which leads towards increment of magnetic moments, they concluded. However, no experimental evidence of these transition metal overlayers supported by Pd(001) in agreement with this theory is available. On the other hand, many studies of Cr deposition on Ag(001) are reported with RT growth leading to multilayer islands and high temperature growth leading 3D island growth and alloying. However, flat monolayer growth was found to occur in a

certain temperature window showing that epitaxial growth was indeed possible for Cr on Ag(001) [91–95]. Monolayer growth of Cr was reported on Ag(001) substrate while deposited at elevated temperature (430–450 K). The face centered cubic (fcc) Ag has a lattice parameter of 4.09 Å whereas the Cr with its body centered cubic (bcc) structure has a lattice parameter of 2.88 Å which is close to  $\sqrt{2}$  times less than the lattice parameter of Ag. Hence Cr shows pseudomorphic growth on Ag(001) with its crystallographic  $\langle 100 \rangle$  direction rotated  $45^\circ$  with respect to Ag. In figure 3.1 (a), the top surface atomic arrangement of Ag(001) substrate is shown with its non-primitive surface unit cell; on the other hand in figure 3.1 (b) a primitive unit cell of 1 ML Cr is presented. Figure 3.1 (c) shows monolayer of Cr deposited on Ag(001) with its unit cell rotated  $45^\circ$  that of the Ag crystal. The estimated lattice mismatch is tiny, only 0.3%, therefore pseudomorphic growth is possible with minimum interlayer strain at the interface.

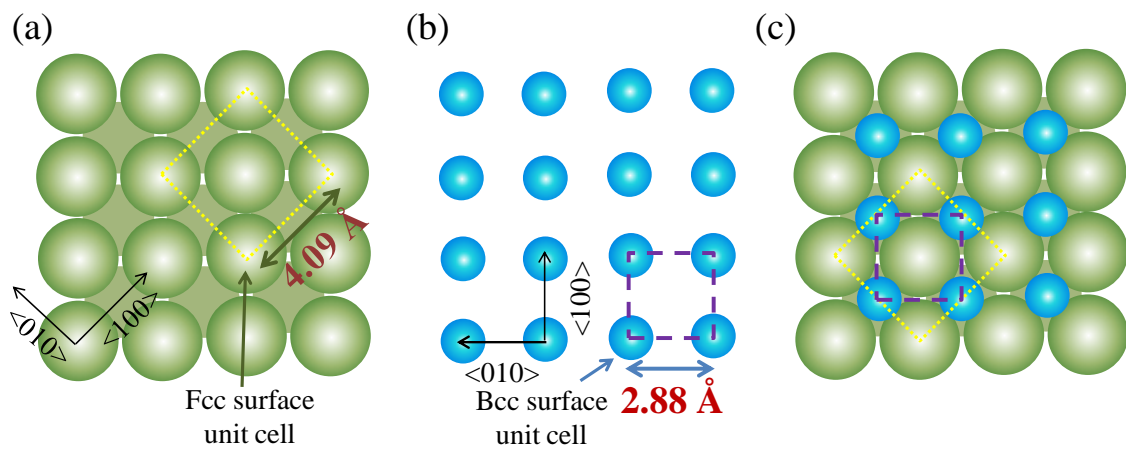


**Figure 3.1:** (a) Top surface of Ag(001) fcc crystal; the surface non-primitive unit cell is shown which has lattice constant 4.09 Å (b) 1 ML Cr with its surface unit cell having lattice constant 2.88 Å (c) bcc Cr grows on fcc Ag(001) crystal epitaxially with its  $\langle 100 \rangle$  crystallographic direction  $45^\circ$  rotated.

However, there is an opposing factor in the growth of Cr on Ag(001); the Cr surface energy ( $2400 \text{ mJ/m}^2$ ) almost double than that of Ag ( $1250 \text{ mJ/m}^2$ ), according to Bauer's criterion [96] and would only form (if at all) under non-equilibrium growth

conditions. Hence at RT, bi or multilayer epitaxial Cr island formation on top of Ag(001) is expected in order to minimize the surface free energy, which is proved from many earlier spectroscopic and diffraction studies [82, 84, 85, 97, 100, 101]. STM experiments [89, 90] also confirmed multilayer Cr island formation under RT growth condition. Under low temperature (100 K) deposition, Cr grows rather non-uniformly or randomly on top of Ag(001). The epitaxial quality of the film is significantly worse as concluded by Hanf *et al.* [94] from their LEED studies. The spot size in the diffraction pattern is broad, with low spot intensity and the Cr film is quite like ‘hit and stick’ type. The Cr atoms, as they come from the evaporator, stick to the same position on the Ag(001) substrate surface where they hit, due to much reduced surface mobility at this low temperature. The rough growth and bad crystalline order at 100 K was also confirmed by Steadman *et al.* [91] from their *in situ* surface x-ray diffraction studies where they observed a weak x-ray intensity oscillation with a quick intensity decay. On the other hand, deposition at higher temperature (430 - 450 K) increases the in-plane mobility of Cr atoms and drifts them to cover the Ag(001) surface resulting in the formation of flat Cr monolayer, which is reported by the group of Hanf *et al.* [82, 97, 100–103].

We have deposited 1 ML Cr film on Ag(001) substrate at various growth temperatures and performed LEED as well as ARPES experiments to optimize the most suitable growth condition for the preparation of flat monolayer Cr film. Different major parameters that controls the growth phenomena also have been identified as well as optimized to obtain Cr monolayer film with highest antiferromagnetic order.

## 3.4 Experimental details

### 3.4.1 Growth

The complete growth procedure of Cr film on Ag(001) was performed within UHV preparation chamber of the ARPES system at Saha Institute of Nuclear Physics,

Kolkata. As mentioned in chapter 2, this chamber is equipped with  $\text{Ar}^+$  ion sputtering, sample annealing, metallic or metal-oxide evaporation facilities and also a Low Energy Electron Diffraction (LEED) apparatus. Cr was evaporated from a highly pure rod of 2 mm diameter (99.5%, American Elements, USA) kept inside an electron beam evaporator which was pre-calibrated by a water cooled quartz microbalance. A well polished Ag(001) single crystal, of 10 mm diameter and 2 mm thickness (from MaTeck GmbH, Germany), was mounted on a sample holder capable of either resistive or electron beam heating the sample with a K-type thermocouple fixed on it to measure the sample temperature. The Ag crystal was prepared by repeated cycles of sputtering with  $\text{Ar}^+$  ion (Ar pressure =  $3 \times 10^{-6}$  mbar, beam energy = 600 eV, integrated ion current =  $1.0 \mu\text{A}$ ) for 20 minutes followed by annealing at 823 K for 30 minutes until a sharp and bright  $p(1 \times 1)$  four-fold LEED pattern is observed. Cr was evaporated from the well-degassed electron beam evaporator at a rate of about  $0.2 \text{ \AA}/\text{min}$  and deposited on Ag(001) crystal. The quartz microbalance was mounted on a Z-shift; hence the deposition rate was measured by placing it at exactly the same growth position where the substrate was kept during Cr deposition. This helps to obtain better accuracy in deposition rate measurement. The chamber pressure was maintained below  $2 \times 10^{-10}$  mbar during deposition. For high temperature deposition the sample temperature was brought down to RT immediately after deposition is over and was placed under the LEED apparatus to detect the crystalline quality of the film.

### 3.4.2 Low Energy Electron Diffraction studies

Low Energy Electron Diffraction studies performed on the 1 ML Cr film deposited on Ag(001) provide important information on the structural symmetry and magnetism for this film. Low energy electrons (1 - 200 eV) coming through the four-grid LEED apparatus (OCI Vacuum Microengineering, Canada) impinges on the sample surface

and the elastically backscattered electrons produce the diffraction pattern on the phosphor screen. Low energy electrons having very low penetration depth (5-10 Å) are highly surface sensitive probing mainly the top most surface structure. As described earlier, the Ag(001) surface is prepared very well before deposition of metallic layers over it. In figure 3.2 (a) the LEED pattern of Ag(001) crystal is shown

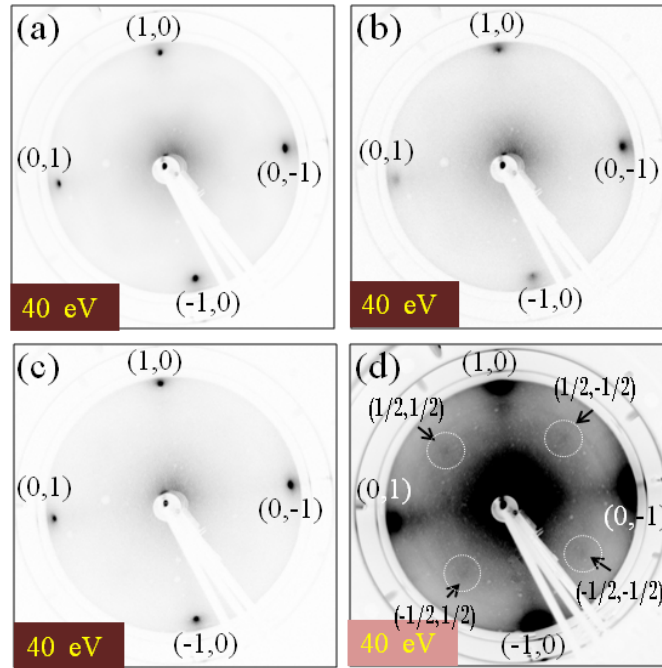


**Figure 3.2:**  $p(1 \times 1)$  LEED pattern showing the four fold integer order spots in case of (a) clean Ag(001) substrate (b) 1 ML Cr deposited on Ag(001) at 300 K (RT). (c) 1 ML Cr deposited on Ag(001) at 428 K. (d) Enhanced contrast of figure (c); four extra low intensity spots are visible at  $(1/2, 1/2)$  positions.

at beam energy 40 eV. The  $p(1 \times 1)$  diffraction pattern has a four-fold symmetry. When 1 ML Cr is deposited on it at RT, no deviation from  $p(1 \times 1)$  LEED pattern is observed [figure 3.2 (b)], except the  $(1,0)$  spot intensities goes down a bit and their FWHM increases compared to bare clean Ag. In figure 3.2 (c), the LEED of an 1 ML Cr film grown over Ag(001) at 428 K is shown for same electron beam energy of 40 eV. There is no apparent deviation of the LEED pattern from  $p(1 \times 1)$  symmetry, however the LEED spots are sharper compared to RT growth. Under

enhanced contrast of the LEED image, as shown in figure 3.2 (d), four extra spots with  $c(2 \times 2)$  symmetry are observed. These extra spots have very weak intensities compared to the integer order (1,0) spots. They are only visible with highly sensitive 12 bit peltier cooled camera associated to our LEED apparatus under high aperture and high gain parameter mode. Assuming the specular spot to be the center with coordinate (0,0), these extra spots are located at  $(1/2, 1/2)$  positions and hence they are termed as ‘half-order’ spots. These half-order spots are completely absent for sample growth at RT, indicating that very high quality of the monolayer film grown at 428 K are responsible for these half-order spots.

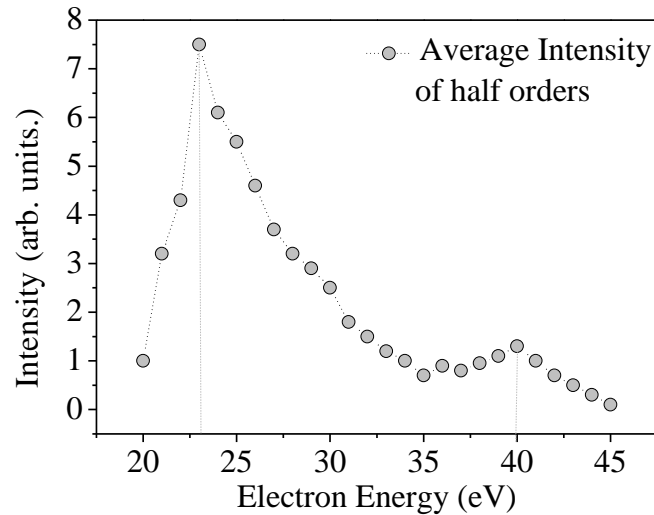


**Figure 3.3:** (a) The average intensity plot of the  $c(2 \times 2)$  half orders (LEED IV) is shown against electron beam energy range 20-45 eV.

These half-order spots appear in the diffraction pattern within a narrow beam energy range of 20-40 eV and further beyond 60 eV they are hardly detectable. Due to their very low intensity, they are distinctly visible until the integer order spots enter into the field-of-view of the LEED screen. At higher beam energies, the (1,0) spots enter the LEED screen and these weak half-order spots are masked by the background of the high intensity integer orders making them invisible. In case of elevated temperature deposition, when the crystal is placed under LEED immediately

after the growth of 1 ML film, the half-order spots are almost undetectable; their intensity becomes gradually visible as the sample cools down to RT. LEED images are collected for different beam energies and averages intensities of all the four half-order spots (I) are plotted against primary electron energy (V), formally called LEED IV plot. Experimental IV plot of the  $c(2 \times 2)$  half-order spots of an 1 ML Cr/Ag(001) is shown in figure 3.3 for the beam energy range of 20-45 eV. Only above 20 eV, the half-order spots enter the LEED screen. It is evident that at 23 eV beam energy the spots show maximum intensity. Intensity falls down significantly with increment of beam energy with a hump visible close to about 40 eV. Beyond 40 eV, the intensity is extremely low and could not be measured with our LEED system, though the spots were barely visible up to 60 eV. On the other hand, integer order (1,0) spots have the maximum intensity at about 55 eV beam energy. Thus at the respective intensity maximas, the intensity ratio between half-order spots to that of the integer order spots is about 2%, when measured at RT.

Though  $c(2 \times 2)$  half-order spots are visible even at higher beam energy upto 60 eV with our LEED apparatus the intensity of these spots are extremely low here and is hardly detectable. On the other hand, below 20 eV the half orders do not enter into the field of view of LEED screen. In figure 3.4 (a), the LEED pattern is shown at 23 eV beam energy for monolayer Cr film deposited on Ag(001) substrate at growth temperature of 428 K. The LEED data is collected at RT, where distinguishable four-fold pattern is visible. Apparently, these pattern appears to be of  $p(1 \times 1)$  type. But, these are actually half-order  $(1/2, 1/2)$  spots with  $c(2 \times 2)$  symmetry. The first integer order spots are yet to enter the field-of-view of LEED screen at this low electron beam energy. These half-order spots are believed to appear due to exchange interaction between the incident electrons and the surface Cr magnetic moments [34, 104, 105]. The Cr moments of the monolayer are antiferromagnetically arranged being supported by the Ag(001) crystal. Their proposed spin ordering [77] has been demonstrated in the schematic diagram of figure 3.4 (d). As the exchange

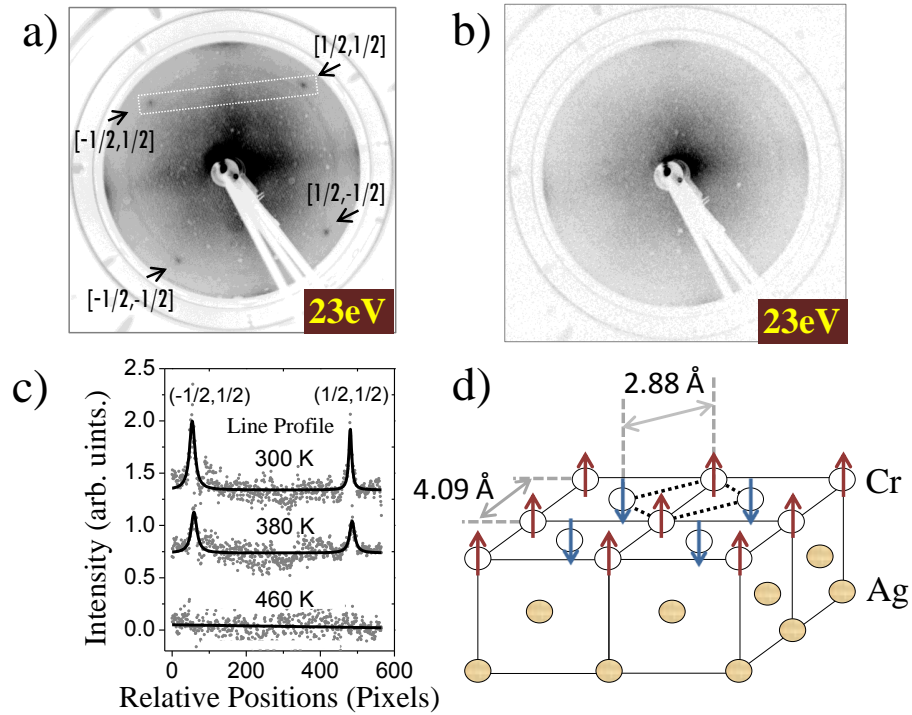


**Figure 3.4:** (a) LEED pattern of monolayer Cr film deposited at 428 K; existence of distinguishable four-fold half-order  $(1/2, 1/2)$  spots. Integer order  $(1,0)$  spots do not enter into the field-of-view of LEED screen at this low beam energy. (b) LEED pattern of monolayer Cr film deposited at 300 K; no existence of  $(1/2, 1/2)$  spots. (c) Line profile drawn over half-order spots at different sample temperatures: 300 K, 380 K and 460 K; showing intensity variation of half orders at different temperatures. (d) Schematic of antiferromagnetic spin arrangement in monolayer Cr film over Ag(001).

scattering is much weaker force compared to the coulomb (or charge) scattering (which creates the integer spots in LEED), intensity of the half-order spots are significantly lower than the integer spots. In figure 3.4 (c), line profiles are drawn over the half-order spots within the rectangular area indicated in figure 3.4 (a) for different sample temperatures. At RT (300 K), the half-order intensity is quite stronger, while it decreases to almost half of its initial value at 380 K. When the film is heated to 460 K, their intensity vanishes to almost zero. Intensity variation of the half-order spots are shown rigorously and discussed in detail in the next section. The observed weak intensity of the half-order spots, their appearance only at low electron

energy region and their diminishing intensity with increasing electron energy as well as the temperature dependence of these spots, all confirm their antiferromagnetic origin and rules out other possibilities such as formation of ordered  $c(2 \times 2)$  surface alloy structure or a displacive reconstruction of the top layers [87, 106]. Rather, they are evidences of the 2D antiferromagnetism persistent in the monolayer Cr film grown over Ag. As the exchange interaction strength is much lower than the coulomb interaction, the intensity of the half-order is only 1-2% compared to the integer orders. In fact, the existence of half-order spots due to surface antiferromagnetism is already known in the literature. The first observation of extra (half-order) spots in LEED due to exchange scattering was reported in case of NiO single crystal by Palmberg *et al.* [34]; the temperature dependence of these exchange reflection intensity was also performed by them [104, 105] and few other groups [107, 108] which determined the Néel temperature quite correctly for that sample. In fact, we performed rigorous LEED studies on NiO (100) single crystals as well as epitaxial thin films grown on Ag(001) which reveals existence of  $p(2 \times 2)$  half-order spots similar to the observation by Palmberg *et al.* [39]. Surface antiferromagnetic twin domains in NiO samples were imaged by us using the dark-field (DF) mode of the Low Energy Electron Microscope (LEEM) and have been described in detail in reference [109] as well as in chapter 7 of this thesis. For the case of monolayer flat monolayer Cr film, the existence of  $c(2 \times 2)$  half-order spots were first observed by Hanf *et al.* [82] and further many studies were undertaken by the same group [87, 88, 92–94, 97, 100, 101, 106]. Many of these studies were found to be self contradictory and in spite of extensive study by the same group, no conclusive picture of the structural and magnetic ordering were arrived at. Moreover as mentioned earlier, no other group could reproduce these experiments and could not obtain the half-order spots confirming the antiferromagnetic ordering of the Cr monolayer grown on Ag(001). However, their studies have reported that that there is a persistent antiferromagnetic order of the Cr sites with enhanced magnetic moments in the flat monolayer Cr film grown at 430-450 K on Ag(001)

which is reflected in the existence of  $(1/2, 1/2)$  spots for LEED at beam energy less than 60 eV. Therefore, our observation of LEED half-order spots unambiguously support the antiferromagnetic ordering in the monolayer Cr film. As it is evident that the antiferromagnetic strength of the sample and hence the half-order spot intensity as well as width is strongly correlated with the size of monolayer Cr domains formed over Ag(001), we have used half-order spots as a vital and most crucial tool to optimize different growth parameters for obtaining flat Cr films with maximal antiferromagnetic ordering.

### 3.4.3 Temperature dependence of half-order spots: interfacial intermixing

As shown in figure 3.4 (c), a flat monolayer Cr/Ag(001) film show distinguishable intensity of the half-order spots at RT. The characteristic intensity path/curve followed by half orders is evident from figure 3.5, where the intensity plot of half-order spots are shown against temperature of the film. The film was cooled down

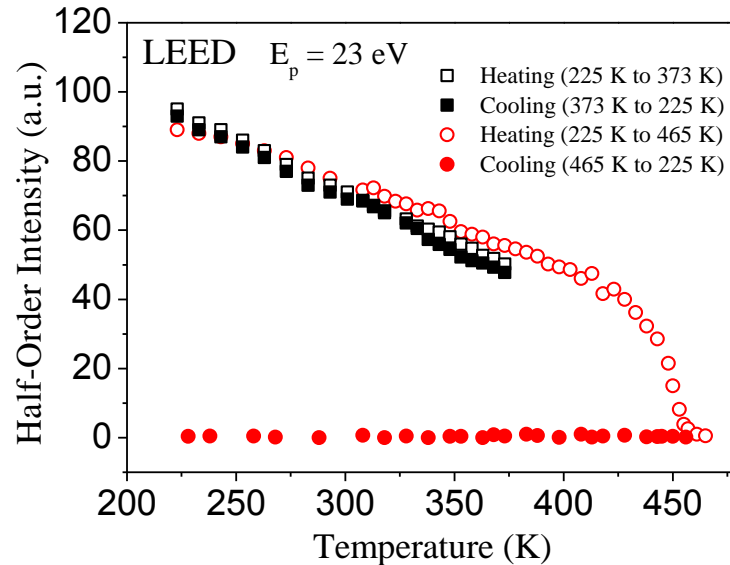


**Figure 3.5:** Temperature variation of LEED  $(1/2, 1/2)$  spots. Once their intensity vanishes to zero they do not reappear back upon cooling down the sample.

to liquid nitrogen temperature first and then heated up gradually to measure the intensity variation of the half-order spots and after completion of heating cycle the sample was again cooled back to low temperature. Heating of the sample from 225 K to 373 K shows almost linear decrement of half-order intensity as shown by the open black squares data points. When the sample is cooled back to low temperature, it follows back almost the similar path (filled black squares). The magnetic strength/ordering of the sample decreases due to thermal fluctuations which indicates the trend of a transition from antiferromagnetic to paramagnetic phase. However, when the sample temperature exceeds above 420 K an exponential decay in the half-order spot intensity is observed (open red circles). Close to 455 K, intensity of the half-order spots almost vanishes and above which their intensity remains zero. The experimental results are consistent with the antiferromagnetic to paramagnetic transition for the case of 2D antiferromagnets with a Neel temperature of about 455 K, which is much higher than that for the case of bulk Cr (311 K). Similar experimental results have been observed by Hanf *et al.* [88] where they observed a transition temperature of 462 K. Similar temperature dependence of the surface antiferromagnetism is also observed for the case of NiO single crystals [107, 108] as well as for NiO thin films (see Chapter 7). However, when the sample is cooled down to lower temperature the half-order spots do not reappear back. Even after measurements down upto 225 K (filled red circles), we do not observe any trace of  $c(2 \times 2)$  half-order spots. This indicates that the magnetic transition that we had observed from antiferromagnetic  $c(2 \times 2)$  phase to paramagnetic phase is not a reversible one! From further experiments (see in next sections), it is evident that the antiferromagnetic order is strongly dependent on the physical structure of the film. In fact, it is clear that the flat monolayer structure Cr film breaks due to Cr-Ag intermixing at the interface [110] which destroys the antiferromagnetism of the film completely. This intermixing/alloying is an irreversible process and the antiferromagnetic order of the film can not be recovered even when sample cooled

back to 225 K. Thus here, the magnetic and structural factors are intermixed and is difficult to define the transition temperature observed ( $T_t$ ) as the Neel temperature ( $T_N$ ) of the sample. Further experiments using surface structure sensitive techniques together with half-order LEED experiments are required to address this issues in detail and will be part of the future plan.

#### 3.4.4 Optimization of the growth temperature

In figure 3.6, LEED pattern measured at RT of 1 ML Cr film deposited on Ag(001) for different substrate temperatures are shown for electron beam energy of 23 eV. LEED pattern at 300 K [figure 3.6 (a)] does not show any half-order spots as discussed in figure 3.4. Faint  $c(2 \times 2)$  spots are visible for 373 K grown sample [figure 3.6 (b)], while the half-order intensity increases further for 406 K grown sample. Clearly distinguishable half-order spots appear for growth temperature 417 K [figure 3.6 (d)]; whereas maximum intensity of the half orders is visible for 428 K deposition [figure 3.6 (e)]. The half-order intensity decreases with further enhancement of growth temperature as shown in figure 3.6 (f); the half-order spots are barely visible for deposition at 455 K substrate temperature. This indicates that the antiferromagnetic order of the 1 ML Cr film sensitively depends on the growth temperature. Our experimental data shows the sample grown at 428 K has the maximum magnetic exchange interaction strength and hence the highest antiferromagnetic order. Now, we have utilized the antiferromagnetic characteristics of flat Cr monolayer film to optimize the best growth temperature. 1 ML Cr (as calibrated from quartz thickness monitor) has been deposited on Ag(001) substrate kept it at different temperatures. Intensity of LEED  $c(2 \times 2)$  half-order spots has been measured for each case at RT keeping the same imaging parameters. In figure 3.7, we show the growth temperature dependence of the average intensities (of the four)  $c(2 \times 2)$  half-order spots extracted from the LEED images for 1 ML Cr film measured at RT (as shown in figure 3.6).

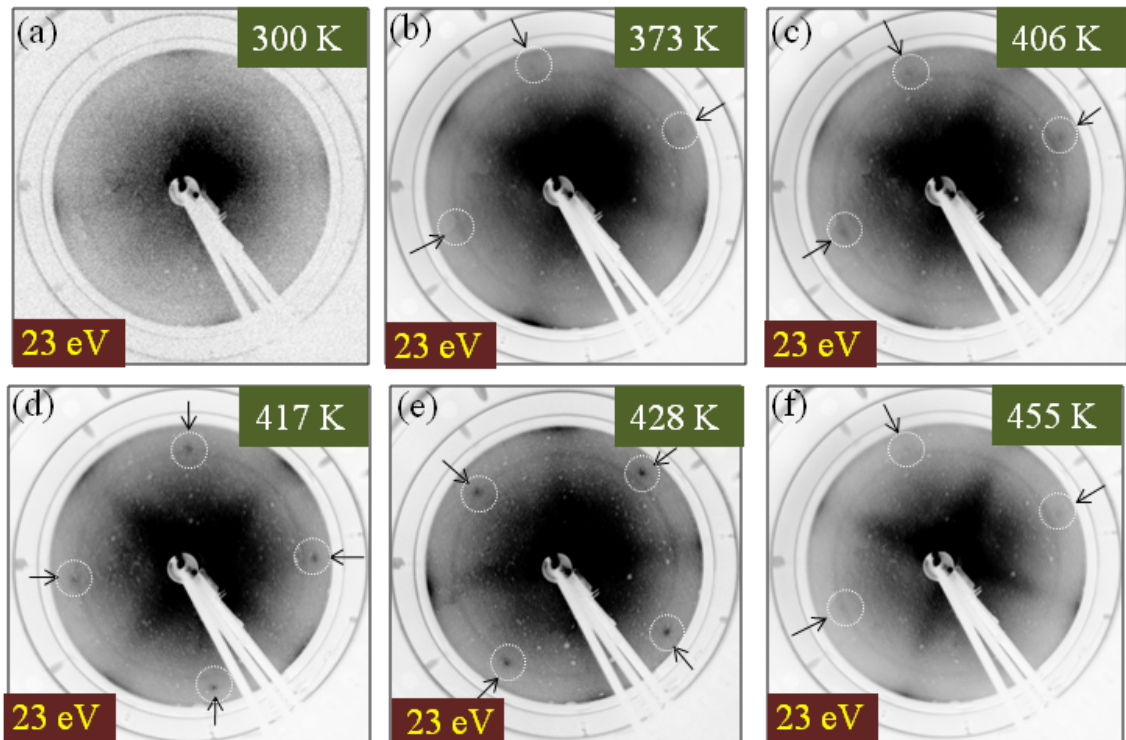


**Figure 3.6:** LEED of 1 ML Cr film deposited on Ag(001) at various growth temperatures : (a) 300 K (b) 373 K (c) 406 K (d) 417 K (e) 428 K (f) 455 K. All the LEED data are presented for 23 eV electron beam energy with enhanced contrast to show the half-order ( $1/2, 1/2$ ) spots. Location of the  $c(2\times 2)$  half-order spots are indicated by small arrows. The integer order spots do not enter into the field of view of screen at this low beam energy. Position of the half orders appear to be rotated in different images due to mounting of Ag(001) crystal substrate on the sample holder. Maximum half-order intensity is visible at 428 K growth temperature.

Very faint intensity of the half-order spots are observed for growth at 373 K which increases with higher deposition temperature. Maximum intensity of the half orders are visible at 428 K. Above this temperature, the half-order intensity falls down again and almost vanishes close to 463 K growth temperature. Not only the spot intensities but also the full width at half maxima of the spots vary for growth at different temperatures. Line profiles drawn over the half-order spots for 1 ML Cr film deposited at different temperatures is shown in Inset I of figure 3.7, clearly indicating the maximum intensity for half-order spots at when grown at 428 K. Not only the

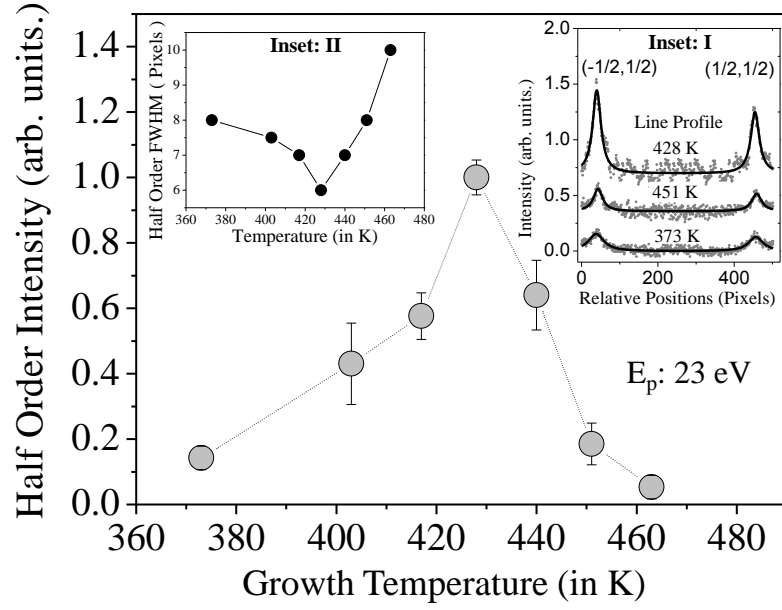


**Figure 3.7:** Average intensity of  $c(2 \times 2)$  half-order spots of 1 ML Cr film deposited on Ag(001) at different substrate temperatures. Inset I: Line profile over LEED half-order spots of 1 ML Cr film deposited at different temperatures. Inset II: FWHM values (in pixels) of the half-order line profiles of 1 ML Cr film deposited at various temperatures.

spot intensities, but also the full width at half maxima (FWHM) of the  $c(2 \times 2)$  half-order spots vary for the growth at different temperatures. In fact, this variation of the FWHM of the half-order spots in pixels for different growth temperatures are shown in inset II of the figure 3.7. Here we clearly observe that the minimum value of the FWHM occurs at the same temperature where the half orders have a maximum intensity (at 428 K), which can also be observed in the line profile of Inset I. The average FWHM values of the spots are inversely proportional to the physical size of the monolayer Cr islands formed on Ag (001) surface. Since electron diffraction is a  $k$  (momentum) space phenomenon, formation of larger  $c(2 \times 2)$  domains results in sharper half-orders with lower FWHM. At the growth temperature of 428 K, the maximum intensity of the half orders points to a long range antiferromagnetic order, resulting in maximum size of the monolayer  $c(2 \times 2)$  Cr island domains. This is consistent with the observation in inset II that we have the minimum FWHM for

428 K with maximum intensity. Taking inverse of the FWHM of half-order spots in proper units, a rough estimate of the the average antiferromagnetic  $c(2\times 2)$  Cr domain sizes can be estimated [110]. Hence, the best growth temperature for deposition of monolayer Cr domains on Ag(001) substrate is assured to be close to 428 K from growth cum LEED studies.

As mentioned earlier, the higher surface energy of Cr is a barrier for the flat layer by layer growth of Cr, wetting the Ag(001) surface. But at elevated temperature, the enhanced in-plane thermal mobility attained by the Cr atoms helps them to distribute all over the Ag(001) surface, forming monolayer Cr domains. But, this 1 ML Cr/Ag(001) system is deprived of thermodynamic stability because of enhanced surface energy of the system. To minimize the surface energy and to attain stability, it is found that a monolayer of Ag atoms segregates over the Cr monolayer. Enhanced mobility of the Ag atoms at higher growth temperature also helps them to segregate on top the Cr monolayer and to dynamically reduce the surface free energy during the growth. Hence, in case of deposition of monolayer Cr at 428 K, it grows in a 1 ML Ag/1 ML Cr/ Ag(001) sandwich structure [111]. On the other hand, at RT deposition, Cr grows in multilayer island mode. Thus, RT deposited Cr monolayer may also include some monolayer islands along with bi- and multilayer islands. Details of the geometric as well as magnetic structures of Cr monolayer will be discussed in the fourth chapter.

#### 3.4.5 Valence band photoemission studies

The valence band photoemission studies of 1 ML Cr film grown at different substrate temperatures were performed in the analysis chamber of the ARPES system after in-situ transfer from the growth (preparation) chamber. Figure 3.8 (a) shows ARPES line profiles at  $\bar{\Gamma}$  position (for details regarding the Brillouin Zone and symmetry directions, please see Chapter 5) for 1 ML Cr films deposited on Ag(001) with He  $I_{\alpha}$

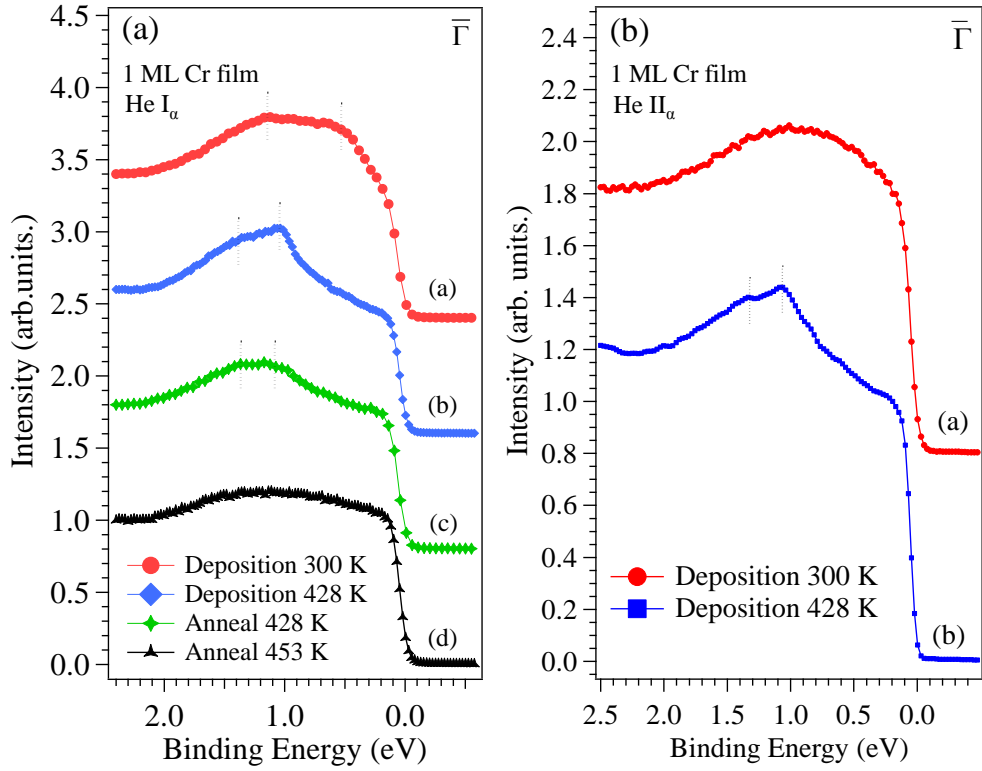


**Figure 3.8:** Figure (a): ARPES spectra from 1 ML Cr film at  $\bar{\Gamma}$  using He I $_{\alpha}$  photons for different cases; spectra (a) film deposited at RT (300 K), spectra (b) deposited at 428 K, spectra (c) deposited at 428 K and further annealed at 428 K, spectra (d) deposited at 428 K and annealed at 453 K are shown. Figure (b): ARPES spectra from 1 ML Cr film at  $\bar{\Gamma}$  using He II $_{\alpha}$ ; spectra (a) film deposited at RT (300 K), spectra (b) deposited at 428 K. All measurements have been performed at RT.

was used as photon source ( $h\nu = 21.2$  eV). All the spectral data presented here were collected at RT if not mentioned otherwise. For RT deposited 1 ML Cr film [spectra (a), red] there are two main features visible. Close to the Fermi level there is a feature at about 0.6 eV binding energy; a second feature having a weak intensity is visible at 1.1 eV. The spectral character becomes quite different in case of 1 ML Cr film deposited at 428 K. In this case, [spectra (b), blue] two features appear respectively at 1.05 and 1.4 eV binding energy positions (marked by ticks). As it is established from the LEED data that the 428 K sample possesses the long-range antiferromagnetic ordering and the valence band structure is expected to show the antiferromagnetic

band structure. In fact, these two bands observed are indeed corresponds to the antiferromagnetic Cr 3d bands with  $\Gamma_5$  and  $\Gamma_1$  symmetries respectively, in good agreement with the expected antiferromagnetic band structure reported earlier [16, 32]. Further details on the dispersions and comparison with theoretical calculations will be discussed in Chapter 5. There exists no band close to the Fermi level for the antiferromagnetic Cr monolayer (see chapter 5); on the other hand, in case of RT deposited Cr monolayer the band at 0.5 eV binding energy is a dispersive one and it crosses the Fermi level as seen in the ARPES data (not shown here). This feature resembles to the surface states found in bulk Cr(001) [112] and expresses metallic nature of the film deposited at RT. The multilayer Cr islands formed on Ag(001) under RT deposition give rise to this state. However, the feature at 1.15 eV for the RT grown sample does not match with that of bulk Cr(001) states, but is very close to the antiferromagnetic feature observed for 428 K grown sample. Thus, this feature is likely to be originating from the antiferromagnetism of few monolayer platelets (among the multilayer islands) present in the RT grown sample. After the deposition of monolayer Cr film at 428 K, when it is passed through annealing at the same growth temperature for 30 min, the antiferromagnetic band intensity is found to decrease significantly [see the spectra (c), green]. Now, the  $c(2 \times 2)$  half-order LEED spots are also almost invisible. A further annealing at even higher temperature of 453 K results in complete destruction of the antiferromagnetic band structure as clear from the flattening of line spectra [spectra (d), black]. Thermal treatment helps in Ag-Cr intermixing process to take place at the interface. The crystalline as well as antiferromagnetic order of the process to take place film is gradually lost by this intermixing process. As the antiferromagnetic strength of the film decreases, intensity of the half-order spots diminishes, also the intensity of the Cr 3d band features weakens. After annealing at 453 K, there forms Ag-Cr alloy all over the Ag(001) surface destructing the crystalline order of the film completely. Almost equal

illumination is visible over the whole 0-2 eV binding energy range in the ARPES data in this case [see spectra (d)].

Similar features were observed in the valence band of 1 ML Cr when a different photon energy source (He II $_{\alpha}$ ,  $h\nu = 40.8$  eV) was used to excite the valence electrons, as seen in figure 3.8 (b). For RT deposited film a broad feature is observed close to 1 eV, similar to the He I $_{\alpha}$  data show in figure 3.8 (a), in agreement with the multilayer island growth mode at RT. The elevated temperature deposited film, on the other hand, shows two well resolved features at 1.09 eV and 1.4 eV; similar antiferromagnetic features as observed with He I $_{\alpha}$  photon source. The photoemission cross-section and hence the intensity of the Cr  $3d$  bands decreases with increasing probing photon energy ; probably is the reason why we do not observe a clear/distinct feature at 1.1 eV binding energy for the RT grown sample with He II $_{\alpha}$  data. The bare Ag(001) substrate has no bands at  $\bar{\Gamma}$  position within the binding energy window of 0-2.5 eV (not shown here) and has only flat featureless low background. Because of better intensity and resolution of the valence band features, we prefer to use He I $_{\alpha}$  photon source for optimizing different growth parameters for better accuracy.

### 3.4.6 Direct *vs.* step deposition of Cr

As we observed that annealing the Cr film results in Cr-Ag intermixing, it is best to cool down the sample as soon as the deposition at elevated temperature is over. We further observe that a step deposition (incremental) growth of monolayer Cr result in alloying of Cr and Ag at the interface resulting in the destruction of antiferromagnetic phase. On the other hand, a direct (single shot) deposition of 1 ML Cr on Ag(001) at elevated temperature prepares a good quality flat monolayer Cr with long range magnetic ordering. In figure 3.9 we show line profiles over LEED half-order spots along with ARPES line profiles at  $\bar{\Gamma}$  position for three different converges 0.2 ML, 0.4 ML and 1 ML Cr film deposited on Ag(001). In figure 3.9 (a) and (c) the data are

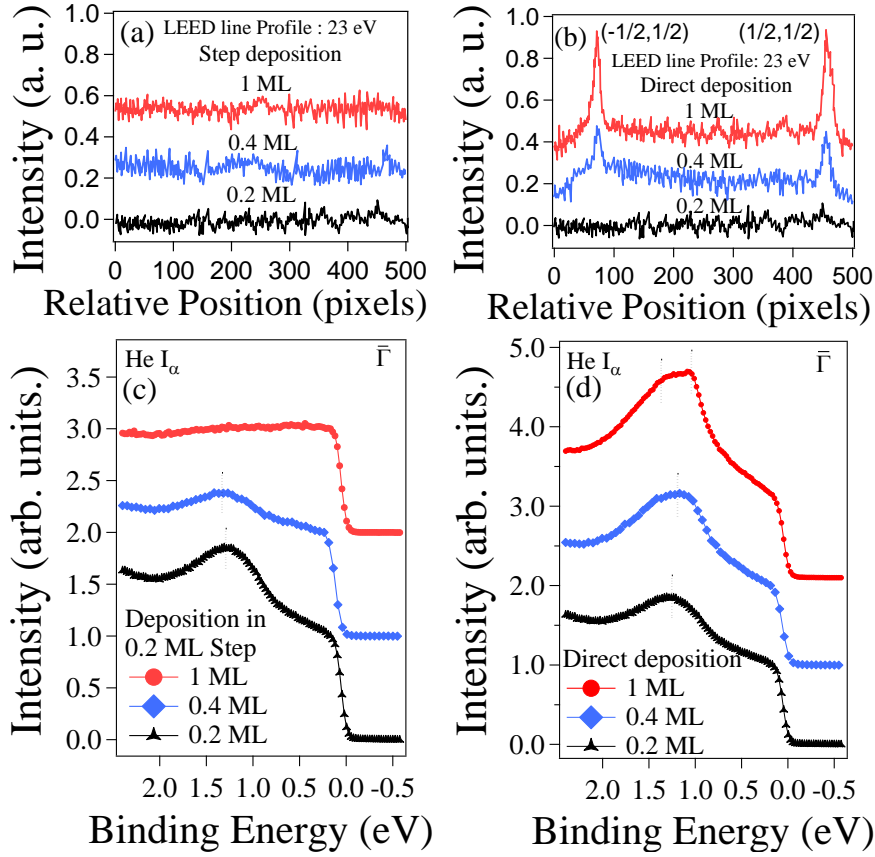


**Figure 3.9:** Line profiles over LEED half-order spots for Cr film coverages 0.2, 0.4 and 1 ML respectively; (a) deposition in step of 0.2 ML coverage (b) deposition of desired thickness in single shot. ARPES line scan of these Cr coverages at  $\bar{\Gamma}$ ; (c) deposition in step of 0.2 ML (d) direct deposition.

shown for Cr film deposited with a step of 0.2 ML coverage, which means, a 0.2 ML of Cr is deposited first on Ag(001) substrate at 428 K and then the film is cooled down to RT for performing LEED and photoemission measurements. Another 0.2 ML Cr is deposited on Ag(001) again at 428 K to prepare 0.4 ML film and so on. On the other hand, figure 3.9 (b) and (d) represents data for the same three thicknesses where each desired thickness is grown directly (in single shot). In figure 3.9 (a) as we observe a weak feature in the ARPES line spectra close to 1.4 eV binding energy position for the case of 0.2 ML coverage (in-fact for 0.2 ML, the step-deposition and direct deposition is the same); the dispersion of these bands (see chapter 5) in the ARPES data suggests these bands to be of antiferromagnetic nature. However, no half-order

spots are visible in LEED for 0.2 ML coverage and no peaks were observed in the LEED line profiles (see 0.2 ML coverage in figure 3.9 (a)). It is expected that tiny monolayer Cr islands will form, since the coverage is only 0.2 ML. For low coverage of the film, the size of the antiferromagnetic domains will be limited to the physical size of the film islands (platelets). Therefore the antiferromagnetic interaction strength of the sample is weak (as the antiferromagnetic correlation lengths here are much smaller than the LEED coherence lengths of about 30-50 nm) which is reflected in LEED where the half orders are almost invisible, or may be of so weak intensity that they are masked by the background intensity. When 0.4 ML Cr film is formed by step deposition, no half-order spots still appear in the LEED pattern; moreover, the antiferromagnetic Cr *3d* band feature intensity significantly reduces. Even for 1 ML Cr film deposited in this step deposition process, no half-order spots are visible in the LEED line profiles and the antiferromagnetic band feature are also completely vanished from the ARPES spectra. However, the Cr films grown in the direct deposition method gets the maximum intensity for the LEED half-order spots as well as for the antiferromagnetic Cr *3d* band intensity, in comparison to step deposition method. The Ag-Cr intermixing process at the interface under thermal treatment is at the root cause behind this phenomena. When a second 0.2 ML Cr is deposited on Ag(001) at elevated temperature, the first 0.2 ML already grown on the substrate is annealed and mixes up with Ag forming interfacial alloy which destroys the antiferromagnetic structure of the film. In this way, the step deposited film forms an alloy upon repeated annealing, completely destroying the crystalline as well as antiferromagnetic structure of the film. The situation is completely different in case of direct depositions. As the deposited film grows in flat monolayer mode and their domain size increases as we deposit higher coverages. Bigger domain size corresponds to longer antiferromagnetic correlation length and more exchange scattering strength, which is reflected in the increment of  $c(2 \times 2)$  (1/2, 1/2) spot intensity and enhancement of the Cr *3d* antiferromagnetic band features. 0.4 ML Cr

film deposited directly at 428 K on Ag(001) shows distinguishable half-order intensity in LEED and higher Cr  $3d$  band intensity than 0.2 ML film. A direct deposition of 1 ML Cr film results in increment of LEED half-order intensity more than 2.5 times than 0.4 ML film. In ARPES line profile, the peak is now resolved into two different features at 1.1 eV and 1.4 eV respectively with their significantly enhanced intensity.

Thus for the optimal deposition of antiferromagnetic Cr film, it is essential to deposit the desired coverage in a single shot at elevated temperature. A step-by-step coverage deposition even at 428 K will not prepare the two dimensional antiferromagnetic Cr film.

#### 3.4.7 Optimizing Cr deposition rate

For the growth of high quality epitaxial films, it is well known that a lower growth rate is desirable as the atoms on the surface has sufficient time to find the optimum positions as well as to relieve off any undesirable strain. Through rigorous studies on optimizing different growth parameters we found that having suitable Cr deposition rate is also an important parameter while growth occurs at elevated temperature. It is worthwhile to mention that because our focus is confined within Cr film coverage below 1 ML and the thermodynamics plays a significant role in formation of flat film covering up the Ag(001) surface, a high rate of Cr deposition is not appropriate. However in the case of Cr flat monolayer growth at elevated temperatures, we find that if we use a very low rate then the interfacial alloying is favorable, disrupting the flat growth mode as well as the crystalline ordering of the overlayers. This leaves us with the necessity to fine tune the growth rate and to obtain the optimal Cr rate in order obtain the highest quality flat Cr monolayer. According to our experimental results, the  $c(2 \times 2)$  half-order intensity becomes 1.5 times higher in case of growth rate of 0.2 Å/min than a comparatively three times lower rate of 0.06 Å/min. Intensity of the antiferromagnetic Cr  $3d$  feature in ARPES line scan

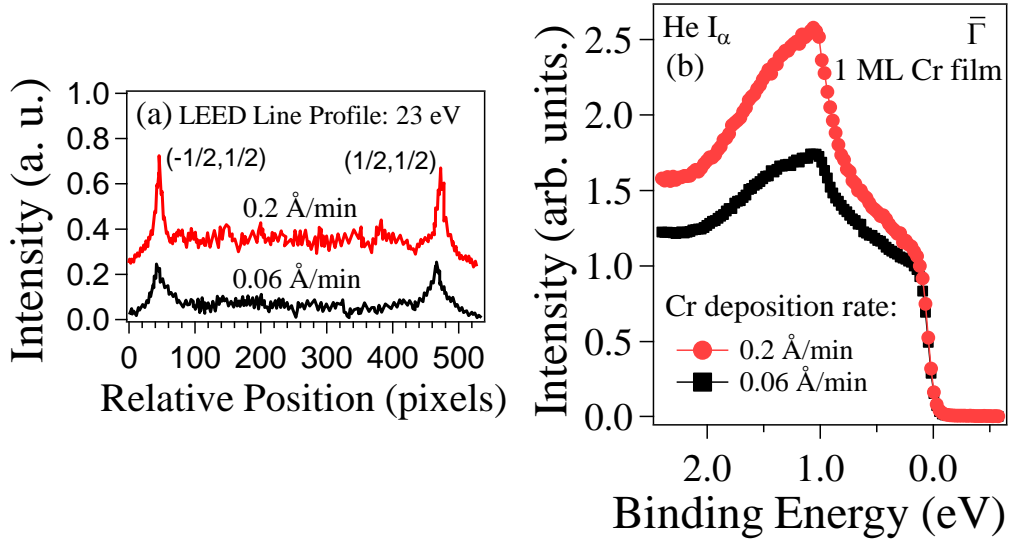


**Figure 3.10:** (a) Line profiles over LEED  $c(2 \times 2)$  half-order spots for 1 ML Cr films grown with deposition rates 0.2 Å/min and 0.06 Å/min. (b) Line profile scan at the  $\bar{\Gamma}$  position of ARPES data for bare Ag(100) substrate, 1 ML Cr grown at 428 K.

also increases almost by 2 times; showing a similar trend. A very slow deposition rate implies a longer deposition time which helps to set in significant amount of Cr-Ag intermixing at Ag(001) surface. A growth rate of 0.2 Å/min is found to be the optimal growth rate for good structural quality as well as high degree of antiferromagnetic ordering.

### 3.4.8 Importance of a smooth substrate surface

As we discussed, a flat growth of monolayer Cr film is essential to achieve two dimensional (2D) antiferromagnetic long range order. Therefore atomic flatness of the substrate is a very important parameter because its smoothness and structural perfection controls the quality of the overlayer film. As discussed by Hanf *et al.* [82], at the initial stages of deposition, the Cr atoms have interaction with the step edges and defect sites. Moreover, substrate surface with terraces and islands posses potential energy barriers at the step edges which reduces surface mobility of the adatoms and eventually affects the crystalline order of the film. Hence a very high

quality substrate surface free from defects, terraces and impurities are expected to favor the growth of flat Cr monolayer islands when deposited under optimized growth condition. According to our experimental results, we never observed the

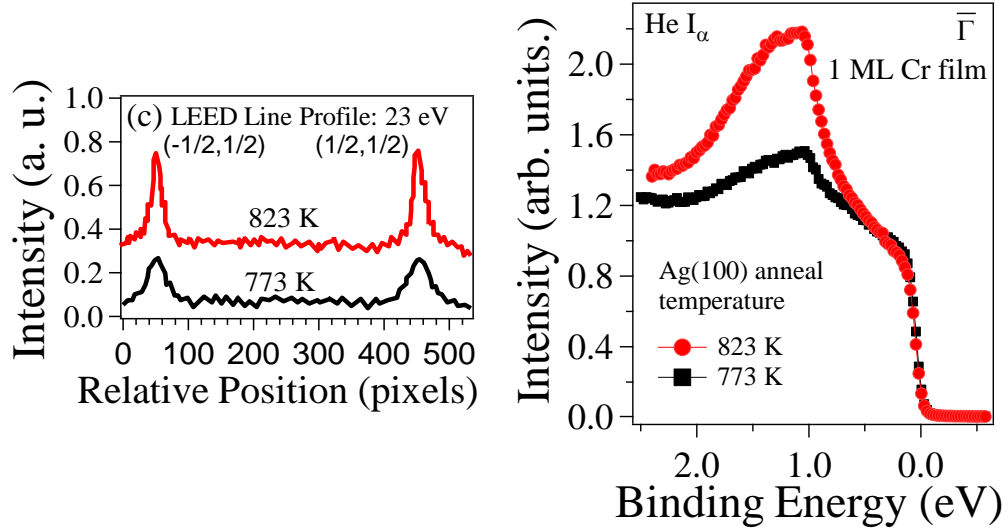


**Figure 3.11:** (a) LEED line profiles drawn over half orders for 1 ML Cr film deposited on Ag(001) substrate annealed at 823 and 773 K. (b) corresponding ARPES line profiles drawn at  $\bar{\Gamma}$ .

antiferromagnetic half-order LEED spots in case of monolayer Cr film until the Ag(001) crystal was annealed at temperature higher than 673 K. In figure 3.11 ARPES line profiles drawn at  $\bar{\Gamma}$  position are shown for Cr films deposited at the same growth condition but on Ag(001) substrate annealed at two different temperatures along with LEED line profile drawn over half-order spots. In case of annealing the substrate at 773 K, the intensity of both half-order spots as well as ARPES features are lower. However, annealing the substrate at higher temperature (823 K) improves the surface quality as evident from the enhanced intensity of integer order  $(1, 0)$  spots of bare Ag(001). A monolayer Cr film deposited on it at optimized condition shows half-order intensity almost double than that on substrate prepared at 773 K. Intensity of the valence band features also become 2.5 times in comparison to the deposition on 773 K annealed substrate.

### 3.5 Summary

A detailed study on the growth of monolayer Cr film has been performed and various assisting parameters essential for the formation of flat monolayer Cr film with long range antiferromagnetic ordering has been optimized and discussed [110]. The growth temperature is the one of the most crucial parameters which determines the multilayer or monolayer growth mode. The direct deposition during high temperature growth is another important parameter; an antiferromagnetic Cr monolayer can never be prepared under step deposition growth mode. The other parameters which helps in growth of flat Cr monolayer with better crystalline quality are Cr deposition rate and annealing temperature for preparation of the Ag(001) substrate. A post deposition annealing of the sample destroys the crystalline quality as well as 2D antiferromagnetism of the film as evident from LEED and ARPES studies, whereas depositing Cr on Ag(001) with all the above mentioned parameters optimized and immediately cooling down the sample after deposition to RT prepares a high quality flat monolayer Cr film having highest long range antiferromagnetic ordering.

## Structure of antiferromagnetic Cr monolayer on Ag(001)

### 4.1 Introduction

The recent emergence of the field of spintronics has led to renewed interest in the electronic and magnetic properties of surfaces and interfaces of ferromagnetic and antiferromagnetic metals. The reduced dimensionality of such surface and interface systems leads to a host of interesting properties that could conceivably be exploited for device applications. Increment of volume of the unit cell and narrowing of electronic band structure near Fermi level can be related with change in magnetic behavior at the surface and in ultrathin films. For instance, theoretical *ab initio* density functional theory (DFT) studies by Freeman and Fu [73–75] and by Blügel *et al.* [77–79] predicted strong enhancement of magnetic moments on the surfaces of 3d transition metals, as well as their overlayers on noble metal and other non-magnetic substrates. As examples of this, calculations [77] have shown that late transition metal (Fe, Co and Ni) overlayers on the Pd(001) surface prefer a ferromagnetic  $p(1 \times 1)$  configuration, whereas early transition metal (V, Cr and Mn) overlayers

---

*This work has been published in Physical Review B, 91, 125435 (2015).*

favor an antiferromagnetic  $c(2\times 2)$  spin superstructure. Moreover, due to the current demand for size reduction of spintronic devices, there is a search for novel materials with anisotropic magnetoresistance. It has been shown that not just ferromagnetic, but also antiferromagnetic (AFM) materials, could become promising candidates for this purpose. [113,114] While there have been a large number of experimental studies on the properties of such two-dimensional (2D) ferromagnetic overlayers, there has been relatively little exploration of 2D antiferromagnetism in such systems, primarily due to the experimental difficulties in detecting surface antiferromagnetism.

Among the transition metals, Cr is expected to be particularly sensitive to changes in coordination and symmetry, as it possesses a half filled  $3d$  band. Earlier *ab initio* DFT calculations have pointed out that one obtains enhanced magnetic moments (close to atomic moments) on Cr surfaces, [73–75] and on Cr monolayers (MLs) on metal surfaces. [77, 78] It has been found that the 2D electronic nature of a freestanding monolayer is essentially retained when the monolayer is deposited onto a noble metal substrate, as there is very little hybridization between the noble metal  $d$  bands and Cr  $d$  states, leading to electronic isolation. [73, 78] This leads to huge (almost 500-600%) enhancement of magnetic moment in flat Cr monolayer.

At first, Cr might appear to be an ideal candidate for epitaxial growth on Ag(001) for two reasons: (i) the nearest-neighbor separation in face-centered-cubic Ag (2.89 Å) is only 0.3% greater than the lattice parameter of bcc Cr (2.88 Å), and (ii) there is a large miscibility gap for the Cr-Ag binary system above the melting point, indicating that intermixing and alloy formation would be energetically unfavorable. These factors would tend to favor the epitaxial growth of Cr on Ag(001), with its  $\langle 100 \rangle$  direction rotated  $45^\circ$  relative to the substrate, along with a sharp Cr-Ag interface with little intermixing. However, there is also an opposing factor, *viz.*, the fact that the surface energy of Cr ( $= 2400 \text{ mJ/m}^2$ ) is much higher than that of the Ag substrate ( $= 1250 \text{ mJ/m}^2$ ) [115]; according to Bauer’s criterion, [96] a flat growth mode (surface wetting) is favored when the surface free energy of the deposited metal

is sufficiently lower than the free energy of the substrate, under thermodynamic equilibrium. For this reason, instead of the growth of a flat Cr overlayer, one may have the growth of multilayer domains or islands, or even a flat layer of Cr buried under one or more Ag layers, if the kinetic barriers can be overcome.

We have shown in Chapter 3 that the growth of monolayer of Cr on Ag(001) is indeed possible and have optimized the growth conditions. However, it is crucial to have a detailed idea about the structure of Cr film at its ultrathin (sub-monolayer) film thickness range as we find that its magnetic properties have intimate correlations with its physical structure. The structure of the film depends on different growth modes which can be achieved at various deposition conditions. The importance of optimizing various growth parameters has already been discussed in the third chapter. In this chapter, our focus is confined within the structural aspects of monolayer Cr film.

## 4.2 Earlier studies

The results from previous experimental and theoretical studies on the deposition of Cr on Ag(001) have resulted in an accumulation of data that is quite contradictory and often puzzling, regarding the growth mode, the geometric structure of the films, and their magnetic properties. At low temperatures (100 K) growth proceeds *via* the hit-and-stick (random-deposition) mode, as has been shown experimentally. [91, 97] On the other hand, very high temperatures (above 500 K), result in Cr agglomeration, as well as Ag segregation. [89, 90] The room temperature (RT) growth of sub-monolayer Cr films on Ag(001) has been extensively studied; [87, 88, 91, 116] it has however been found to result in poorly ordered films, with bilayer or multilayer Cr islands exposing a significant amount of the uncovered Ag substrate. However, it was experimentally observed by the group of Gewinner [82, 87, 88, 99, 106, 115–117] that it was possible to grow flat monolayer of Cr on Ag(001) substrate within the non-equilibrium growth

conditions when deposited at moderate substrate temperatures (430-450 K). Further, they were also able to observe a weak but distinct  $c(2\times 2)$  superstructure spots with very different characteristics that one usually observes on ordered  $c(2\times 2)$  surface alloys. Their weak intensity, energy dependence and temperature dependence have confirmed their origin as resulting from the surface AFM ordering of the Cr layer as discussed in detail in Chapter 3..

Studies using inverse photoemission technique [85] supported the growth of Cr monolayer on Ag(001) when grown at 440 K along with enhanced Cr magnetic moments, however failed to observe the  $c(2\times 2)$  LEED superstructural spots. Steadman *et al.*, [91] using *in situ* x-ray surface diffraction also found a growth mode at 430 K on Ag(001) in which Cr forms a flat monolayer structure, covered however with one monolayer of Ag. In contrast, scanning tunneling microscopy (STM) studies on the same system [89,90] did not support the existence of flat monolayer growth, observing instead Cr agglomeration up to a growth temperature of 440 K. The authors of these studies concluded from their detailed STM investigations [89,90] that the growth of a perfectly flat monolayer film of Cr is not possible on the Ag(001) surface. However, it is worth noting that they could not observe the  $c(2\times 2)$  AFM LEED spots from these Cr monolayer surfaces. This runs contrary to claims that the initial mode of formation of the flat monolayer is largely determined by the in-plane AFM interactions stabilizing the Cr in a metastable monolayer configuration, suggesting that one should expect flat Cr monolayers to occur only in the presence of long-range in plane AFM interactions. A large part of these temperature-dependent differences in growth mode and structure presumably arise because the mobility of the Cr atoms is enhanced as the growth temperature is increased. The possibility of some degree (about 20-30 %) of intermixing between Cr and Ag has also been postulated in the literature, [91,97] due to the far-from-equilibrium growth mode. The experimental observation of Ag segregation on the Cr monolayer films, even at

moderate temperatures, has also been reported, [117] supported by STM [89] and surface x-ray diffraction [91] studies.

Regarding the magnetic properties, various authors have reported both high and low moments on the Cr atoms, and either ferromagnetic or antiferromagnetic ordering. Some of this confusion may arise from the variety of growth modes that have been observed, since the geometric and magnetic structures are intimately connected. In accordance with the theoretical prediction of Freeman and Fu [73–75], angle resolved photoemission measurements by Klebanoff *et al.* [80] on the Cr *3d* valence band structure have concluded that a  $(2.4 \pm 0.3) \mu_B$  magnetic moment is there at the Cr(001) surface, much higher than bulk Cr moment  $0.59 \mu_B$ . Self consistent calculations of Victora *et al.* [8] has also predicted enhancement of magnetic moment at the surface of bulk Cr(001). Electron spectroscopic studies on the growth and magnetic behavior of Cr film deposited on Ag(001) by Newstead and his coworkers [84] have shown a rapid reduction of the magnetic moment with coverage which they confirm from Cr 3s multiplet splitting. Similar conclusion has been drawn by Johnson *et al.* [81] by their polarized neutron reflection measurements. Both observations proposed formation of monolayer Cr domains with long range ferromagnetic order upto 0.33 ML Cr coverage above which bilayer growth mode starts and and magnetic moment of Cr sites decreases significantly. The observation of coherently exchange-scattered half-order spots in LEED confirmed the existence of a  $c(2 \times 2)$  AFM ground state for the flat Cr monolayer grown on Ag(001) at moderate substrate temperatures (430-450 K), as reported by the group of Gewinner marking a significant step in the exploration of 2D AFM systems. However in spite of rigorous studies using different surface sensitive techniques, they were not able to come to a conclusion on the exact structure of the Cr monolayer on Ag(001). Moreover, the inability of other groups in reproducing the  $c(2 \times 2)$  AFM LEED spots also raised some doubt about the validity of these results as well as the geometric and magnetic structure of Cr/Ag(001). Considerable interests have been shown by researchers in the properties of transition metal overlayers

supported by oriented noble metal substrates. Calculations of Fu *et al.* [13] has also predicted a magnetic moment of  $3.7 \mu_B$  for a ferromagnetically ordered Cr monolayer on Au(001). It is only slightly reduced to  $3.1 \mu_B$  when covered by a further Au layer in a Au/Cr/Au sandwich. However Hanf *et al.* [82] has shown that diffusion occurs into the substrate during the initial growth of Cr on Au(001) and forms a Au-Cr alloy up to more than 4 ML thick. Thus, the theoretical predications can not be experimentally verified in case of Cr/Au(001) system. A detailed experimental evidence regarding the structure of monolayer Cr film on Ag(001) can be found in the report by Steadman *et al.* [91] who have grown monolayer Cr on Ag(001) at various temperatures within a vast temperature range from 100 K to 473 K. At very low temperature (100 K), a poorly ordered layer-by-layer growth with sufficient surface roughness was observed due to lower surface mobility. Multilayer island like growth mode was expected from their *in situ* surface x-ray diffraction experiments where the second layer formation starts before completion of the first layer, while deposited at RT. Situation improves at higher temperature deposition where growth of a flat Cr monolayer with better crystalline quality was observed. From the best data fit, for the case of 430 K deposited Cr monolayer, the film was expected to be covered by Ag layer on the top with a  $22 \pm 13\%$  exchange of Cr and Ag sites. The separation of the Cr layer from the substrate was estimated to be increased by  $0.11 \pm 0.12 \text{ \AA}$  and that between the Cr and the outer Ag layer by  $0.31 \pm 0.10 \text{ \AA}$  [91].

Given the variations in the experimental observations made in earlier studies, and the discrepancies in some cases between experiment and theory, we feel it is worthwhile to re-examine the flat monolayer growth of Cr on Ag(001). In this chapter, we present our results from a combined experimental and theoretical study of the growth and structural aspects of ultrathin Cr films on a Ag(001) substrate at 428 K. Our combined LEED and photoemission experiments confirm the presence of AFM order at the surface, and probe the Cr coverage dependence of magnetic long-range ordering in the system. In agreement with our experimental results, our *ab initio*

density functional theory (DFT) studies show that the stable surface structure of the system consists of the Cr layer being buried one layer deep, i.e., under one atomic layer of Ag. They also confirm that the magnetic ground state of the system is a  $c(2\times 2)$  AFM configuration.

### 4.3 Cr Coverage dependence: LEED studies

As shown in chapter 3, we have grown 1 ML Cr film on Ag(001) at different temperatures and from the average intensity of the  $c(2\times 2)$  half-order spots we confirmed that 428 K is the best temperature for growth of a flat monolayer film. We also standardized all other auxiliary parameters (direct deposition of desired thickness, rate of Cr evaporation, smoothness of the substrate *etc.*) essential for growth of flat film. We performed rigorous studies on the coverage dependence of LEED half-order  $(1/2, 1/2)$  spot intensity where each coverage is deposited with all the previously estimated parameters. In figure 4.1, LEED pattern for different Cr coverages on Ag(001) is presented at electron beam energy 23 eV. Each coverage is deposited keeping the substrate at 428 K; and the sample is immediately cooled down to RT after deposition is over. For very small coverage of 0.2 ML [figure 4.1 (a)], it is expected that tiny monolayer Cr domains will form on Ag surface. This limited domain size restricts the antiferromagnetic ordering range and hence exchange interaction strength. No half orders are visible in this case; may be intensity of the  $(1/2, 1/2)$  spots is so weak that they are suppressed by the intense background of the integer order spots and beyond the scope of visibility with our laboratory LEED instrument. However, in case of 0.5 ML coverage, broad and weak intensity half-order spots are observable in LEED [figure 4.1 (b)]. Half orders become distinctly visible for a film coverage of 1 ML [figure 4.1 (c)]. Surprisingly, maximum intensity of the half-order spots is observed for an 1.2 ML Cr coverage [figure 4.1 (d)]; and not for an 1 ML coverage. Repeated experiments have driven us to reach the same conclusion.

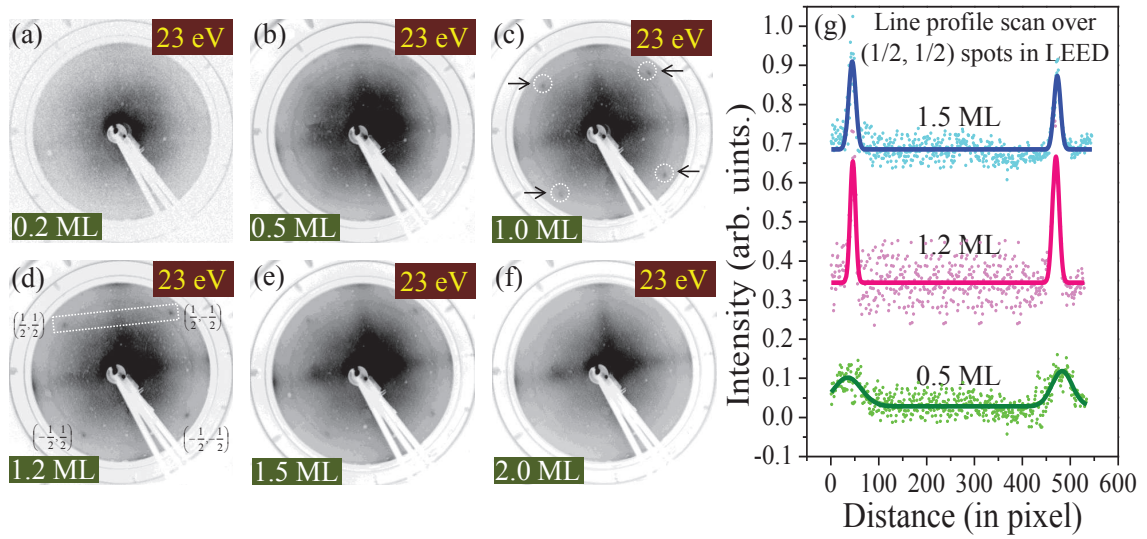


**Figure 4.1:** LEED pattern at beam energy 23 eV for different Cr coverages on Ag(001): (a) 0.2 ML, no  $c(2 \times 2)$  reconstruction visible (b) 0.5 ML, faint and broad half orders (c) 1 ML,  $(\frac{1}{2}, \frac{1}{2})$  spots are distinctly visible (d) 1.2 ML, maximum intensity of the half-order spots (e) 1.5 ML, half orders visible with lower intensity (f) 2 ML, half orders almost invisible. (g) Line profile scan over LEED half-order spots for different Cr coverage. All the line profiles are drawn along the same direction as shown in the rectangular box enclosing the  $(\frac{1}{2}, \frac{1}{2})$  spots in figure (d).

At thickness more than 1.2 ML decrement in half-order intensity as can be seen for the case of an 1.5 ML Cr coverage [figure 4.1 (e)]. Close to 2 ML film coverage, where the monolayer Cr is almost completely covered up by another Cr overlayer, half-order intensity diminishes to zero [figure 4.1 (f)].

In figure 4.1 (g), line profile scan drawn over  $c(2 \times 2)$  half-order spots are shown for three different Cr coverages of 0.5, 1.2 and 1.5 ML. The line profiles are drawn over the  $(\frac{1}{2}, \frac{1}{2})$  and  $(\frac{1}{2}, -\frac{1}{2})$  spots as shown in figure 4.1 (d) enclosed by white dotted rectangle. The broadness of the half-order spots in case of 0.5 ML coverage is clear from the full width at half maxima (FWHM) is twice than that of 1.2 ML coverage) of the line profiles, whereas the weakness of the spot intensity is evident from the low peak values. On the other hand, in case of 1.2 ML Cr film, the spots

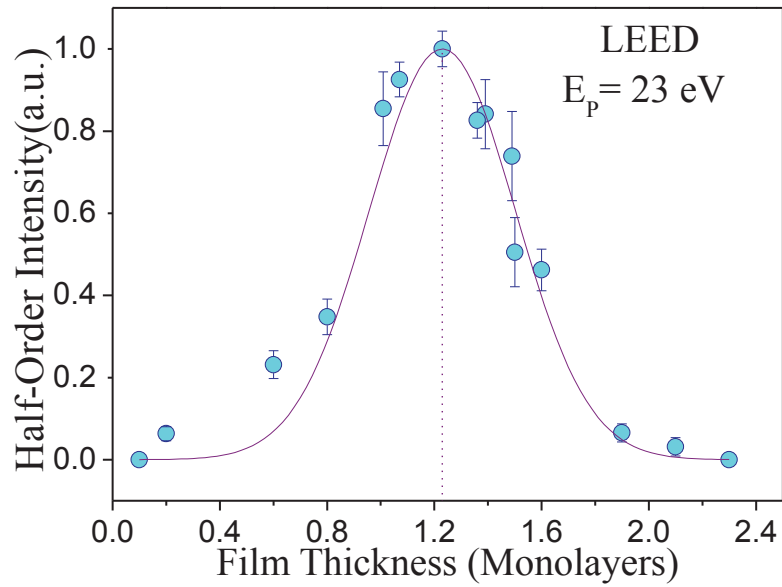


**Figure 4.2:**  $c(2\times 2)$  half-order spot intensity variation with Cr coverage. Beam energy 23 eV.

are sharp having lower FWHM values. Intensity of the half orders decreases to half of the maximum value when 1.5 ML Cr is deposited on Ag(001).

Figure 4.2 gives an overview of the half-order intensity distribution upon Cr coverage. The average intensity of the four-fold  $c(2\times 2)$   $(1/2, 1/2)$  spots has been plotted as a function of Cr coverage over 0.2 to 2.4 ML. A fitting of the data plot shows an overall gaussian distribution where the maximum intensity of the half orders is visible at 1.2 ML. Each intensity value (i.e. data point) is normalized by the electron emission current of the LEED instrument where electron beam energy is 23 eV for each case. The average half-order intensity in case of 0.2 ML coverage is just pixel intensity at the position of half-order spots; as mentioned earlier they are hardly visible with naked eye for this tiny amount of deposition in the very early stage. Visible half-order intensity appears from more than 0.5 ML which increases with film coverage with maximum intensity occur at about 1.2 ML. Then half-order intensity start falling down and vanishes above 2 ML. The  $c(2\times 2)$  reconstruction in LEED is well visible within a coverage range from 0.8-1.5 ML according to our

experiments. The intensity distribution nature is quite similar to earlier observations by Hanf *et al.* [92]; where they also observed a maximum intensity of the half orders close to 1.3 ML thickness. However they observed finite intensity of the half-order spots at 2 ML film coverage. According to their observation intensity of the half-order spots vanished completely close to 3 ML film coverage. Our experimental results, however, have been cross checked through many repeated experiments to reach the conclusion; which are supported by theoretical calculations.

#### 4.4 Cr Coverage dependence: ARPES studies

For each Cr coverage of figure 4.2 we performed Angle Resolved PhotoEmission Spectroscopy (ARPES) to probe the valence band structure of Cr film. We used monochromatic He I $_{\alpha}$  (21.212 eV) and He II $_{\alpha}$  (40.81 eV) photon sources to excite the valence electrons. But as mentioned earlier in chapter 4, with He II $_{\alpha}$ , the intensity of the Cr *3d* bands are lower due to photoemission cross section. In figure 4.3 (a), the ARPES line profiles drawn at  $\bar{M}$  position for different Cr coverage are shown (photon source: He I $_{\alpha}$ ); where each of the coverages are grown at 428 K in a single shot deposition. For bare Ag(001), there are no *sp* bands at the  $\bar{M}$  position within 0-2.5 eV binding energy window. Upon deposition of 0.1 and 0.2 ML Cr, a broad feature is visible. Observing the feature at 0.2 ML coverage it appears that there are three bands close to each other and therefore not so well resolved. The lowest feature is at 1.05 eV; the other two features are at 1.25 eV and 1.6 eV binding energy positions. At the 0.5 ML coverage these three features appears to be shifted in binding energy positions. The lowest binding energy feature appears at 1.09 eV position; whereas the other two features are at 1.25 eV and 1.7 eV binding energy positions respectively. Intensity of the second feature (at 1.25 eV) diminishes significantly with Cr coverage. Probably, this feature is contributed by the edge Cr atoms at the domain boundaries. For very little amount of Cr deposition of 0.1 or 0.2 ML, very tiny nanodomains are

formed; hence number of edge Cr atoms are higher which contributes to this feature. With formation of higher domain sizes their contribution decreases comparative to other features. At 0.5 ML this feature almost vanishes. A coverage of 0.8 ML shows two distinct features at 1.09 eV and 1.7 eV are well visible while the middle feature vanishes completely. Intensity of these two bands shows maxima for Cr coverage of 1.2 ML; beyond which band intensity decreases again and close to 2.2 ML their intensity almost vanishes. At a coverage of 3 ML the nature of the bands shows more like a paramagnetic behavior rather than being antiferromagnetic.

In figure 4.3 (b), intensities of the lower binding energy antiferromagnetic feature at  $\bar{M}$  position has been plotted for various Cr coverages as displayed in figure 4.3 (a). The maximum intensity of the band is close to 1.2 ML (marked with a dotted line). Data points above and below this thickness has been fitted with two different exponential curves. The overall nature of the graph is quite different from the LEED half-order intensity distribution which shows a gaussian characteristic over the 0.2 - 2.2 ML coverage range. The different correlation (coherence) lengths of these two techniques (LEED and ARPES) are probably responsible behind different shape of these curves.

In figure 4.3 (c), ARPES spectra at  $\bar{M}$  position for similar Cr coverages probed by He II $_{\alpha}$  are shown. The intensity dependence of the valence bands on the coverage is displayed in corresponding figure 4.3 (d). The characteristics of the intensity distribution is same as shown in figure 4.3 (b) while probed by He I $_{\alpha}$ . The only major difference in the spectral nature with He II $_{\alpha}$  is that unlike figure 4.3 (a) relative intensity of feature at 1.7 eV is higher than the 1.09 eV feature. Figure 4.3 (d) has been plotted counting the higher intensity feature at 1.7 eV. The relative intensity variation of these two bands due to different probing photon energy is notable.

Observation of antiferromagnetic feature at deposition of very small coverages like 0.1 and 0.2 ML is interesting. Though these features are not well resolved and their intensities are extremely low, dispersions of Cr  $3d$  bands at these low coverages (not

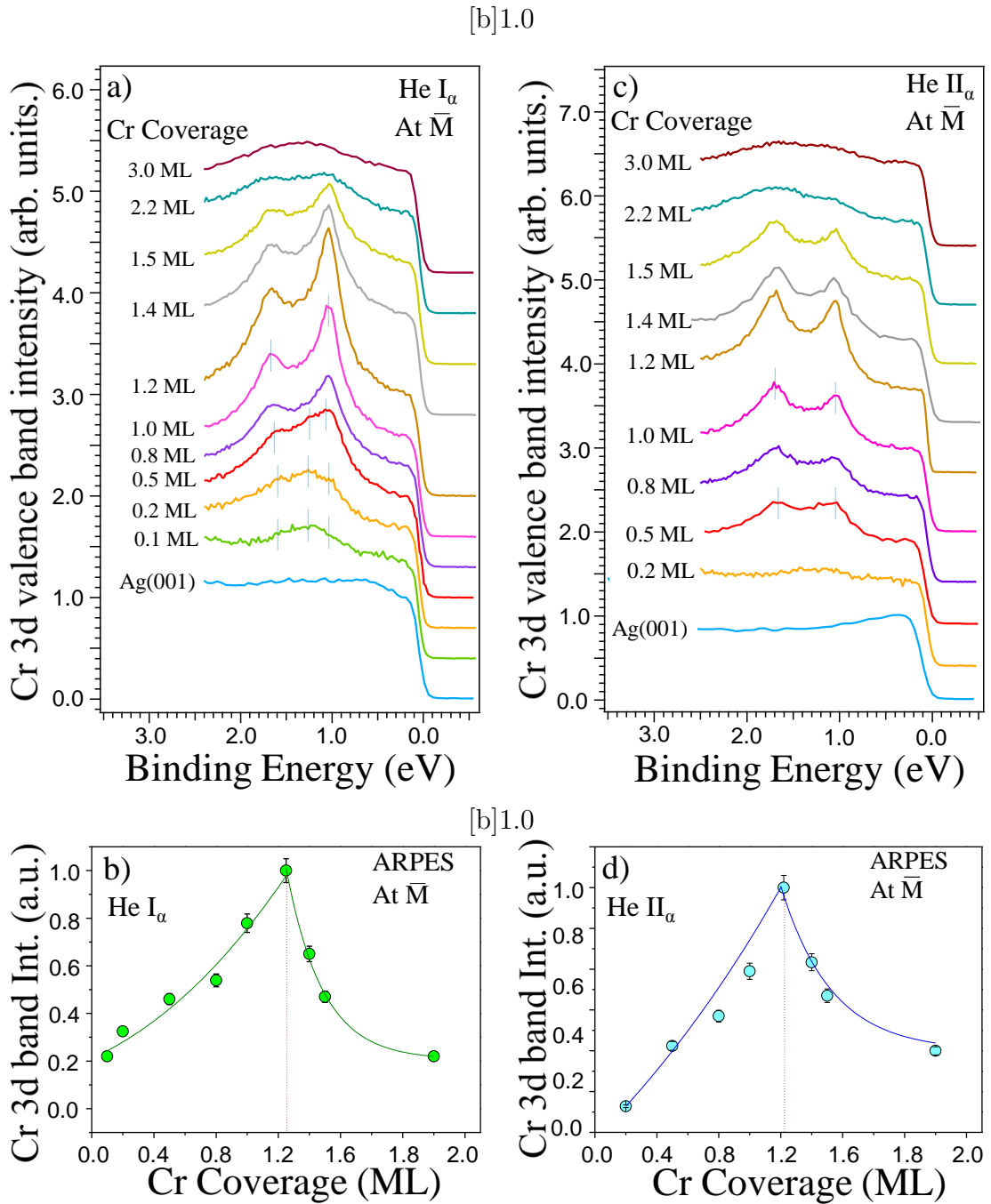


**Figure 4.3:** (a) Antiferromagnetic Cr  $3d$  valence band at  $\bar{M}$  symmetry point for different film coverages probed by He I $_{\alpha}$ . (b) Band intensity vs. Cr coverage plot corresponding to figure (a). (c) Cr  $3d$  valence band at  $\bar{M}$  symmetry point for different film coverages probed by He II $_{\alpha}$ . (d) Band intensity plot vs. Cr coverage corresponding to figure (c).

shown here) resembles quite well with the dispersion of the antiferromagnetic bands at 1 ML Cr coverage. From this one can certainly conclude about the antiferromagnetic nature of these bands, though no  $c(2 \times 2)$  half-order spots are observed in LEED at this (below 0.2ML coverage) level. In fact, we found that photoemission technique is more capable to probe the 2D surface antiferromagnetism compared to electron diffraction technique. Therefore, looking at the ARPES spectral data a significant growth model of Cr monolayer on Ag(001) can be proposed. At elevated temperature deposition, the Cr atoms do not just distribute randomly over the Ag(001) surface, even for a very small amount of Cr deposition of 0.1 or 0.2 ML these deposited Cr atoms nucleates to have a crystalline order and form tiny monolayer Cr nano-domains. Each of these tiny domains possesses antiferromagnetic order of the Cr moments. As explained earlier, due to tiny size of these domains the range antiferromagnetic ordering gets limited and therefore electron diffraction can not produce magnetic half-order spots strong enough to be distinguishable. But, photoemission technique probes the antiferromagnetic nature of these monolayer Cr domain which is reflected in the Cr  $3d$  valence band structures. The high sensitivity in ARPES is possible due to the weak background of the ARPES signal of Ag(001) close to  $E_F$ . Therefore, even a tiny signal shows up; even for 0.1 ML, there is sizable signal showing similar dispersions as that of ML sample. As significant amount of Cr is deposited at elevated temperature, monolayer Cr domains of bigger sizes are formed on Ag(001) with long range antiferromagnetic ordering, hence magnetic  $c(2 \times 2)$   $(1/2, 1/2)$  spots become visible in LEED as well as intensity of antiferromagnetic Cr  $3d$  band feature increases in ARPES.

Another important observation is that Cr film has maximum antiferromagnetic strength at the coverage of about 1.2 ML and not at 1 ML; which is evident from the maximum half-order intensity in LEED and highest intensity of Cr  $3d$  antiferromagnetic features observed in ARPES spectra at  $\overline{M}$  position. A possible explanation of this phenomena is the Cr-Ag intermixing at the interface which cause

removal of Cr atoms from the top Cr overlayer. When Cr is deposited at elevated temperature (428 K), the thermal mobility of the Cr as well as that of Ag atoms increases. As we shall be discussing in the next section that Ag layer segregates on top of Cr overlayer during higher temperature growth. Through this procedure, there a possibility that 20% Cr exchanges their position with Ag sites and hence are removed from the monolayer Cr weakening the antiferromagnetic ordering of the Cr monolayer. Now, at elevated temperature, when we deposit 1 ML equivalent amount of Cr on Ag(001) it actually forms approximately 0.8 ML of Cr antiferromagnetic overlayer. Therefore at nominal 1 ML thickness we do not observe maximum intensity for the half order spots. However, deposition of 1.2 ML Cr produces a complete monolayer Cr antiferromagnetic overlayer which covers up the whole Ag(001) surface; showing maximum antiferromagnetic strength *via* both LEED and photoemission data.

## 4.5 Segregation of Ag on Cr monolayer

As the surface free energy of Cr is almost double than Ag, at RT Cr grows on top of Ag(001) in the form of multilayer islands, as stated earlier. A multilayer growth mode minimizes the effective surface area of the overlayer material and therefore the surface free energy (which is proportional to surface area). Hence, growth of monolayer Cr domains on Ag(001) is not possible at RT. On the other hand, the scenario is quite different in case of elevated temperature growth. The Cr atoms acquire in-plane mobility to spread over the Ag(001) surface and cover up the substrate surface. Consideration of surface free energy demands existence of thermodynamic instability in this system. To achieve energy stability, Ag segregates on top of Cr monolayer and covers up the two-dimensional antiferromagnetic overlayer. The existence of Ag on top of Cr monolayer is proved from our photoemission studies.

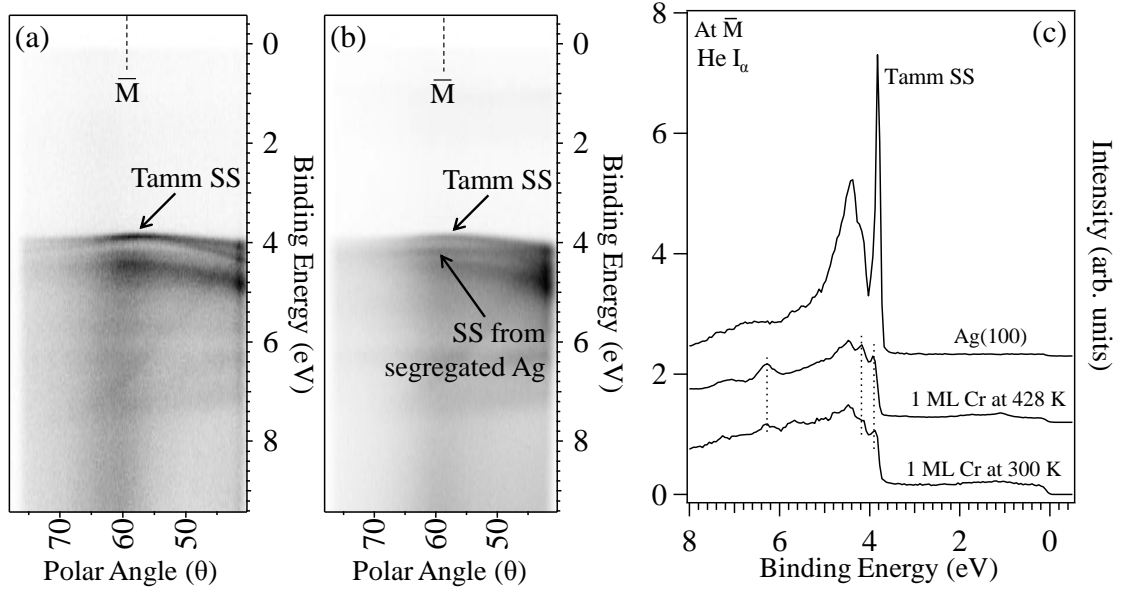


**Figure 4.4:** ARPES data at  $\bar{M}$  symmetry point (a) clean Ag(001). (b) 1 ML Cr deposited on Ag(001) at 428 K. Photon energy: 21.2 eV (He I $_{\alpha}$ ) (c) ARPES line profile spectra drawn at  $\bar{M}$  position for 1 ML Cr deposited on Ag(001) at 300 K (RT) and 428 K. Data are displayed for a broader binding energy range 0-8 eV. Intensity variation of Ag Tamm surface state upon deposition of monolayer Cr is shown.

Figure 4.4 (a) shows the ARPES data of clean Ag(001) surface at  $\bar{M}$  symmetry point (binding energy vs. polar angle plot). Whereas figure 4.4 (b) shows the ARPES data after monolayer Cr has been deposited on Ag(001) at 428 K. In figure 4.4 (c), the ARPES line profile drawn at  $\bar{M}$  position is shown within a wide binding energy range of 0-8 eV, for the case of bare Ag(001), 1 ML Cr deposited at RT (300 K) and 1 ML Cr deposited at 428 K, respectively. For clean Ag(001) surface, a high intensity band is visible at 3.9 eV binding energy position, called the Tamm surface state [118]. The top Ag layer on the Ag(001) substrate has a different (reduced) symmetry and a reduced potential than its bulk counterpart. The symmetry decoupling of the  $d_{xy}$  orbitals in neighbouring planes is broken by spin-orbit interaction at the  $\bar{M}$  point of the surface Brillouin zone on Ag(001). The  $d_{xy}$  orbitals are completely nearest-neighbor antibonding within a layer and completely non-bonding to similar orbitals in nearest neighbor layers. The  $4d$  states of Ag top layer are hence pushed

out of the bulk continua at the maximum of bulk  $d$  bands. The excess  $s$ ,  $p$  electron density at the surface is also responsible behind this phenomena. Therefore, high intensity of Tamm surface state also implies a clean Ag surface and deposition of an overlayer material results in decrement of surface state intensity. Thus, on deposition of 1 ML Cr, both at RT (300 K) and 428 K, intensity of the Tamm surface state decreases significantly. Decrease of the intensity of bulk Ag  $4d$  bands is also notable. After deposition of 1 ML Cr on Ag(001) at 428 K, two extra features are observed at 6.3 eV and 4.2 eV binding energy positions in comparison to RT depositions as observed in figure 4.4 (c). The 6.3 eV feature which is not there in clean Ag(001) surface is contributed by the topmost Ag monolayer. This peak confirms that Ag segregates on top of monolayer Cr grown at 428 K. The 4.2 eV feature has the similar dispersion like Tamm surface state on clean Ag(001) and they are also contributed by the top segregated Ag layer over Cr monolayer. The dispersion of the surface state from top Ag layer implies that the top layer is ordered and it has  $p(1 \times 1)$  symmetry. Similar features observed by Krembel and his group [117] leading to the conclusion of Ag segregation over antiferromagnetic monolayer Cr. The  $p(1 \times 1)$  order of Ag overlayer may also be predicted from our LEED observation. Low energy electrons are extremely sensitive to the surface. If there occurs a random segregation where Ag atoms are scattered over the Cr film without having any crystalline phase then a significant decrement in the intensity of integer order (1,0) spots should be there which contradicts our observation.

The thickness of segregated Ag is another important topic to be investigated. Whether 1 ML or multilayer Ag will come on top of Cr monolayer to energetically stabilize the system is a matter of further study. Our DFT calculations successfully demonstrates that segregation of a 1 ML Ag on top of Cr monolayer is the most stable configuration. The magnitude of Cr moments and their long range antiferromagnetic ordering which favors the energy stability over ferromagnetic spin arrangement has also been calculated.

## 4.6 Theoretical calculations

Spin polarized density functional theory (DFT) calculations implemented in quantum EXPRESSO code [119] has been performed by our collaborating group of Prof. Shobhana Narasimhan at Jawaharlal Nehru Centre for Advanced Scientific Research (JNCASR), Bangalore. A brief overview of these calculations are mentioned here for completion sake while the full details of the calculations can be obtained from elsewhere [111, 120]. A plane-wave basis set was used to expand the electronic wavefunctions in these calculations. The kinetic energy cutoffs for the wavefunctions were set to 40 Ry, while the cutoffs for the related charge densities were set to 400 Ry. Ultrasoft pseudopotentials [121] were used to describe the interactions between the valence electrons and ionic cores. A generalized gradient approximation with the Perdew-Burke-Ernzerhof form was used to approximate the exchange-correlation functional [122].

A 15 atomic layer thick slab was used to model Ag substrate. Four different atomic configurations were considered for the deposited Cr on Ag(001). Cr monolayer was considered at the top and bottom both surface of Ag(001) such that it became a 17 atomic layer thick slab. The first configuration was (i) Cr/Ag(001), where a single flat monolayer of Cr was considered on either side of the Ag(001) substrate. The other configurations used were: (ii) 1Ag/Cr/Ag(001), where the Cr monolayer is buried under one atomic layer of Ag, (iii) 2Ag/Cr/Ag(001), where the Cr monolayer is buried under two atomic layers of Ag, and (iv) 3Ag/Cr/Ag(001), where the Cr monolayer is buried under three atomic layers of Ag. The stacking, in all cases, were considered to be ABAB... stacking characteristic of face centered cubic structure along  $\langle 001 \rangle$  direction. The atomic layers, except the middle three layers of the slab, were allowed to relax, so as to obtain a relaxed geometry. The Broyden-Fletcher-Goldfarb-Shanno (BFGS) algorithm was used to move atomic coordinates until the forces on the relaxed atoms were less than 0.001 Ry/bohr along each Cartesian direction. Brillouin zone

System	Results for magnetic structures			
	FM		AFM	
	$\Delta E$ (meV/Cr atom)	$m_{Cr}^{FM}$ ( $\mu_B$ )	$\Delta E$ (meV/Cr atom)	$m_{Cr}^{AFM}$ ( $\mu_B$ )
Cr/Ag(001)	797	4.71	475	4.46
1Ag/Cr/Ag(001)	393	4.19	0	4.36
2Ag/Cr/Ag(001)	463	4.20	18	4.29
3Ag/Cr/Ag(001)	456	4.20	62	4.32

**Table 4.1:** Results from DFT calculations for the energetics of various ferromagnetic (FM) and antiferromagnetic (AFM) configurations of Cr on Ag(001) systems studied here.  $\Delta E$  denotes the energy of a given configuration with respect to the lowest energy configuration, i.e., the AFM configuration of 1Ag/Cr/Ag(001).  $m_{Cr}$  is the magnetic moment per Cr atom in the given system.

sums were carried out using Monkhorst-Pack meshes [123] that were approximately commensurate with a  $17 \times 17 \times 1$  sampling for the  $(1 \times 1)$  surface unit cell, along with Marzari-Vanderbilt [124] smearing with a width of 0.001 Ry.

Thermodynamically most stable physical configuration was found out through DFT calculations though in real experiment the kinetic barrier may prevent the system to achieve the ground state structure. Aim of the calculation was to find out that whether a bare Cr overlayer or Cr layer buried under 1 ML of Ag is energetically the most stable structure. If buried structure is more stable then under how many Ag layer the AFM Cr layer becomes stable. For the magnetic structure, two collinear magnetic configurations: the  $p(1 \times 1)$  ferromagnetic (FM) one and a  $c(2 \times 2)$  antiferromagnetic (AFM) one has been considered. Table 4.1 shows the results of their calculations for the energetics for each magnetic phase in the eight configurations considered.

According to their calculations, AFM 1Ag/Cr/Ag(001) was found to be the most stable configuration. However, AFM 2Ag/Cr/Ag(001) is almost degenerate with this, lying only 18 meV/Cr atom higher in energy. Therefore it is quite evident that Cr monolayer is buried under monolayer Ag and the low energy electrons probe

the AFM order of Cr monolayer, showing existence of the  $c(2 \times 2)$  half-order spots, buried underneath 1 ML Ag. This results also support our experimental observations mentioned in section 2.5 as well as the in-situ surface x-ray diffraction results of Steadman *et al.* [91] that Cr monolayer is covered with 1 ML of Ag. Probably that is why the intensity of the half-order spots are originating from the underlying Cr layers only 1-2% of the integer spots in our experiments, lower than the theoretical prediction of 2-4% by Blügel *et al.* [35]. If 2 ML Ag segregates on top of the AFM Cr layer, then the intensity of the half-order spots would have reduced so much that they would become almost invisible. All these considerations suggest that Cr layer is covered by 1 ML Ag only, a condition which is satisfied by theoretical calculations and our experimental results.

The calculated magnetic moment associated with each Cr site in table 2.1 shows that the magnetic moment in case of AFM structure of bare Cr monolayer on Ag(001) is  $4.46 \mu_B$ . This magnitude reduces to a  $4.36 \mu_B$  when the Cr layer is covered by a Ag monolayer on top. Vicinity of a non magnetic metallic overlayer decreases the Cr magnetic moment which is expected. But, this reduction is not of a significant amount, this is due to the fact that electronic hybridization of Ag  $4d$  with Cr  $3d$  is negligibly small. A detailed discussion on the magnetic structure of Cr layer is beyond the scope of this chapter and will be a topic of next chapter.

In figure 4.5 (a) and 4.5 (b), we show presents the top and side view respectively of 1 ML Ag segregated on Cr antiferromagnetic monolayer supported by Ag(001); hence a 1 Ag/1 Cr/Ag(001) structure. In this model structure, the top few layers are relaxed and their inter-planner distance differs compared to bulk. In figure 4.5 (c), inter-planner relaxation is displayed, where  $\Delta_{ij} \equiv [(d_{ij} - d_b)/d_b] \times 100$ ; where  $d_{ij}$  is the interlayer spacing between i-th and j-th layer, and  $d_b$  is the bulk interlayer spacing. The magnetic moments of Cr atoms are enhanced in their reduced dimension and magnitude of the moments do not go down significantly even when Cr layer is buried under Ag layers. The spin resolved projected density of states (PDOS) are plotted in

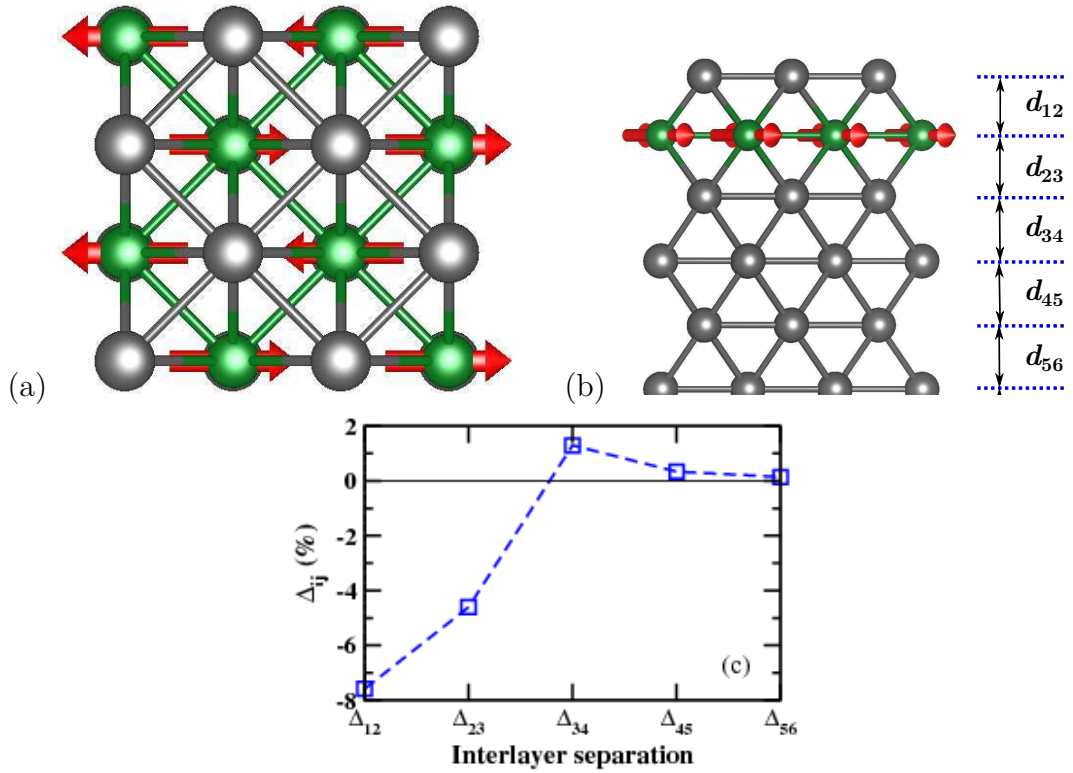


**Figure 4.5:** Geometry of the energetically most favored structure AFM 1Ag/Cr/Ag(001). (a) top view, (b) side view of the system. light gray and dark gray (green online) spheres represent the Ag and Cr atoms, respectively. The red arrows indicate the directions of spins. Note that in the absence of spin-orbit interactions, in-plane and out-of-plane spin directions are equivalent. (c) shows  $\Delta_{ij}$ , the percentage change in interlayer separations, for the first few surface layers. See the text for the definition of  $\Delta_{ij}$  and figure (b) for the convention used in numbering layers.

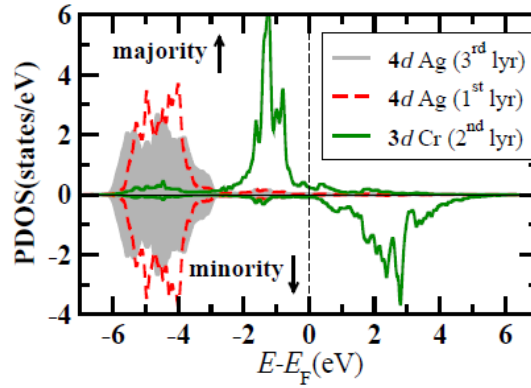


**Figure 4.6:** Theoretically calculated results for the spin-polarized projected densities of states (PDOS) of 1Ag/Cr/Ag(001) in the AFM configuration. The dashed line, solid line and the filled curve indicate the PDOS from first layer Ag  $4d$  states, second layer Cr  $3d$  states and third layer Ag  $4d$  states, respectively.

figure 4.6 for Cr  $3d$  states, Ag  $4d$  states of the top segregated Ag monolayer as well as the third Ag layer in immediate vicinity at the bottom of Cr layer.

Reduced atomic coordination of the Ag atoms in the first layer results in the reduction of the Ag  $4d$  bandwidth as apparent in figure 4.6. Note also the clear spin-polarization of the Cr atoms. On performing a calculation for an isolated monolayer of Cr atoms, maintained at the same in-plane lattice constant, in the  $c(2 \times 2)$  AFM configuration, we obtain a magnetic moment per Cr atom of  $4.45 \mu_B$ . Thus, we see that when Cr is present as an overlayer on the Ag(001) substrate, the magnetic moment on Cr atoms is essentially unchanged, and it is only very slightly reduced when the Cr layer is buried. For Cr/Ag(001) our value of  $m_{Cr}^{AFM} = 4.46 \mu_B$  is larger than a previously reported value of  $\sim 3.8 \mu_B$ ; we believe that the main reason for this discrepancy is that the interlayer spacings were not optimized in this very early previous calculation.

## 4.7 Conclusion

We have revisited the question of the growth of a Cr monolayer on an Ag(001) substrate, and have provided both experimental and theoretical confirmation that the thermodynamically most stable structure of this system consists of an antiferromagnetically ordered flat Cr monolayer film buried under a layer of Ag atoms. Experimentally, we have found that at an optimum growth temperature of 428 K, the signature of the AFM ordering is clearly observed in the LEED images as a weak  $c(2\times 2)$  superstructure, which is only observed at low energies (below 60 eV), and found to vanish above a transition temperature of  $\sim 450$  K. Further proof of the AFM ordering in the Cr monolayer is the observation of Cr  $3d$  bands with  $c(2\times 2)$  symmetry in the ARPES spectra of the system. The intensity of these Cr  $3d$  bands closely follows the half-order spot LEED intensity as a function of the Cr coverage, with a maximum at a Cr coverage of 1.2 ML, suggesting a small intermixing of Cr and Ag atoms in the topmost layer.

Our LEED and ARPES data suggest that the  $c(2\times 2)$  AFM domains are formed from the very early stages of growth of Cr on Ag(001), at 428 K. This suggests that the Ag/Cr/Ag(001) sandwich structure is present from the initial stages of growth, in agreement with the observation of Ag steps in STM studies [89,90]. According to the reports of Hanf *et al.* [94], at very low coverages (lower than 0.3 monolayer) the Cr atoms are in some way incorporated in the subsurface plane possibly by preferential interaction with step edges or other defects, and covered by a pure Ag monolayer. From 0.3 to 0.7 monolayer, most of the Cr atoms are still incorporated in the inverted structure. By 0.7 monolayer the defected regions become less reactive and the Cr adatom density on the defect-free terraces becomes large enough to nucleate 2D islands, therefore half-order intensities in LEED becomes gradually prominent. For 1 to 1.3 monolayer, the system consists of an inhomogeneous surface with coexisting patches of  $p(1\times 1)$  Ag and  $c(2\times 2)$  Cr monolayer platelets. But our experimental and

theoretical studies supports formation of  $c(2\times 2)$  Cr domains covered by  $p(1\times 1)$  Ag monolayer from the earliest stage of growth at high temperature. Further detailed microscopic studies are necessary to obtain a better understanding of these issues.

## Electronic structure and magnetism of monolayer Cr film

### 5.1 Introduction

Ultrathin metallic films, mostly monolayers of 3d transition metals, generated a great deal of interest in their structural, electronic and magnetic properties which are radically different from their bulk counterparts. Theory predicts strong enhancement in magnetic moment ordered in 2D even for weakly magnetic or non-magnetic metals like Cr and V [73, 74]. For a Cr monolayer on Au(100) or Pd(100), a  $c(2 \times 2)$  antiferromagnetic structure with a large local moment ( $3.5 \mu_B$ ) is found to be the most stable configuration [77, 78] using DFT calculations. These predictions are consistent with the general tendency of the metals in the middle of the transition-metal series toward antiferromagnetism or structures based on a twofold superlattice. From an experimental point of view, the characterization and preparation of flat ordered monolayers of  $3d$  metals with a sufficient degree of perfection is reportedly a difficult task and is only possible upon taking care of many important growth parameters as well as proper choice of the substrate which is already discussed in chapter 3.

Electronic isolation between the Cr monolayer and the Ag(001) substrate leads to huge enhancement of the Cr magnetic moments, and the intra-layer interaction between results in 2D antiferromagnetic arrangement. The enhancement of magnetic moments at the Cr(001) single crystal surface has already been proven by photoemission spectroscopic studies [125] as well as theoretical calculations [126]. Lack of electronic overlap between overlayer Cr and substrate Ag also results in narrowing of the antiferromagnetic  $3d$  bands in Cr monolayer (as shown in Chapter 2). For a free standing Cr monolayer, an even higher enhancement of the Cr magnetic moment, effectively a value close to  $3.8 \mu_B$  has been calculated [73]. When adsorbed on Au(001), the magnetic moment of each Cr atom in a monolayer is reduced (to about  $3.7 \mu_B$ ); though the reduction is significantly small as the energy difference between the Cr and Au  $d$  states is close to 5 eV and hence their coupling is small [74]. Experimental studies by different groups have shown a sufficient (4 ML at 480 K) surface alloying between Cr and Au with an enhancement of Cr moment to a magnitude of  $4 \mu_B$  [97, 102, 103]. On the other hand, Ag(001) was established to be a good candidate for growth of monolayer Cr film due to good lattice matching, electronic isolation and having a large miscibility gap above their melting point.

Photoemission study on ultrathin Cr film within the sub-monolayer coverage range as deposited over Ag(001) was first performed by Newstead *et al.* [84]. They observed Cr  $3s$  multiplet splitting which decreases rapidly with film coverage indicating sharp reduction in the magnetic moment which is also supported by the neutron diffraction experiments of Johnson *et al.* [81]. Photoemission investigation on the initial growth mode of Cr on Ag(001) at RT was first investigated by Krembel *et al.* [115]. They reported that at RT growth Cr agglomeration occurs even at coverage as low as 0.5 ML. The Tamm surface state at  $\bar{M}$  symmetry point, intensity of which is proportional to the bare Ag(001) surface area, shows that about 2.5 ML Cr must be deposited in order to quench completely the Ag surface state. Their valence band data clearly indicates that epitaxial growth of Cr certainly takes place at RT but in the form of

island, though there is a sufficient degree of disorder. Later, ARPES experiments performed by the same group demonstrated that deposition of Cr on a mildly heated (440 K) Ag(001) crystal helps in formation of ordered Cr monolayer with a good degree of perfection. For the ordered flat monolayer, the characteristic two-dimensional dispersion of the Cr  $3d$  energy bands and their symmetry at  $\bar{\Gamma}$  was determined by them [87]. The substrate temperature during deposition is critical since lower (300 K) or higher (500 K) temperatures result in an inhomogeneous rough Cr layer formation. They have also performed ARPES and XPS to reveal the electronic and crystallographic structure of Cr monolayer on Ag(001) [95]. Even after deposition of 3 ML Ag upon a monolayer of Cr on Ag(001), the ARPES spectra show the persistence of Cr  $3d$  reduced features characteristic of the 2D Cr monolayer, according to their report. Photoemission and LEED investigation by the same group [94] established the existence of  $c(2\times 2)$  half-order spots in LEED at low electron energies in case of a flat monolayer Cr film whereas antiferromagnetic valence band features are visible close to the Fermi level *via* ARPES studies.

In this chapter, the valence band electronic structure of monolayer Cr film has been discussed under deposition at RT and 428 K. The valence electronic structure is probed by monochromatic He  $I_{\alpha}$  (21.2 eV) and He  $II_{\alpha}$  (40.8 eV) respectively using ARPES. The valence band structure in both cases has been discussed in correlation with the observation of  $c(2\times 2)$  half-order spots in LEED and the multilayer and monolayer growth mode under different deposition conditions. Different bands have been identified and the existence of antiferromagnetic band structure has been confirmed in case of flat Cr monolayer in comparison with ab-initio DFT calculations. Coverage dependence of Cr layer while deposited at elevated temperature has also been in context with the evolution of antiferromagnetic valence band. From the dispersion of antiferromagnetic Cr  $3d$  bands, the  $c(2\times 2)$  symmetry of the magnetic lattice has been confirmed. The core level electronic structure was probed by monochromatic Al  $K_{\alpha}$  (1486.6 eV) photon source. The shift of Cr  $2p_{1/2}$  peak in the submonolayer

thickness range grown under different deposition temperatures indicates to different growth modes (monolayer or multilayer formation).

The flat free-standing Cr monolayer on top Ag(001), with their antiferromagnetically ordered enhanced magnetic moments, is an example of a purely two-dimensional Ising antiferromagnet. The magnetic behavior of this system has also been discussed in this chapter in a separate section.

## 5.2 Valence band: ARPES studies

### 5.2.1 Surface brillouin zone and symmetry directions

Before I present the ARPES data where the band dispersions are presented along different symmetry directions, let us have a general brief discussion over the bulk and surface brillouin zone (BZ) and different symmetry directions in fcc and bcc lattice, because the Ag(001) substrate used in our experiment is a fcc system, whereas Cr has a bcc lattice. In figure 5.1 (a), schematic of the well known fcc lattice has been shown where each face of the cube contains effectively two atoms. The reciprocal lattice of fcc is a bcc lattice. Now if one considers a Wigner-Seitz cell [127] in a bcc structure, it takes the form of a truncated octahedron as shown in figure 5.1 (b) which is the bulk brillouin zone (BBZ) of a fcc lattice. The center of BBZ is the most symmetric point known as  $\Gamma$ . Along the  $\langle 100 \rangle$  crystallographic directions, there are four square faces the center of which is the  $X$  point. The lines joining  $\Gamma$  and  $X$  point are known as  $\Delta$  directions. In the BBZ, any two adjacent hexagonal faces are attached by a common line, the middle point of which is known as  $K$  point. The directions from  $\Gamma$  to  $K$  are known as  $\Sigma$  direction. Projection of BBZ along the  $[001]$  direction produces the square which is the surface brillouin zone (SBZ). The SBZ has symmetry points;  $\bar{\Gamma}$ , the center of the surface which is the projection of  $\Gamma$ - $X$  direction along  $[001]$  direction. Other symmetry points are  $\bar{M}$  (along  $\Delta$ ) and  $\bar{X}$  (along  $\Sigma$ ) which are the corners and middle points of the SBZ square sides, respectively.

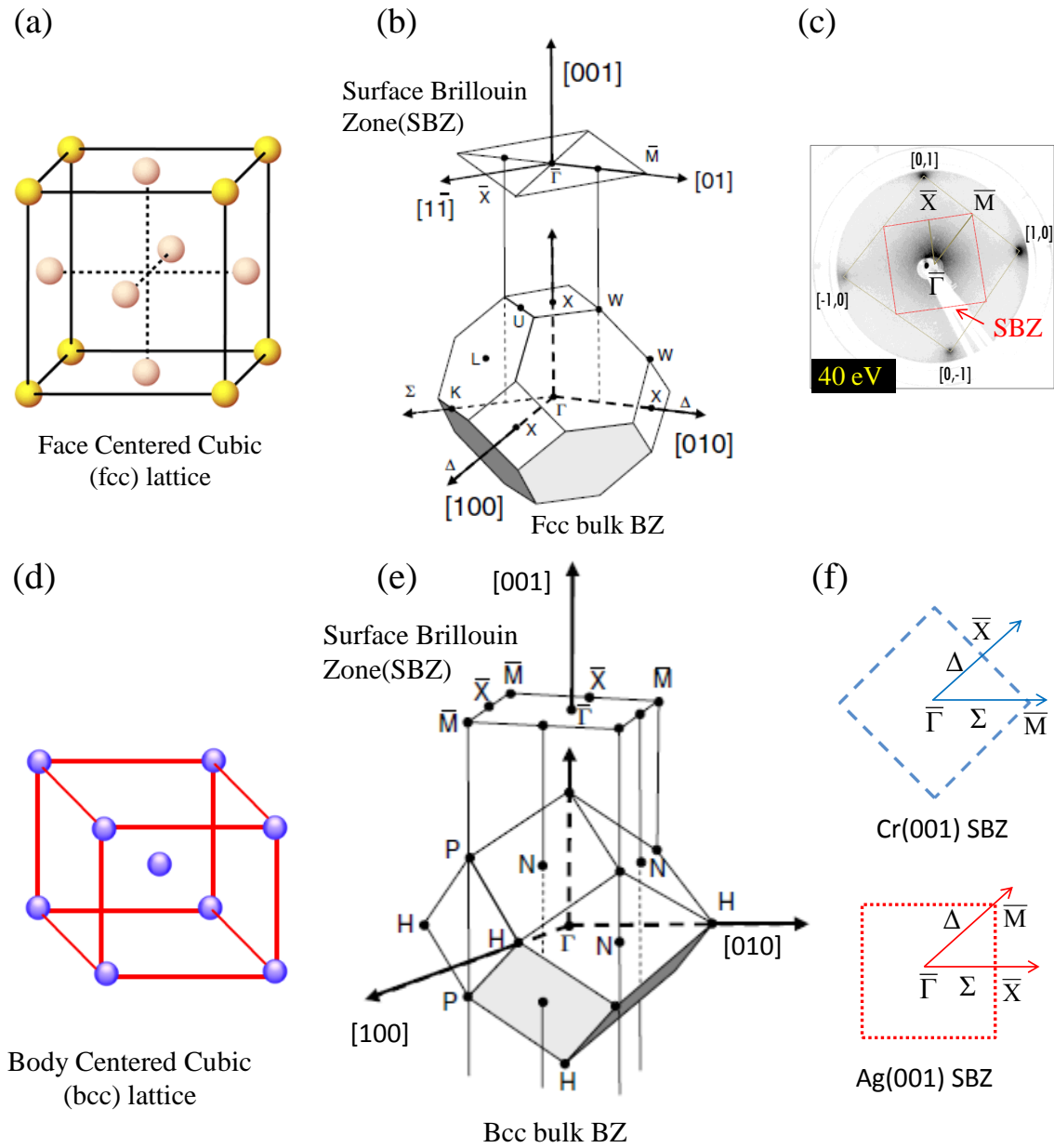


**Figure 5.1:** (a) Schematic diagram of an face centered cubic (fcc) lattice. (b) fcc bulk Brillouin zone (BZ) and its projection to  $\langle 001 \rangle$  direction showing the surface Brillouin zone (SBZ) is depicted. (c)  $p(1 \times 1)$  LEED pattern of Ag(001) surface showing the first integer order  $(1,0)$  spots; the Wigner-Seitz (WS) cell drawn in the reciprocal space, which is actually the surface Brillouin zone is indicated in red square. The  $\bar{\Gamma}$ ,  $\bar{M}$  and  $\bar{X}$  high symmetry points are shown. (d) Schematic diagram of an body centered cubic (bcc) lattice. (e) Bulk Brillouin zone of bcc lattice and its surface projection along  $[001]$  direction. (f) Surface Brillouin zone and symmetry directions of bcc and fcc lattice.

Any diffraction pattern (x-ray, electron *etc.*) is a representation of the reciprocal lattice. Therefore LEED pattern can be considered as a two dimensional representation of the surface reciprocal lattice. A Wigner-Seitz cell drawn in this reciprocal lattice represents the surface brillouin zone (SBZ). In figure 5.1 (c) the four-fold LEED pattern with (1,0) pots of Ag(001) is shown for beam energy 40 eV. The SBZ is indicated with red square. The symmetry points  $\bar{\Gamma}$ ,  $\bar{M}$  and  $\bar{X}$  are denoted on the LEED image.

Similarly, the body centered cubic (bcc) bulk brillouin zone which is a dodecahedron is shown in figure 5.1 (e). The surface projection along [001] direction (i.e. bcc SBZ) and the high symmetry points are indicated. There is a major difference between the symmetry directions of Ag and Cr [see figure 5.1 (f)]. In case of bcc Cr, the  $\bar{\Gamma}$  to  $\bar{X}$  direction is denoted as  $\Delta$  which is the [100] crystallographic direction. In contradiction, for the case of fcc Ag, the  $\bar{\Gamma}$  to  $\bar{X}$  direction is denoted as  $\Sigma$  which is the [110] crystallographic direction. These two crystallographic directions are  $45^\circ$  rotated to each other. Interestingly, as described in chapter 3, lattice parameter of Ag is  $\sqrt{2}$  times the lattice parameter of Cr and hence Cr grows on top of Ag(001) epitaxially with the [100] direction  $45^\circ$  rotated with respect to each other. Hence the  $\Delta$  direction of Cr and the  $\Sigma$  direction of Ag aligns towards the same direction and therefore SBZ brillouin zone matches exactly. The SBZs for these two different systems are shown in figure 5.1 (f) for better understanding of the phenomena. ARPES with monochromatic ultraviolet photon is performed to probe the valence band electronic structure along these symmetry directions of SBZ.

### 5.2.2 Valence band of flat Cr monolayer

In the previous chapters, we have already shown the existence of (1/2, 1/2) spots in LEED at  $c(2\times 2)$  symmetry positions for a flat monolayer Cr film grown at 428 K. Their appearance at very low beam energy with significantly weak intensity and

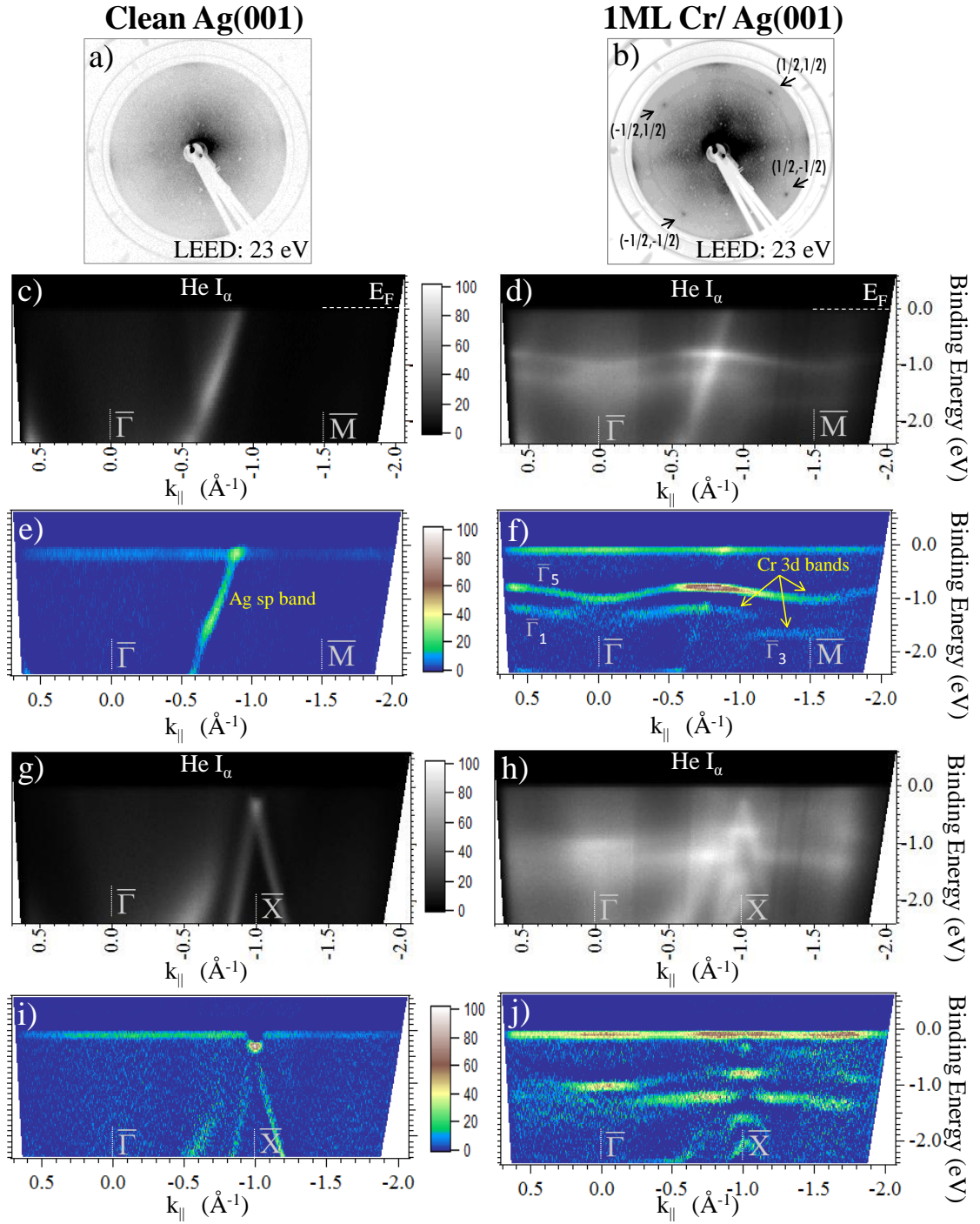


**Figure 5.2:** Comparison of LEED at beam energy 23 eV: (a) clean Ag(001) (b) 1 ML Cr grown on Ag(001) at 428 K; antiferromagnetic  $(1/2, 1/2)$  spots visible. ARPES data probing the valence bands along  $\bar{\Gamma}$ - $\bar{M}$  (c) Bare Ag(001) (d) 1 ML Cr/Ag(001). (e) Second derivative of figure (c). (f) Second derivative of figure (d). ARPES data probing the valence bands along  $\bar{\Gamma}$ - $\bar{X}$  (g) Bare Ag(001) (h) 1 ML Cr/Ag(001). (i) Second derivative of figure (g). (j) Second derivative of figure (h). Photon source monochromatic He  $I_{\alpha}$  (21.2 eV).

their temperature dependence confirm their antiferromagnetic origin as a result of exchange scattering between unpolarized electrons and the antiferromagnetically arranged Cr moments. But ARPES studies using ultraviolet photons which probes the Cr  $3d$  valence bands for Cr film at submonolayer coverage range, confirms the antiferromagnetic nature of the film unanimously. In fact, there is a strong correlation between the intensity of ‘half-order’ spots and the antiferromagnetic Cr  $3d$  valence band intensity which is already illustrated in chapter 4, but the dispersion of these bands over different  $k_{\parallel}$  positions were not discussed. In this chapter, different Cr  $3d$  antiferromagnetic bands along different symmetry directions have been shown in their ‘binding energy ( $E_B$ ) vs. momentum ( $k_{\parallel}$ )’ plot. In figure 5.2 (a) and (b), the LEED patterns of bare Ag(001) has been compared to the 1 ML Cr film deposited on it for beam energy 23 eV. In case of 1 ML Cr film, the LEED shows four-fold ( $1/2, 1/2$ ) spots whereas these spots are not there in bare Ag(001). In figure 5.2 (c) and (d), the valence band electronic structures of bare Ag(001) and 1 ML Cr/Ag(001) has been shown respectively within binding energy range 0 - 2.4 eV for symmetry direction  $\bar{\Gamma}-\bar{M}$  where monochromatic He  $I_{\alpha}$  ( $\hbar\omega = 21.2$  eV) is used as probing photon source. The 2D second derivative of the data has been plotted in figure 5.2 (e) and (f) respectively. Figure 5.2 (e) shows that there exists no other bands within the binding energy window 0 - 2.4 eV except for the Ag  $sp$  band. The Ag  $4d$  bands appear within 4-7 eV binding energy, existence of no Ag bands within 0-2.4 eV binding energy results in no hybridization between Cr and Ag bands. On the other hand, figure 5.2 (d) and (f) shows that there exists three different Cr  $3d$  bands (marked by arrows) in case of monolayer Cr film deposited on Ag(001) at 428 K. The most intense band visible at  $\bar{\Gamma}$  (normal emission;  $k_{\parallel} = 0$ ) is located at 1.05 eV. The second band at 1.4 eV binding energy has weak intensity at  $\bar{\Gamma}$ . The third band, furthest from Fermi level ( $E_F$ ), is only visible close to the  $\bar{M}$  position. Figure 5.2 (g) shows the Ag  $sp$  bands along  $\bar{\Gamma}-\bar{X}$  direction for the bare Ag(001). After deposition of 1 ML Cr, the  $3d$  bands are visible in figure 5.2 (h). The second derivative of the ARPES data in

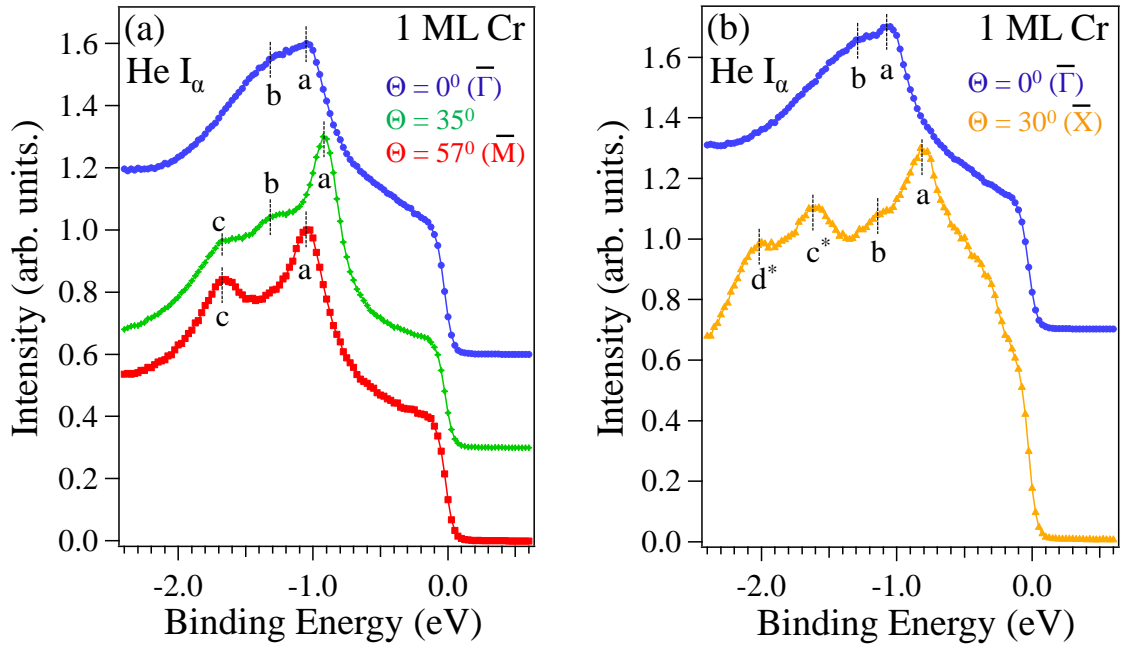


**Figure 5.3:** (a) Line profile drawn over the ARPES data at different emission angles; at  $0^\circ$  ( $\bar{\Gamma}$ ),  $57^\circ$  ( $\bar{M}$ ) and  $35^\circ$ . (b) Line profile drawn over the ARPES data at different emission angles; at  $0^\circ$  ( $\bar{\Gamma}$ ) and  $30^\circ$  ( $\bar{X}$ ). Photon source monochromatic He I $\alpha$  (21.2 eV).

figures 5.2 (g) and (h) are presented in figure 5.2 (i) and (j). Upon taking second derivative, the Cr  $3d$  bands of figure 5.2 (h) becomes distinct in figure 5.2 (j). At  $\bar{\Gamma}$  position, the most intense band is at 1.05 eV similar to figure 5.2 (f); the other bands at 1.4 eV is relatively weaker in intensity. On the other hand, the shape of the Cr bands at  $\bar{X}$  appears to be modified by the presence of Ag  $sp$  bands. The band at 0.8 eV binding energy position has higher intensity at  $\bar{M}$ , another band at 1.2 eV has significant intensity at both sides close to  $\bar{M}$  but appears to be discontinuous right at  $\bar{M}$ . Two extra dispersive features which appears only at  $\bar{M}$  and vanishes very quickly at both sides have their band edges at 1.7 eV and 2 eV respectively. All the Cr  $3d$  antiferromagnetic bands have low dispersion and their bandwidth is  $<1$  eV according to our experimental data.

In figure 5.3 (a) and (b), APRES line profiles are shown, which are drawn over figure 5.2 (d) and (h), respectively. Figure 5.3 (a) demonstrates three spectra drawn

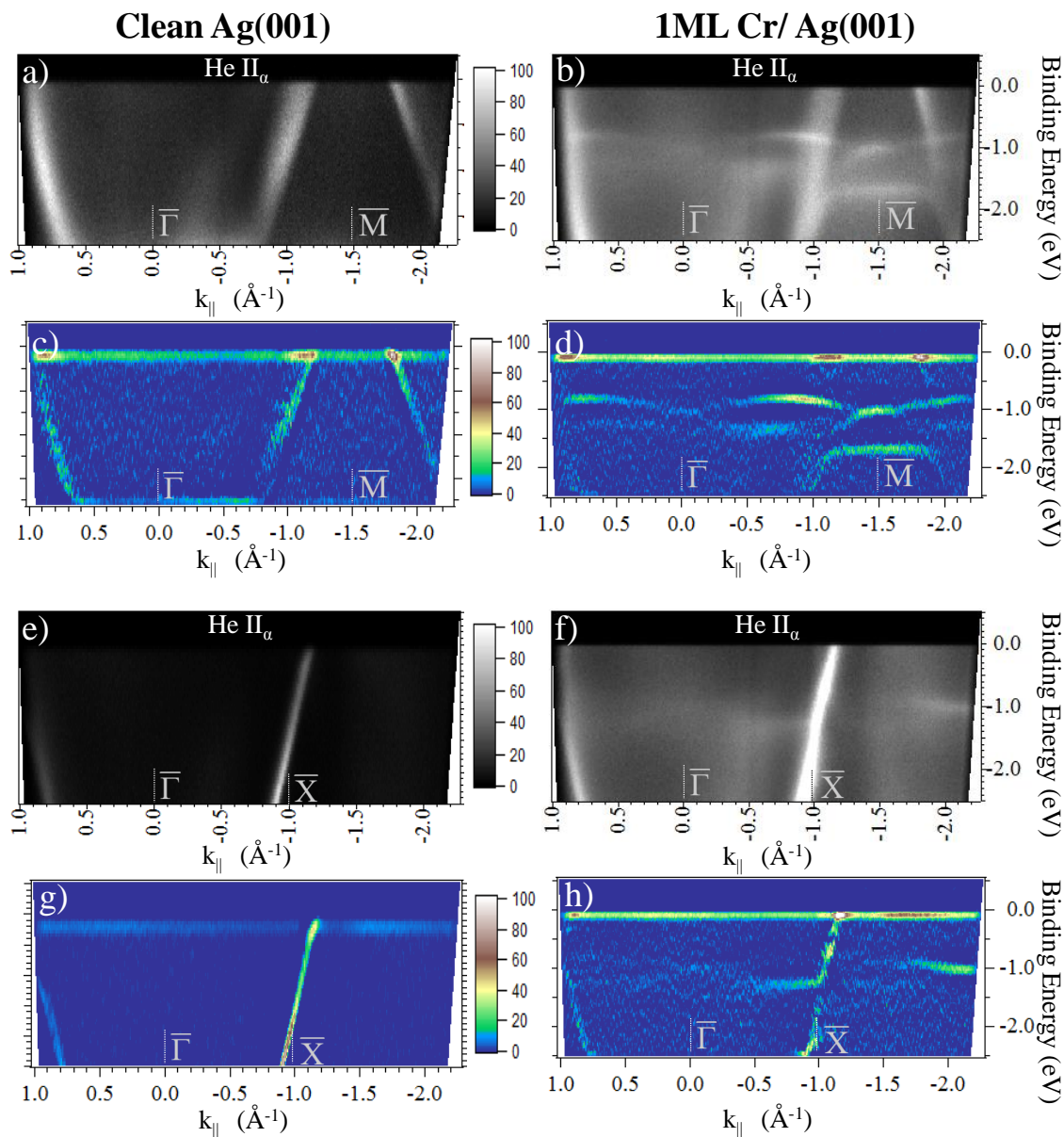


**Figure 5.4:** ARPES data probing the valence bands along  $\bar{\Gamma}$ - $\bar{M}$  (a) Bare Ag(001) (b) 1 ML Cr/Ag(001). (c) Second derivative of figure (a). (d) Second derivative of figure (b). ARPES data probing the valence bands along  $\bar{\Gamma}$ - $\bar{X}$  (e) Bare Ag(001) (f) 1 ML Cr/Ag(001). (g) Second derivative of figure (e). (h) Second derivative of figure (f). Photon source monochromatic He II $_{\alpha}$  (40.8 eV).

at  $\bar{\Gamma}$  (normal emission, polar angle  $0^\circ$ ),  $\bar{M}$  (polar angle  $57^\circ$ ) and somewhere in the middle of these two symmetry points (polar angle  $35^\circ$ ). At normal emission, two features close in their binding energy positions are observed. The feature at 1.05 eV (denoted as ‘a’) is of higher intensity whereas the second feature (denoted as ‘b’) at 1.3 eV has lower intensity. As mentioned earlier, there exist totally three antiferromagnetic features in the band structure which is clear from the line spectra drawn at  $35^\circ$  emission angle. We observe three features in the line spectra at  $35^\circ$  degree, at 0.9 eV (‘a’), 1.3 eV (‘b’) and 1.7 eV (‘c’) respectively. Intensities of both of the features ‘b’ and ‘c’ are much lower compared to ‘a’. The feature ‘c’ becomes prominent at emission angle  $57^\circ$  ( $\bar{M}$  point). Dispersive nature of the Cr  $3d$  bands becomes also clear from these line profiles. Similarly, ARPES line profile drawn in figure 5.3 (b) shows two closely lying features at normal emission. However, line profile at  $\bar{X}$  shows presence of four different features. The high intensity feature ‘a’ exists close to 0.8 eV, the second feature at 1.15 eV has higher intensity at both sides close to  $\bar{X}$  but it is discontinuous just at  $\bar{X}$  point and therefore have very low visible intensity. Two other feature at higher binding energies exist which have band edges at 1.63 eV (c\*) and 2 eV (d\*), respectively. These are highly dispersive features exists just at  $\bar{X}$  position and their intensities fades away sharply at both sides. The dispersive nature of these bands are different from the general dispersion behavior of antiferromagnetic Cr  $3d$  bands. However, they are undoubtedly Cr  $3d$  bands, though their dispersive behavior at  $\bar{X}$  appears to be significantly modified by the presence of Ag  $sp$  bands there. Interestingly, our theoretical calculations in collaboration with Prof. Shobhana Narasimhan, JNCASR, Bangalore could reproduce these highly dispersive features which will be discussed later in this chapter.

The antiferromagnetic  $3d$  valence band structure of Cr monolayer probed by a different photon source (monochromatic He II $_{\alpha}$ ,  $\hbar\omega = 40.8$  eV) reveals more interesting information about them. The Cr  $3d$  antiferromagnetic bands are visible along  $\bar{\Gamma}$ - $\bar{M}$  in figure 5.4 (b), which shows there exist three bands [clear from the second derivative

of the data in figure 5.4 (d)]. Intensity of the bands at  $\bar{\Gamma}$  is significantly low compared to  $\bar{M}$  position. The two bands at lower binding energy positions merge together at  $\bar{M}$  position, which was not visible while probed with He I $_{\alpha}$ . The third band at 1.7 eV is visible only near  $\bar{M}$  position and its dispersion is affected by the presence of the Ag *sp* bands. On the other hand, Cr *3d* valence bands are of quite weak intensity and barely visible along  $\bar{\Gamma}$ - $\bar{X}$  direction. Therefore, the highly dispersive features at  $\bar{X}$  which are visible with He I $_{\alpha}$  [see figure 3.2 (h)], can not be distinguished in figure 5.4 (f). In fact, the overall band intensity is weaker when He II $_{\alpha}$  is used as probing photon source rather than He I $_{\alpha}$ , due to the lower photoemission cross section of Cr *3d* bands at higher photon energy.

### 5.2.2.1 Evidence of 2D antiferromagnetism

The experimental band structure of the overlayer shows that there is an excellent agreement between the data for different photon energies (He I $_{\alpha}$  and He II $_{\alpha}$ ) which testifies the two-dimensional character of these bands. As can be seen in figure 5.2, three clearly resolved bands are visible along the  $\bar{\Delta}(\bar{\Gamma}$ - $\bar{X})$  and  $\bar{\Sigma}(\bar{\Gamma}$ - $\bar{M})$  symmetry lines of monolayer Cr on Ag(001). For symmetry reasons [128], only  $\bar{\Gamma}_5$  and  $\bar{\Gamma}_1$  initial states can be observed at normal emission. Our experimental data show that the  $\bar{\Gamma}_5$  state is located at 1.05 eV binding energy position, whereas the  $\bar{\Gamma}_1$  state lies at 1.4 eV. The  $\bar{\Gamma}_5$  is  $d_{xz}$ ,  $d_{yz}$  derived band. On the other hand, the  $\bar{\Gamma}_1$  state is  $d_{3z^2-r^2}$  derived band. The third feature that lies at shallow level being at 1.7 eV binding energy position have weak intensity in the ARPES data at  $\bar{\Gamma}$  position. It is detectable only at  $\bar{M}$  position as can be seen in figure 5.2 (f) and 5.4 (d). This state is either  $\bar{\Gamma}_3$  ( $d_{x^2-y^2}$ ) or  $\bar{\Gamma}_4$  ( $d_{xy}$ ) state which is forbidden at normal emission. This is in accordance with the theory if the Cr layer has four-fold symmetry [128].

Figure 5.5 (a) shows the calculated band structure of a paramagnetic transition metal arranged in a 2D square lattice [129]. Dispersion of the *d* bands can be

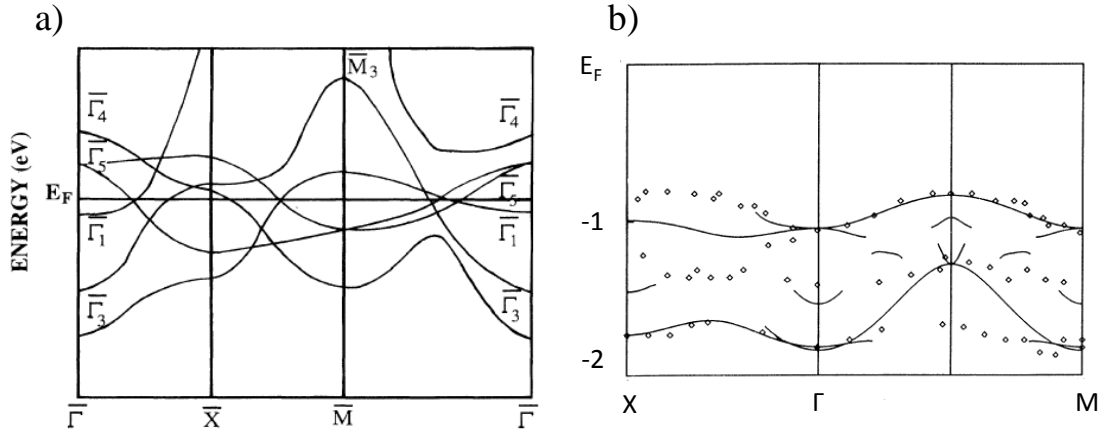


**Figure 5.5:** (a) Calculated band structure for a paramagnetic transition metal on a square lattice by Wang [129]. (b) Tight binding calculations of electronic structure of Cr layer adsorbed on Ag(001) surface by G. Allan [133].

understood from simple tight binding considerations. The  $d_{xz}, d_{yz}$  derived bands along  $\bar{\Gamma}-\bar{M}$  show antibonding character at  $\bar{\Gamma}_5$  and bonding character at  $\bar{M}$ , whereas the  $d_{3z^2-r^2}$  ( $d_{x^2-y^2}$ ) derived bands are bonding at  $\bar{M}_1$  ( $\bar{M}_3$ ). A more realistic calculation by Richter *et al.* [130] where a  $3d$  metal monolayer supported by a noble metal substrate was considered and a similar behavior of the bands near  $\bar{\Gamma}$  and  $\bar{M}$  was preserved. However, our experimental data shows bonding character for  $\bar{\Gamma}_5$  band. Cr has half-filled  $3d$  shell, which means the  $E_F$  should be located at the middle of the  $d$  bands as supported by all these theoretical calculations. Therefore,  $\bar{\Gamma}_5$  should be unoccupied in paramagnetic Cr and the  $d$  band should exist in the neighborhood of Fermi level. Experimentally no  $d$  states are observed to cross the Fermi energy  $E_F$ , rather there is a gap of 0.8 eV below the  $E_F$ . Moreover, according to the calculations of Fu *et al.* [13] the occupied band width should be about 1.5-2 eV with high density of states at  $E_F$ , which should be in case of a paramagnetic  $p(1 \times 1)$ . This suggests that the Cr monolayer must be stabilized by some mechanism which opens a large gap at  $E_F$ . Also, the observed dispersions are much smaller than expected from a paramagnetic Cr monolayer. The experimental width of the  $d_{xz,yz}$  bands ( $\bar{\Gamma}_5$  symmetry) along  $\bar{\Sigma}$  ( $\bar{\Gamma}-\bar{M}$ ), as shown in figure 5.2 (f), is about 240 meV as compared

to 1.0 eV calculated theoretically [130]. Hence, the observed band topology is not compatible with the one expected from a paramagnetic Cr monolayer.

Again, ferromagnetism would result in much larger total bandwidth, about 2.5 eV and a substantial density of states at  $E_F$  as shown by previous calculations [131]. Also, ferromagnetism is incompatible with the  $c(2\times 2)$  symmetry as well as with the small observed band dispersions. It is interesting to observe that, the Cr  $3d$  bands shown in our experimental data actually indicate a  $c(2\times 2)$  superstructure rather than a  $p(1\times 1)$  translational symmetry. Specifically for the  $\bar{\Gamma}_5$  band there is a nearly perfect symmetry at the midpoint of  $\bar{\Sigma}$  line in the  $p(1\times 1)$  SBZ as clear from figure 5.2 (f) and 5.4 (d). From the dispersive behavior of the  $\bar{\Sigma}$  band, it appears that the  $\bar{\Gamma}$  and  $\bar{M}$  are equivalent points. Tight binding model calculations for the  $d$  bands of an isolated Cr layer arranged in a square lattice was performed by Krembel *et al.* [132] were in agreement with the dispersive nature of the experimental  $d$  bands along  $\bar{\Sigma}$ . A more realistic calculation was performed by G. Allan [133] where electronic structure of a Cr overlayer adsorbed on Ag(001) surface was calculated in tight binding approximation. In its ground state a  $c(2\times 2)$  antiferromagnetic Cr monolayer structure has magnetic moment close to  $3.6 \mu_B$ . The 2D energy-dispersion curves were calculated for an antiferromagnetic Cr monolayer along two different symmetry directions of the SBZ as shown in figure 5.5 (b). These calculated band structure matches reasonably well with our experimental band dispersion data. The 2D band dispersion and symmetry of the  $d_{xz,yz}$  are in agreement with our experiments which supports the existence of  $c(2\times 2)$  symmetry. However, the tight binding model does not include the mixing of Cr  $d$  states with Ag  $s$  states therefore for the deeper lying bands the agreement between theory and experiment is worse, e.g. the highly dispersive features observed in our data at around  $\bar{X}$ , as visible in figure 5.2 (h) are not predicted by these tight binding calculations as these are thought to be originated by the Cr  $d$  and Ag  $sp$  hybridization. In fact, the previous experimental results by C. Krembel *et al.* also do not observe these highly dispersive features around  $\bar{X}$ .

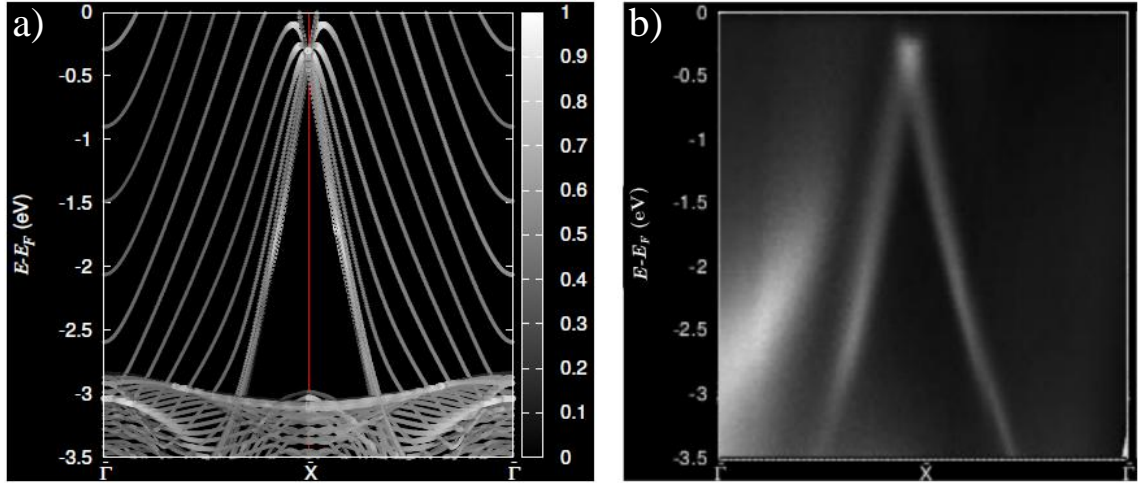


**Figure 5.6:** (a) Calculated band structure of bare Ag(001) at the high symmetry point  $\bar{X}$  performed by the group of Prof. Shobhana Narasimhan *et al.* [120] (b) Corresponding experimental ARPES data from our measurements on Ag(001) surface.

We have performed the ab-initio DFT calculations in corroboration with the group of Prof. Shobhana Narasimhan, JNCASR, Bangalore. The details of the calculations and complete results can be found in the Ph. D thesis of Sananda Biswas [120]. Here, we are only showing some of the calculational results for direct comparison with our experimental ARPES data. The calculated band structures of bare Ag(001) surface is shown in figure 5.6 (a) with the experimental data in figure 5.6 (b) along high symmetry direction  $\bar{\Gamma}-\bar{X}-\bar{\Gamma}$ . The gray scale represents the amount of projection from the atoms of these layers; while ‘white’ color represents the bands with highest projection, ‘black’ color represents the bands with zero projection. For this calculation, they have used the  $(1 \times 1)$  unit cell of Ag(001), and no band unfolding was required. The calculated band structure is in good agreement with our ARPES data obtained for bare Ag(001) surface. As we discussed in Chapter 4, the lowest energy configuration of the system is found to be 1 Ag/1 Cr/Ag(001) where the ML Cr was buried under a ML of Ag layer. The valence band dispersions of this system was calculated and is shown in figure 3.7 (a) along with the second derivative of experimental ARPES data for the 1 ML of Cr grown on Ag(001) at 428 K. Here, the

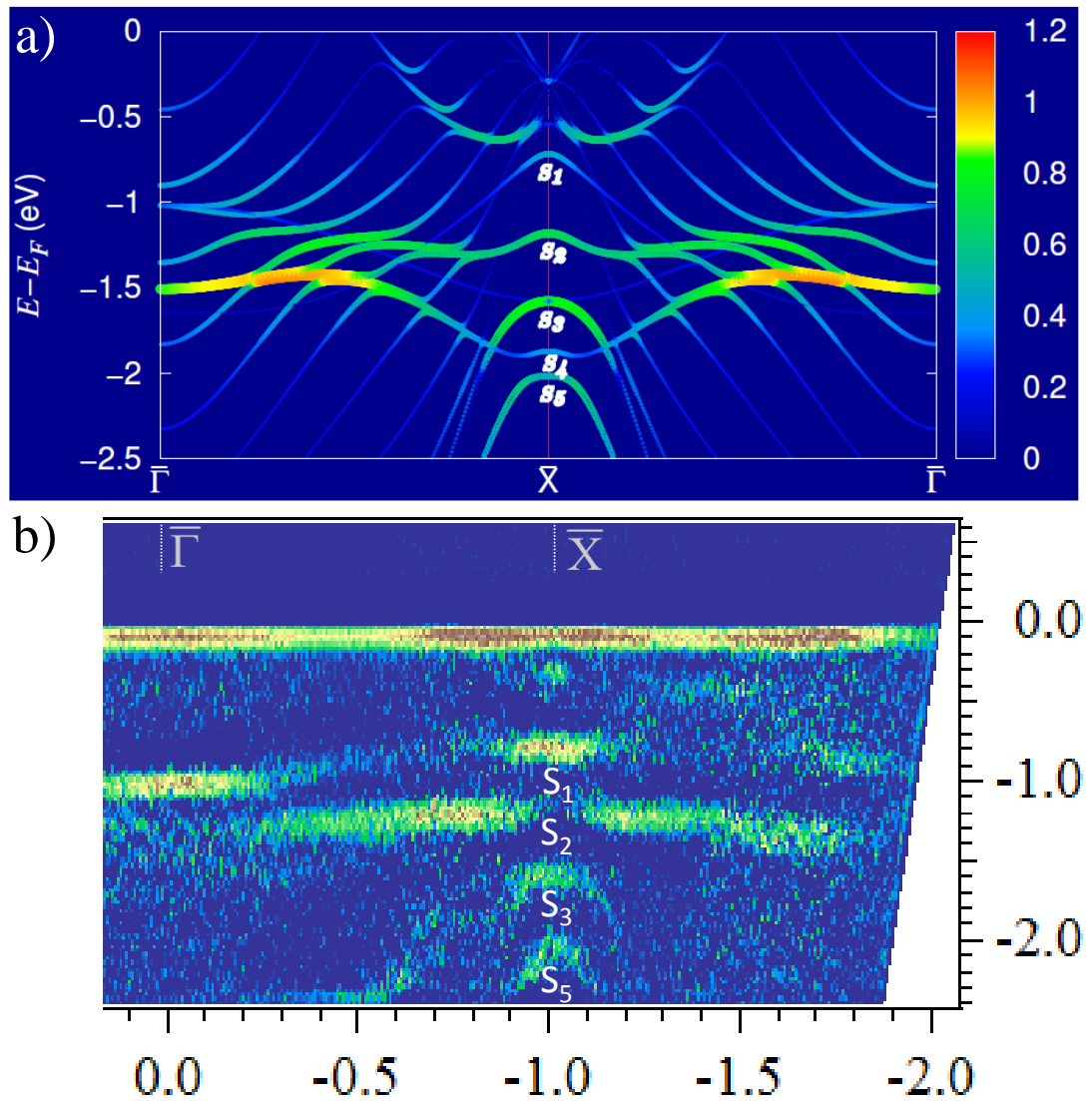


**Figure 5.7:** (a) Calculated band structure for 1 Ag/1 Cr/Ag(001) performed by the group of Prof. Shobhana Narasimhan *et al.* [120] (b) Experimental band structure along  $\bar{\Gamma}-\bar{X}$ .

color scale represents the amount of projection of the atomic states corresponding to the states of the top two layers of the slab, (i.e., the segregated Ag atoms and the second layer Cr atoms) onto the unfolded bands. The ‘red’ color represents the bands with highest projection, while the ‘dark blue’ color represents the bands with zero projection. The majority and minority bands are found to be degenerate in the entire energy range considered here. It was found that the band structure gets modified significantly and additional states appear in the Ag *sp* band region due to the presence of Cr. As shown in figure 5.7 (a), these states are denoted as S1, S2, S3, S4 and S5, with band edges ( $E - E_F$ ) at -0.72 eV, -1.18 eV, -1.58 eV, -1.87 eV and -2.02 eV, respectively. It is clear from the comparison between the calculated and the experimental data in figure 5.7 that there is a reasonable agreement between them. Even though there are differences in the exact binding energy positions as well as on the precise nature of the dispersions, but there is an overall qualitative agreement between them. In figure 5.7, we are showing the second derivative of the data for a comparison of the dispersions, though for the intensity comparison has to be made between the raw experimental ARPES data and calculations. The intensity of S<sub>1</sub> appears to be very high in the experimental data [see figure 3.2 (d)]; however, the calculations only show a weak intensity structure in comparison. Upon taking into account the projections from the Ag layers which are below the Cr layer, no change was observed in the intensity of S<sub>1</sub>. In fact, S<sub>1</sub> is found to originate primarily from the Cr atoms with Cr1  $3d_{x^2-y^2}$  orbital symmetry. However, it is found that the calculated dispersions of the S1 states are found to disperse upward towards the  $E_F$  and eventually crossing the  $E_F$ . But no such behavior was found for the experimental bands, which in fact shows a band gap of about 0.8 eV below  $E_F$  without any states crossing the  $E_F$ . This will be the subject of a future investigation. For both the majority and minority spins, it was found that all the surface states are two-fold degenerate states, except for S<sub>3</sub>, which is a 4-fold degenerate state. For the

other states (S2, S3 S4 and S5), there is a general agreement with the experimental dispersions.

From the charge density calculations [120], we find that the state S1 mainly originates from the Cr1  $3d_{x^2-y^2}$ , the state S2 mainly originates from the Cr1  $3d_{z^2}$  and Cr2  $3d_{xy}$ , S3 mainly originates from the Cr1  $3d_{yz}$ , S4 mainly originates from the Cr1  $3d_{z^2}$  and S5 mainly originates from the Cr1  $3d_{xy}$ .

In general, the *ab initio* calculations of the 1 Ag/1Cr/Ag(001) describes the experimental band dispersions reasonably well even though there are some quantitative differences between them which need to be investigated in detail. As we have already discussed, the observed band topology is incompatible with paramagnetic or ferromagnetic phase of monolayer Cr. Rather, the band dispersion matches well with a  $c(2\times 2)$  translational symmetry; compatible with the observation of LEED  $(1/2, 1/2)$  spots for low energy electrons. Structural effects including reconstructions, periodic lattice distortion or charge density waves are incompatible with the observed LEED since any distortion would produce strong extra spots or diffraction pattern. Thus, we are left with a magnetic stabilization mechanism. The small dispersion of the bands, their low band-width, creation of band gap near Fermi level and most importantly compatibility with antiferromagnetic band calculations, along with the presence of LEED half-order spots favor the stabilization of a Cr overlayer on Ag(001) through antiferromagnetic in-plane interaction of the enhanced magnetic moments.

### 5.2.3 Valence band: Cr coverage dependence

Interesting results were found when ARPES studies were performed as a function of Cr coverage dependence. As we already discussed in chapter 3 that a direct deposition is a must for the growth of antiferromagnetically ordered Cr domains on Ag(001) at submonolayer range. We have deposited different Cr coverages on Ag(001) in single step (in direct deposition mode) while the growth temperature was

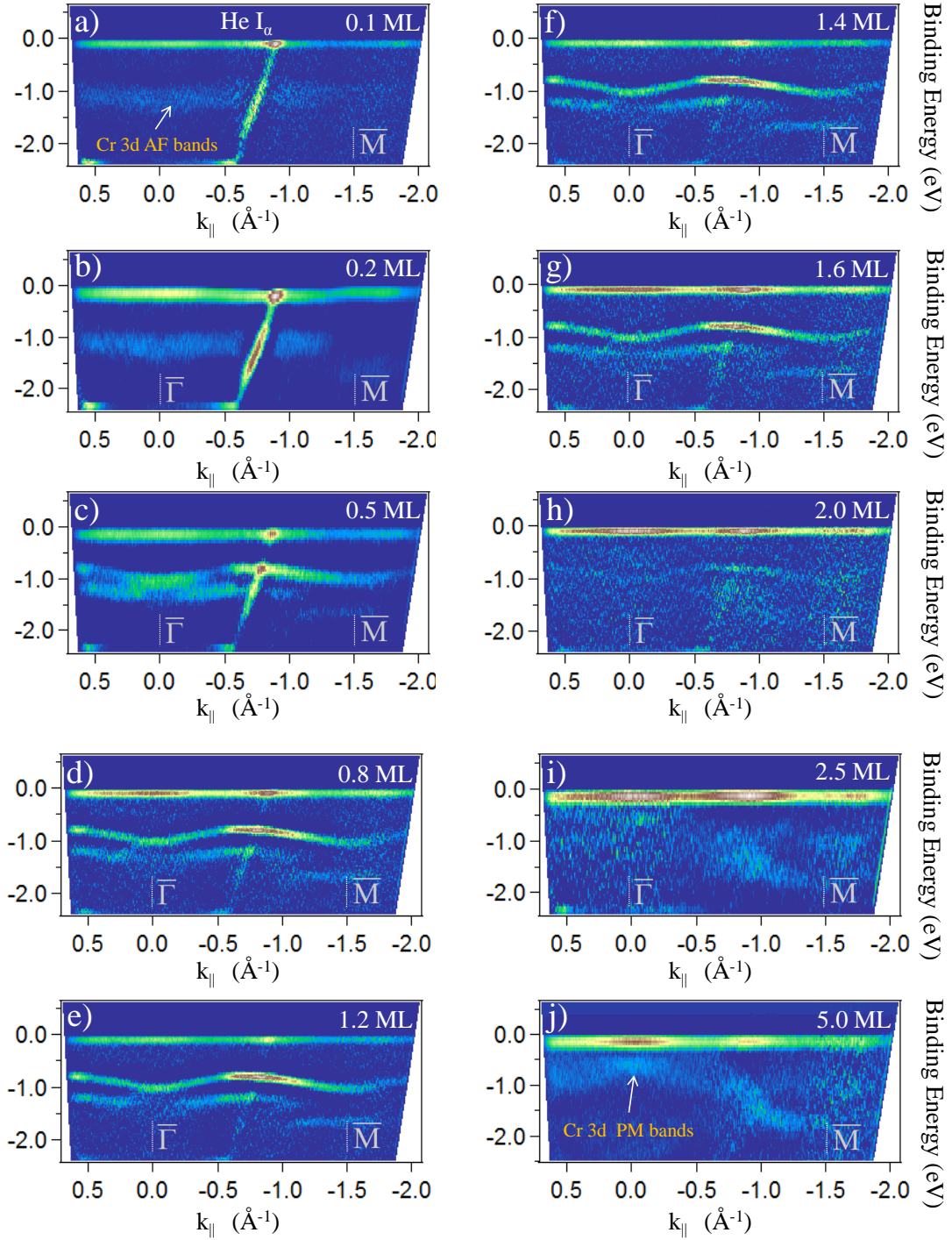


**Figure 5.8:** Second derivative of experimental ARPES data at different Cr coverage: (a) 0.1 ML. (b) 0.2 ML. (c) 0.5 ML. (d) 0.8 ML. (e) 1.2 ML. (f) 1.4 ML. (g) 1.6 ML. (h) 2 ML. (i) 2.5 ML. (j) 5 ML. Each film was deposited directly on Ag(001) crystal kept at 428 K. Band structure along  $\bar{\Gamma}$ - $\bar{M}$ . Photon source He I $_{\alpha}$ . ( $\hbar\omega = 21.2$  eV). The antiferromagnetic Cr 3d valence band structure is visible from 0.1 ML; Intensity of the AF bands is highest at 1.2 ML. The band structure changes from antiferromagnetic to paramagnetic from coverage greater than 2 ML.

maintained at 428 K for each case. The films were studied under LEED to check the presence of  $c(2 \times 2)$   $(1/2, 1/2)$  spots everytime. The intensity behavior of these ‘half-order’ spots at different Cr coverages were already discussed in detail in chapter 4 of this thesis. Intensity of Cr  $3d$  antiferromagnetic valence band at  $\bar{M}$  symmetry point was also discussed in this context. Though the details of band dispersion, band intensity at different  $k_{\parallel}$  values, bandwidth of the antiferromagnetic features and their resolution were still unexplored; which we are going to discuss here in detail. In figure 5.8, the experimental ARPES data of the Cr  $3d$  valence bands have been shown along  $\bar{\Sigma}(\bar{\Gamma}-\bar{M})$  direction of the SBZ for different Cr coverages. However, weak band intensities are not clear in the raw data, therefore second derivative of each data has been presented for each case to visualize the transition of valence electronic states from antiferromagnetic to paramagnetic nature. Upon deposition of very tiny amount of Cr equivalent to 0.1 ML, we observe a very faint band close to 1 eV binding energy position having a bandwidth of 0.7 eV [figure 3.8 (a)]. Intensity of this broad feature gets stronger upon direct deposition of 0.2 ML Cr [figure 3.8 (b)]. This band appears to be almost flat; it has very small dispersion though. Upon deposition of 0.5 ML [figure 3.8 (c)], this band resolves into two separate, closely lying bands at  $\bar{\Gamma}$  (at 1.05 and 1.4 eV binding energy positions) and their dispersion becomes more prominent showing symmetry between  $\bar{\Gamma}$  and  $\bar{M}$  points. A faint intensity at higher binding energy position (1.7 eV) is also visible at  $\bar{M}$ . The characteristic of the band now appear to be same with the antiferromagnetic Cr  $3d$  band structure. Interestingly, antiferromagnetic half-order spots in LEED, though broad and faint, were visible from this stage only. At the very low coverages of 0.1 and 0.2 ML Cr over Ag(001), half orders were not distinguishable due to their very weak intensity and presence of high intensity integer order spots, though the valence band structure reveals their antiferromagnetic nature (see chapter 4). From 0.8 to 1.6 ML [figure 3.8 (d) to 3.8 (g)], the antiferromagnetic Cr  $3d$  valence band structure is distinctly visible with the presence of all the three  $[\bar{\Gamma}_5, \bar{\Gamma}_1$  and  $\bar{\Gamma}_3]$  bands. The maximum average

band intensity appears at 1.2 ML coverage, whereas the antiferromagnetic band intensity gradually diminishes upon exceeding this optimum Cr coverage. For higher Cr coverages above 2 ML, the experimental band dispersions are found to match with that of the paramagnetic state rather than the AF state. In fact, the 2 ML film [figure 3.8 (h)] shows a mixture of both antiferromagnetic and paramagnetic bands, where intensity of both features are weak. The only state  $\bar{\Gamma}_5$  is present faintly, since it is the strongest state of the antiferromagnetic band structure. The paramagnetic band structure becomes more prominent at 2.5 ML coverage [figure 3.8 (i)]; states are visible at  $E_F$  for normal emission ( $\bar{\Gamma}$  position) revealing the metallic nature of Cr film. In case of a 5 ML film [figure (j)], its valence band electronic structure is almost similar to that of the bulk Cr(001) band structure.

#### 5.2.4 Valence band: Growth temperature dependence

In this section, we discuss the valence band structure of monolayer Cr film deposited at 300 K and 428 K, and conclude about the growth modes and structures of the films under these two different growth conditions through comparative analysis of the experimental ARPES data. In figure 5.9, the valence band electronic structures of 1 ML Cr films grown at RT (300 K) [left column] and at elevated temperature (428 K) [right column] are shown along  $\bar{\Sigma}$  and  $\bar{\Delta}$  symmetry directions using He  $I_\alpha$  photons. All the data are represented by the 2D second derivative of the raw data for better visualization. When figure 5.9 (a) and (b) are compared, it leads to some interesting conclusions. Figure 5.9 (b) shows the antiferromagnetic band structure of monolayer Cr film (grown at 428 K) along  $\bar{\Gamma}$  to  $\bar{M}$ , the details of which has already been discussed in earlier sections. In figure 5.9 (a), which shows the Cr  $3d$  valence band structure of monolayer Cr grown at 300 K, faint antiferromagnetic features are visible. Intensity of the antiferromagnetic bands are very weak and the features are broad and not-so-well-resolved [similar to the case of figure 5.8 (a) or (b)]. However,

a strong band is visible near the Fermi level (at 0.5 eV) close to  $\bar{\Gamma}$  position. This band crosses the Fermi level reminding of the metallic nature of the Cr film. The band structure indicates that Cr film deposited at RT is mostly of paramagnetic nature. As we discussed in earlier chapters, Cr deposited at RT forms bi or multilayer islands on Ag(001). These epitaxial  $p(1 \times 1)$  bi or multilayer domains are of paramagnetic nature which is reflected in the presence of bands crossing the  $E_F$ . Moreover, among the multilayer islands, the presence of few monolayer Cr  $c(2 \times 2)$  platelets can not be ruled out. These tiny monolayer domains under Ag layer has 2D antiferromagnetic arrangement of the Cr moments. As the effective area of these monolayer platelets are significantly smaller and have short range in-plane magnetic order, very weak intensity of the antiferromagnetic bands are observed in the ARPES of monolayer Cr deposited at RT. It is worthwhile to remember that no magnetic ‘half orders’ were visible in case of the RT deposited film as we have already shown in the earlier chapters. Hence it may be conclude that at RT deposition, the monolayer Cr film is composed of bigger multilayer epitaxial Cr domains with paramagnetic ordering and a few monolayer Cr domains covered by which have the AF ordering. Comparison between figure 5.9 (c) and (d), where band structure is presented along  $\bar{\Gamma}$  to  $\bar{X}$ , also indicate to the same conclusion.

Our observations are in agreement with valence band studies by Krembel *et al.* [115,132]. They reported that at lower temperature (100 K) the growth of Cr on Ag(001) is random with very poor crystalline order, which results in non-dispersive and faint Cr  $3d$  bands. The crystalline disorder of Cr growth at low temperature was also supported by the surface x-ray diffraction studies by Steadman *et al.* [91]. On the other hand, the good quality crystalline order of monolayer Cr at elevated temperature (428 K) was reported by both groups. Here, from our experimental ARPES data, we show that at an intermediate temperature 300 K the growth quality is moderate, having a mixture of both multilayer and monolayer domains.

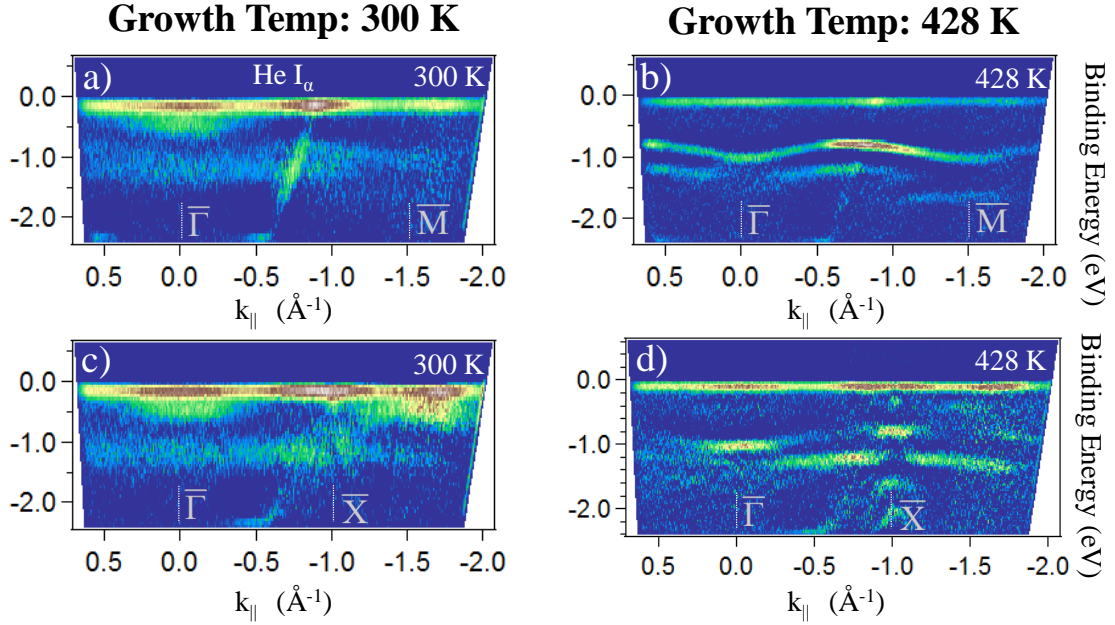


**Figure 5.9:** ARPES data along  $\bar{\Gamma}$ - $\bar{M}$  for 1 ML Cr film deposited at (a) 300 K (b) 428 K. Along  $\bar{\Gamma}$ - $\bar{X}$  for 1 ML Cr film deposited at (c) 300 K (d) 428 K. Photon source He I $\alpha$ .

### 5.3 Core levels : X-ray photoemission studies

X-ray photoemission spectroscopic (XPS) studies were performed in UHV chamber on different Cr film coverages deposited on Ag(001). Monochromatic Al K $\alpha$  ( $\hbar\omega = 1486.6$  eV) x-ray source was used for this purpose. XPS studies were fruitful from the viewpoint of different aspects. It helped to quantify the monolayer Cr coverage on Ag(001) as a compatible tool to optimize the growth. Any Cr coverage deposited after the quartz microbalance calibration can be rechecked by the XPS intensity of Cr  $2p_{1/2}$  peak. We found, one layer equivalent Cr corresponds to a Cr  $2p_{1/2}$  to Ag  $3d$  signal-height ratio of 0.0153, according to our calibration (see chapter 2 for details). This was used to check the coverage of the Cr films deposited on Ag(001) and in all the cases, they were found to be very close to that obtained from the quartz microbalance.

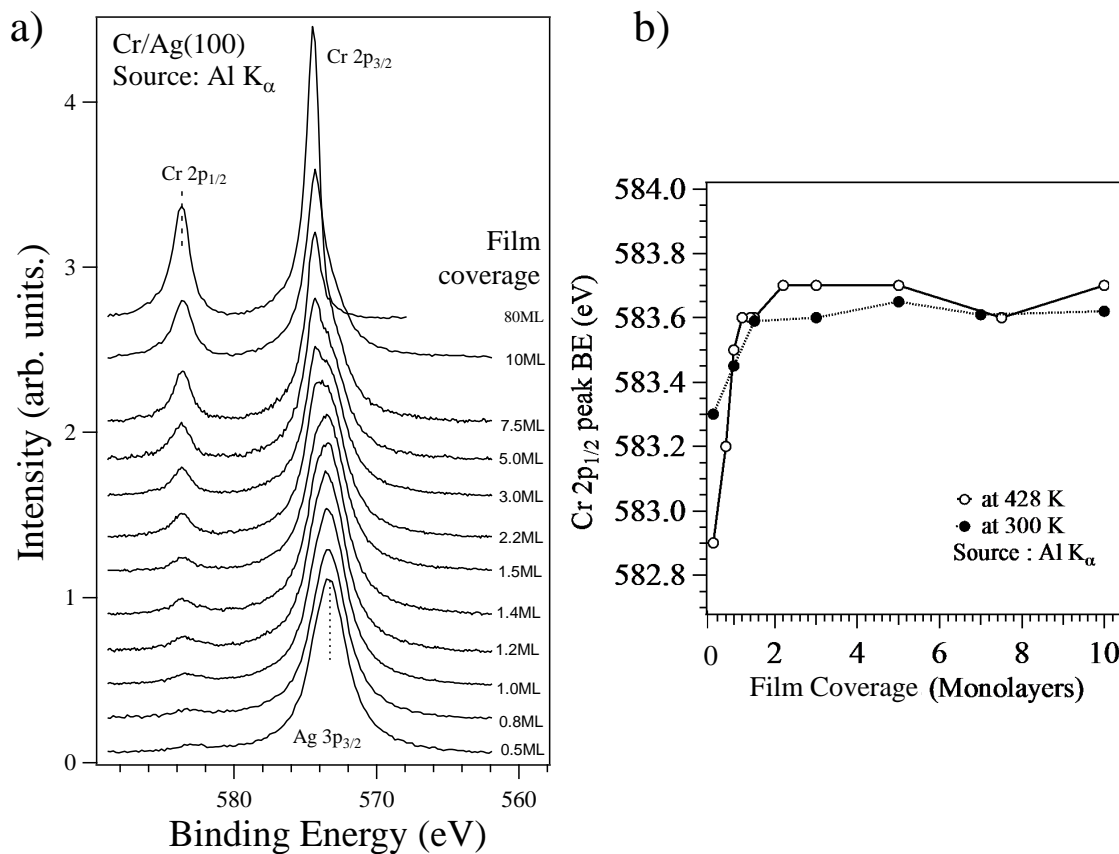


**Figure 5.10:** (a) X-ray photoemission spectral data of Cr  $2p$  peaks for different Cr coverages. (b) Binding energy shift of Cr  $2p_{1/2}$  at submonolayer coverage for deposition temperature 300 K and 428 K.

A more interesting phenomena observed in our XPS studies is the shifting of binding energy of Cr  $2p_{1/2}$  peak at the submonolayer film coverage. In figure 5.10 (a), Cr  $2p$  peaks were presented at different coverages for growth temperature 428 K. Though Cr  $2p_{3/2}$  peak has double intensity than the Cr  $2p_{1/2}$  peak, the higher intensity peak can not be used for comparison since the Ag  $3p_{3/2}$  of the substrate appears at similar binding energy position. In figure 5.10 (b), the binding energy position of Cr  $2p_{1/2}$  peak has been plotted as a function of film coverage for Cr films deposited at RT (300 K) and 428 K. The binding energy position of Cr  $2p_{1/2}$  peak of a 0.5 ML film is closer to its bulk value in case of RT (300 K) deposition compared to the elevated temperature (428 K) deposited film. This happens because of drastic change in Cr environment and coordination in the submonolayer range. At RT deposition, the Cr film starts to grow in multilayer island mode from its initial stage of growth. It has different chemical coordination than in monolayer Cr film which grows at 428 K deposition. This reconfirms the multilayer and monolayer growth mode of Cr film on Ag(001) at room temperature and elevated temperature respectively. Similar observations are reported by the group of Krembel *et al.* [132], but the binding energy shifting curve obtained by them differs from our observation. This may be due to the fact that monochromatic x-ray source, with much better resolution, has been used for our experimental purposes; whereas Krembel *et al.* has used non-monochromatic source. Therefore more superior quality of data is expected in our case.

## 5.4 Magnetism of Cr monolayer: Ising behavior of $c(2\times 2)$ 2D antiferromagnet

Within the Heisenberg model, which is the most general way to describe the magnetic moments of an ideal two-dimensional (2D) film, no long range order can exist at finite temperature [134]. However, the presence of uniaxial anisotropy as expected

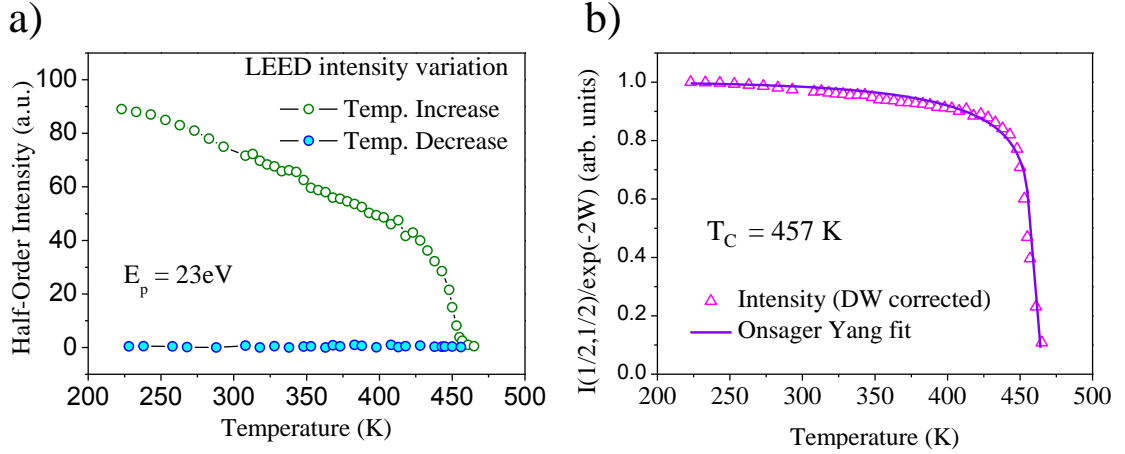


**Figure 5.11:** (a) Temperature dependence of  $(1/2, 1/2)$  spot intensity in LEED at beam energy 23 eV (raw data). (b) Data normalized by Debye-waller factor and fitted by Onsager-Yang equation.

in real samples, the system is predicted to become Ising-like near the transition temperature [135]. The transition between ferromagnetic and paramagnetic state has been studied for different ultrathin film systems; e.g. Co/Cu(111) [136], Fe/W(110) [137, 138], Fe/Ag(001) [139], Fe/Pd(001) [140] and V/Ag(001) [140] using different experimental techniques such as spin polarized low energy electron diffraction [137], electron capture microscopy [140], magneto optic Kerr effect [139] etc. For these films the magnetization  $M(T)$  is properly described by the asymptotic power law,  $M(T) \equiv (T_c - T)^\beta$ , where the value of the critical exponent is close to  $1/8$  [88]. In contrast, very few works have been devoted to the antiferromagnetic-paramagnetic transition for thin layers. As for these systems the net magnetization is equal to zero, and techniques generally used for ferromagnetic layers are not suitable. Low-energy electron diffraction (LEED) can be used to study the surface of antiferromagnetic systems or 2D antiferromagnetic layers such as 1 ML Cr/Ag(001). Indeed the small difference between scattering amplitudes at spin-up and spin-down atoms due to exchange scattering produces additional spots on the LEED diagram, whose intensity is proportional to  $\langle M_S \rangle^2$ , the square of the thermal average of the spin moment

component of the scattering atom [141]. In fact, this fact reflects in the existence of sharp but low intensity  $(1/2, 1/2)$  spots in our LEED data, as already shown and discussed. In this section we are going to show the temperature variation of the half-order intensity and fit the experimental data with the exact solution of the 2D Ising model given by Onsager and Yang [88].

In figure 5.11 (a), the average intensity of  $(1/2, 1/2)$  spots at 23 eV beam energy has been presented against temperature in case of 1.2 ML Cr film where we observe the maximum intensity for the half-order spots. Raw data has been presented, after considering background subtraction of each spot and calculating the average intensity of all the four ‘half-order’ spots. The sample was cooled down to 220 K with liquid nitrogen (reaching even lower temperature was not possible due to some technical difficulties during this particular experimental run) and then heated up with a slow ramp. Intensity of half-order spots falls down linearly upto 400 K; beyond that intensity jumps down exponentially to zero value at about 455 K sample temperature (open circles). Once the half-order intensity vanishes, they do not reappear back upon cooling down the sample to lower temperature, showing the irreversibility of the procedure (filled circles), as already discussed in Chapter 3 of this thesis. Generally, LEED spots intensity are known to decrease with increasing temperature because of the thermal motion of atoms. In single scattering theory, the beam intensity is reduced by the Debye-Waller factor,  $\exp(-2W)$ , where  $W$  is proportional to temperature  $T$ . The contribution of multiple scattering events is certainly strong in our present case, as data are taken at low incident energy (23 eV), where the superstructure is the most visible. However, the experiment has shown that even in the presence of multiple scattering, LEED spot intensities usually closely follow a simple temperature dependence in the form,  $I = I_0 \exp(-\alpha T)$ , but the dependence of  $\alpha$  on spot indices and incident energy is not the one expected from simple Debye-Waller theory. The Debye-Waller factor has been extracted using the linear part of the  $\ln[I(1/2,1/2)]$  curve and our raw data has been normalized by this

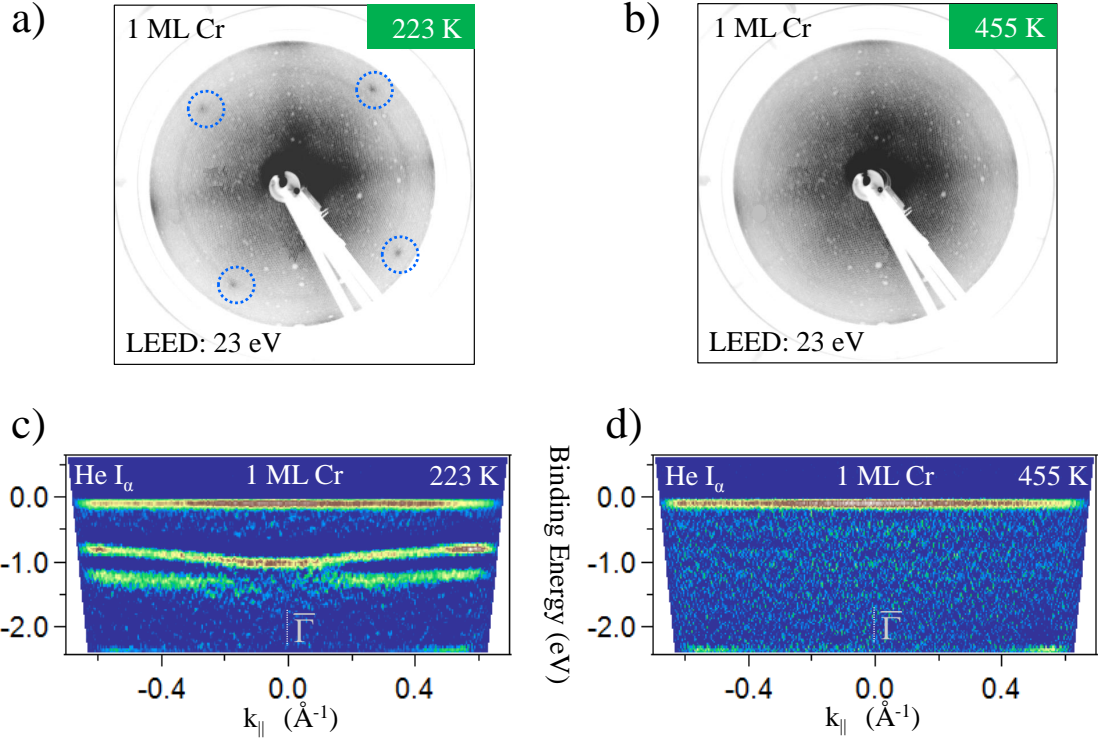


**Figure 5.12:** LEED  $(1/2, 1/2)$  spots of monolayer Cr film at beam energy 23 eV for sample temperature (a) 223 K (b) 455 K. ARPES data at  $\bar{\Gamma}$  position, sample temperature (c) 223 K, high intensity antiferromagnetic Cr  $3d$  bands visible. (d) 455 K, antiferromagnetic bands vanished.

factor to obtain the temperature dependence of  $\langle M_S \rangle^2$  only. This data has been plotted in figure 5.11 (b). The data has been fitted with the solution of 2D Ising model given by Onsager [142] and Yang [143] for the sublattice magnetization:

$$\langle M_S \rangle = (1 - 1/[\sinh(\ln(1 + \sqrt{2})T_c/T)]^4)^{0.125} \quad (5.1)$$

The magnitude of transition temperature obtained from our fitting is  $T_c = 457$  K. It can be seen that the 2D Ising model provides a good description of the magnetic order of the Cr 2D islands for  $220 \text{ K} < T < 456 \text{ K}$ , i.e., for  $T/T_c$  ranging between 0.48 and 0.998 [88].

In figure 5.12 (a), a LEED image of 1 ML Cr film is shown at 223 K corresponding to the figure 5.11 (a) where strong intensity of half orders is visible, LEED image

shown in figure 5.12 (b) is collected at sample temperature of 455 K where half-order intensity vanishes completely. One may wonder if the  $c(2\times 2)$  intensity evolution could be explained by the formation of an ordered Cr-Ag surface alloy. However in such a scenario, during the annealing procedure, the LEED superstructure intensity is expected initially to grow with temperature, then to reach a maximum, and finally decrease with further increase in temperature because of the destruction of the ordered Cr-Ag surface alloy domains. In fact as shown in figure 5.11 (a), spot intensity decreases continuously with increasing temperature, so the data cannot be interpreted in terms of formation of a  $c(2\times 2)$  Cr-Ag surface alloy. Again, our ARPES data, where existence of antiferromagnetic Cr  $3d$  valence bands are visible, is a direct proof of antiferromagnetic phase persistent in the film. In figure 5.12 (c), intense valence band features at  $\bar{\Gamma}$  position are shown at the low temperature of 223 K in support with the existence of half-order spots in LEED in figure 5.12 (a). The antiferromagnetic bands disappear [figure 5.12 (d)] at 455 K when the half orders also disappear.

## 5.5 Summary

The details of two-dimensional antiferromagnetic valence bands structure of monolayer Cr film along different symmetry directions has been discussed in this chapter. The experimental ARPES data has been established in support with the DFT calculations. The coverage dependence of Cr layer as well as the growth temperature dependence of monolayer Cr has been illustrated. The Cr  $2p$  core levels have been probed by XPS studies and the monolayer and multilayer growth modes at different temperatures have been concluded. The variation of LEED half-order  $(1/2, 1/2)$  intensity with temperature has been studied and the data was fitted with Ising model solution to find out the critical transition temperature ( $T_c$ ) of this 2D Ising antiferromagnet.

## **Growth of NiO film on Ag(001): characterization of electronic structure**

### **6.1 Introduction**

The interest in the research of oxide surfaces and thin films are still steadily growing since decades due to their challenging fundamental properties and to their actual and potential applications in catalytic systems, chemical sensors, electronic and magnetic devices, and functional and aesthetic coatings. Special efforts have been directed at the study of ultrathin oxide films. Such two-dimensional systems are emerging as important new materials where the relevant phenomena are induced by the extreme vertical confinement, and new phases and structures are stabilized, which cannot be obtained in the bulk form. Last but not least, the possible use of thin oxide films as model systems to substitute for bulk oxides has been shown to be very appealing. Critical properties basically depend on the reduced dimensionality, as well as on the stoichiometry, defects and morphology of the films, on the extent of the crystalline order, and on the sharpness of the interfaces between film and substrate or between different films in multilayers, which are to a great extent determined by the preparation method. Therefore a main driving force in the development of oxide materials in the form of ultrathin films has been the progressive improvement of the fabrication procedures.

Transition metal oxides constitute probably one of the most interesting classes of solids, exhibiting a variety of structures and properties. The nature of metal-oxygen bonding can vary between nearly ionic to highly covalent or metallic. The unusual properties of transition metal oxides are clearly due to the unique nature of the outer  $d$ -electrons. Late  $3d$  transition-metal oxides are arguably among the most intensely studied compounds in condensed matter physics today. This is so not only because they have shown great promise on a wide range of important applications, but also because they have for a long time challenged our ability to construct a truly many-body theory of the solid state. First of all, they display a wide range of ground states, with their electrical and magnetic properties ranging from insulating, semiconducting, metallic, superconducting, ferromagnetic, ferrimagnetic and antiferromagnetic. They show dramatic changes in their physical properties as a sensitive function of temperature, pressure and stoichiometry. Secondly, they include the Mott-Hubbard insulators, in which a large on-site Coulomb repulsion suppresses charge fluctuations and prevents metallicity, even in materials with an odd number of electrons per unit cell. Finally, they comprise the high-temperature superconductors which are closely related to the antiferromagnetic Mott-Hubbard insulators.

The late  $3d$  transition metal monoxides (MnO, FeO, CoO, NiO) are particularly important thanks to their appealing properties such as relatively high Néel temperature, the chemical and mechanical stability, the low lattice mismatch with respect to the corresponding FM metals and their alloys, and their large electronic gap. For example Nickel Oxide (NiO), though it has relatively simpler rocksalt (NaCl) structure, its optical properties, electronic structure and mainly the complicated magnetic structure have drawn a lot of scientific studies on this simple-oxide system since few decades. Above its Néel temperature  $T_N$ , NiO has a rocksalt crystallographic structure. Below  $T_N$ , magnetostrictive effects leads the NiO crystal structure to undergo a rhombohedral deformation. If we make the simplifying assumption of NiO being an ionic crystal, it has the formula  $\text{Ni}^{2+} \text{O}^{2-}$ . The Ni cations are then in a

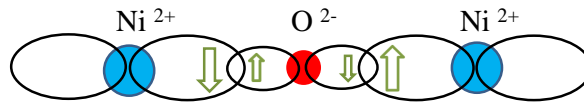


**Figure 6.1:** superexchange interaction in NiO.

$3d^8$  ground state. Since NiO is an insulator, all itinerant or direct interactions to convey a magnetic order are weak, leaving as only effective mechanism the so-called superexchange, i.e. the hopping of electrons between two cations *via* a ligand bond. The formation of a covalent bond with a cation on either side of the oxygen atom leads to antiparallel spin alignment of the neighboring cations (see figure 6.1).

Transition metal (TM) monoxides belong to a wide class of materials where the electronic properties are strongly affected by electron-electron correlation effects, and where the single particle approximation fails in describing their electronic structure [144, 145]. The most obvious problem in the description of late TM oxides is that they have a partially filled  $d$  band but are nonetheless insulators with large gaps. For example, MnO, FeO, CoO and NiO have band gaps 3.6, 2.4, 3.0 and 4.3 eV respectively. In particular, NiO has been considered the prototypical representative of this class of strongly correlated materials since the publication of Mott's seminal work [146] and has been extensively studied for many years [147]. In fact, NiO is the first material where Neutron diffraction studies were performed for antiferromagnetic characterization; and many studies are still performed on NiO now-a-days [148].

Interest in thin NiO films is mainly motivated by catalytic applications (where the oxide serves either as a catalytic material or as an inert support for catalytic metal clusters [149, 150]) and by the potential use in magnetic nano-devices (where the antiferromagnetic NiO layers are used to pin the magnetization of ferromagnetic layers [151]), as well as by the key role played by this material in the fundamental studies of electron correlation in solids [151, 152]. Also NiO thin films on metallic substrates provide a possible way out to dramatic charging problems which severely

hamper the study of this insulator by electron spectroscopy and other surface science techniques based on electrically charged probes. For this reason, in recent years there has been an increasing interest in the preparation and characterization of metal supported oxide films which are by now widely employed as model systems to study the surface properties of highly insulating oxides [153–155]. In fact, in recent years, the physical properties of two-dimensional metal-oxide epilayers on metal substrates have become a topic of great interest [156–160]. Films of a few monolayers can be deposited epitaxially on metal substrates by ultrahigh vacuum techniques, yielding reproducible and well-characterized systems. It has been shown that the energy gap ( $E_g$ ) of the oxide, in the oxide/metal system, can be modulated by the film thickness [161–163]. The demonstrated ability to control film thickness and hence the band gap represents therefore a new technological opportunity for band gap engineering. It has also been argued that the presence of the metal substrate can alter significantly the electronic structure of the oxide and influence its chemical properties, with a prospective range of important applications [162]. In fact, many studies have been performed to investigate the magnetic structure of NiO films deposited on metallic substrates whereas studies on the electronic structure of this metal oxide insulator film is rare which opened up scopes to reinvestigate the growth and electronic properties of this simple mono-oxide film which is the main focus of this chapter.

## 6.2 Background works on NiO thin film growth

Many chemical and physical routes are already reported for the preparation of NiO films. All these track leads to formation of polycrystalline, amorphous and powder NiO samples. Chemical vapor deposition method, pulsed laser deposition, sol-gel techniques and physical method like annealing Ni foil in oxygen environment are very good ways to prepare NiO films of moderate purity. The advent of ultrahigh vacuum

deposition technique using molecular beam epitaxy (MBE) assured more controlled deposition with better accuracy of nickel to oxygen stoichiometry and ordered NiO film growth. The applications of metal oxide ultrathin films in the field of electronics prompted the demand of more controlled growth of oxide films. A very strong impact comes from the field of (nano) electronics where, on the one hand, oxide films are necessary as a dielectric material, e.g. to fabricate metal-oxide semiconductor field-effect-transistors (MOS-FET). Here, the rapidly decreasing size of integrated circuits is a challenging problem. On the other hand, oxide films serve as tunneling barriers for many different nano electronic devices. For these applications, the oxide films have to be extremely thin (in the thickness range of 1 nm) to guarantee sufficiently large tunneling currents at low applied voltages. Nowadays, much attention is paid to the combination of the tunneling effect with ferromagnetic materials. Here, the effect of tunneling magneto resistance (TMR) plays an important role for magnetic storage devices since the spin-dependent tunneling transport through oxide barriers can be used as a sensor to detect the orientation of the magnetization of both electrodes. In addition, for instance, (antiferromagnetic) NiO films are used as spin valves to pin the magnetization of ferromagnetic films [151]. Bauer [96] pointed to the important role of surface and interface energies for the wetting or non-wetting behavior of epitaxial films. Considering the surface and interface energies of oxide-metal systems, one expects that oxide films wet metallic substrates since, due to their ionic binding, the surface energy of oxides is very often lower than the surface energy of metals. Furthermore, the atomic structure (lattice mismatch, crystal structure) has to be taken into account. Large lattice mismatch produce increasingly large stress in pseudomorphic films. Thus, dislocations are introduced for films thicker than a critical thickness to relax the film structure and to minimize the total energy. The critical thickness depends on the lattice mismatch and elastic properties of both the film and the substrate. Therefore, it is advantageous to select oxide-metal systems with lattice mismatch as small as possible and surface orientations which coincide

with the non-polar surfaces of the oxide film. In addition, however, kinetic effects may lead to the formation of inhomogeneous films, especially for deposition at low temperatures. The growth of NiO films on Ag(001) has been studied intensively by the group of Neddermeyer [164–166]. NiO films are formed by reactive growth and show high quality on Ag(001) probed by high intensity ordered Low Energy Electron Diffraction (LEED) spots and photoemission studies. The structure and morphology of NiO films on the Ag(001) substrate has already been investigated by many surface sensitive techniques such as LEED and Auger as well as photoelectron electron diffraction [167], scanning tunneling microscopy (STM) [168,169], spot profile analysis (SPA)-LEED [170], primary-beam diffraction-modulated electron emission (PDMEE) [171], and specular x-ray reflectivity [172]. NiO is known to grow in layer by layer fashion in an initially pseudomorphic, tetragonally distorted rocksalt phase. As the thickness of the oxide film increases, the formation of mosaics on the film surface has been observed and ascribed to the process of relaxation of the misfit strain. A significant substrate disruption was observed by STM studies. The effect of different oxygen dosage on the on the structure and composition of ultrathin NiO layers grown on Ag(001) was investigated by C. Giovanardi *et al.* [173]. They confirmed from their LEED, photoemission and PDMEE studies that the growth of structural  $1\times 2$  phases at low oxygen pressure whereas regular  $1\times 1$  phase forms at moderate pressure. Reflection High Energy Electron Diffraction (RHEED) experiments by Himba and Peacor [174] showed that  $\text{NO}_2$  is a better oxydizing reagent for the growth of NiO than regular molecular  $\text{O}_2$  source. Experiments of C. Giovanardi *et al.* [173] has shown the growth of monolayer NiO film on Ag(001) is quite smoother while atomic oxygen is used rather than molecular oxygen; a  $c(2\times 2)$  structural pattern was observed [175]. The drastically increasing interest in the (surface) properties of (bulk) oxides and ultrathin oxide films is demonstrated by the strongly increasing number of scientific publications in this field. One major motivation for this increasing interest in the growth and characterization of oxide films is the large variety of their applications.

For instance, excellent overviews on the epitaxial growth of ultrathin oxide films have been presented recently by Ventrice and Geisler [176] and Chambers [177]. The interfacial strain has been calculated by Netzer and his group [178] from SPA-LEED analysis for the case of NiO films deposited on Pd(001) where the lattice mismatch is 7.8%. Casassa *et al.* [179] has used ab-initio density functional theory to calculate structural, magnetic and electronic properties of NiO monolayer epitaxially grown on Ag(001). Giovanardi *et al.* [180] has deposited 3-20 ML NiO film on Ag(001) by reactive deposition to investigate the structure and morphology by LEED, STM and XPS studies. The geometric parameters of NiO film deposited on Ag(001) were determined by Lamberti *et al.* [181] using two different experimental techniques (PDMEE and Polarization dependent XAS) and *ab-initio* simulations. They claimed that NiO film grows with O on top of Ag and the oxide/metal interface distance is  $d = 2.3 \pm 0.1 \text{ \AA}$ .

There are much more studies on NiO bulk and many studies on NiO epitaxial thin films. However, there are far too less experimental electronic band structure studies, or ARPES studies. The only ARPES studies on the NiO single crystals has been by Shen *et al.* [182–184] in the early 90's and the electronic band structure of the system has not been further explored experimentally since then. The main reason has been the strong insulating nature and the strong charging effects on these compounds which prevented the detailed experiments. This problem can be solved by the growth of NiO thin films. Still, there has only been one study on the NiO film [185], which is not a detailed work. Thus, the motivation of our study has been to explore the electronic structure of the NiO thick films without any charging effects and compare it with the single crystal case as well as to study the effect of NiO film thickness on the electronic structure. Moreover, as the Néel temperature changes with the thickness of the film, the study of the electronic structure as a function of the thickness might enable us to understand how the AFM affects the electronic band structure of the NiO system.

## 6.3 Experimental Details:

### 6.3.1 Choice and preparation of the substrate

Epitaxy is the ordered growth of one crystalline layer upon a pre-existing crystalline surface, and the close lattice matching of overlayer and substrate is an important parameter to support epitaxial growth. In heteroepitaxy, i.e. the growth of one type of material on a different substrate material, perfect lattice matching is rarely encountered. The resulting lattice mismatch at the interface leads to strain in the overlayer [186] and defects in form of misfit dislocations to reduce this strain. Lattice strain influences the electronic structure of the material [187] and its chemical reactivity [188], whereas dislocations cause the loss of coherence of the lattice, reducing the mobility of charge carriers and thus are detrimental to the electrical transport properties. As NiO have lattice constant of 4.18 Å, a proper substrate must be chosen to reduce lattice mismatch and hence make the epitaxial quality better. MgO has lattice constant of 4.2 Å, which implies only 0.4% lattice mismatch with NiO indicating a good epitaxial quality growth. Studies are there where growth and characterization of NiO film on MgO has been reported [174, 189–191]. The insulating nature of NiO is a constraint for performing photoemission experiments on its bulk counterpart due to the sample charging problem. On the other hand, MgO is an wide band gap insulator itself; therefore deposition of NiO film on top of this strong insulator does not help from the viewpoint of charging problem. Moreover, consideration of surface free energy gives us a general idea that oxides has lower surface energy than metal. Hence, in case of deposition of oxide film on metal surface, the film will spread covering up all over the surface area of the metal reducing the probability of island formation. Pd(001) has notable lattice mismatch with NiO, 7.8% which shall produce significant strain at the interface affecting its physical as well as electronic structure [192]. On the other hand, Ag(001), the metal with face

centered cubic (fcc) unit cell, has bulk lattice parameter 4.09 Å, which indicates a 2% lattice mismatch with NiO. Also there is less probability for alloy formation of Ni with Ag at finite temperature, except at the vicinity of exact interface. Therefore Ag(001) may be chosen as a proper substrate for growth of NiO film for rigorous study with photoelectron spectroscopic experiments.

The Ag(001) single crystal from Mateck GmbH, Germany was cleaned through sputtering and annealing cycles. The polished crystal was bombarded by Ar<sup>+</sup> ion for 20 min with energy 0.7 keV,  $I_C$  (sample current) = 6.0 μA; where the Ar pressure was fixed at  $3 \times 10^{-6}$  mbar. The sputtering procedure was then followed by annealing at 673 K for 30 min. There was electron beam heating arrangement fitted in the PTS 1200 sample holder [Prevac sp. z.o.o. (Ltd.)], where a 2 Amp current was passed through a tungsten filament which was held at 500 Volt negative potential than the Ag(001) crystal which was grounded (at zero potential). The thermionic emitted electrons driven by the attractive potential towards the crystal hit the sample with sufficient kinetic energy to warm up the sample faster (electron emission current  $I_e = 6$  mA). The whole procedure of sputter and anneal was performed in the preparation chamber (base pressure:  $1 \times 10^{-10}$  mbar) which equipped with sputter gun and Low Energy Electron Diffraction (LEED) set up. Starting with a new Ag crystal, it takes about 10-12 of sputter and anneal cycles to prepare its surface such that a highly intense and sharp four fold  $p(1 \times 1)$  LEED pattern was observed. The crystal was then transferred to the analysis chamber to check for impurities on the surface under x-ray photoemission spectroscopy (XPS) survey scan and was confirmed to be clean.

Mounting of the crystal on the sample holder is another important factor to be taken care of before starting the substrate preparation procedure. The crystal was circular in our case and was mounted according to a particular crystallographic direction predetermined (by a notch) on the single crystal. Moreover, the flatness of the crystal surface was checked ex situ by a pointed laser beam reflection and to rectify any minor tilt or inclination of the sample surface before insertion into the

UHV system (or prep. chamber). A flat surface geometry is essential mainly for ARPES studies.

### 6.3.2 Calibration of Ni effusion cell

A Knudsen cell (from MBE Komponenten GmbH, Germany) with a BeO crucible mounted on it was used for evaporation of nickel. The K-cell was able to reach upto high temperature 2173 K by auto-controlled resistive heating. High purity (99.995% pure) Ni slugs (from Alpha Aesar) were put inside the crucible to melt them above the melting point of nickel (1726 K), such that the top surface of melted nickel inside the crucible becomes flat and maintain equal evaporation rate from all over the surface. The cell temperature was increased slowly to reach a temperature just higher than the Ni melting point and immediately cooled down back towards to lower temperature. After melting of nickel, the cell was calibrated for different Ni evaporation rates at different cell temperatures and stability of the evaporation rate at each temperature was confirmed. Cell temperature was measured by a type-C thermocouple attached with the BeO crucible within the cell. The evaporation rates were measured by quartz microbalance thickness monitor mounted on a Z-shift placed at the position of the sample. Different Ni evaporation rates at various cell temperatures are enlisted in table 4.1, below.

Cell Temperature (K)	Ni evaporation rate ( $\text{\AA}/\text{min}$ )
1543	0.13
1553	0.15
1563	0.18
1573	0.26
1623	0.5
1673	2.0
1723	6.0

**Table 6.1:** Ni evaporation rate at various temperatures of Knudsen cell

Choosing 1573 K as optimum evaporation temperature, different thickness of Ni film was grown on top of Ag(001) at room temperature (RT). The thickness of the film obtained from quartz microbalance thickness monitor was cross checked by XPS. In figure 6.2, XPS of Ni  $2p$  and Ag  $3d$  peaks are shown at different Ni film thickness. Figure 6.2 (a) shows the Ni  $2p_{3/2}$  peak for Ni film thickness 0.2, 1, 2, 3, 4, 6, 8 and 10 ML respectively. The Ni  $2p_{3/2}$  is visible at 853.2 eV; the Ni  $2p$  satellite at 6 eV higher binding energy position is also there. In figure 6.2 (b), the gradually decreasing intensities of Ag  $3d_{5/2}$  and  $3d_{3/2}$  are shown. Non-monochromatic Mg  $K_{\alpha}$  source (1253.7 eV) was used to probe core levels in all cases. Correction for x-ray satellite and also the shirley background subtraction was performed for each data. In figure 6.2 (c), both Ag  $3d$  and Ni  $2p$  peak intensities has been plotted against the Ni thickness in monolayers. The curves can be fitted by formula of type  $I^{\infty}(\text{Ni})(1-\exp(-d/\lambda))$  and  $I^{\infty}(\text{Ag})\exp(-d/\lambda)$ , where  $d$  is the film thickness and  $\lambda$  is the inelastic mean free path in Ni film. Film thickness was converted in to monolayer by considering  $1 \text{ ML Ni} = 1.77 \text{ \AA}$ .

### 6.3.3 Oxidizing Ni/Ag(001): LEED and XPS studies

In figure 6.3, the LEED patterns are shown for the case of bare Ag(001) crystal [figure 6.3 (a)] and Ni film deposited on it. For bare substrate, the  $p(1 \times 1)$  pattern is sharp and distinct. After deposition of 0.5 ML, the intensity of LEED spots decreases to less than 50% of its initial value as can be seen in figure 6.3 (b). Figure 6.3 (c) shows very faint, almost vanishing LEED spots after deposition of 1 ML Ni on top of Ag(001). No LEED pattern is visible after deposition of 2 ML Ni film. Even after deposition of higher film thickness, no LEED pattern appeared. The growth of Ni is not epitaxial on Ag(001) as may be confirmed from our LEED studies according to expectation where a significant lattice mismatch is there between Ni (bcc, l.c.  $3.55 \text{ \AA}$ ) and Ag (fcc, l.c.  $4.09 \text{ \AA}$ ) causing huge strain at the interface. Growth and structure

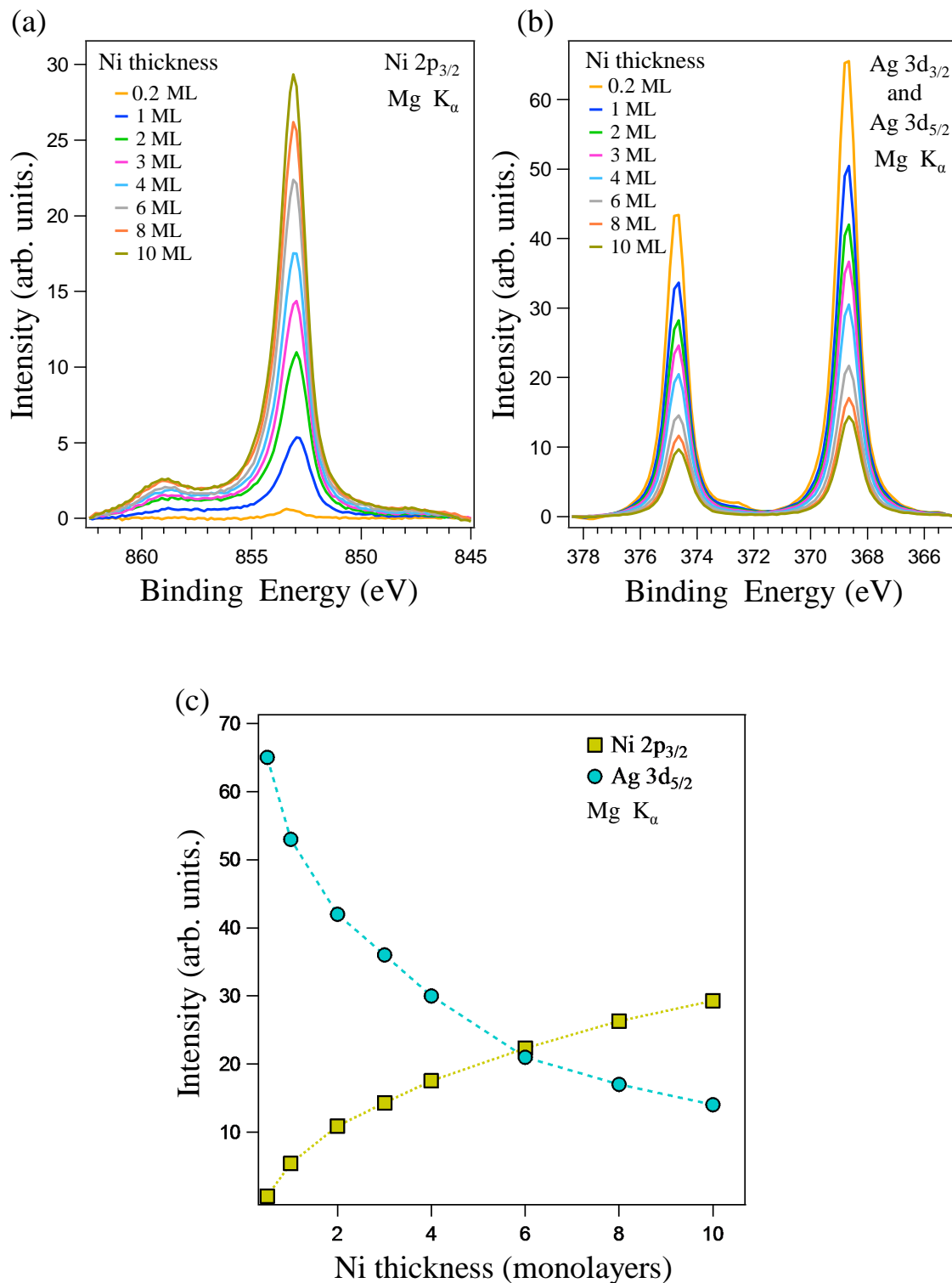


**Figure 6.2:** (a) XPS Ni  $2p_{3/2}$  peak intensity for deposition of different Ni thickness (in monolayers). (b) Intensity of Ag  $3d$  under deposition of various Ni film thickness. (c) The exponentially increasing Ni  $2p_{3/2}$  intensity and exponentially decaying Ag  $3d_{5/2}$  intensity are plotted against Ni monolayers.

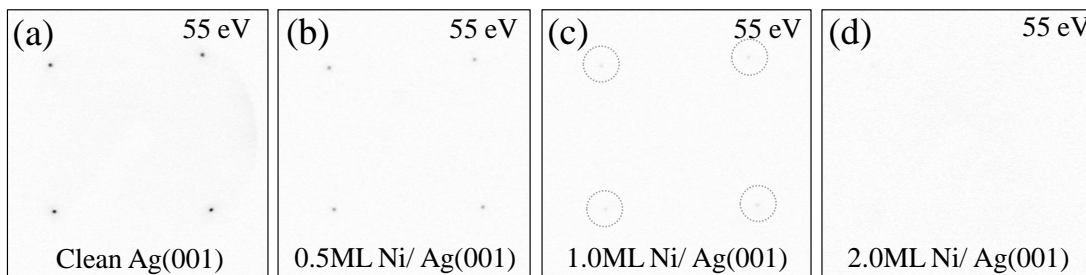


**Figure 6.3:** Low Energy Electron Diffraction pattern of (a) clean Ag(001) (b) 0.5 ML Ni/Ag(001) (c) 1 ML Ni/Ag(001), the spots have been encircled to indicate their positions (d) 2 ML Ni/Ag(001). Electron energy 55 eV.

of Ni on Ag(001) was studied by Caffio *et al.* [193]. Their STM images showed that Ni grows on Ag(001) forming three dimensional islands even for a deposition of 0.1 ML. Low energy ionic scattering (LEIS) spectra shows that Ni islands are almost completely covered by Ag. The non-epitaxial growth of Ni on Ag(001) was reported by them in accordance with our experimental observations.

After deposition of a 10 ML Ni film (from quartz microbalance calibration) on Ag(001), the film was exposed to molecular oxygen pressure  $5 \times 10^{-6}$  mbar for 30 min while the sample temperature was raised up to 473 K. A capillary mounted on a Z-shift was arranged inside preparation chamber to have a directed oxygen flow towards the sample surface and to maintain a higher local  $O_2$  pressure. At least the top Ni layers of the film are expected to be oxidized in this process and a NiO/Ni/Ag(001) superlattice should form. In fact, XPS studies performed on the sample shows that the Ni  $2p_{3/2}$  peak is shifted towards 1.7 eV higher binding energy in the NiO film as result of chemical shifting. Moreover, beside the main peak (denoted by ‘a’) few satellite peaks (b, c and d) also appear at higher binding energy position. In figure 6.4, the Ni  $2p_{3/2}$  peaks are shown both for Ni and NiO film. Earlier trials to form epitaxial NiO film on Ni(001) single crystals and films by oxygen adsorption was in vain as reported by different groups [194–196]. Our LEED observations also does not show any LEED pattern after oxidation of the Ni

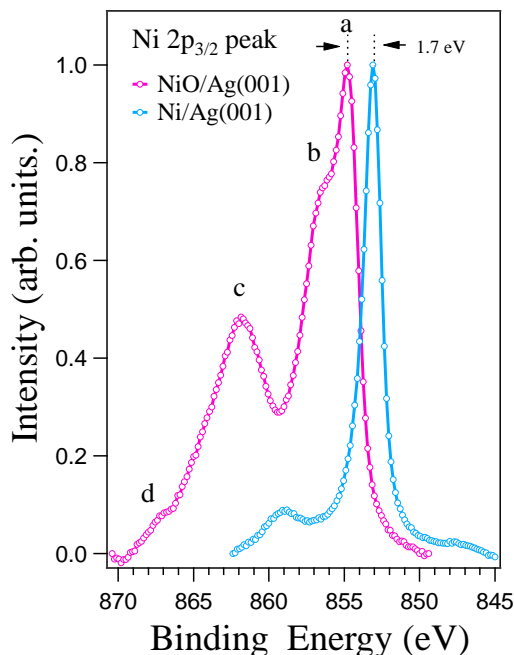


**Figure 6.4:** XPS Ni  $2p_{3/2}$  peaks for Ni and NiO film are shown. There is 1.7 eV chemical shift in the main line due to oxidation. Photon source: Mg  $K_{\alpha}$  (1253.7 eV)

film. Therefore epitaxial growth of NiO film on Ag(001) is not possible through this process.

#### 6.3.4 Epitaxial growth of NiO at different growth conditions

Deposition of Ni on Ag(001) in oxygen environment resulted in formation of epitaxial NiO film with good crystalline quality, as pre-claimed by many previous studies [161, 162, 164–166, 175]. Evaporation rate of nickel was kept below 0.2 Å/min. Nickel was deposited at various oxygen pressures within the preparation chamber, keeping the Ag(001) at RT as well as at different elevated temperatures. The duration of deposition to grow a desired oxide film thickness was calculated from the Ni deposition rate at quartz microbalance considering the surface density of Ni on NiO(001) film. The duration of growth of monolayer NiO film was supposed to be 1.4 times than

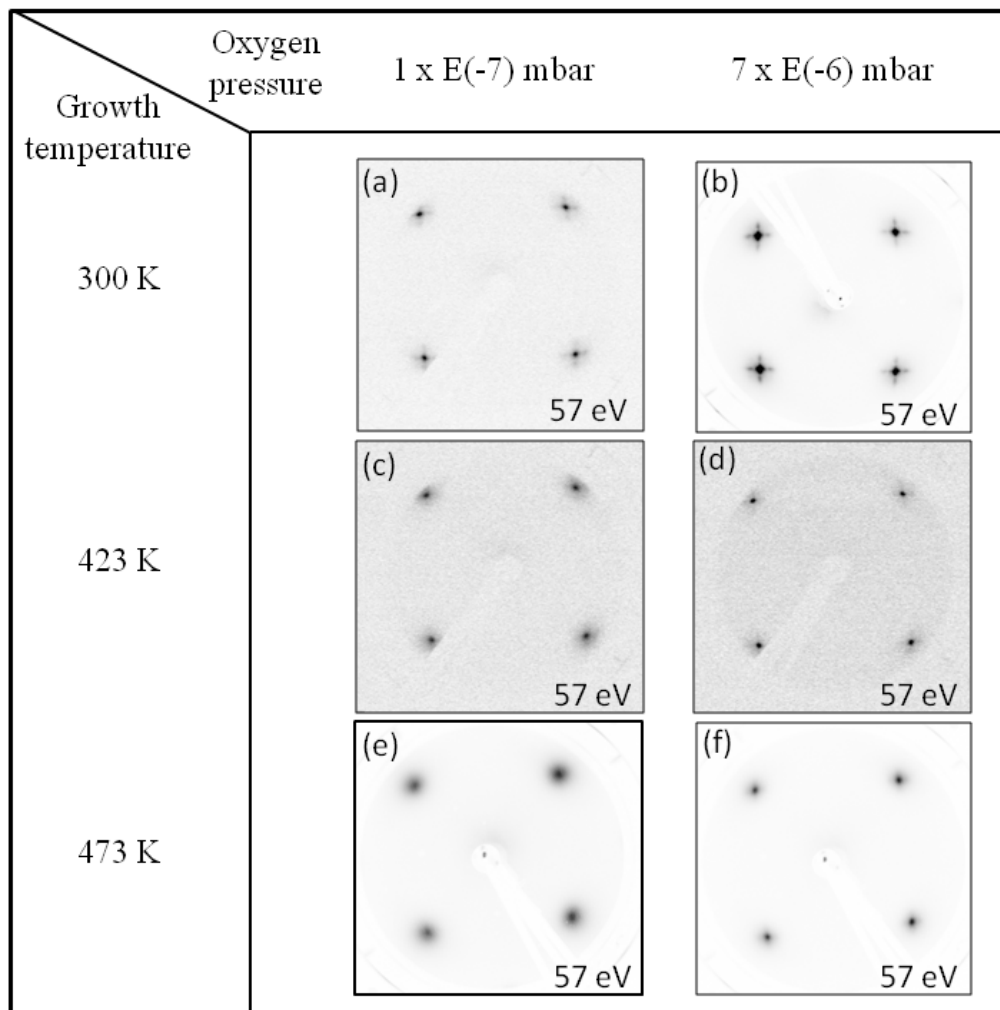


**Figure 6.5:**  $p(1 \times 1)$  LEED pattern of 10 ML NiO films deposited on Ag(001) at various growth conditions. Beam energy 57 eV. Rows stand for three different growth temperatures. Columns stand for two different oxygen pressure during growth.

the growth of monolayer Ni film. The lattice parameter of 1 ML NiO = 2.088 Å, followed throughout our experiments.

#### 6.3.4.1 LEED studies

Figure 6.5 shows LEED patterns of 10 ML NiO films grown at different deposition conditions using primary electron beam energy  $E_p=57$  eV. LEED images are arranged for three different growth temperatures 300 K, 423 K and 473 K has been shown

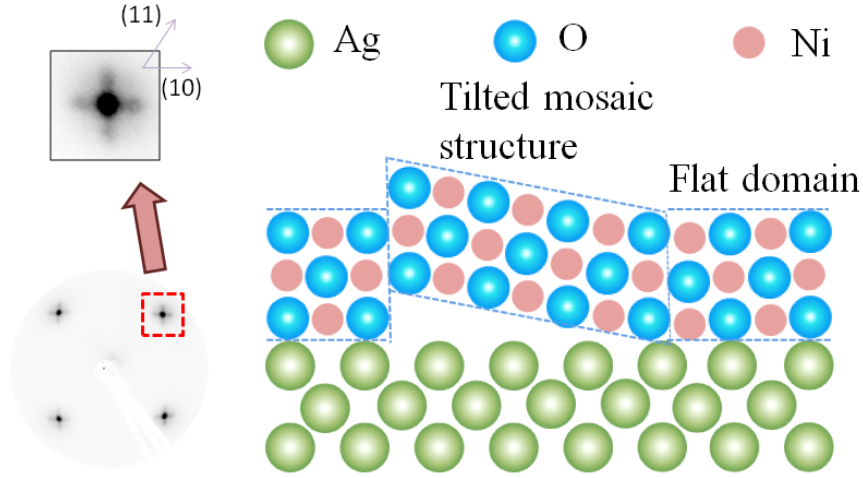


**Figure 6.6:** The  $p(1\times 1)$  LEED pattern with a zoomed in view of (1,0) spot has been shown. The mosaic formation due to misfit dislocation has been schematically represented.

along different rows. For each growth temperature, LEED images for two different oxygen pressures has been presented along the columns. Similar to Ag(001) substrate a  $p(1\times 1)$  LEED pattern is visible, and no superstructure can be observed. The LEED spots of the Ag substrate are smaller in size than the LEED reflexes of the NiO film. For RT (300 K) growth [figure 6.5 (a) and (b)] of 10 ML NiO film the normal reflexes are surrounded by four additional spots, which are clearly observed for higher oxygen pressure ( $7\times 10^{-6}$  mbar). The satellites which are located towards  $\langle 001 \rangle$  directions can be easily resolved; line profile drawn along perpendicular to the  $\langle 001 \rangle$  directions over any spot shows minimum FWHM while along the  $\langle 001 \rangle$  it is streaky. This indicates that domains in the film has small size along  $\langle 001 \rangle$  directions compared to its perpendicular directions. But, lattice mismatch between the film (NiO) and the substrate (Ag) produces stress at the interface in case of pseudomorphic films. Thus, dislocations are introduced for films thicker than a critical thickness to relax the structure and to minimize the energy. For NiO films, misfit dislocations with  $\{110\}$  glide planes occurs for coverage larger than 5 ML [197] resulting in mosaic formations within the film. In figure 6.6, the mosaic formation in

NiO film due to misfit dislocation has been shown with a zoomed in view of (1,0) LEED spot where the additional four spots are visible surrounding the central spot, which is similar to the observations of Wollschlaeger *et al.* [198]. Mosaic grows and flattens with increasing film thickness. A post deposition annealing of the film at 573 K in oxygen environment for 30 min results in vanishing of the four extra satellite spots. Intensity of the additional spots decreases for higher temperature growth also as can be seen for growth at 423 K and 473 K (see figure 6.5). The temperature driven lattice vibrations help in reducing the dislocation and defect densities resulting in the formation of smoother oxide film of higher epitaxial quality. Moreover, oxygen partial pressure during growth is another important parameter specially at higher temperatures where the sticking coefficient of oxygen on the surface reduces. For oxygen pressure of  $1 \times 10^{-7}$  mbar, the LEED spots are broad, having circular ‘halo’ background with FWHM almost 2.5 times larger than the Ag(001) LEED spots. O<sub>2</sub> deficiency in the sample produces defects which affects the Ni to O stoichiometry as well as the crystalline quality of the sample which is reflected in the broadening of LEED spots. On the other hand, the epitaxial quality of the oxide film appear to be better at higher oxygen pressure and therefore growth of good quality NiO film on Ag(001) at  $P_{O_2} = 7 \times 10^{-6}$  mbar at elevated Ag temperature may be chosen as a proper growth condition.

#### 6.3.4.2 Ni to O stoichiometry

In figure 6.7, the O *1s* to Ni *2p* XPS peak intensity ratio has been plotted for different growth conditions of 10 ML NiO film on Ag(001). The slope of the curves indicate that oxygen pressure during growth has a greater control on the oxygen to nickel stoichiometry ratio at higher temperature. At RT (300 K) deposition, the quantity of oxygen (with respect to nickel) in the sample does not increase significantly with increasing oxygen growth pressure. But at elevated temperature the sticking

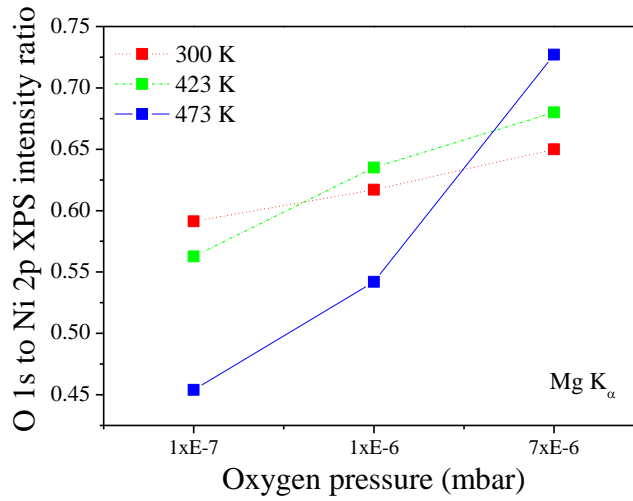


**Figure 6.7:** O 1s to Ni 2p XPS intensity ratio for different growth conditions of NiO.

coefficient of oxygen decreases. Therefore, the oxygen deficiency in the sample for lower oxygen growth pressure ( $1 \times 10^{-7}$  mbar) at 473 K is evident. The oxide film becomes more and more oxygen enriched when growth pressure is higher and a better stoichiometry is observed in the sample grown at 473 K. We expect to have even more oxygen enriched sample at higher oxygen pressure, though we restricted to a maximum oxygen pressure of  $7 \times 10^{-6}$  mbar due to technical limitations in the UHV environment.

### 6.3.5 XPS: Thickness dependence of NiO film

In figure 6.8 the Ni  $2p$  and O  $1s$  XPS peaks have been shown as a function of film thickness. Monochromatic Al  $K_{\alpha}$  (photon energy: 1486.6 eV) has been used as the probing photon source. The features in the Ni  $2p$  spectrum show distinguishable modulations with film thickness. The core level spectra of NiO is well-investigated. NiO is a  $3d^8$  charge transfer oxide and its ground state is a mixture of  $3d^8$ ,  $3d^9L^{-1}$  and  $3d^{10}L^{-2}$  configurations [199–202], where  $L^{-1}$  represents a hole created in ligand band. This gives rise to a complex line shape of the experimental spectra when using spectroscopic techniques, in particular x-ray photoemission spectroscopy (XPS). The

Ni  $2p$  photoemission peak line shape of NiO shows a multip peaked structure. The Ni  $2p$  spectra shown in figure 6.8 can be divided into two edges split by spin-orbit coupling, referred to as the  $2p_{1/2}$  (870-885 eV) and  $2p_{3/2}$  (850-869 eV) edges, respectively. The different multiplet features of the Ni  $2p$  spectrum may be explained in a simplified manner in the following way. A hole is created in the  $2p$  core level of Ni by the photoemission process; this state is represented as  $c^{-1}$ . This results in strong coulomb repulsion with the holes in the localized  $3d$  orbital. The lowest energy state will then be of  $c^{-1}3d^9L^{-1}$  character which is the main line (feature 'a'), where  $L^{-1}$  represents a hole in the ligand band, whereas the ground state is predominantly of  $3d^8$  character. The satellites at higher binding energies (858-870 eV) can be assigned to unscreened  $c^{-1}d^8$  (feature 'c') and screened  $c^{-1}d^{10}L^{-2}$  (feature 'd') final states. The spectrum presents a shoulder shifted 1.5 eV toward higher binding energies from the main line. The reason behind existence of this peak was unresolved for long time and was beyond the scope of general cluster models. Therefore a more extended explanation has been proposed by Van Veenendaal and Sawatzky [203]. They considered clusters consisting of more than one transition-metal ion. This allows the metal sites and ligands to interact. A consequence of this is that a core hole can also be screened by an electron coming from a neighboring NiO<sub>6</sub> unit, and does not necessarily have to come from the ligands at the core-hole site. This type of screening mechanism which requires at least two sites is referred to as non-local screening. The understanding of the non-local screening effect has been schematically represented in figure 6.9. In our XPS data presented here, one can clearly see a layer thickness dependence of the satellite feature at 1.5 eV, while all other features in the spectrum are well reproduced and do not significantly depend on the sample thickness. In fact, the main line shape of Ni  $2p$  spectrum for the case of 0.25 ML NiO is similar to metallic Ni. The non-local screening satellite appears prominently beyond 1.5 ML film thickness. In the submonolayer thickness range, the number of neighboring Ni sites for contributing to the non-local screening effect reduces significantly because of the reduced dimension

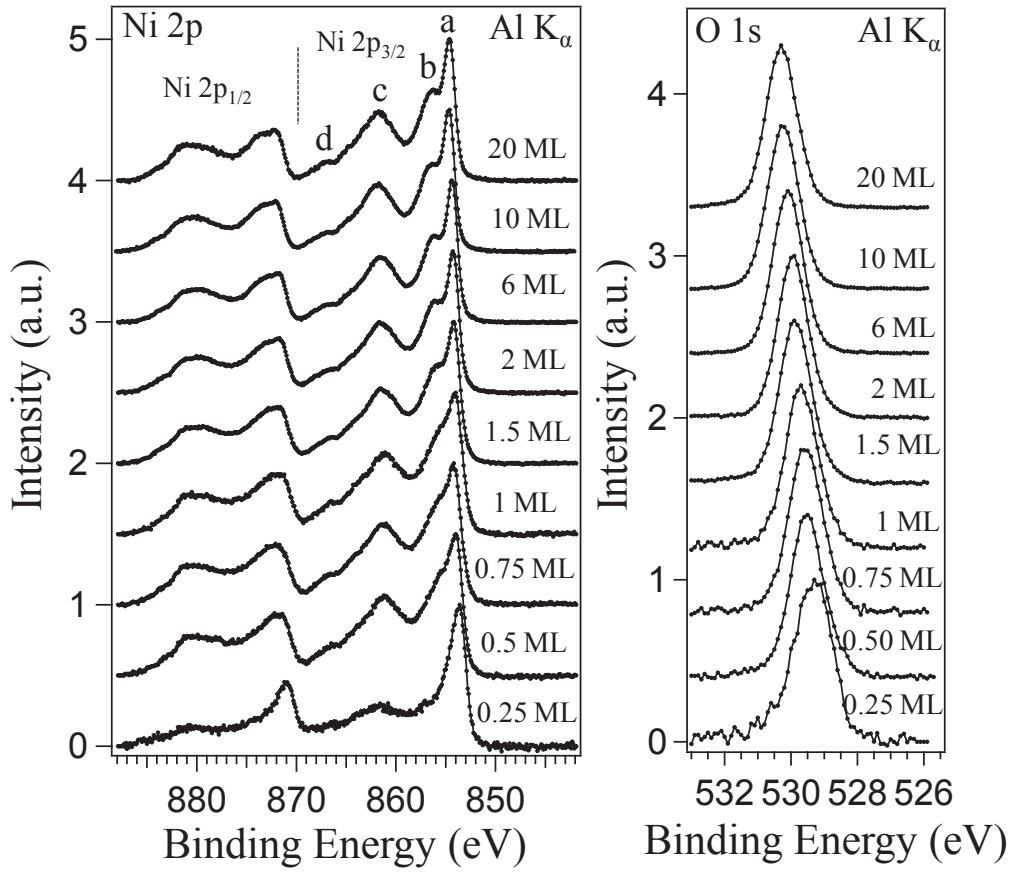


**Figure 6.8:** XPS Ni 2p and O 1s peak intensity plotted for different film thickness. X-ray source: monochromatic Al  $K_{\alpha}$  (1486.6 eV).

and symmetry. Therefore, the 1.5 eV higher binding energy satellite feature is not visible here. Figure 6.9 shows the screening mechanism schematically. After the creation of a core hole  $d^n \rightarrow c^{-1}d^n$ , the energy of the system can be lowered by screening the core hole by the electrons from neighboring sites. This yields  $c^{-1}d^n \rightarrow c^{-1}d^{n+1}L^{-1}$ . Nonlocal screening involves at least two sites, and is the process where an electron is transferred from a neighboring  $\text{NiO}_6$  unit  $c^{-1}d^n$ ;  $d^n \rightarrow c^{-1}d^{n+1}$ ;  $d^n L^{-1}$ . In the case of NiO, this yields a local configuration of mainly  $2p^5 3d^9$  character at the core-hole site and an extra hole  $3d^8 L^{-1}$  in a neighboring unit. In connection with the identification of defect structures, this satellite in the Ni  $2p$  XPS spectrum has conventionally been assigned to  $\text{Ni}^{3+}$  species existing on the surface [204]. The model proposed by Van Veenendaal and Sawatzky demonstrates that this feature

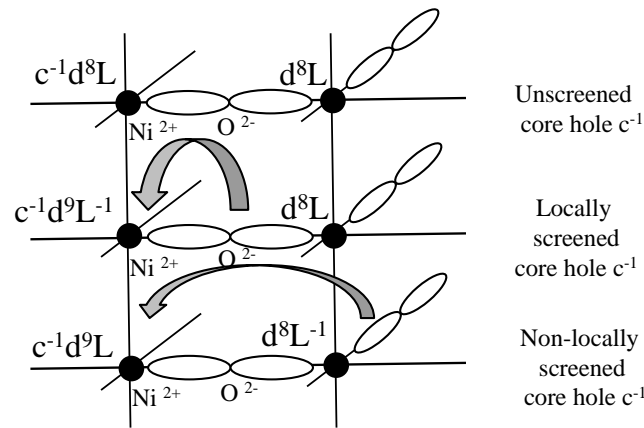


**Figure 6.9:** (Top) Two metal ion sites with a core hole on one site. (Middle) Screening of an electron from the surrounding oxygen ligands. (Bottom) Nonlocal screening from an electron from a neighboring unit.

is intrinsic for this compound. The dependence of the satellite intensity on film thickness can be related to the changes in the local structure around Ni atom, since the intensity is a result of the interplay between local and intersite screening. As predicted by the calculations, nonlocal screening is more important for surface than for bulk atoms. This subtle mechanism also explains why there is no consensus about the experimental results reported in the literature, since the intensity of the satellite is an intrinsic function of the local environment and is therefore extremely sensitive to sample preparation, defects, and surface crystallinity. A gradual shifting of the Ni  $2p$  peak towards the higher binding energy is observed with increasing film thickness. For the case of O  $1s$  a single peak is observed, which does not have any satellite structure. This demonstrates that the studied surface of the film is clean, because oxygen related compounds like H<sub>2</sub>O or OH groups would give rise to higher binding energy satellites. This is because the O<sup>2-</sup> ( $2p^6$ ) band is almost full. Contradicting observations of Sawatzky *et al.* [205], we observe a continuous shift of O  $1s$  peak towards higher binding energy with increasing film thickness.

The binding energy of Ni  $2p_{3/2}$  and O  $1s$  for different thickness of NiO film has been shown in figure 6.10 (a) and (b), respectively. Both graphs show increment of

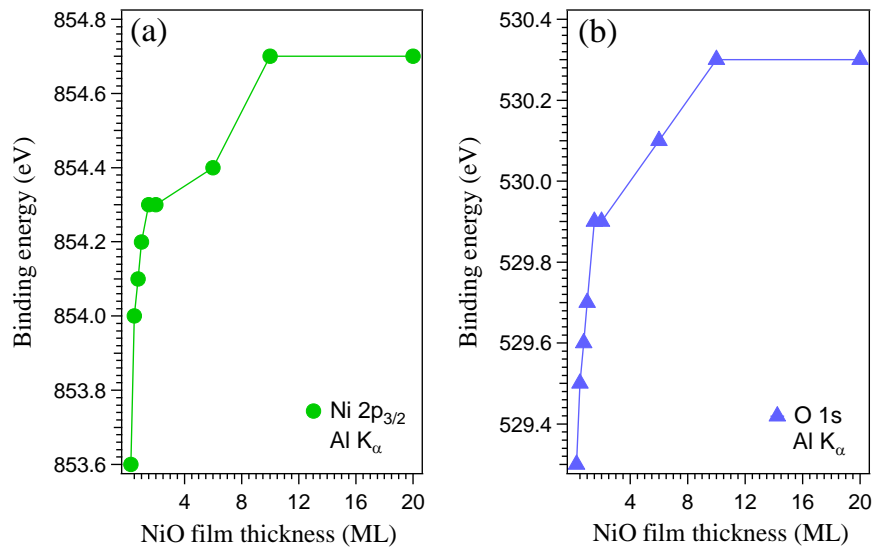


**Figure 6.10:** The binding energy position shown for different thickness of NiO film. (a) Ni 2p<sub>3/2</sub> (b) O 1s. Binding energy increases with film thickness for both cases.

binding energy of the characteristic peaks with the film thickness. Shifting of the peaks is larger at the submonolayer film thickness range and it ceases at a thickness of 10 monolayer where the peak positions are similar to bulk.

### 6.3.6 Valence band structure of NiO/Ag(001)

#### 6.3.6.1 Earlier works

Photoemission studies of NiO have played a critical role in understanding the electronic structure of this prototype compound of the strongly correlated electron systems [206, 207]. The appropriate description of the electronic structure of strongly correlated materials has always been an important task in condensed matter physics [208], especially since the discovery of the cuprate superconductors where the electron correlations are also found to be very important [209]. The angle-integrated photoemission studies on NiO has been reported by many earlier research groups. Detailed studies on the valence and conduction band of bulk NiO has been performed by Hufner [210–212] by UV and x-ray photoemission and inverse photoemission,

respectively. More details of the electronic structure of this mono-oxide compound was provided by Kim [213]. Matsunami and Taguchi *et al.* [214] have reexamined the valence-band (VB) and core-level electronic structure of NiO by means of hard and soft x-ray photoemission spectroscopies and compared their experimental data with cluster model calculations. The angle-integrated photoemission data of NiO has now usually been interpreted by the cluster model of the Anderson Hamiltonian where the translational symmetry is completely ignored [199,205]. On the other hand, the angle resolved photoemission spectroscopy by Shen *et al.* [182–184] has revealed more important aspects of bulk NiO electronic structure. The electronic structure of NiO has mainly three interesting aspects: the electron correlation effects as a result of the strong Coulomb (on-site) interaction, the band effect as a result of the translational symmetry, and the influence of the antiferromagnetic ordering precisely, this is another form of the electron correlation effects and is related with the large Coulomb interaction). Among these three interesting aspects of the electronic structure of NiO, the correlation effects due to the large Coulomb  $U$  has previously been the most extensively studied issue. NiO has continuously been at the center of the controversy between the localized Mott-Hubbard picture and the one-electron band picture for a class of materials often called Mott insulators, because of its correlated insulating nature as a result of the large Coulomb  $U$  [215,216]. Band theory provides us with the basic concept of metals and insulators: a metal corresponds to a material which has a partially filled band, while an insulator corresponds to a material which has a gap between filled bands and empty bands. However, NiO and other transition-metal monoxides can not be described by the simple band theory. According to the band theory, they should be metals but, they are experimentally found to be insulators. In fact NiO is an insulator with 4.3 eV band gap [205,217]. According to Mott, Hubbard, and Anderson, the one-electron picture fails to predict an insulating nature for these oxides is due to the intrinsic limitation of the one-electron approach. Many transition metal monoxides are insulators because of strong Coulomb interaction among the  $3d$

electrons, so that the one-electron approximation breaks down [218–220]. Based on a simple hydrogen like model, Mott illustrated that the simple band picture breaks down and a gap opens when the Coulomb interaction energy ( $U$ ) is larger than the bandwidth ( $W$ ) [219]. That is why these transition metal oxides are called ‘Mott insulators’.

Slater [221], on the other hand, argued that this failure of the one-electron band theory to predict an insulating ground state was related to certain approximations in the calculation, but was not because of the band theory itself. He recognized that a Mott insulator often has an antiferromagnetic order below its Néel temperature; therefore, this magnetic order should be included in the calculation. This is the so-called Slater antiferromagnetism approach. In fact, some sophisticated spin-polarized band calculations gave small gaps for materials like NiO and this was regarded as a demonstration of the success of the one-electron band theory [222]. However, the calculations gave a very small energy gap value of 0.2 eV, much lower than the experimentally obtained value.

To understand the excited state properties of the transition-metal mono-oxides, photoelectron spectroscopy (PES) was extensively used since few decades [199, 205, 223–229]. Sawatzky and Allen, Fujimori and Minami revised the Mott-Hubbard description of these insulators. In this revised picture, the  $p$ - $d$  charge transfer energy which involves the energy  $\Delta$  is considered, as well as the  $d$ - $d$  charge fluctuation which involves the Coulomb energy,  $U$ . As a result in case of NiO, the localized Ni  $3d$  band splits up into two bands, the upper Hubbard band which is empty and the filled up lower Hubbard band. The oxygen band resides in between the upper and lower Hubbard band and forms a charge transfer gap with the upper Hubbard band. From this viewpoint, NiO has been assigned as a charge transfer insulator. This picture of NiO has been widely accepted with few exceptions [230].

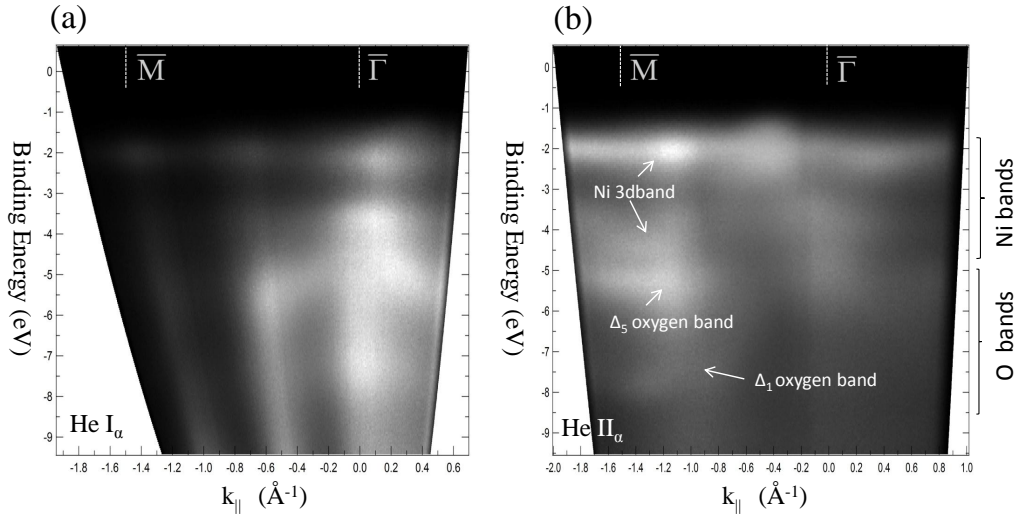


**Figure 6.11:** The valence band structure of 20 ML NiO film deposited over Ag(001). Photon source (a) He I $_{\alpha}$  (b) He II $_{\alpha}$ . Bands are shown along  $\bar{\Gamma}$  to  $\bar{M}$  direction.

### 6.3.6.2 ARPES studies

In figure 6.11 (a) and (b), the valence band electronic structures of a 20 ML NiO film are shown for monochromatic photon sources He I $_{\alpha}$  [ $h\nu = 21.2$  eV] and He II $_{\alpha}$  [ $h\nu = 40.8$  eV] respectively. The ultraviolet photons, with their limited probing depth, are unable to probe the substrate [Ag(001)] bands and hence they are quite similar to the bulk NiO band structure. In figure 6.12, the LDA calculations along with experimental data by Shen *et al.* [184] has been shown. The data are presented along [100] direction [ $\Gamma$ -X] for bulk NiO. Their theoretical calculations were able to explain the experimental band dispersions reasonably well. Our experimental results in fig. 4.11 for the case of NiO (001) thin film is quite similar to the experimental results of Shen *et al.* for the case of bulk NiO crystal along (001) direction. The almost non-dispersive Ni  $3d$  bands are narrow and lies about 2 eV below the Fermi level, opening up a gap from the conduction band. This non-dispersive Ni  $3d$  band is well separated from from the rest of the  $d$  bands. Since the antiferromagnetic order is formed by the magnetic moments at the Ni sites, its effect on the O  $2p$  band is not much evident. The dispersive feature from 4 to 8 eV is assigned as  $\Delta_1$ , the another

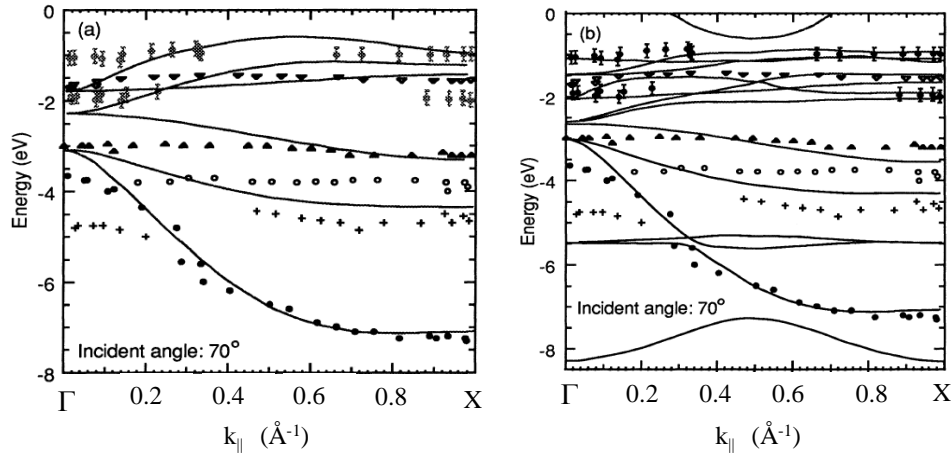


**Figure 6.12:** LDA band calculations and experimental data of bulk NiO by Shen *et al.* [184] along [100] direction. (a) Non-magnetic calculations. (b) Antiferromagnetic calculations.

non-dispersive O  $2p$  band known as  $\Delta_5$ ; both these  $\Delta_1$  and  $\Delta_5$  features are visible in our experimental data in figure 6.11, in agreement with the LDA calculations by Shen *et al.* [184]. According to the off-normal experimental data of Shen *et al.* an extra feature is observed at the  $\bar{\Gamma}$  point in the energy range of  $\Delta_5$  band which they have assigned as the folded-back band from the  $(\pi/a) \langle 111 \rangle$  to  $(\pi/a) \langle 311 \rangle$  direction as a result of the antiferromagnetic order. Contradicting their observation, we did not observe any such feature at  $\bar{\Gamma}$  position [see fig. 4.11 (a) and (b)]. Though in figure 6.11 (a) the oxygen band appears to be broadened at  $\bar{\Gamma}$ , but not well-resolved. Therefore, observation of the folded-back band can not be concluded from our experimental data, with limited photon energy as angular resolution. We observe another feature close to 8 eV binding energy at  $\bar{\Gamma}$  position when probed by He I $_{\alpha}$  [figure 6.11 (a)]. Intensity of this feature is very weak when He II $_{\alpha}$  photon source is used. This resembles to the observation another backfolded band in the antiferromagnetic calculation of Shen *et al.* The oxygen  $2p$  bands are heavily hybridized with the nickel  $3d$  bands, therefore they are strongly influenced by the effect of antiferromagnetic order on the nickel sites. Another discrepancy between our observations and the data reported by Shen

*et al.* [182–184] is that we did not observe any satellite band below the oxygen  $2p$  bands with the limited photon sources in our laboratory. Since intensity of these bands are significantly low, resonance photoemission may be able to probe these bands. As we are probing the surface valence band structure (He  $I_\alpha$  and He  $II_\alpha$ ) photon sources, discrepancies are expected from the experimental data of Shen *et al.* who investigated the bulk band structure of NiO with synchrotron radiation sources, because there are difference in electron escape depth for different photon energies. However, the antiferromagnetic phase of the 20 ML NiO/Ag(001) film was confirmed from low energy electron diffraction (LEED) pattern before and after photoemission studies. The appearance of  $p(2\times 2)$  half-order spots at lower electron energy stands for the stability of surface antiferromagnetic order at room temperature (RT), which will be elaborately discussed in chapter 7 in this thesis. Hence, the valence band structure probed by our photoemission studies at RT are expected to be the antiferromagnetic NiO band structure.

### 6.3.6.3 ARPES: Thickness dependence

The valence band electronic structures of NiO films for different film thicknesses on Ag(001) are shown in figure 6.13. He  $I_\alpha$  ( $\hbar\omega = 21.2$  eV) were used as excitation source. The  $sp$  bands of Ag has lower intensity compared to  $d$  bands. Therefore the Ni  $3d$  bands are easily detectable from the very initial stage of 1 ML NiO film thickness. However, the O  $2p$  bands can not be distinguished clearly before film thickness of 7 ML. Due to the lower kinetic energy of the photoelectrons coming from the Ag 4d band at about 5 eV binding energy, the escape depth is higher for the He  $I_\alpha$  photons through the NiO film. Hence, the highest intensity 4d band feature of the Ag substrate is faintly visible even for a 10 ML thick NiO film. In figure 6.14 the valence band electronic structure of NiO films of various thickness grown on Ag(001) has been shown, where the ARPES experiments have been performed by

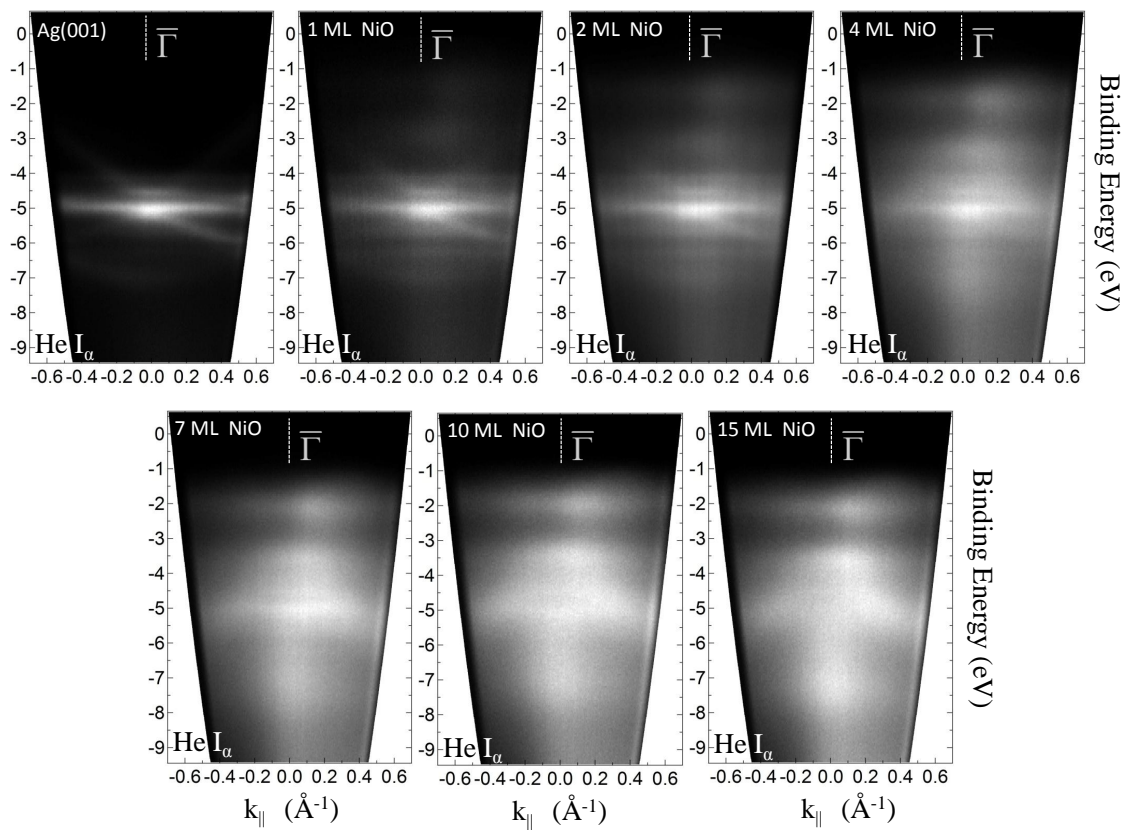


**Figure 6.13:** The valence band structures of NiO film deposited over Ag(001) for different film thicknesses. Photon source: He I $_{\alpha}$ . Bands are shown at  $\bar{\Gamma}$  position along  $\bar{M}-\bar{\Gamma}-\bar{M}$  direction.

He II $_{\alpha}$  photon source. With He II $_{\alpha}$  radiation, the kinetic energy of the electrons of the Ag  $d$  bands are about 31 eV whose escape depth is much less (see inelastic mean free path vs kinetic energy in chapter 2). So, for He II $_{\alpha}$  photons, the Ag bands are much suppressed by 4 ML of NiO and the NiO bands can be clearly observed. The non-dispersive Ni  $3d$  bands have higher intensity than the O  $2p$  bands. The band features and their relative intensity variation at different thicknesses can be easily realized in the spectral mode. In figure 6.15 (a) and (b), the ARPES line profiles drawn at  $\bar{\Gamma}$  position are shown for NiO(001) films grown on Ag(001) for different film thicknesses for He I $_{\alpha}$  and He II $_{\alpha}$  photon energies. The high intensity feature at 5.1 eV binding energy position as can be seen in figure 6.15 (a) is due to the presence of Ag  $4d$  band which decreases in intensity for higher NiO film thickness. Both in figure 6.15 (a) and (b), there are mainly four features. The features ‘a’ and ‘b’ corresponds to Ni  $3d$  band whereas ‘c’ and ‘d’ are supposed to be O  $2p$  band. The relative intensity variation of these features for different photon energies are notable. Another interesting observation is the presence of states [encircled by rectangles] at the Fermi level for 1 and 2 ML film. These states does not appear for film thickness beyond 4 ML. These states, as demonstrated by earlier studies appear from the interfacial first Ni layer at the close vicinity of Ag. Yang *et al.* [231] has performed photoemission studies on NiO film deposited on Ag(100) at 450 K within ultrathin film thickness range and observed appearance of these states at  $E_F$  by probing the sample at different photon energies. Cheng *et al.* [185] has deposited 1.2 ML NiO films both at RT and 453 K. Their photoemission results shows existence of states at Fermi level for the high temperature prepared film but the RT grown film does not posses these states. They concluded that there must be segregation of metallic nickel at the subsurface region of Ag substrate which contributes to these states at Fermi level. Hence they proposed that good quality epitaxial growth of NiO on Ag(100) is preferred at RT rather than high temperature with less unreacted metallic Ni. DFT calculations by Cinquini *et al.* [232] has proposed a model of stoichiometric 1 ML

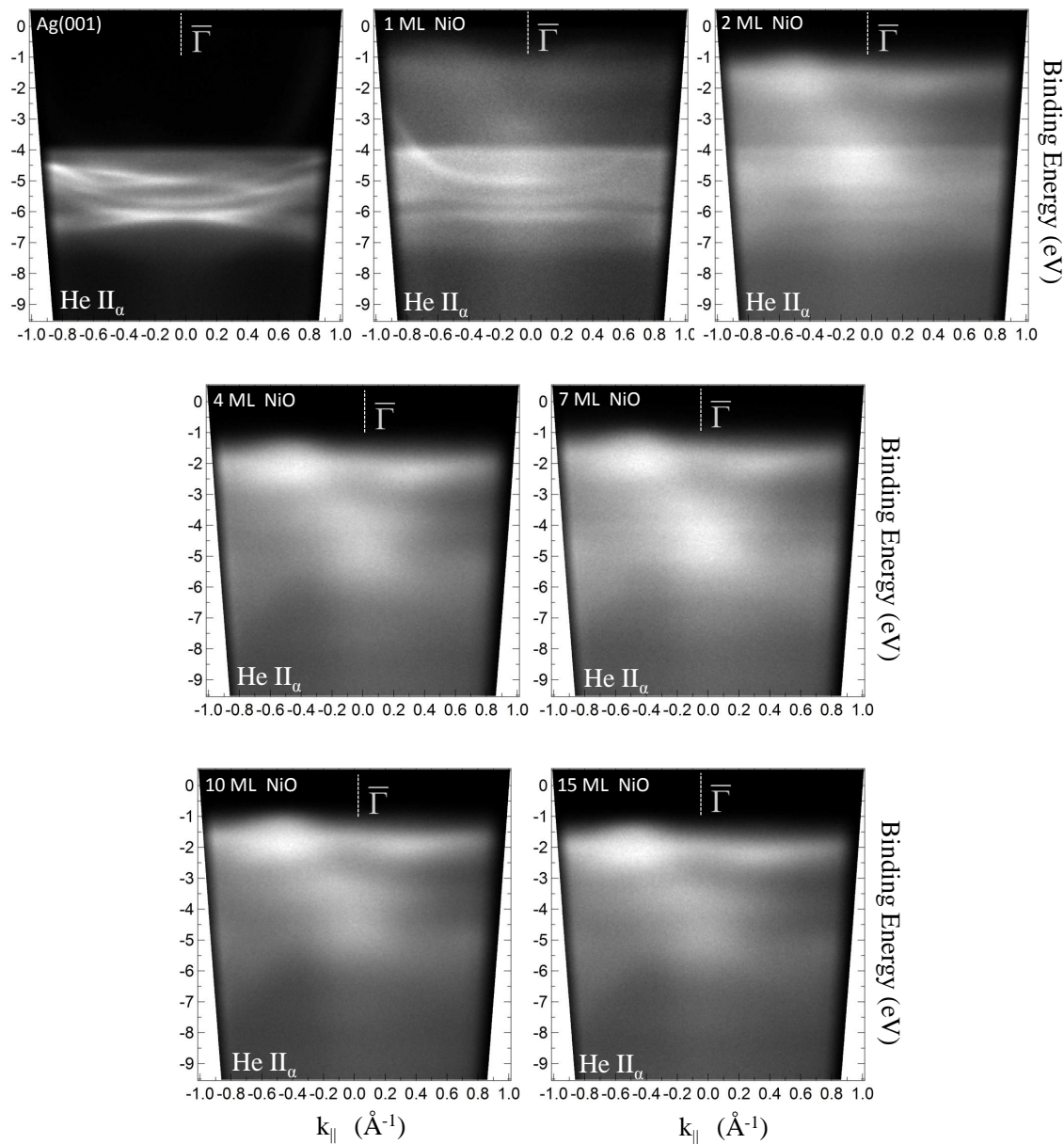


**Figure 6.14:** The valence band structures of NiO film deposited over Ag(001) for different film thicknesses. Photon source: He II $_{\alpha}$ . Bands are shown at  $\bar{\Gamma}$  position along  $\bar{M}-\bar{\Gamma}-\bar{M}$  direction.

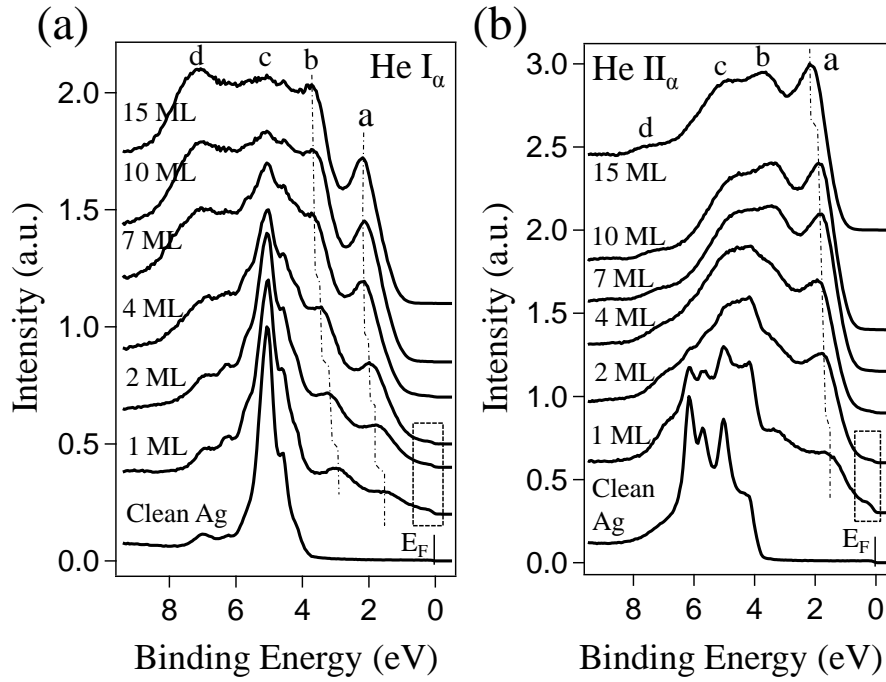


**Figure 6.15:** Line profiles drawn at  $\bar{\Gamma}$  position for bare Ag(001) and different thickness of NiO film. Photon energy: (a) He I $_{\alpha}$  (b) He II $_{\alpha}$ .

NiO overlayer supported by Ag(100) substrate contributes to states at  $E_F$ . Their DOS calculation shows that both Ni and O atoms of the first (interfacial) NiO layer contributes to this state, whereas 2nd or 3rd layer on top of this interfacial layer behaves quite bulk-like having no such states close to  $E_F$ . They found that a free (no substrate) NiO layer has no such states and they concluded that the first NiO layer adhere to the substrate with a covalent bond which contributes to the DOS at Fermi level. This DOS calculations is a direct proof that incorporation of metallic Ni segregation is not required to explain the states at  $E_F$ .

#### 6.3.6.4 ARPES: Temperature dependence

The large on-site coulomb interaction between the  $d$  electrons in NiO results in localization of these electrons yielding an insulating behavior of this material. It is also expected that the valence band structure of this transition metal mono-oxide

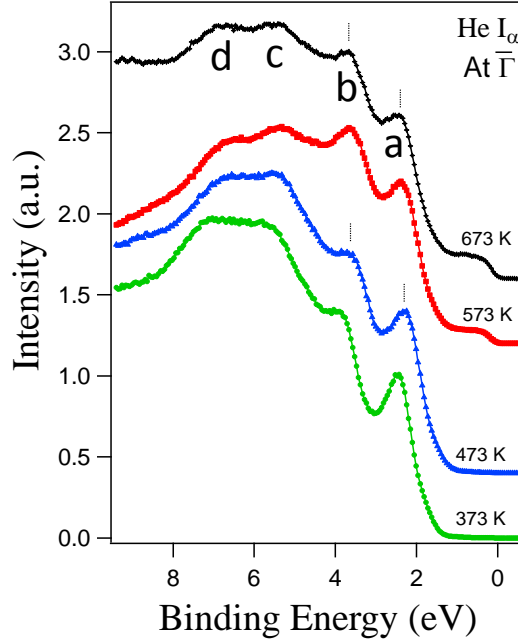


**Figure 6.16:** ARPES line profiles drawn at  $\bar{\Gamma}$  position for NiO(001)/Ag(001) film at different sample temperatures. Photon energy: He  $I_{\alpha}$ . Film thickness 20 ML

will be affected by the intrinsic magnetic ordering below Néel temperature [ $T_N$ ]. Density functional theory (DFT) based on local density approximation (LDA) often include the fact that the transition metal oxides, as NiO and others, are magnetically ordered, and predict drastic changes in the band structure at the magnetic phase transition. This makes it highly interesting to perform photoemission experiments on NiO above and below the Néel temperature in order to investigate the effect of the magnetic ordering on the electronic structure. In figure 6.16, the ARPES line profiles drawn at  $\bar{\Gamma}$  position for different film temperature are shown, all the data are collected for NiO film thickness 20 ML. Our photoemission data represents no significant changes in the electronic structure, though there exists minor temperature dependence of the corresponding features. We observe relative intensity changes of the four observed features at various temperatures. The another significant thermal modulation of the band structure is that the features ‘c’ and ‘d’ becomes well resolved at higher temperature. No significant modulation in the band dispersion or evolution

of new band was observed except thermal broadening of the bands. A very faint state appears gradually close to  $E_F$  with increasing film temperature, which is the result of creation oxygen vacancy defect at higher temperature. This result has two possible explanations. One is that local magnetic ordering or the short-range magnetic correlations persists even above the transition temperature within the paramagnetic phase whose correlation length scales are more than the photoemission correlation lengths. The other situation is that the magnetic ordering has no or little effect on the electronic structure of NiO eventhough this is unexpected from the present theoretical understandings. Further detailed analysis of the experimental results will be required to come to a conclusion on these issues. Similar conclusions were reached by Tjernberg *et al.* [233] when they performed photoemission studies on NiO single crystal at different temperatures and failed to observe any significant changes in the electronic structure. Experiments on the NiO single crystals were complicated by the charging effects as well as the surface cleaving effects. Our experiments on the high quality epitaxial thin films show that the absence of significant changes in the electronic dispersions within the AFM phase as well as in the PM phase is an intrinsic effect. The most likely scenario is expected to be the role of short-range magnetic fluctuations persistent within the PM phase with larger correlation length than that of the photoemission process itself.

#### 6.3.6.5 ARPES: Photon energy dependence

The Ni  $3d$  and O  $2p$  bands responds differently for different probing photon energies due to their variation of photoemission cross-sections. The UPS and XPS valence band spectra are shown in figure 6.17 for He  $I_\alpha$  ( $\hbar\omega = 21.2$  eV), He  $II_\alpha$  ( $\hbar\omega = 40.8$  eV) and Al  $K_\alpha$  ( $\hbar\omega = 1486.6$  eV) photon energies, respectively. It shows that the XPS spectrum gives rather a good representation of the  $d$  states whereas the He  $I_\alpha$  UV source represents the O  $2p$  states better. Energy resolution of the spectra

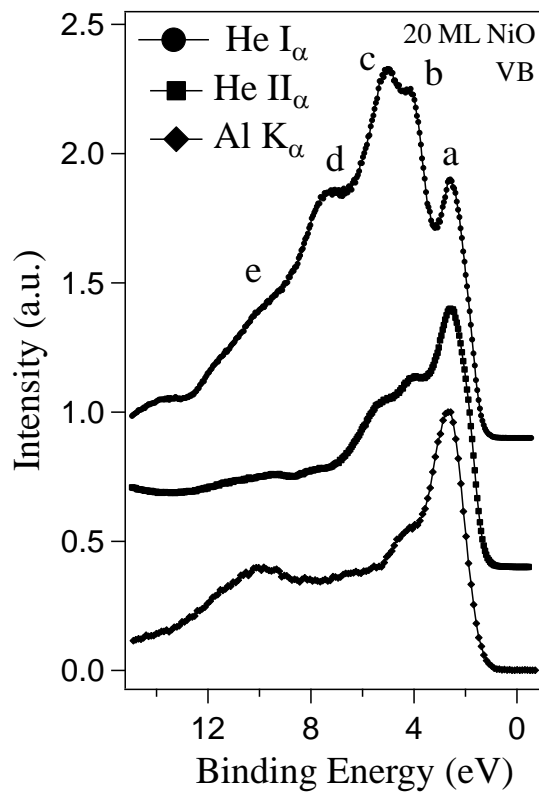


**Figure 6.17:** UPS and XPS to probe the valence band electronic structure of 20 ML NiO film. He I $\alpha$  and He II $\alpha$  photon sources are used as UV sources and Al K $\alpha$  is used as x-ray photon source.

are better for UV sources as per expectation. The XPS VB spectra shows a hump at 10 eV binding energy position. For long time it was believed to originate due to impurities or adsorption on the surface. But later it was assigned as  $d^7$  VB satellite feature which is intrinsic to pure NiO sample.

## 6.4 Conclusion

In short, this chapter describes the procedure of NiO epitaxial growth on top of Ag(001) substrate and characterization of its electronic structure. LEED is used to obtain a qualitative idea about the crystalline order at the sample surface. The valence bands are excited *via* monochromatic UV (He I $_{\alpha}$  and He II $_{\alpha}$ ) photon sources where ARPES technique is used to reveal band dispersions and also using monochromatic x-ray (Al K $_{\alpha}$ ) source using XPS technique. The Ni  $2p$  and O  $1s$  core levels are also probed by x-ray photons. The dependence of electronic structures on the film thickness, stoichiometry, probing photon energy and sample temperature are described in this context.

## Magnetic structure of epitaxial NiO film

### 7.1 Introduction

Ferromagnetic materials at reduced dimensions have been a topic of immense interest due to their relevance both in fundamental physics as well as in technological applications connected with digital data storage and spintronics, such as reading heads and sensors, high density storage media, magnetic random access memories, spin-valves *etc.* The low co-ordination number, reduced symmetry, strain induced by mismatched substrates, the possibility to stabilize metastable states, and the presence of interfacial or surface states can profoundly alter the electronic and magnetic properties of thin films or surfaces with respect to the bulk, with the possibility to induce new magnetic behaviors in a controlled way. Transport properties of multilayer structures where ferromagnetic layers are separated by non magnetic (NM) spacers are affected by spin-dependent electron confinement and spin filtering, leading to oscillating magnetic coupling and giant magnetoresistance.

On the other hand, investigation of the magnetic properties of antiferromagnetic materials, thin films, interfaces and surfaces has got comparatively much less scientific

---

*A part of this work has been published in Physical Review B, 84, 132402 (2011).*

attention mainly because of the limited number of available experimental techniques that are sensitive to the antiferromagnetic properties of surfaces and ultrathin films as well as of systems confined over a nanometric length scale. However, the phenomena of exchange bias in a heterogenous system, where a FM material (films/ overlayers) interacts with an antiferromagnetic material (film or substrate), have aroused a great scientific as well as technological interest in the study of antiferromagnetic systems. It is by now widely accepted that the key to understanding this intriguing phenomena is the antiferromagnetic spin structure and in particular, the dynamical changes occurring not only at the AFM-FM interface, but also over deeper layers away from it. Nevertheless, the investigation of the effective role of the antiferromagnetic spin structure is a very hard task due to the great difficulty to experimentally unravel and control complex AFM domain patterns. However, in the last few decades, experimental techniques able to yield information about the magnetic structure of antiferromagnetic thin films and interfaces have been refined. Among them, X-ray Magnetic Linear Dichroism (XMCD) [234, 235] has represented a unique tool since it combines the orbital and elemental selectivity typical of a core-level spectroscopy together with the possibility to extract ground state magnetic properties as the AFM anisotropy and AFM easy axis direction.

The late *3d* transition metal monoxides (MnO, FeO, CoO, NiO) are particularly important thanks to their appealing properties such as the relatively high Néel temperature ( $T_N$ ), the chemical and mechanical stability, low lattice mismatch with respect to the corresponding FM metals and their alloys, and the large electronic gap. Insulating AFM materials, in fact, have the advantage that the indirect exchange interaction due to conduction electrons is ruled out. Thus, they can be, considered as model systems since one would expect that their magnetic properties are determined only by direct nearest neighbor exchange across the AFM film and at the FM-AFM interfaces. In addition, insulating materials can find applications in giant magnetoresistance tunneling devices.

Below  $T_N$ , the ordered moments are oriented along certain directions with respect to the crystallographic axes due to the presence of anisotropy in a solid. Above  $T_N$ , this long range order vanishes within the paramagnetic phase. The most common anisotropy

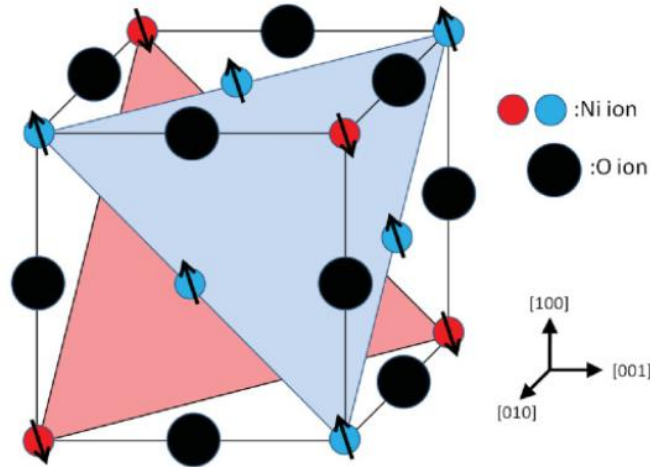


**Figure 7.1:** Collinear arrangement of magnetic cations in a rocksalt monoxide. A domain with (111) ferromagnetic sheets and moments parallel or antiparallel with the  $(\bar{2}11)$  direction is shown.

in these materials is magnetocrystalline anisotropy, which originates due to the spin-orbit interaction. Magnetocrystalline anisotropy biases the moments to lie along easy axes, for which the system energy is reduced to a minimum. The other terms that contribute to the total energy of the AFM materials is the magnetoelastic energy. Formation of magnetic domains in magnetic materials is natural in order to reduce the total energy. In the case of ferromagnetic materials, the magnetic domain formation is strongly determined by the magnetostatic energy [236, 237]. However, the occurrence of magnetic domains in an antiferromagnetic material, such as in Nickel Oxide (NiO), is not very obvious due to its magnetically compensated nature. There is hardly any contribution from the magnetostatic energy term and in such case, weaker magnetoelastic energy term becomes important. Thus, magnetic domain pattern and easy axes in an antiferromagnet are determined by magnetoelastic, short-range dipolar and magnetocrystalline energy contributions to the total energy. The magnetoelastic energy arises from an interaction between moments and the mechanical strain of the lattice and is defined to be zero for an unstrained lattice [236]. The antiferromagnetic domains are described by antiferromagnetic vectors or spin-axes (order parameter). Above their Néel temperature  $T_N$ , MnO, FeO, CoO and NiO have a

rocksalt crystallographic structure. Below  $T_N$ , magnetostrictive effects deform the CoO crystal structure to tetragonal symmetry, while the other three compounds undergo a rhombohedral deformation [238]. In these oxides, the superexchange coupling acting along  $180^\circ$  metal-oxygen-metal bonds [239] imposes the magnetic moments of second-nearest neighboring cations to be antiparallel. The fcc lattice formed by the cations can be thus be viewed as a combination of four simple cubic sublattices. In each sublattice, the moments are forced by superexchange to align ferromagnetically within (111) planes, while adjacent (111) planes are coupled antiferromagnetically. The superexchange interaction does not couple the magnetic moments of cations in different simple cubic sublattices since these are connected by  $90^\circ$  oxygen bonds. The relative orientations of the four lattices with respect to each other and to the crystallographic axes are instead imposed by anisotropic interactions such as, for example, the magnetic dipole-dipole interactions and the magneto-crystalline interactions [240, 241]. The resulting magnetic ordering is characterized by AFM domains in which the moments form FM sheets in one of the four equivalent (111) planes. The FM sheets then stack up in AFM order as shown in figure 7.1, giving a magnetic arrangement known as type II AFM order.

## 7.2 Background works

Unlike ferromagnetic surfaces, magnetic properties of antiferromagnetic surfaces have been poorly studied, due to lack of surface sensitive experimental techniques capable to determine surface antiferromagnetic order. X-ray magnetic linear dichroism (XMLD) measurements, which reflect the linear polarization dependence of X-ray absorption spectrum (XAS), have been successful in studies of surface antiferromagnetism in the last few decades or so [242–256]. Nickel oxide (NiO) is a prototypical system used for the studies of antiferromagnetism and its bulk antiferromagnetic domain structure is well known from early neutron diffraction and X-ray topography experiments [257, 258]. Many works have been performed on the surface magnetism of bulk NiO crystal. Antiferromagnetic domain structures of a NiO(100) surface have been observed using a combined method of photoelectron emission microscopy (PEEM) and soft-X-ray linear dichroism (LD) at

an O K edge by Kinoshita *et al.* [259]. A lot of studies on the surface magnetic domains of bulk NiO(001) has been reported by Ohldag *et al.* [247,260]. Strain-induced nonequilibrium magnetoelastic domain structure and spin reorientation at NiO(100) surface has been studied by Mandal *et al.* [261].

NiO films grown on suitable substrates [like Ag(001) and MgO(001)] has also been studied for magnetic investigation. X-ray linear dichroism (XLD) reports by Wu *et al.* [262] show that antiferromagnetic spins an in-plane spin-reorientation transition from parallel to perpendicular to the step edge direction with increasing the NiO film thickness when a vicinal Ag(118) is used as substrate. Stöhr and his group [254] has used XMLD spectromicroscopy for imaging the antiferromagnetic structure of NiO(100) film surface grown on MgO(001) substrate. Spanke *et al.* [263] has deposited ultrathin NiO films on Ag(001); photoemission images were collected using the Ni  $3p$  photoemission line to probe magnetic domains with a lateral resolution of 150 nm. Altieri *et al.* [245] have shown that Ni  $L_2$  XMLD is fully reversed for NiO(001) films on materials with reversed lattice mismatch.

Another interesting aspect of studying magnetism of antiferromagnetic surface is to investigate its interaction with ferromagnetic material and hence the FM-AFM interface. By using such an interface, it is possible to ‘pin’ the direction of the FM layer magnetization *via* unidirectional exchange bias and to create a magnetic reference layer [264,265]. Using soft x-ray spectromicroscopy, Ohldag *et al.* [266] have shown that NiO(001) exhibits a crystallographic and magnetic domain structure near the surface identical to that of the bulk. Upon Co deposition, a perpendicular coupling between the Ni and Co moments is observed that persists even after formation of uncompensated Ni spins at the interface through annealing. Scholl *et al.* [267] presented evidence for the creation of an exchange spring in an antiferromagnet due to exchange coupling to a ferromagnet. X-ray magnetic linear dichroism spectroscopy on single crystal Co/NiO(001) shows that a partial domain wall is wound up at the surface of the antiferromagnet when the adjacent ferromagnet is rotated by a magnetic field.

Neutron diffraction has been used to obtain valuable information on the AFM order [268], but the lateral resolution of this technique is still limited to few micrometers [269]. Among laboratory-based microscopic techniques, spin-polarized scanning tunneling microscopy (SP-STM) [270] and magnetic exchange force microscopy [271] are mentionable for their good enough resolutions for magnetic domains imaging. Although threshold photoemission electron microscopy (PEEM) has been successfully employed to study FM domains [272], the observed contrast in AFM systems has not been attributed to a magnetic origin [273]. With the development of ultrabright synchrotron sources, several imaging methods come to fruition either using x-ray magnetic linear dichroism (XMLD) spectroscopy contrast [253, 255, 256, 263] or directly probing the magnetic order [274]. Nowadays, the XMLD-PEEM is a widely used technique for AFM imaging, because it provides element specificity, high lateral resolution, and the ability to image surface and buried interfaces. With the imminent advent of aberration corrected instruments [275, 276], PEEM at the state of the art promises to embrace the nanometer scale, but its progress in lateral resolution might be limited by blurring effects due to the strong Coulomb interaction between photoelectrons [277].

In this chapter, we demonstrate the power of the electron microscopy method for imaging surface AFM domains using the observed half-order spots in the low-energy electron diffraction (LEED) pattern of the NiO(100) surface, in a standard low-energy electron microscope (LEEM) [278]. The origin of these half-order spots has already been established as resulting from coherent exchange scattering of electrons from the AFM surface of NiO(100), in the late sixties, by Palmberg *et al.*, [141]. They are directly correlated to the surface antiferromagnetism as they disappear above Néel temperature ( $T_N$ ). Temperature-dependent variation of their intensities has been subsequently exploited [279] to investigate the surface antiferromagnetism at the macroscopic scale. Our approach uses the AFM-induced half-order diffraction beams in the darkfield (DF) operation mode of a LEEM instrument (shortly, AFM-LEEM) to image surface AFM domains.

## 7.3 Magnetic structure of NiO

### 7.3.1 Twin and Spin domains

We focus in this chapter on the evolution and growth of AFM domains in NiO film with increasing film thickness using two techniques, XMLD-PEEM and AFM-LEEM and discuss the correlation between the magnetic and the structural domains in this context. Before we come to the case of thin film, let us direct our attention to NiO bulk single crystal. The AFM superexchange interaction of the Ni-O-Ni bonds along the  $\langle 100 \rangle$  directions leads to the formation of FM-ordered 111 planes, where spins in the adjacent 111 planes align in the antiparallel direction, as shown in figure 7.1. Owing to the magnetostriction caused by AFM ordering, the NiO crystal consists of many twinned crystals for temperatures below  $T_N$ . This crystallographic twinning leads to four different domains, i.e., the so-called twin domains (T domains), with four different contractions along the (111) axes. In figure 7.2 the four T domains of NiO crystal are shown. Due to the superexchange interaction, the three different [100] axes are defined as the intrinsic antiferromagnetic propagation axes in NiO; because along these directions the spins of the adjacent atoms are opposite to each other. Unfortunately, the magnetic symmetry of the fcc nickel sublattice is not yet determined by the intrinsic antiferromagnet propagation axes in the rock salt crystal because the [100] directions do not represent a set of basis vectors in a fcc type lattice. For an unambiguous characterization of the magnetic symmetry the spin order along the [110] directions has to be defined. The [110] directions are the AFM axes corresponding to each T domains. Within a (111) ferromagnetic plane, the Ni moments can point along three different  $\langle 11\bar{2} \rangle$  directions such as  $[\bar{2}11]$ ,  $[1\bar{2}1]$  and  $[11\bar{2}]$ . They forms the Spin (S) domains in each T-domains. So there are four T-domains in NiO, and for each T-domain there are three S-domains. Therefore there are totally 12 AFM-domains in NiO. In table 5.1 the T-domains and the corresponding AFM axes and the S-domains for each T-domains are shown.

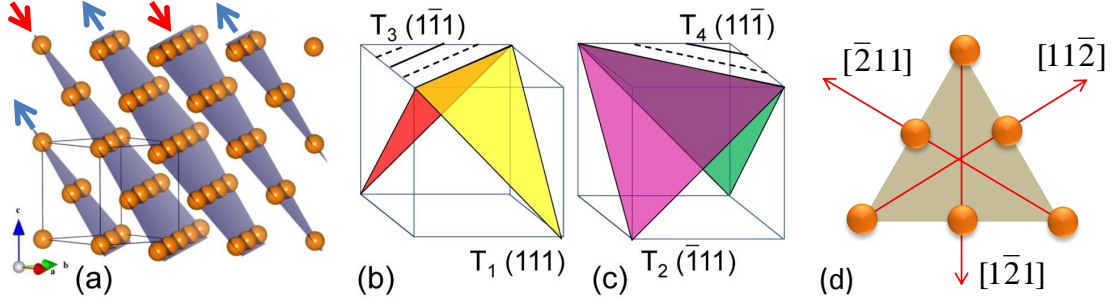


**Figure 7.2:** (a) The antiferromagnetically ordered (111) planes are shown. (b) The T1 and T3 planes. (c) The T2 and T4 planes. (d) Three spin directions that give rise to spin domains within a single twin domain.

Name	FM plane	AFM axes	S-domain
T <sub>1</sub>	(111)	[110] [101] [011]	[11 $\bar{2}$ ] [1 $\bar{2}$ 1] [ $\bar{2}$ 11]
T <sub>2</sub>	( $\bar{1}$ 11)	[1 $\bar{1}$ 0] [ $\bar{1}$ 0 $\bar{1}$ ] [011]	[1 $\bar{1}$ 2] [1 $\bar{2}$ $\bar{1}$ ] [211]
T <sub>3</sub>	(1 $\bar{1}\bar{1}$ )	[1 $\bar{1}$ 0] [101] [01 $\bar{1}$ ]	[ $\bar{1}$ 12] [121] [21 $\bar{1}$ ]
T <sub>4</sub>	(11 $\bar{1}$ )	[110] [10 $\bar{1}$ ] [01 $\bar{1}$ ]	[112] [ $\bar{1}$ 21] [2 $\bar{1}$ 1]

**Table 7.1:** The possible (T)win and (S)pin domains in NiO

### 7.3.2 The real and reciprocal lattice

As can be seen in figure 7.2 (a), the ferromagnetic (111) Ni planes are antiferromagnetically aligned along  $\langle 111 \rangle$  directions. Therefore, the  $\langle 111 \rangle$  directions may be assigned as intrinsic AFM directions in NiO crystal. The (111) planes of Ni atoms are shown in figure 7.3, where the up-spin and down-spin Ni atoms are indicated by filled and blank circles respectively. The oxygen atoms may be neglected during this discussion. The  $\langle 111 \rangle$  direction has been assigned as x-direction while the orthogonal direction is denoted as y-direction. The y-axis hence lies in the FM Ni (111) plane. Along x-axis, the magnetic lattice parameter (magnetic unit cell represented by light pink rectangle) is double than the chemical lattice parameter (structural unit cell represented by dark pink rectangle) in real lattice as shown in figure 5.3 (a). With this configuration in the real lattice let us focus on the reciprocal lattice. Some extra lattice points, as indicated by red dots along  $k_x$  appears

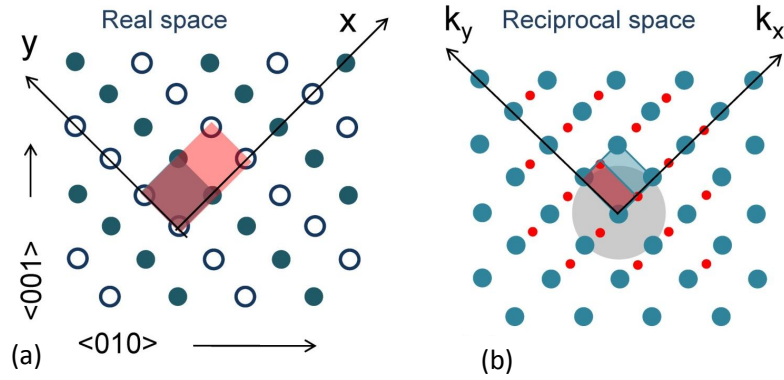


**Figure 7.3:** (a) The antiferromagnetically ordered (111) planes in real lattice. (b) Appearance of extra spots in reciprocal lattice.

at the exact middle of two reciprocal lattice points. Therefore, the effective magnetic lattice parameter along x axis becomes half of chemical lattice parameter. The red dots are visible as 'half-order' spots in low energy electron diffraction pattern. Half-orders along  $\langle 111 \rangle$  can be understood considering the T1/T3 domains of figure 7.2 (b). Whereas along  $k_y$ , no such change in lattice parameter is observed. Half-order spots along  $k_y$  direction can be realized considering the T2/T4 (T)win domains as shown in figure 5.2 (c). Further details of half-order spots and the contributions from different (T)win domains to the formation of half-orders will be discussed further in context of AFM-LEEM imaging later in this chapter. The detailed description of the different T domains and the occurrence of half-order spots for different T-domains can be found in the Ph. D thesis of Dr. Suman Mandal [38].

## 7.4 Technical Details:

The experiments were carried out with the spectroscopic photoemission and low energy electron microscope (SPELEEM) [280] at the Nanospectroscopy beamline of Elettra synchrotron laboratory (Trieste, Italy). The AFM-LEEM measurements were performed in the Dark Field (DF) operation mode of the microscope, selecting individual NiO(100) half-order diffraction spots by means of a 20 micrometer contrast aperture. Corresponding XMLD-PEEM measurements were obtained by measuring the ratio of PEEM images between two Ni  $L_2$ -edge multiplet peak positions [253] and O K-edge energy positions [259].

Commercially available NiO single-crystal cubes were ex-situ cleaved and introduced to the microscope for experiments [38]. For the growth of NiO(001) thin films, an Ag(001) substrate was prepared by standard surface science methods i.e. an ion beam sputtering followed by high temperature annealing as mentioned in earlier chapters. Ni was evaporated from an e-beam evaporator at a rate of 0.2 ML/minute under oxygen partial pressure of  $5 \times 10^{-7}$  mbar on Ag(001) kept at 473 K in the microscope chamber. After deposition each film has been annealed in oxygen environment at 573 K for 30 min and then slowly cooled down to RT (300 K) in same oxygen pressure. This procedure helps in formation of good quality oxygen rich NiO film.

The SPELEEM microscope used for the experiments at the Nanospectroscopy beamline of Elettra synchrotron laboratory (Trieste, Italy), combines into a single instrument LEEM and energy-filtered XPEEM, reach a lateral resolution of about 10 nm in the LEEM mode and about 30 nm in the PEEM mode. For the AFM-LEEM experiments, the best performance in imaging was achieved by aligning the half-order spots to the optical axis of the microscope with a deflection of the incident e-beam. Bandpass energy filtering (0.6 eV for single crystals and 0.3 eV for thin films) was used to remove the secondary electron background. In order to counteract image degradation due to sample drift, all images presented here were obtained by averaging a drift corrected series of consecutive images with maximum single exposure time of 30 seconds. NiO films grown on Ag(001) crystals cleaned by sputter and anneal cycles were mounted on the sample holder and were introduced to the microscope for experiments which operates under ultra high vacuum ( $1 \times 10^{-10}$  mbar). No charging effects were observed even during the experiments on single crystal NiO(100) surfaces as surface defects and dislocations provided sufficient conductivity to the surface. During the growth of NiO(001) thin films, growth rate and film thickness were measured by monitoring intensity oscillations in LEEM and LEED.

## 7.5 Experimental Details

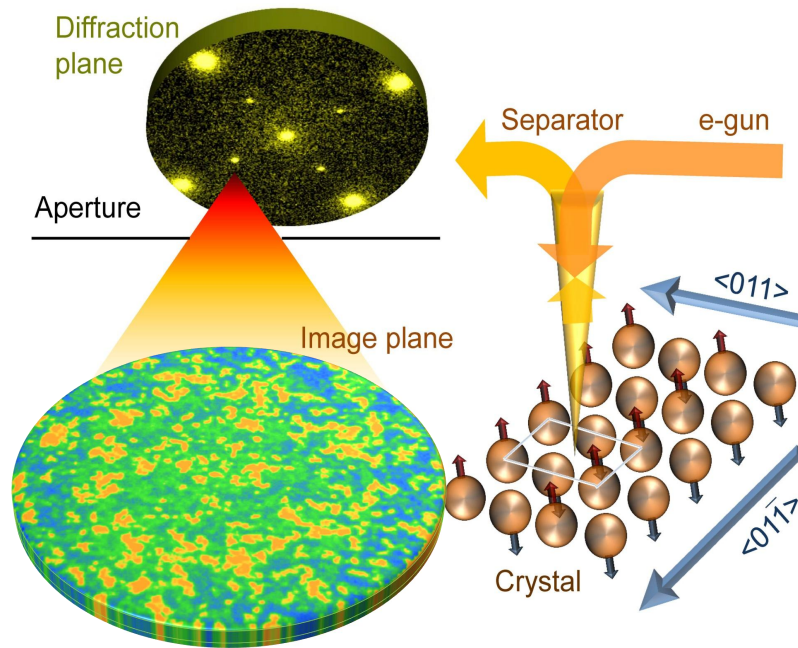


**Figure 7.4:** Schematics of the AFM-LEEM method for imaging AFM domains of NiO/Ag(001). Unpolarized electrons from the electron gun are elastically backscattered by the ordered AFM surface lattice producing half-order diffraction beams. The dark-field images, formed by the electrons originating from the half-order beams, display contrast due to the surface AFM domains. Three different colors (yellow, green and blue) represent different types of domains.

### 7.5.1 Antiferromagnetic Low Energy Electron Microscopy (AFM-LEEM)

Low energy electron microscopy has always been a fruitful technique for imaging sample surfaces, structures and morphologies [278,281]. We have extrapolated the use this technique for imaging surface magnetic domains of antiferromagnetic sample. A significant number of studies on magnetic domains of NiO(100) single crystal has been already reported by our group [109,282]. Figure 7.4 sketches the general concept behind the AFM-LEEM technique. A single half-order diffraction beam is selected so that the LEEM image will show only the sample regions that contribute to the selected spot. The much reduced probing depth (0.2-0.5 nm) of low-energy electrons [283] enables us to explore the top-layer AFM domain structure. Along with the spatial resolution ( $\sim 10$  nm) this makes our method

complementary to the already existing antiferromagnetic domain imaging techniques such as XMLD-PEEM and SP-STM. Rigorous studies have been performed on NiO films of four different thickness 6, 18, 40 and 60 ML films. At each thickness, AFM-LEEM and XMLD-PEEM techniques have been applied to image their antiferromagnetic domains. Bright field imaging have been performed using the specular beam to observe the structure and morphology of the film surface. In figure 7.5, the LEED pattern of a 60 ML NiO film deposited over Ag(001) has been displayed (centre image) at electron beam energy 31 eV. With the first order integer spots, four extra  $(1/2,0)$  spots are visible at  $p(2\times 2)$  symmetry positions. Intensity of these spots are much weaker, 2-3% of the integer order intensity. Origin of these weak intensity spots is the doubling of the magnetic unit cell in NiO with respect to the chemical unit cell as explained in figure 7.3. The weak exchange interaction of the antiferromagnetically ordered Ni moments with the impinging slow (low energy) electrons is responsible for the evolution of these spots [109,141]. With the help of a contrast aperture when these half-order spots are selected to image the sample surface, regions responsible for the creation of these half-orders are illuminated.

In figure 5.5 (a), (b), (c) and (d), the antiferromagnetic domains of the 60 ML NiO films are shown when viewed through  $(0,1/2)$ ,  $(1/2,0)$ ,  $(-1/2,0)$  and  $(0,-1/2)$  half-order spots, respectively. The antiferromagnetic domains morphologies appears to be fractals with their random shape and sizes. In each image, there are three different contrasts visible, the bright, light brown and dark brown domains. A closer observation reveals that the bright domains visible in figure 5.5 (a) turn light brown in figure 5.5 (d) and the bright domains visible in figure 5.5 (d) turn light brown in figure 5.5 (a). Similarly, the bright domains in figure 5.5 (b) are light brown in figure 5.5 (c) and vice-versa. Apparently there are three different types of domains [38,109]. The existence of four different (T)win domains can only be realized after addition of different images and comparing their contrast. In figure 7.6 the same zoomed in portion of the AFM-LEEM images has been presented as viewed through different half-order spots. In figure 7.6 (a) the AFM domains viewed through  $(0,1/2)$  spot is presented. Similarly figure (b), (c) and (d) represents AFM domains viewed through  $(1/2,0)$ ,  $(-1/2,0)$  and  $(0,-1/2)$  spots respectively. The sum of image 5.6 (a) and (d) is figure

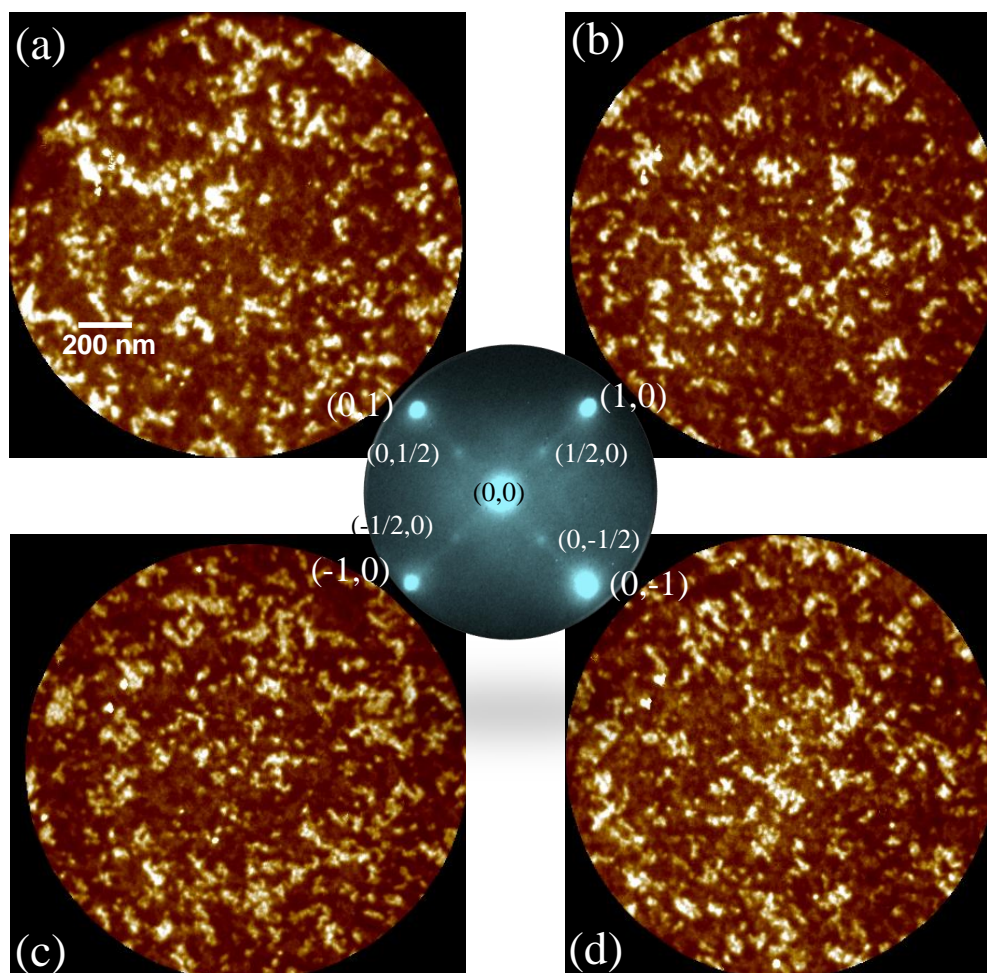


**Figure 7.5:** The LEED pattern of 60 ML NiO/Ag(001) film at 31 eV beam energy has been displayed at the center. Four  $p(2\times 2)$  half-order spots are visible. Their coordinates are denoted as  $(0,1/2)$ ,  $(1/2,0)$ ,  $(-1/2,0)$  and  $(0,-1/2)$ . The AFM-LEEM images corresponding to each half-order spot are displayed in figure (a), (b), (c) and (d) respectively.

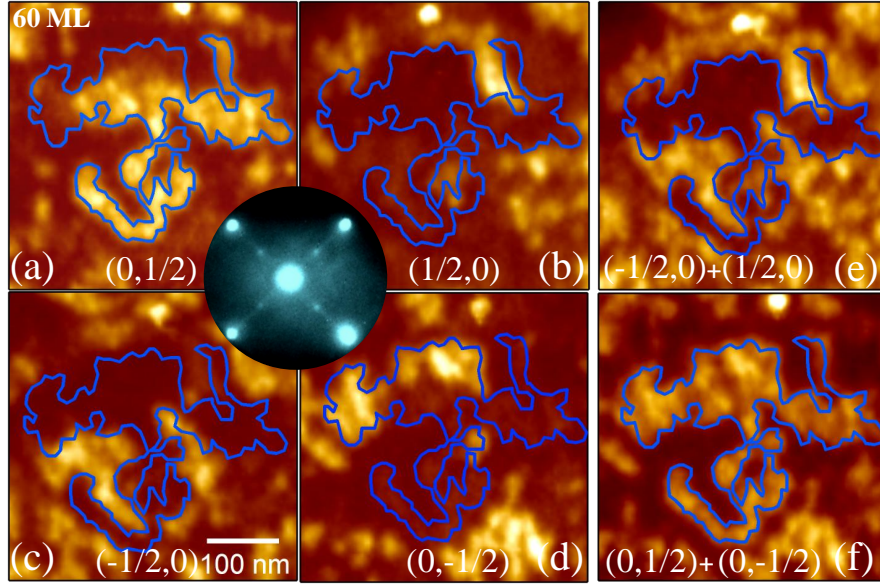


**Figure 7.6:** The LEED pattern of 60 ML NiO/Ag(001) film at 31 eV beam energy has been displayed at the center. Four  $p(2\times 2)$  half-order spots are visible. Their coordinates are denoted as  $(0,1/2)$ ,  $(1/2,0)$ ,  $(-1/2,0)$  and  $(0,-1/2)$ . A feature has been encircled by blue boundary to its contrast in different images when viewed through different half-order spots.

(f); whereas figure (e) is the result of summation of image (b) and (c). Now, as we focus on figure 5.6 (e) and (f), it is evident that they have opposite contrast, which mean the bright region of image (e) appears dark in image (f) and vice-versa. Looking at figure 5.6 (e) and (f) it appears that there are two different types of domains, bright and dark. However, each of these bright and dark domains behave differently (i.e. have different contrast) when viewed through different the half-order spots. This proves the existence of four (T)win domains in NiO film. It is worthwhile to mention that unpolarized electron diffraction can not probe the (S)pin domains as they are not sensitive to the antiferromagnetic spin axes.

In figure 7.6 (a), within the region encircled by the blue line, some part is bright and the rest of the domains are light brown. This happens because there are contributions from different (T)win domains. If the bright portion represent T1 (or T2) domain then the light brown portion must be contribution from T3 (or T4) domain. This concept will be clear from figure 7.7, which shows that the half-order spots in the x-y plane are the summation of projections from the half-order lattice points at different  $k_z$  position in the

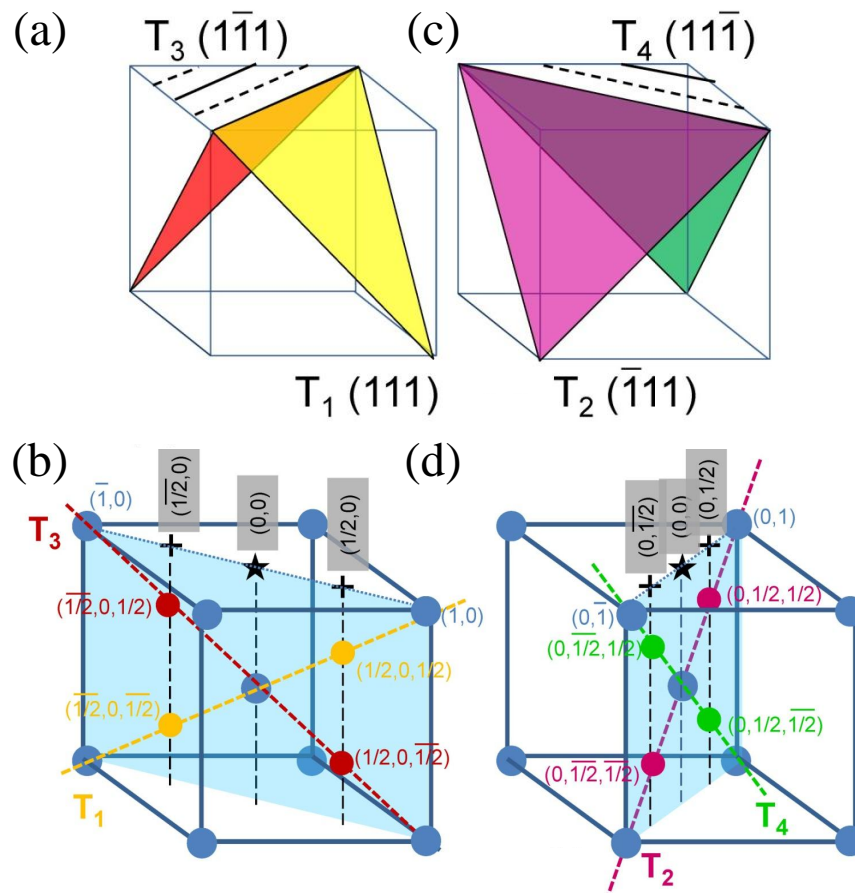


**Figure 7.7:** (a) The  $T_1$  and  $T_3$  domains/planes, (c) The  $T_2$  and  $T_4$  domains/planes, in real lattice. (b) The reciprocal lattice of figure (a) showing the  $T_1$  and  $T_3$  axes, (d) The reciprocal lattice of figure (c) showing the  $T_2$  and  $T_4$  axes, on which the 3D half-order lattice points are shown at exact middle of two integer order lattice points.

3D reciprocal lattice. In figure 7.7 (a) the  $T_1$  and  $T_3$  twin domains, which are basically the FM  $(111)$  and  $(\bar{1}\bar{1}\bar{1})$  planes, are shown. Along these two crystalline directions, the FM planes are antiferromagnetically ordered, as already discussed before. The 3D reciprocal lattice of this structure is displayed in figure 5.7 (b). The dotted yellow line which is the  $T_1$  axis corresponds to the  $T_1$  planes in real lattice, similarly the red line corresponds to the  $T_3$  planes. In the three dimensional reciprocal lattice, the yellow and red spheres on the yellow and red dotted lines respectively indicates the existence of three dimensional half-order lattice points. Their coordinates are assigned as  $(1/2, 0, -1/2)$  [ $-1/2$  is indicated as  $\bar{1}/2$  in figure 7.7] *etc.* in the 3D reciprocal lattice. In the LEED pattern of NiO film,

we observe  $p(2 \times 2)$  half-order spots which are basically projections of the 3D half-order spots in the reciprocal unit cell. The central (0,0) LEED spot which is the specular beam is marked as ‘\*’ and the half-order spots are indicated as ‘+’. Now it is evident that the (1/2,0) spot of figure 5.7 (b) is the result of projection from two bulk half-order spots with different  $k_z$  values which corresponds to T1 and T3 twin domains. As we shall see in a different section of this chapter, the electron energy dependence of different (T)win domains (figure 5.11) makes the contribution from T1 domain (yellow spot) to be larger than the T3 domain (red spot). Therefore, in the SPELEEM microscope if the (1/2,0) spot is chosen by the contrast aperture to image the sample, one may expect the illuminated regions to be T1 and T3 domains. But, since there is difference between contributions from them (T1 has greater contribution compared to T3), the illuminated regions will have two different contrast. Similar is the case for T2 and T4 domains as shown in figure 7.6 (d). These two different contrasts (‘bright’ and ‘light brown’) are visible in figure 7.6 (a) where the bright regions are contribution from T2 domains and the light brown regions are contributed by the T4 domains. Their contrast gets reversed when viewed through the half-order spot at orthogonal position which is (0,-1/2) as can be seen in figure 7.6 (d). These can also be explained from the schematic of figure 7.7 (d) where the relative position of the violet and green spots changes along the  $k_z$  axis at orthogonal coordinates. Therefore their projected contributions are also reversed, hence the light brown domain becomes bright and vice-versa.

Same thing is true for a 6 ML NiO film as shown in figure 7.8. In figure (a), the AFM-LEEM image of a 6 ML NiO film is shown with field of view  $1 \mu\text{m}$ . A line profile is drawn over few tiny nanodomains, the profile plot has been shown in figure (b). The FWHM shows that average domain size of these domains is about 20 nm. A square has been drawn on image (a). The zoomed in portion encircled by the square has been shown in figure (c), (d), (e) and (f) for different half-order spots. Addition of figure (c) and (d) results into image (g) whereas image (h) is the result of summation of image (e) and (f) respectively. All the four images as viewed through the four half-order spots are added together to obtain the image (i). Image (j) is the bright-filed image of the sample surface

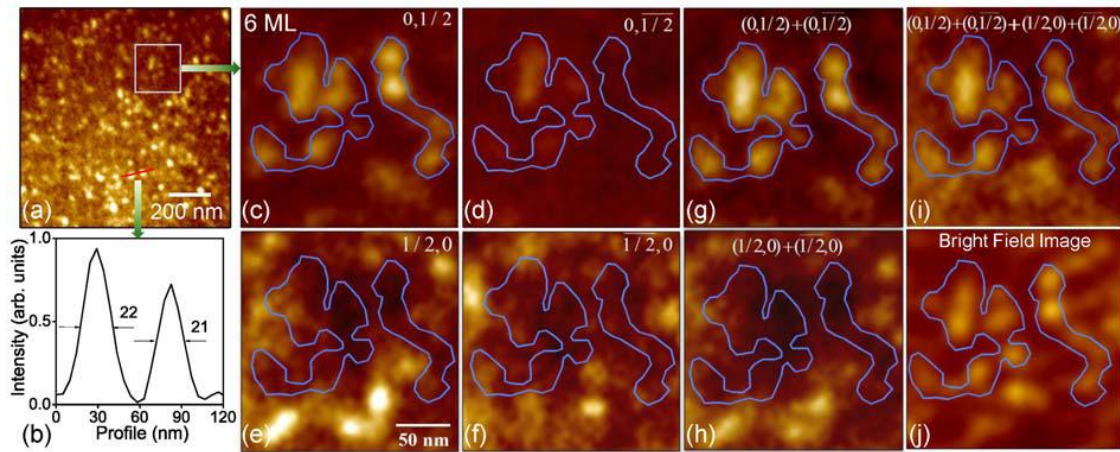


**Figure 7.8:** (a) AFM-LEEM image of the magnetic nanodomains of a 6 ML NiO film. (b) Line profile plot drawn over the domains shows average domain size to be 20 nm. (c), (d), (e) and (f) are same zoomed in portion of figure (a) viewed through  $(0,1/2)$ ,  $(0,-1/2)$ ,  $(1/2,0)$  and  $(-1/2,0)$ . (g) Addition of image (c) and (d). (h) Addition of image (e) and (f). (i) Addition of image (c), (d), (e) and (f). (j) Bright field image viewed through the  $(0,0)$  spot.

(as viewed through the specular  $(0,0)$  spot). Image (i) and (j) appears to be very similar, (though not same). Where image (j) represents the physical domains image (i) represents the sum of all the contributing magnetic domains which should be equivalent to the physical domains.

### 7.5.1.1 AFM-LEEM: Thickness dependence

As mentioned earlier, all the studies have been performed for four different film thickness i.e. 6, 18, 40 and 60 ML NiO films deposited epitaxially on Ag(001). Clearly the domains are fractal-like. Their evolution with film thickness can be realized from figure 7.9. For 60 and 40 ML films, well-defined domains are evidenced in AFM-LEEM images. For thinner films (18 down to 6 ML), AFM-LEEM shows the presence of AFM domains at the length scale of the crystalline granularity. We observe that during the initial stages of growth, nanoscale monodomain grains are nucleated in the thin films. Increasing further the film thickness, the AFM domains grow in size and coalesce to form bigger domains with fractals-like shapes. In figure 7.10, a graph has been plotted comparing the domain perimeter vs. area

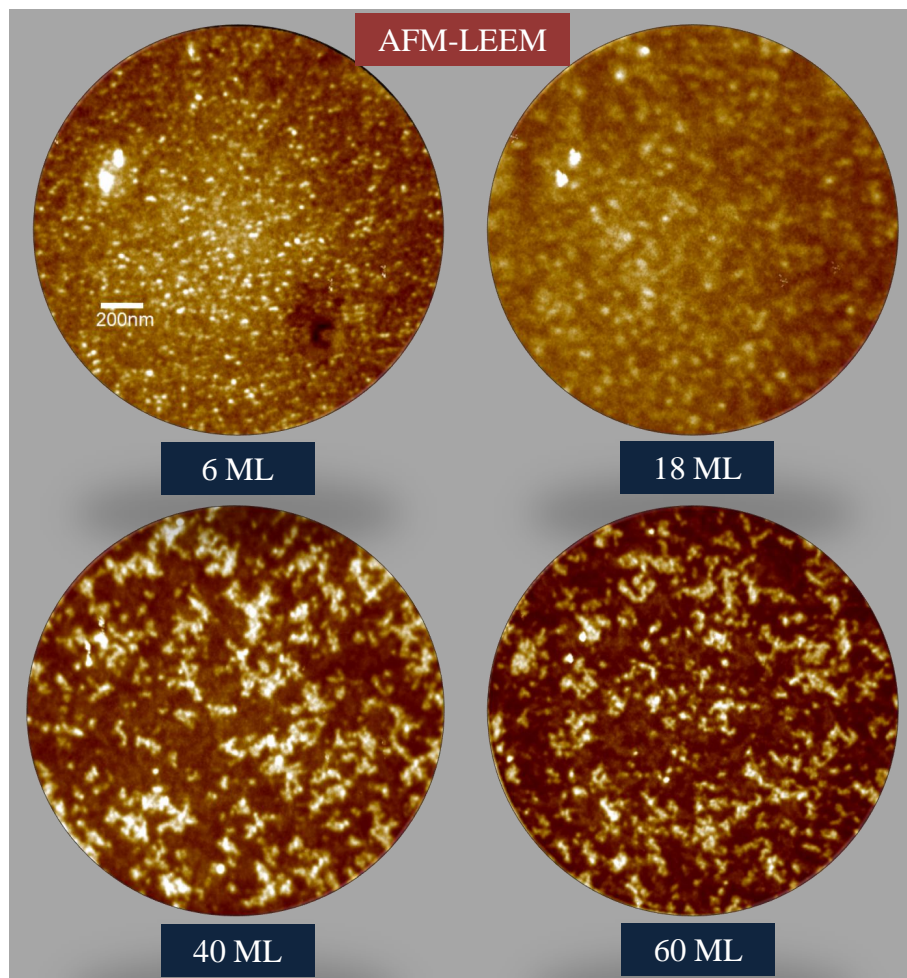


**Figure 7.9:** The magnetic (Twin) domains of NiO films of different thickness (6, 18, 40 and 60 ML) probed *via* AFM-LEEM technique. The same half-order spot (1/2,0) has been used for all the cases. All the images are collected at RT.

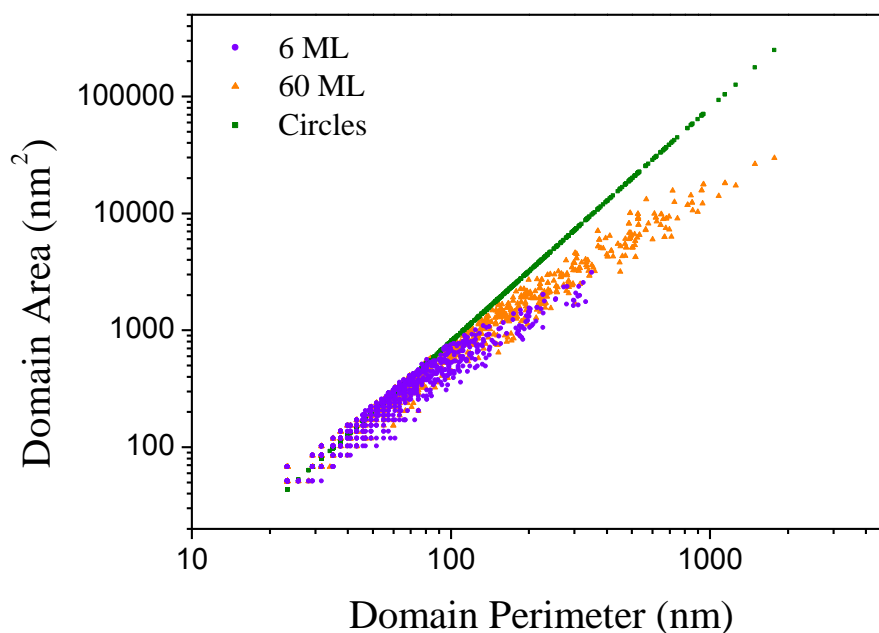


**Figure 7.10:** The area vs. perimeter plot for the fractal domains probed by AFM-LEEM in case of 6 ML and 60 ML NiO film.

for 6 ML and 60 ML NiO films. At lower film thickness (6 ML) the nanodomains are mostly circular in shape. As the film thickness increases domains coalesce and forms random fractal structures and their shape deforms from circular nature. The green straight line data points in figure 5.10, indicate to the areas of circles corresponding to the perimeters along the x-axis. Clearly, for the case of 6 ML film most of the domains are tiny and of circular nature whereas in case of 60 ML film a significant number of domains are deviated from circular shape and are fractal-like with random shapes.

### 7.5.1.2 Beam energy dependence of Twin domains

The electron beam energy dependence of the intensities of (T)win domains represents their  $k_z$  dependence in the reciprocal lattice. In figure 7.11 (a) and (b), AFM-LEEM images of the same magnetic domains shown for two different beam energies 23.5 and 30.5 eV, respectively viewed through a single half-order spot (0,1/2). Different types of (Twin) domains have been encircled by red, blue and black borders. In figure 5.11 (a), at beam energy of 23.5 eV, domains with blue, red and black boundaries are bright, grey and dark

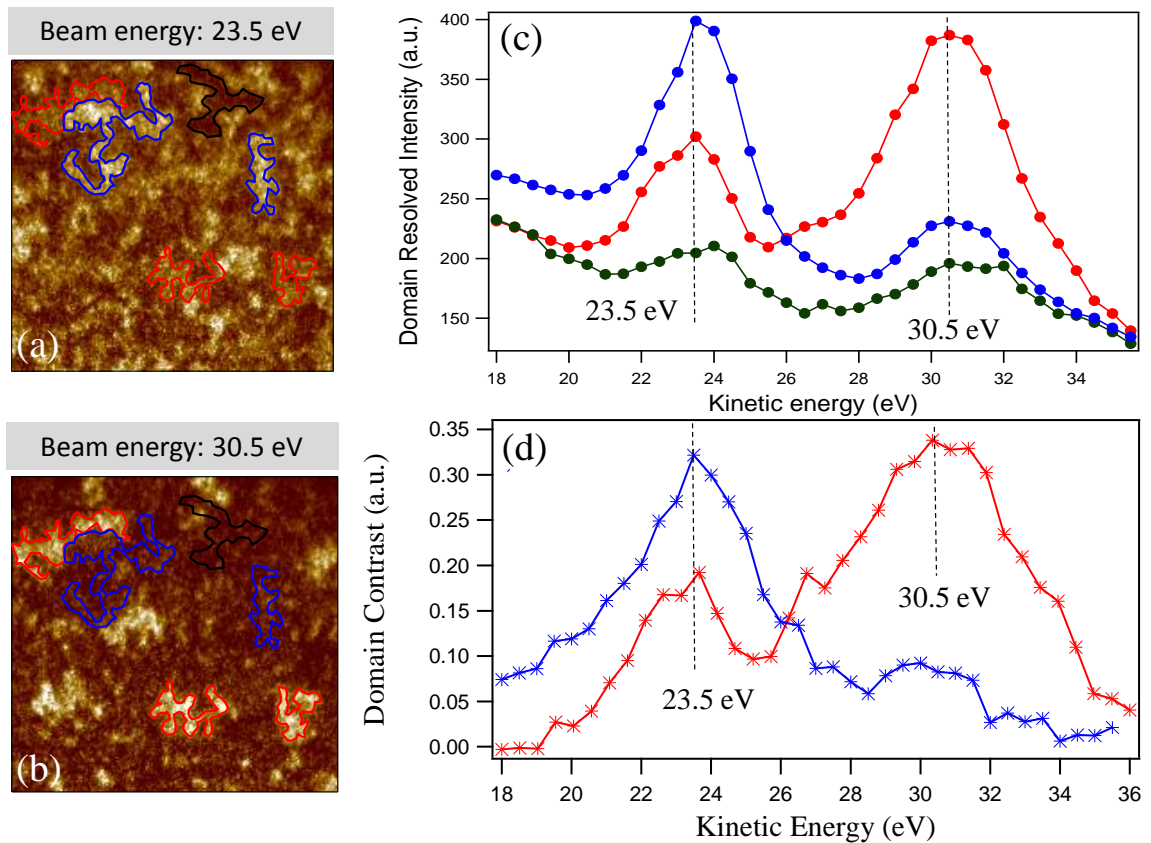


**Figure 7.11:** AFM-LEEM image of a 60 ML NiO film viewed through the  $(0,1/2)$  spot. (a) Beam energy 23.5 eV. (b) Beam energy 30.5 eV. (c) Intensity of different (T)win domains encircled by red, blue and black borders have been plotted at different beam energies. (d) The contrast of the bright and grey domains with respect to the dark domains (encircled by black) has been plotted.

intensities respectively. On the other hand, in figure 5.11 (b), for beam energy of 30.5 eV, domains with blue, red and black boundaries are light brown, bright and dark brown intensities respectively. Evidently, there is an exchange of contrast between the blue and red encircled domains. As discussed before, the half-order spots observed in a LEED pattern are sum of projections from two different bulk half-order lattice points [as shown in figure 7.7] situated at different  $k_z$  positions in the 3D reciprocal lattice. By changing the electron beam energy, one is actually probing different  $k_z$  values and hence the contributions from these bulk half-order spot varies, which is responsible for the different intensities of the twin domains at different beam energies. In figure 5.11 (c) intensities of the different twin domains (with blue, red and black boundaries) are shown as a function of beam energies. This plot (domain-resolved I-V spectra) clearly shows that the contrast between red and blue domains are reversed at beam energy of 23.5 and 30.5 eV. The black line represents intensity of the dark domains as visible in figures (a) and (b) which may be treated as background intensity for these images. Figure (d) represents intensities of blue and red bordered domains with respect to the background intensity. Actually, the dark domains are due to the the other two orthogonal Twin domains. Similar conclusions were obtained by our research groups in case of NiO(100) single crystal [38,109].

### 7.5.1.3 Thickness dependence of Néel temperature ( $T_N$ )

As already demonstrated earlier, existence of  $p(2\times 2)$  half-order spots in LEED for the case of NiO is a direct evidence of the surface antiferromagnetic ordering in the sample. After the discovery of the half-order spots by electron diffraction experiments of Palmberg *et al.* [34,104,105], many efforts have been successfully applied to measure the transition temperature from antiferromagnetic to paramagnetic phase of NiO crystal surface. LEED investigation has been performed by many research groups [108,109,284] in search of the transition temperature of the sublattice magnetization. Loudon [285] has recently observed the existence of  $p(2\times 2)$  half-order spots at (200 or 300 KeV energies) in transmission electron diffraction using a Transmission Electron Microscope (TEM). Where TEM studies by Loudon probed the bulk antiferromagnetism of NiO(100), almost all other LEED

experiments probed the surface magnetic order of NiO(100), where the Néel temperature was confirmed to be about 525 K. Using XMLD at Ni  $L_2$  edge, Altieri *et al.* [286] has discovered substrate effect on a 3 ML NiO film's Néel temperature, hence exploring how interfacial strain (compressive or expansive) modulates the magnetic structure and strength in NiO film. Using a 3 ML NiO(001) film grown on Ag(001) and an identically thin film on MgO(001) as model systems, they observed that the Néel temperature of the NiO film on the highly polarizable metal substrate is 390 K while that of the film on the poorly polarizable insulator substrate is below 40 K. They measured  $T_N$  of a 30 ML NiO film on Ag(001) to be 535 K.

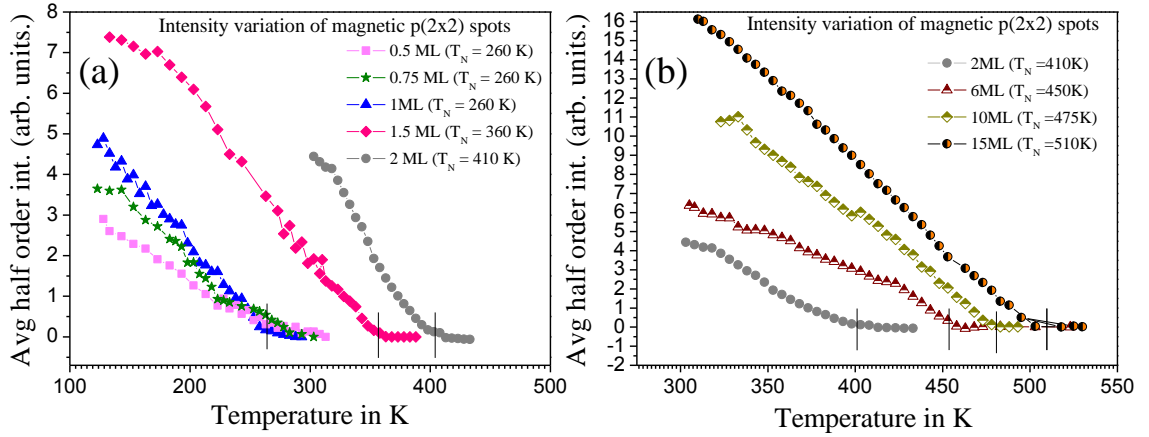


**Figure 7.12:** Average intensity variation of  $p(2 \times 2)$  half-order spots. (a) Lower thickness range, Film thickness 0.5, 0.75, 1, 1.5 and 2 ML. (b) Higher thickness range, Film thickness 2, 6, 10 and 15 ML. Electron beam energy of 24 eV is used.

Here, we have studied thickness dependence of Néel temperature in NiO film grown over Ag(001), mostly at the sub-monolayer thickness range and also at higher thickness. In figure 7.12 (a), the temperature dependence of average intensity of LEED half-order spots has been plotted for film thickness 0.5, 0.75, 1, 1.5 and 2 ML respectively. At RT (300 K), faint  $p(2 \times 2)$  magnetic superstructure is visible for 2 ML NiO film. The temperature dependence of the half-order intensity shows that  $T_N$  of a 2 ML NiO film is 410 K, which is close to the value measured by Altieri *et al.* [286]. Even at 1.5 ML film thickness, half-orders can be detected with highest sensitivity of the detection in the LEED pattern for beam energy of 24 eV at RT. Their intensity becomes prominent when the temperature of the

oxide film is lowered to liquid nitrogen.  $T_N$  of a 1.5 ML NiO film was measured by our experiments as 360 K. For the case of a 1 ML NiO film, no half-order spots were visible at RT. One has to cool the sample down to observe half-order spots which appears at 260 K which is the  $T_N$  for this thickness. Clearly, the antiferromagnetic strength of the film and hence the Néel temperature decreases with lowering the film thickness. For one-monolayer and sub-monolayer film thickness (0.5, 0.75 and 1 ML) Néel temperatures appear to be same, 260 K. In other words, within the submonolayer region, the transition temperature of the film does not drop further below the value of 1 ML film. Only the antiferromagnetic strength of the sample decreases at lower coverage as manifested by the decreased intensity at lower temperatures [see figure 5.12 (a)]. The probable reason behind this phenomena may be that below 1 ML, different film coverages are purely two dimensional (flat) film (formation of bi or multilayer NiO islands are not expected) and only size of the physical domains changes with coverages which determines the antiferromagnetic strength of the sample. Below 0.5 ML, no half-order spots have been observed with our ordinary four-grid LEED instrument in the laboratory, due to lower instrument sensitivities.

Néel temperature of the sample increases with film thickness beyond sub-monolayer range as can be seen in figure 7.12 (b). Néel temperature of 6 and 10 ML film are 450 K and 475 K, respectively. A 15 ML NiO film shows magnetic behavior close to the bulk NiO crystal, showing a Néel temperature about 510 K. Average half-order intensity decreases linearly with sample temperature and vanishes to zero close to the transition temperature of the sample in agreement with the previous studies.

The observation of magnetic half-order spots in the monolayer and sub-monolayer film thickness range is an interesting observation. It provokes questions on the origin of these magnetic spots in this reduced dimension and open up further scope for reinvestigation.

#### 7.5.1.4 XMLD at different film thickness

In addition to AFM-LEEM, we have also used XMLD technique to probe the AFM order of the NiO thin films on Ag(001). In figure 7.13, x-ray absorption spectra at Ni  $L_2$  edge is shown for 60 ML NiO grown on Ag(001) for both vertical and horizontal polarized soft

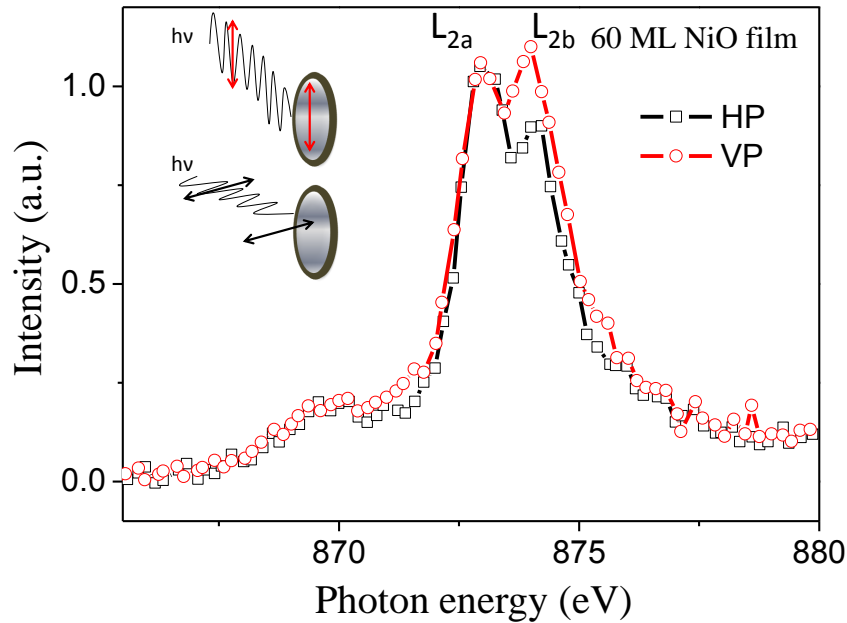


**Figure 7.13:** Higher XMLD signal for VP x-ray absorption indicating in-plane distribution of the Ni moments.

x-ray beam. The  $L_2$  peaks are quite well-resolved.  $L_{2a}$  and  $L_{2b}$  peak appearing at photon energies 873.0 and 874.1 eV, respectively. Both spectra has been normalized at  $L_{2a}$  peaks as the usual practice [38]. When vertically polarized (VP) x-ray is used, the second peak of Ni  $L_2$  edge i.e.  $L_{2b}$  has been increased in intensity, indicating presence of finite XMLD effect. However, the  $L_{2b}$  edge intensity is much weaker for horizontally polarized (HP) beam, indicating that the Ni moments are distributed in-plane, and not out-of-plane of the sample surface. These experimental results are very similar to our earlier spectroscopic XMLD work on NiO(001) thin films.

In figure 7.14, XAS data are shown at Ni  $L$  edges for different film thickness; 6, 18, 40 and 60 ML. Vertically polarized x-ray photon has been used for each case to probe the in-plane magnetic information of the samples. It is evident that multiplet splitting in thin film (6 ML case) is significantly weaker than thicker film (60 ML). For the 60 ML film, the  $L_3$  line appears at 857.2 eV photon energy. The splitted peaks of  $L_2$  are energetically well-resoled; the  $L_{2a}$  peak lies at 873.0 eV and the  $L_{2b}$  peak lies at 874.1 eV photon energy positions.

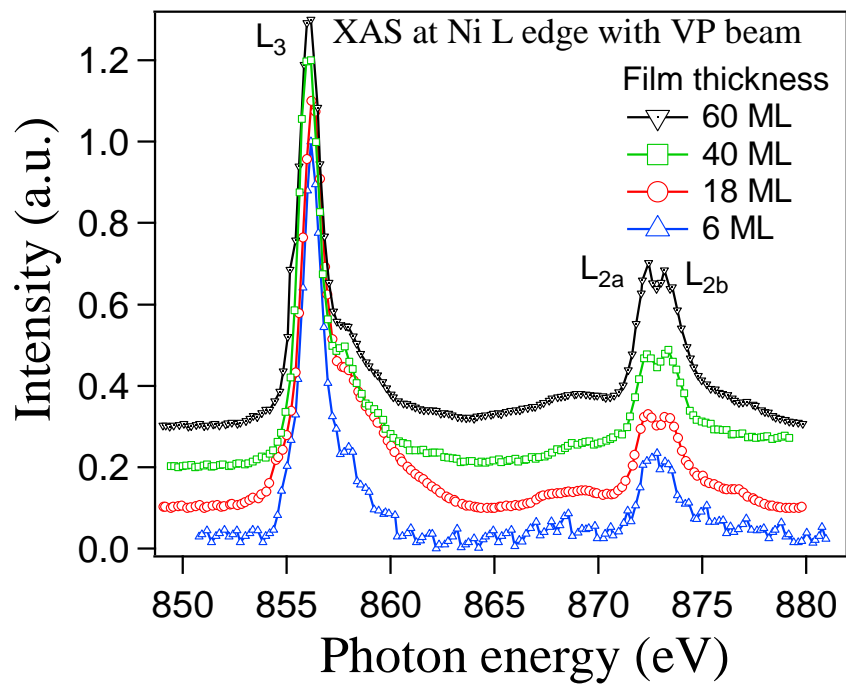


**Figure 7.14:** XAS at Ni L edge with vertically polarized (VP) x-ray beam. Film thickness 6, 18, 40 and 60 ML.

## 7.5.2 XMLD-PEEM: Spectromicroscopy

X-ray absorption images obtained with photoemission electron microscopy (PEEM) is uniquely able to provide morphological as well as elemental information on micro/nano structure at the surfaces of materials. The microscope, spatially resolves and images the electrons emitted from a sample as a result of absorption of photons of a particular energy. When linear polarized x-ray beam is used for absorption experiments, XMLD images can be obtained which maps the AFM contrast or a particular antiferromagnetic domain pattern. In case of XMLD imaging at the Ni  $L_2$  edges of NiO, two images are acquired at each peak within the NiO  $L_2$  resonance. The  $L_2$  resonance is chosen because the isotropic absorption intensity of the two peaks is very similar and the same exposure time can be chosen for the two images. The final XMLD image represents the ratio of the two images with opposite contrast. The details of this technique is already described in the second chapter of this thesis, therefore we may directly focus on the results from the XMLD-PEEM experiments. In our case, the two XMLD images has been collected at the Ni  $L_2$  edge photon energies of 873.0 eV and 874.1 eV. Their ratio has been chosen as the resultant XMLD-PEEM image which contains information of surface antiferromagnetic nanostructures.

### 7.5.2.1 XMLD-PEEM: polarization dependency

From the XAS  $L_2$  peak splitting at vertical and horizontal polarized beam [figure 7.13] and relative intensities of the components, it could be predicted that the Ni moments are arranged preferentially in-plane of the sample surface. Figure 7.15 (a) shows the XAS data at Ni  $L_2$  edge at for the VP and HP x-ray beam in case of a 60 ML NiO film. Both the spectral lines are normalized at  $L_{2a}$ . For the VP light, the data shows higher ‘magnetic dichroism’ effect compared to horizontal polarization. The XMLD-PEEM images for VP and HP light are shown in figure 7.17 (b) and (c) respectively. The VP beam probes the surface magnetic domains and their distributions in case of 60 ML NiO film on Ag(001), as seen in figure 7.17 (b). Since the Ni moments are ordered antiferromagnetically parallel to the sample surface, only VP light, whose polarization vector lies in the plane of the sample due to the experimental geometry, is able to probe the in-plane antiferromagnetic

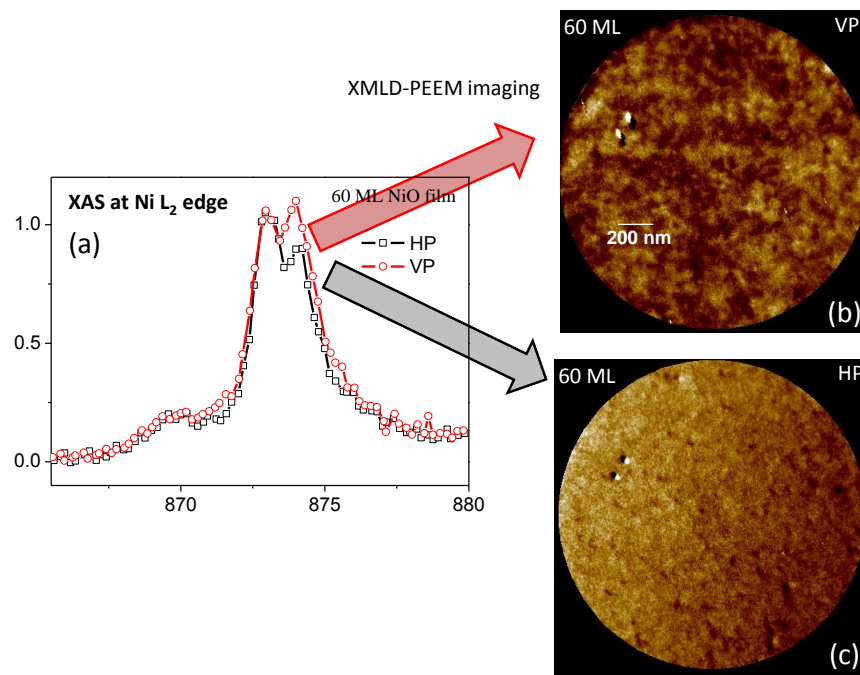


**Figure 7.15:** (a) XAS at Ni  $L_2$  edge in case of a 60 ML NiO film. Both the cases of VP and HP are shown. (b) XMLD-PEEM image for VP beam. (c) XMLD-PEEM image for HP beam.

domains. HP light has polarization vector normal to the sample surface and hence they are insensitive to the in-plane Ni moment distribution. Therefore, no such magnetic features with distinguishable contrast are visible with HP light, in figure 7.17 (c).

### 7.5.2.2 XMLD-PEEM: thickness dependent AFM domains

Ni  $L_2$  XMLD-PEEM images for NiO are sensitive to the relative orientation between the AFM spin axis, crystallographic axis, and light polarization vector providing access to all of the 12 AFM domains (the twin as well as spin domains [38]). In figure 7.16, the XMLD-PEEM images of 60 ML (figure 7.18 a), 40 ML (figure b), 18 ML (figure c) and 6 ML (figure d) has been shown with 2 micron field-of-view at the Ni  $L_2$  edge. Each of these images are obtained by taking the ratio of images collected using VP x-ray beams with energies at 873.0 eV and 874.1 eV. The illuminated features are the different surface magnetic domains visible on the dark background. Clear pattern with nano-sized domains are visible for the case of 60 and 40 ML films. The antiferromagnetic domain size are

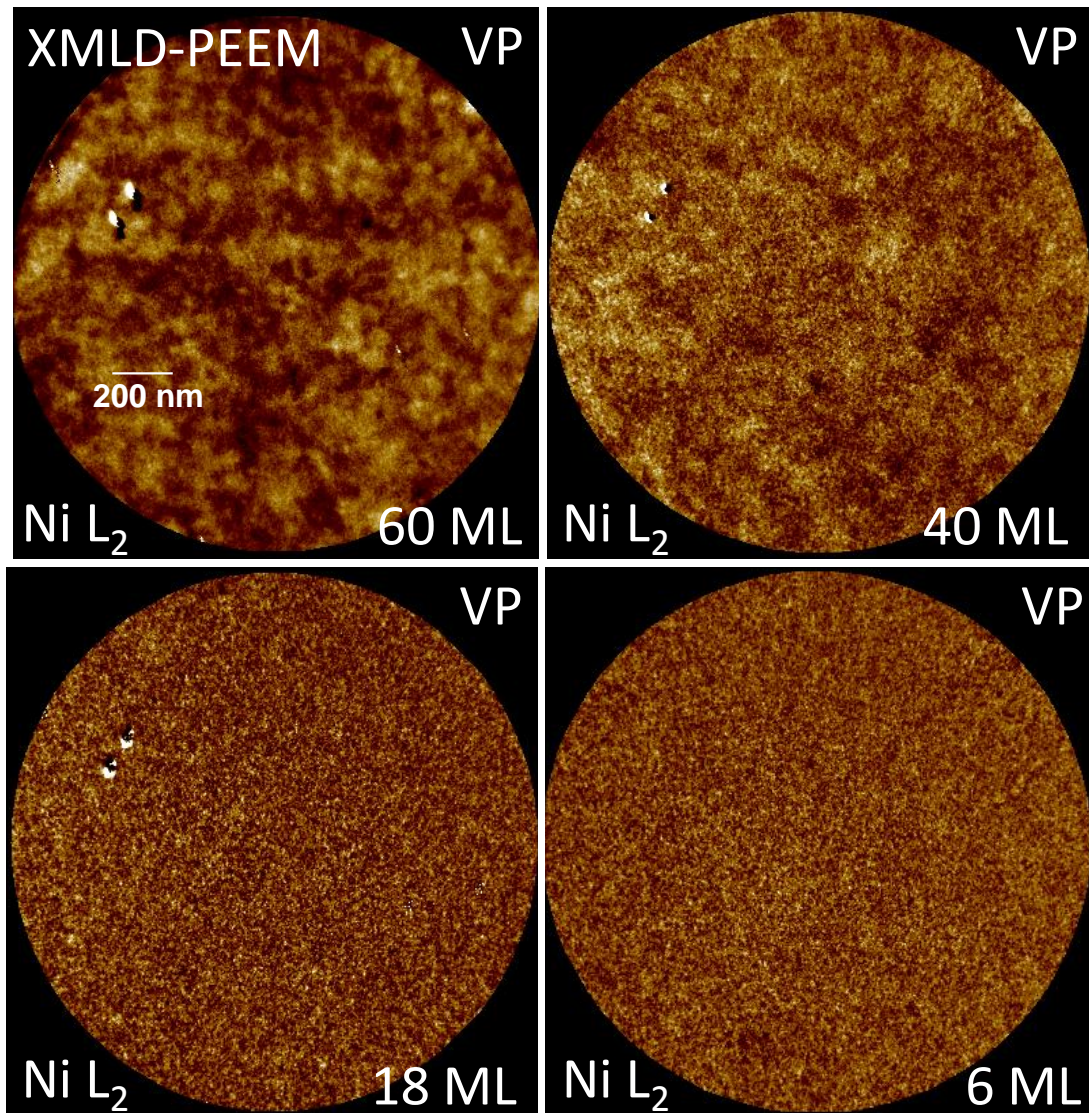


**Figure 7.16:** XMLD-PEEM image at vertically polarized x-ray beam. NiO film of different thickness (a) 60 ML (b) 40 ML (c) 18 ML (d) 6 ML.

limited by the physical domain boundaries in case of ultrathin NiO films (6 and 18 ML). These nanodomains domains are spatially well-resolved and distinguishable for the case of 60 and 40 ML NiO film. But, for the lower thickness of 18 and 6 ML, the domain sizes are extremely small and are beyond the scope of instrumental resolution. Hence, no distinct domains are visible for these low thickness and we only observe a grainy surface for these two cases.

### 7.5.3 Comparison between AFM-LEEM and XMLD-PEEM

Being two complimentary techniques to probe/image surface antiferromagnetism, AFM-LEEM and XMLD-PEEM has advantages and disadvantages over each other. Using XMLD technique is a well known approach to investigate into magnetic domains of NiO films. Based on the phenomena of x-ray absorption, XMLD-PEEM functions due to spin-orbit coupling, crystal field and multiplet splitting in materials. On the other hand, the working principle of AFM-LEEM is based on electron scattering by materials [109]. XMLD at Ni  $L_2$  edge can probe all the 12 AFM spin domains in NiO [259]. The angle between the polarization vector of the incident beam and the AFM axis determines the observed contrast between different domains. AFM-LEEM, in comparison, is insensitive to the AFM axes in the material. Since this technique is based on scattering phenomena, it mainly probes different crystal planes where there are AFM ordering of spins which are the Twin domains in NiO. Therefore this technique can only probe the twin domains and can not probe the spin domains. In figure 7.17, the same sample regions of the NiO films has been shown while two different techniques has been applied to probe them. In the upper row, all the images are probed by AFM-LEEM; while the lower row represents the XMLD-PEEM images of the same region for direct comparison. Figure 7.19 (a), (b), (c) and (d) are the AFM-LEEM images of 60, 40, 18 and 6 ML NiO films, respectively while figure 7.19 (e), (f), (g) are the XMLD-PEEM images of the 60, 40 and 18 ML films. Clearly, domain size decreases at lower film thickness. In figure 7.19 (h), average domain size has been plotted as a function of film thickness. This plot shows that the domain size almost saturates above 40 ML film thickness. An overall view of the growth of AFM nanodomains may be developed

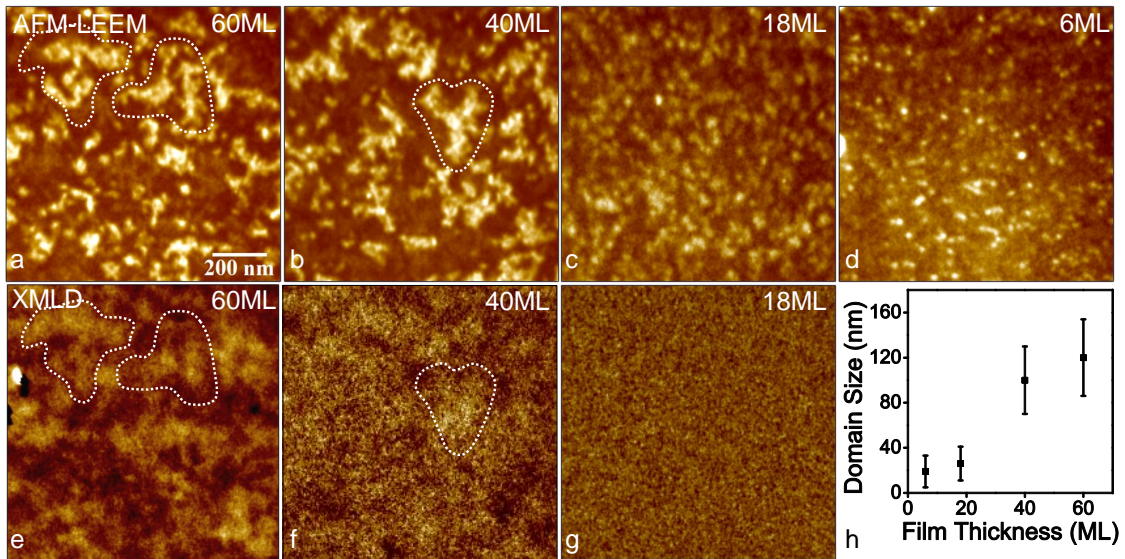


**Figure 7.17:** The zoomed in AFM-LEEM images of NiO films of various thickness. (a) 60 ML (b) 40 ML (c) 18 ML and (d) 6 ML. The corresponding XMLD-PEEM images at Ni  $L_2$  edge shown at the same region (e) 60 ML (f) 40 ML (g) 18 ML. (h) Film thickness vs. average domain size plot.

from this figure. At the very initial stage, nanoscale monodomain grains nucleate. Tiny domains formed at 6 ML NiO film coalesce to form bigger domains. In figure 7.19 (a), (b), (e) and (f), few domain features are encircled by dotted white boundaries. This helps in direct comparison between the AFM-LEEM as well as XMLD-PEEM techniques. When we compare these features in figure 7.19 (a) and (e), we observe that resolution in AFM-LEEM images are much better than XMLD-PEEM. In fact, for 18 and 6 ML NiO films the domain size goes beyond the resolution of XMLD-PEEM technique. While AFM-LEEM has spatial resolution of  $<10$  nm at RT, XMLD-PEEM has a spatial resolution about 30 nm. This shows that the AFM-LEEM has a dramatic advantage over the XMLD-PEEM for imaging the tiny magnetic nanodomains for low thickness films. As we see in figure 7.8, the AFM-LEEM can probe even the tiny monodomains of 20 nm size or lower in 6 ML NiO film.

When the encircled domain features of figure 7.17 are compared, they appears to be very similar, but not the same. This may be due to the fact that XMLD probes the magnetic spin domains whereas AFM-LEEM only probes the magnetic Twin domains. Another

reason which may be responsible behind the difference in the domain features probed by these two techniques is the probing depth of these two techniques. While the low energy electrons are highly surface sensitive (1-2 monolayers), the XMLD technique can probe the shallow surface layers, typically reaching to about 20-30 ML. Hence, another major advantage of AFM-LEEM is its ultra-sensitivity to the surface (top-layer) magnetism.

XMLD-PEEM has material (elemental) sensitivity. This advantage makes it useful to probe the magnetic domains of any antiferromagnetic surface buried under a magnetic or non-magnetic layer as well as the interfacial magnetic behavior which is beyond the scope of AFM-LEEM.

## 7.6 Summary

In this chapter, the antiferromagnetic domain structure of NiO has been discussed in detail. Two different techniques, first one, AFM-LEEM based on electron diffraction developed by us, second one, XMLD-PEEM based on polarized x-ray absorption, are used for imaging the antiferromagnetic twin and spin domains of NiO film of various thickness grown on Ag(001). Four different film thickness 6, 18, 40 and 60 ML of NiO films has been chosen for study. Moreover,  $p(2\times 2)$  magnetic superstructure has been found in LEED pattern for beam energies lower than 40 eV [see the figure 7.11 (c)]. Intensity variation of half-order spots has been performed to determine the Néel temperature variation with film thickness. Evolution of tiny nanodomains at the very initial stage (6 ML) and the nucleation of smaller domains to grow in their size with increasing film thickness (60 ML), can be framed through the magnetic domain imaging studies. The advantage of higher spatial resolution of AFM-LEEM over XMLD-PEEM can be realized in this context.

## Effect of oxygen vacancy defects on the electronic structure and magnetism of NiO film

### 8.1 Introduction

Detailed understanding of the role played by defects in ionic crystalline solids has been a matter of immense importance in the field of material research since decades. Point defects like cation or anion vacancies, interstitials, color centers as well as line defects like dislocation, slip *etc.* have strong impact on properties like electrical conductivity and strength of materials. Various theoretical and experimental efforts have been employed to study how the electronic structure of the strongly correlated prototype insulator NiO is affected by the simplest crystal imperfection like oxygen vacancy point defect ( $V_O$ ), also known as Schottky defect.

Reinert *et al.* [287] introduced holes in NiO crystal by doping  $Li^{3+}$  ions and created excess electrons in this oxide material by vacuum annealing the sample at sufficiently higher temperature, thus producing metallic  $Ni^0$ . They studied the effect of both *p* and *n*-type doping on the core level and valence band electronic structure by XPS, UPS and EELS (electron energy loss spectroscopy). Altieri *et al.* [288] performed rigorous XPS studies on Ni *2p* core level in  $Ni_xMg_{1-x}O$  crystals with  $0.03 < x < 1$  and compared the experimental data with their cluster model calculations in the impurity limit. Another example of p-type

doping the NiO crystal and studying the core and valence electronic structure with XPS and BIS was demonstrated by Sawatzky and his group [289]. Valeri *et al.* [290] have done a detailed study of Ni to O stoichiometry dependence on the surface structure and electronic structure of ultrathin NiO film deposited on Ag substrate using quantitative XPS analysis and LEED. Many other groups have studied the creation of Ni and O vacancy defects and production of Ni<sup>3+</sup> and O<sup>-</sup> ions within the film, surface adsorption of oxygen containing species like H<sub>2</sub>O, CO *etc.* and their effect on the core as well as valence electronic structure in last few decades [291–293].

The aim of our present work is to reinvestigate the effect of anion (oxygen) vacancy on the core and valence level electronic structure in a NiO epitaxial film grown on top of Ag(001) crystal by XPS and UPS studies. A thorough study on the creation of these V<sub>O</sub> sites and formation of metallic Ni<sup>0</sup> by Ar<sup>+</sup> bombardment as well as high temperature UHV annealing is performed by us. The evolution of defect states at the film surface with Ar<sup>+</sup> sputtering time and their partial and complete destruction as a result of vacuum/oxygen anneal is rigorously studied where the comparison between surface and bulk electronic states have been drawn with the help of angle-dependent XPS studies. A LEED study of surface structure of the NiO film under sputtered and annealed conditions are also discussed in brief.

As shown in the previous chapter, LEED pattern at low electron energy reveals the presence of surface antiferromagnetism exposing the existence of  $p(2\times 2)$  magnetic half-order spots. The Néel temperature of NiO films has also been determined for various film thicknesses. In this chapter, we present the effect of defects (mostly oxygen vacancy and surface disorder) on the magnetic strength of NiO/Ag(001) film *via* change in the half-order intensity and the Néel temperature of the sample.

NiO, with its rocksalt structure have lattice constant of 4.18 Å. Hence it grows epitaxially on Ag(001) (lattice constant 4.09 Å) with only 2% lattice mismatch. Being a strongly correlated material, NiO has been well studied to understand the correlation effects of localized  $d$  electrons and its relation with the insulating nature and also the antiferromagnetic properties of this transition metal oxide system. In the core level excitation process,

the creation of a core hole in Ni  $2p$  is accompanied by a strong coulomb repulsion with the holes within the localized  $3d$  orbital. The lowest energy state will thus be of the form  $c^{-1}3d^{n+1}L^{-1}$ , here  $c^{-1}$  represents a core hole,  $L^{-1}$  is hole created in ligand oxygen band; whereas the ground state is predominantly of  $3d^n$  character [244]. The electronic structure of NiO film has already been discussed in detail in earlier chapter. In this chapter, the relative intensities of several peaks and appearance of new features both in valence and conduction band electronic structures have been focussed on.

## 8.2 Experimental details

### 8.2.1 Effect on electronic structures

A direct way to create oxygen vacancy in the NiO film is  $\text{Ar}^+$  ion sputtering. When the surface of a multicomponent system like NiO is sputtered, there is always a preferential sputtering occurs; i.e, the cross-section for sputtering for Ni and O are very different, which results in the preferential sputtering. The preferential sputtering also depends on the ion beam energy. For lower ion beam energies (about 500 eV), the sputtering yield for oxygen is much higher in comparison to Ni. This yields a far higher number of oxygen vacancies are created in comparison to the Ni vacancies. So here, one may ignore the effect of the Ni vacancies on the electronic structure up on mild sputtering of NiO film.

Oxygen vacancy defects may also be created in the deposited NiO films by annealing the sample in UHV at higher temperature which removes oxygen from the film surface affecting Ni:O stoichiometry. Both process were applied in our experiments, for the creation of oxygen vacancy defects in the NiO thin film surface.

#### 8.2.1.1 Modification of core levels

The cation core level electronic structure is significantly modified as anion vacancies are created by inert ion ( $\text{Ar}^+$ ) bombardment on the NiO film surface. The Ni  $2p$  and O  $1s$  core level x-ray photoemission spectra probed by monochromatic Al  $K_\alpha$  are presented in figure

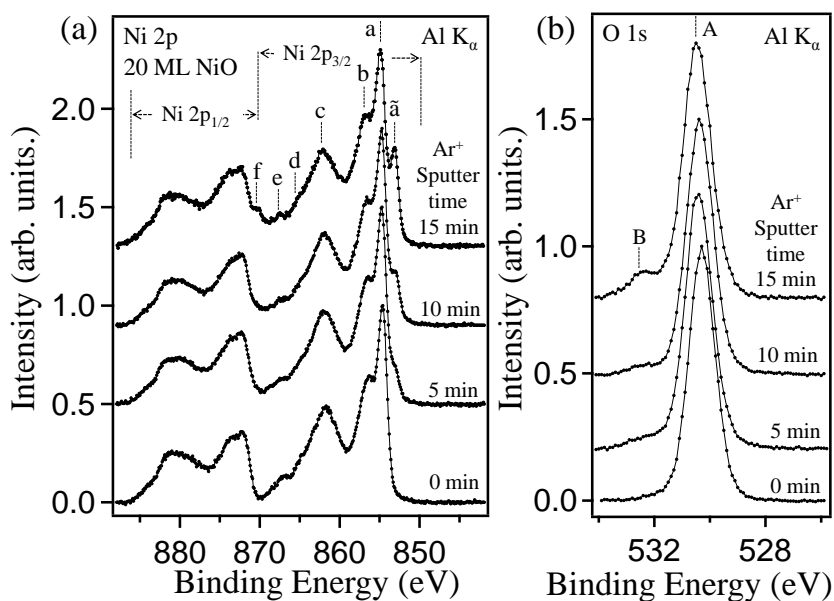


**Figure 8.1:** XPS core levels (a) Ni  $2p$  (b) O  $1s$  of 20 ML NiO film probed by Al  $K_{\alpha}$  under different  $\text{Ar}^+$  sputter time.

8.1 (a) and (b), respectively as a function of mild (500 eV)  $\text{Ar}^+$  ion sputtering duration. Bombarding the 20 ML NiO/Ag(001) film by inert ions desorbs the oxygen atoms from the film, increasing the number of oxygen vacancy sites at the film surface. This results in creation of metallic nickel ( $\text{Ni}^0$ ) sites mostly at the top surface and shallow surface region of the oxide film. As  $\text{Ar}^+$  is sputtered over increased time period, an extra feature appears at 1.6 eV lower binding energy position than the Ni  $2p_{3/2}$  main peak [marked as ‘a’] ( $c^{-1}d^9L^{-1}$ ) at 854.6 eV. This lowest binding energy feature [denoted as ‘ $\tilde{a}$ ’] corresponds to metallic  $\text{Ni}^0$  formed at the oxide film surface which increases in intensity as more oxygen vacancies are created with increased sputtering time. The satellite feature ‘b’ ( $c^{-1}d^9$ ) which lies at 1.5 eV higher binding energy than Ni  $2p_{3/2}$  main line increases almost 3% under Ar sputter of 15 min. This feature which was attributed to  $\text{Ni}^{3+}$  sites present in the sample by many groups [294] in earlier days is now well established to originate from the non-local screening process [289, 295], where electrons are contributed to a nickel site not from the ligands associated with that site but from the ligands of neighboring nickel sites. Satellite feature ‘c’ ( $c^{-1}d^{10}L^{-2}$ ) as well as ‘d’ ( $c^{-1}d^8$ ) does not undergo any significant modification due to Ar bombardment. Intensity of feature ‘e’ goes down and the feature ‘f’ which

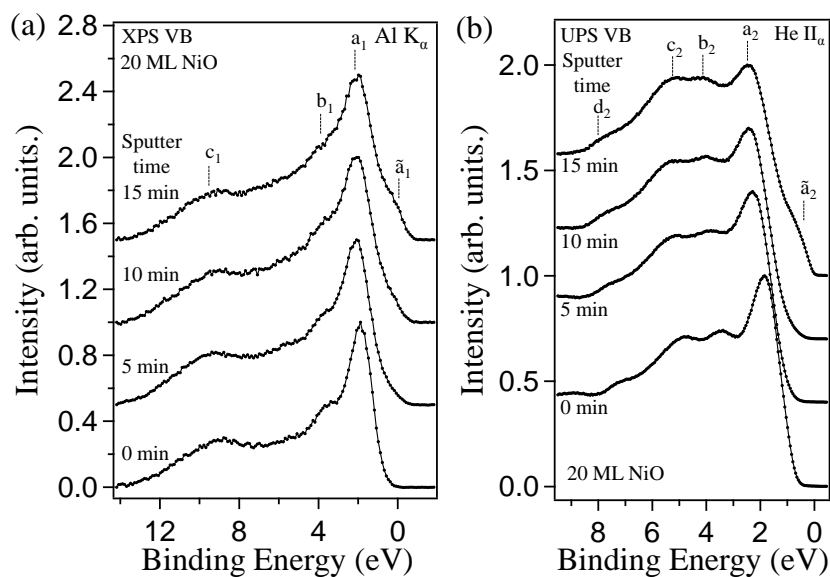


**Figure 8.2:** Valence band spectra of 20 ML NiO film under different Ar sputter duration probed by (a) Al  $K_{\alpha}$  (1486.6 eV) x-ray source (b) He  $II_{\alpha}$  (40.8 eV) ultraviolet photon source.

corresponds to  $2p_{1/2}$  peak of metallic nickel  $Ni^0$  gets enhanced under Ar ion sputtering for longer duration. The overall Ni  $2p$  spectrum shifts towards higher binding energy of about 270 meV under 15 min Ar bombardment. The O  $1s$  peak on the other hand shifts towards 200 meV higher binding energy position due to 15 min of Ar sputter [figure 8.1 (b)]. Moreover an extra hump (denoted as ‘B’) gradually appears in the spectra at 1.9 eV higher binding energy position from O  $1s$  main peak (marked as ‘A’) which may be the contribution from surface impurities due to sputtering.

### 8.2.1.2 Modification of valence band

Along with modifications in the core levels there occurs changes in the valence band of NiO also with  $Ar^+$  ion sputtering duration. In figure 8.2 (a), the gradual changes in the valence band (VB) electronic structure of a 20 ML NiO film is shown where monochromatic Al  $K_{\alpha}$  photon source ( $h\nu = 1486.6$  eV) is used to excite the valence electrons. The main line which is  $d^8L^{-1}$  state near 2 eV binding energy is denoted as ‘ $a_1$ ’ corresponds to Ni  $3d$  state and the feature at about 1.5 eV binding energy above the main line marked as ‘ $b_1$ ’

corresponds to mixture of Ni  $3d$  and O  $1s$  bands. Another feature denoted by ‘ $c_1$ ’ which corresponds to the  $d^7$  state is a satellite state at 7.0 eV higher binding energy from the main line. Relative intensity of both the feature ‘ $b_1$ ’ and ‘ $c_1$ ’ with respect to the the main line decreases with Ar ion sputtering. The 15 min  $\text{Ar}^+$  bombarded surface shows a distinct feature close to the Fermi level which is denoted by ‘ $\tilde{a}_1$ ’. Intensity of this state increases gradually as a function of sputtering time. For mild sputtering, these DOS close to Fermi level may be considered a result of oxygen vacancy defects created by  $\text{Ar}^+$  ion sputtering; though after longer sputtering duration the contribution of surface metallic nickel to this state can not be ignored. There is a spectral shift of about 200 meV of the valence band towards higher binding energy under  $\text{Ar}^+$  sputter. Figure 8.2 (b) shows the VB of the same film as shown in figure 8.2 (a) probed by ultraviolet He  $\text{II}_\alpha$  photon source ( $h\nu = 40.8$  eV). The features ‘ $a_2$ ’, ‘ $b_2$ ’ and ‘ $c_2$ ’, ‘ $d_2$ ’ corresponds to the Ni  $3d$  and O  $2p$  bands respectively. The relative intensity of Ni  $3d$  main peak at 2 eV (denoted as ‘ $a_2$ ’) decreases significantly as a result of bombardment for longer duration. The defect states near Fermi level (denoted as ‘ $\tilde{a}_2$ ’) is of higher intensity while probed by ultraviolet photons rather than x-ray which indicates that the defect states are contributed mainly by the top most surface of the NiO film where the number of  $V_O$  sites are maximum. Under mild  $\text{Ar}^+$  sputtering for shorter duration (5 min), there occurs maximum spectral shift (about 400 meV); however no defect states are observed close to Fermi level. Under sputter for longer duration (15 min) there occurs no further significant spectral shift anymore but the defect states evolves gradually.

### 8.2.1.3 Angle dependent XPS studies: Core levels

To have a qualitative study of the defect state density distribution along the surface normal of the film, angle dependent Ni  $2p$  and O  $1s$  core level studies were performed using monochromatic Al  $K_\alpha$  x-ray source. Due to limited inelastic mean free path, the x-ray photoelectrons emitted at a grazing angle ( $\theta = 70^\circ$ ) comes mostly from the surface region of the film carrying more surface information, whereas the normally emitted ( $\theta = 0^\circ$ ) electrons rather consists more of bulk information. In figure 8.3 (a), the angle dependent x-ray core level studies of Ni  $2p$  are shown under different conditions. When the as prepared NiO film

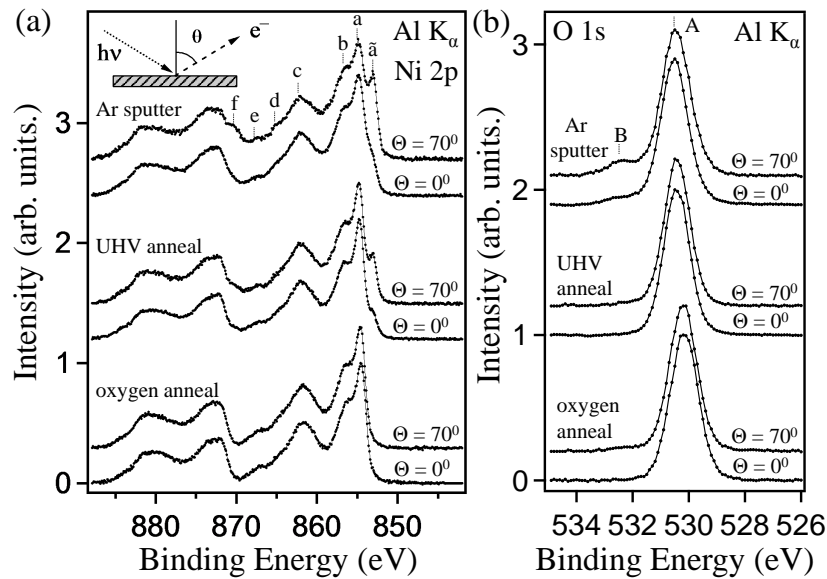


**Figure 8.3:** Angle dependent XPS study for two different electron emission angles; normal emission ( $\theta = 0^\circ$ ); grazing emission ( $\theta = 70^\circ$ ); core levels (a) Ni  $2p$ . (b) O  $1s$ . NiO film thickness 20 ML.

is sputtered by  $\text{Ar}^+$  ions for sufficient duration significant amount of oxygen vacancies are created mostly close to the 20 ML NiO surface layers. Nickel to oxygen stoichiometry at bulk region of the film is expected to be less disturbed compared to the surface region. A 40% increment in the metallic nature of the sample is observed close to the surface from the grazing emission data compared to the normal emission spectra. As the sputtered film is annealed in UHV at 573 K for 30 min, a significant reduction in the quantity of metallic nickel at the surface and shallow surface region under grazing angle electron emission is observed which directly implies the oxygen vacancy reduction on the film surface. UHV annealing for sufficient time duration triggers the drifting of oxygen atoms from the bulk of the film towards the surface region to help in partial compensation of the surface  $V_O$  sites. While under annealing at same temperature in oxygen environment hardly any change can be observed in the Ni  $2p$  core level between normal and grazing electron emission angle implying almost a complete reduction of oxygen vacancy defect in the sample surface and a homogeneous Ni:O stoichiometry at different depths of the film. Under  $\text{Ar}^+$  ion sputtering, the O  $1s$  peak shows an extra feature at higher binding energy position whose intensity gets prominent at grazing angle emission [shown in figure 8.3 (b)]. This extra component

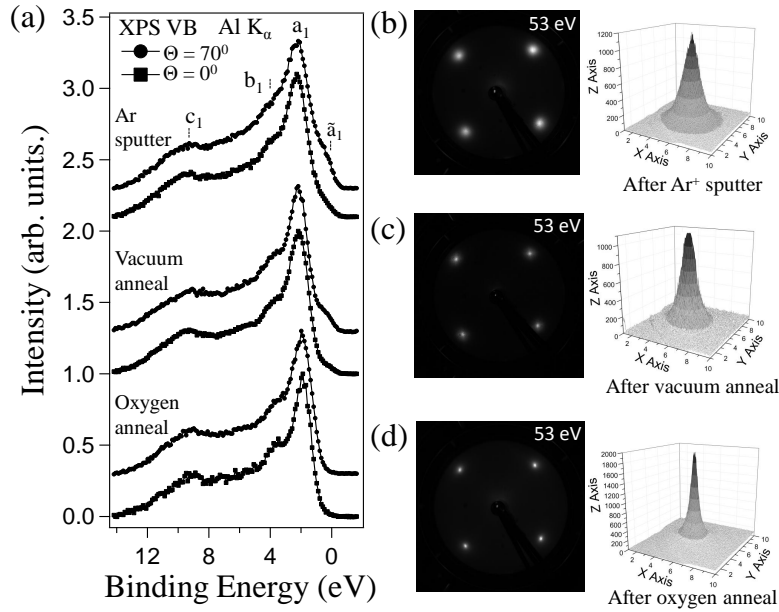


**Figure 8.4:** (a) Angle dependent XPS valence band study of 20 ML NiO film for electron emission angles; normal emission ( $\theta = 0^\circ$ ); grazing emission ( $\theta = 70^\circ$ ) for Ar sputtered, vacuum annealed and oxygen annealed film.  $p(1 \times 1)$  LEED pattern of 20 ML NiO film at 53 eV (b) Ar sputtered (c) UHV annealed (d) Oxygen annealed.

vanishes under both vacuum and oxygen anneal. There are no differences between the spectral characteristics of O  $1s$  peak between the normal and grazing emission angles after annealing the film. A spectral shift of 300 meV of the O  $1s$  core level towards the higher binding energy under  $\text{Ar}^+$  ion sputter compared to the oxygen annealed film is notable.

#### 8.2.1.4 Angle dependent XPS studies: Valence band

The defect states are localized at the near surface region of the film whereas the bulk of the NiO film remains quite unperturbed under  $\text{Ar}^+$  ion sputtering as evident from figure 8.4 where in the XPS VB the feature ' $\tilde{a}_1$ ' near the Fermi level only exists while the surface of the film is probed by x-ray at  $70^\circ$  electron emission angle. In figure 8.4, the XPS VB also shows reduction of the defect states at the surface under UHV anneal and almost complete compensation of the oxygen vacancy sites under oxygen anneal of the film. Intensity of the feature ' $b_1$ ' reduces significantly at the surface of the film under  $\text{Ar}^+$  sputter, probably due to quantitative reduction in surface oxygen whereas the satellite ' $c_1$ ' ( $d^7$  state) intensity

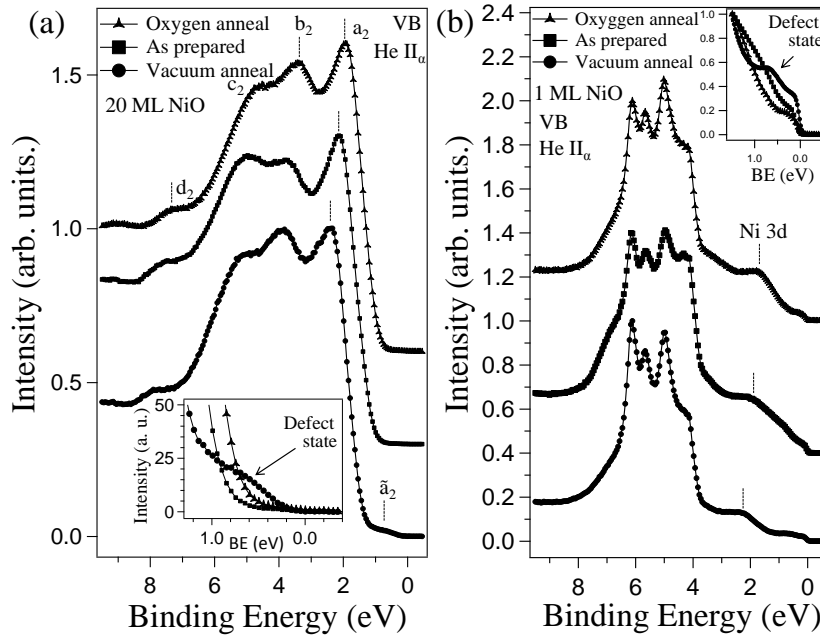


**Figure 8.5:** UPS valence band of NiO film at different conditions; As prepared, vacuum annealed and oxygen annealed case. (a) 20 ML NiO/Ag(100). (b) 1 ML NiO/Ag(100). Inset: appearance of defect state near Fermi level after vacuum annealing the film.

does not undergo through any distinguishable change. The LEED pattern of the film surface at 53 eV electron beam energy is shown for Ar sputtered, UHV annealed and oxygen annealed cases in figure 8.4 (b), (c) and (d), respectively. The 3D profile of (1,0) LEED spot for each case are displayed in the right side of every LEED image. The appearance of circular ‘halo’ surrounding the LEED spot is prominent for the Ar<sup>+</sup> sputtered film; on the other hand, the oxygen annealed film shows the sharpest peaks with minimum FWHM value.

### 8.2.1.5 Effect of vacuum and oxygen annealing

Annealing the NiO film at elevated temperature in UHV for sufficient time duration results in reduction of NiO by removal of oxygen atoms from the sample surface creating vacancy sites in the shallow surface region and introducing slight metallicity at the film surface. The Ni<sup>0</sup> centers pin the Fermi energy depending on the amount of V<sub>O</sub> sites produced. Figure 8.5 (a) (main panel) shows 450 meV shifting of the feature  $a_2$  of the NiO VB towards

higher binding energy under vacuum anneal at 573 K for 30 min as a result of  $E_F$  pinning. A shift of 200 meV towards the higher binding energy is also observed in the Ni  $2p$  core level under vacuum anneal (not shown here). Vacancy defect states are created near 0.5 eV binding energy close to the  $E_F$  as shown in the inset of the figure 8.5 (a). The effect of UHV annealing on the stoichiometry of the film is more prominent in case of 1 ML NiO film because of its reduced dimension. In figure 8.5 (b), the VB electronic structure of 1 ML NiO film (probed by He  $II_{\alpha}$ ) is shown for the as prepared film, UHV annealed film and oxygen annealed film, respectively. The Ni  $3d$  band shifts 0.5 eV towards higher binding energy after UHV anneal due to Fermi level pinning whereas the Ag  $4d$  bands show no shifting. In the inset of figure 8.5(b), the appearance of an extra band corresponding to defect states is observed at 0.6 eV binding energy position. APRES image [not shown here] demonstrates the non-dispersive character of these bands, as expected in case of the vacancy states.

### 8.2.1.6 Discussion

Sufficient  $Ar^+$  ion bombardment as well as high temperature vacuum annealing produces significant amount of oxygen vacancies in the NiO film. These defect sites mostly confined within the top few layers resulting in metallic Ni enriched oxide surface as evident from our angle dependent photoemission studies. In case of Ni  $2p$  XPS, the main line ‘a’ at 854.6 eV and the 1.5 eV higher energy satellite ‘b’ appears due to the local and non-local screening effect, respectively. The electrons contributed to the nickel atom by octahedrally surrounding ligand oxygen sites produces the local screening effect while electrons contributed by the ligands of neighboring nickel sites create the non-local screening effect [289,295]. Theoretical cluster model calculations shows that breakage of octahedral symmetry at the top surface of NiO decreases electron contribution from neighboring ligands which in effect increases the contribution of non-local electron screening process [296]. Satisfying the theoretical calculations, experimental evidences are there showing relative increment of non-local screening satellite peak ‘b’ when surface region of NiO rather than the bulk contributes more in the XPS spectra [297]. Moreover, the removal of surface oxygen atoms by  $Ar^+$

sputter or UHV annealing results in creation of anion vacancy sites surrounding the nickel atoms at the film surface which reduces the effective local electron screening process thus promoting the non-local screening effect. Therefore in Ni  $2p$  spectra, 15% increment of feature ‘b’ is observed for Ar<sup>+</sup> bombarded film while photoelectrons are collected at a grazing angle as shown in figure 8.3 (a). Within the binding energy range of 858-870 eV, the screened satellite ‘c’ ( $c^{-1}d^{10}L^{-2}$ ) and the unscreened satellite ‘d’ ( $c^{-1}d^8$ ) does not show any significant change in their intensity under Ar<sup>+</sup> sputtering at 0.5 keV similar to the observations of McKay *et al.* [291]. They reported a distinct enhancement in these features only under sputtering by high energy (5 keV) Ar<sup>+</sup> ions. The appearance of a small hump at 1.9 eV higher binding energy from the O  $1s$  main peak under Ar<sup>+</sup> bombardment for sufficient time as well as enhancement of this peak at the sputtered film surface compared to the bulk is reported by many earlier research works [298,299]. Roberts and Smart [299] reported the higher binding energy component of O  $1s$  (marked as ‘B’) and Ni  $2p_{3/2}$  (marked as ‘b’) can be correlated with oxygen defect structure. Norton *et al.* suggested that the high binding energy peak of O  $1s$  originates due to formation of Ni<sup>3+</sup> ions at the film surface as a result of Ar bombardment. Kim and Winograd [298] proposed that there is good probability that Ni<sub>2</sub>O<sub>3</sub> is formed on nickel oxide surfaces except Ni is oxidized at high temperature while many other studies denied the formation of Ni<sub>2</sub>O<sub>3</sub> on this oxide surface. Evolution of the O  $1s$  higher binding energy component under chemisorption of oxygen containing species is experimentally well established [255,300]. Uhlenbrock *et al.* [294] has experimentally demonstrated that an Ar sputtered NiO surface becomes quite reactive for adsorption than a freshly cleaved surface [294]. They have shown that the reactivity of NiO surface highly increases upon severe sputtering dosage. In accordance with their observation no trace of this high binding energy component is observed in our experiment in case of freshly prepared NiO film in our study. This component is only present when the oxide film is Ar sputtered for sufficient time and its intensity becomes prominent while performing the grazing excident experiments. It vanishes completely when the sputtered film is annealed in UHV or in O<sub>2</sub> environment as evident in our data of figure 8.3 (b). It is observed from figure 8.4 (a) that the defect states are still persistent within the oxide film

surface even after UHV annealing. They vanish completely only under oxygen annealing. Therefore it may be concluded that the higher binding energy component of O  $1s$  is in no way directly connected to the creation of  $V_O$  defects or  $Ni^{3+}$  ion on the film surface by sputtering. A tiny amount of  $H_2O$  adsorption on the reactive surface of sputtered NiO is responsible for this extra feature in O  $1s$  which is banished off the surface under thermal treatment.

The requirement of a charge neutralized surface demands that two electrons will be effectively confined at the  $V_O$  centers. The electronic charge entrapped at the vacancy sites will be distributed among the surrounding Ni atoms depending upon the symmetry of relaxation of the top surface [291]. When the density of these vacancy sites increases, sufficiently the defect states overlap to form a surface conduction band within the band gap zone as per our experimental observations (figure 8.2 and 8.4). Spin-polarized GGA calculations by Park *et al.* [301] showed that in case of non-stoichiometric oxides with higher density of vacancies; the vacancy-vacancy interaction can trigger a certain type of defect ordering. According to their report, the most stable defect ordering is in simple cubic style for nickel vacancies ( $V_{Ni}$ ), while in case of oxygen vacancies there is tendency to form defect clustering. Our experimental observations are in support to their calculations which predicts formation of occupied defect states close to  $E_F$  though no splitting of these defect states could be detected in our studies. In context to the stability of these defects, Zhang *et al.* [302] demonstrated from their first principle calculations that  $V_O$  and  $V_{Ni}$  are the most stable defects in O-poor and O-rich samples, respectively. Their electronic structure calculations resemble with our experimental finding of defect state evolution in the band gap region close to  $E_F$ . Moreover, presence of a donor level close to the conduction band minimum (CBM) due to  $V_O$  in their calculation is a direct proof of n-type doping of the oxide film, thus reducing the band gap and tending towards semiconducting behavior from insulating nature. Appearance of this donor level near CBM due to oxygen vacancy defect was experimentally observed by inverse photoemission studies [293]. According to Zhang *et al.* impurity states are contributed by the dangling  $d$  orbital of nickel atoms coordinating

the vacancy site. They have also shown that the contribution of O  $2p$  states to the impurity states is minor compared to the Ni  $3d$  states.

When a freshly prepared NiO film is Ar sputtered, anion vacancies which are basically point defects, are created in the film with their maximum density at the top surface; thereby creating a concentration gradient from the top surface to the bulk of the film. An excess sputtering leads to the formation of Ni<sup>0</sup> metals at the oxide film surface. A thermal treatment (like UHV annealing) accelerate the diffusion process of these defect sites to have an uniform distribution throughout the film. Oxygen atoms drift from bulk region to film surface to occupy surface oxygen vacancy sites thus producing schottky point defects at bulk region of the film. The trapping of electrons at the oxygen vacancy sites, make them to behave like F-centers. On the top surface, the atomic crystalline order may rearrange under thermal treatment in presence of  $V_O$  sites, such as exchange of Ni<sup>2+</sup> and vacant sites, formation of vacancy clusters *etc* occurs. These  $V_O$  site clusters may form M-centers and R-centers at the film surface. These electron trapped complex multi-defect clusters strongly affect the surface electronic structure of the film.

### 8.2.2 Effect the oxygen vacancies on magnetism

In NiO, two neighboring Ni atoms are bound *via* an oxygen atom through the superexchange interaction. One spin-up and another spin-down adjacent Ni sites form stable bonding providing a well arranged antiferromagnetic order throughout the NiO lattice. Therefore, the absence of oxygen site will eventually affect the antiferromagnetic order, reducing the magnetic of the sample. In fact, our experiments prove the reduction in Néel temperature ( $T_N$ ) with the creation of oxygen vacancies at NiO film surface.

As mentioned earlier,  $p(2 \times 2)$  half-order spots are visible in LEED for NiO films at lower beam energy range due to the presence of surface magnetic order. In figure 8.6 (a), the half-order spots of a 20 ML NiO film grown on Ag(001) is shown at RT (300 K) for beam energy 23 eV. The half-order spots have four-fold symmetry, the integer order spots do not enter into the field-of-view of LEED screen at this low beam energy. Intensity of the half-orders completely vanishes at 523 K, which is above the Néel temperature of the

film. The average intensities of half-order spots are shown in figure 8.6 (c), at various

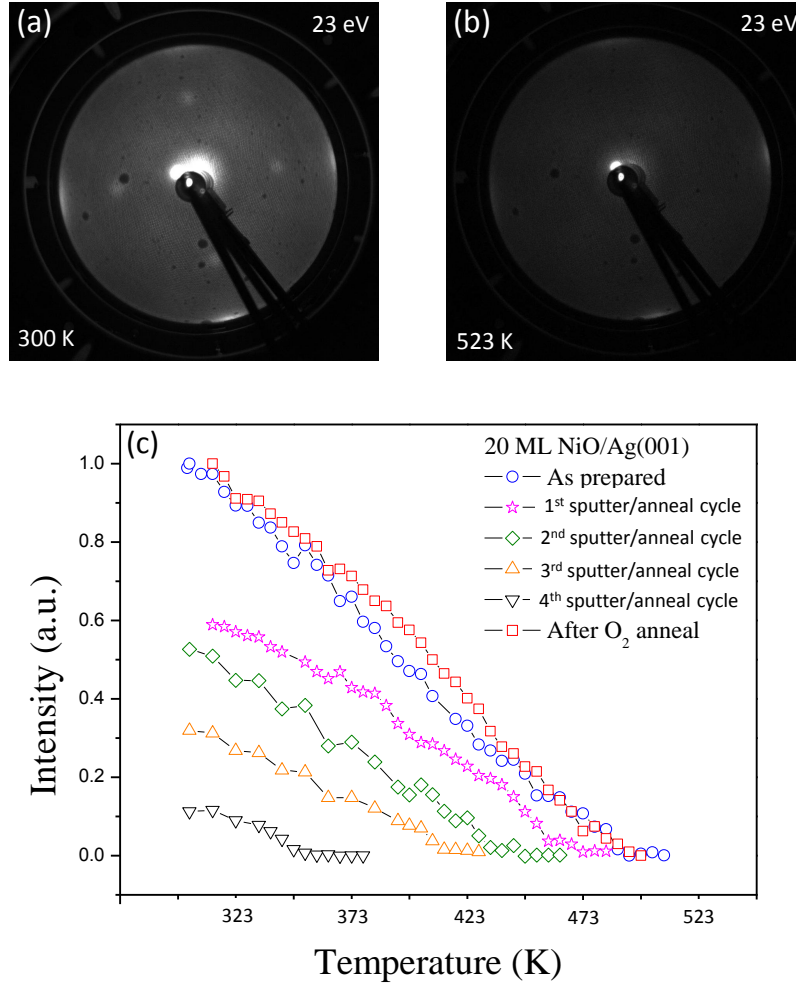


**Figure 8.6:** LEED  $p(2\times 2)$  half-order spot intensity (a) 300 K (RT) (b) 523 K (above  $T_N$ ). (c) Temperature dependence of half-order intensity of the ‘as prepared’ 20 ML NiO film grown on Ag(001). Néel temperature variation of the film after passing through various number of sputter and anneal cycles are also shown.

sample temperatures for different sputtered and annealing conditions. The ‘as prepared’ film shows a linear variation of half-order spot intensity with temperature and shows a  $T_N$  close to 500 K. No significant change in the nature of this intensity curve was observed when the sample was annealed in UHV for few hours at 673 K (not shown here). This is possibly due to the reduced number of oxygen vacancies created at the NiO surface by this UHV annealing process. Significant difference in Ni to O stoichiometry has been created through sputtering the sample with Ar<sup>+</sup> ion (500 eV) for 15 minutes followed by

UHV annealing at 673 K for 30 min. Sputtering ravages the surface crystalline quality of the sample destroying the magnetic order, hence the half-orders vanishes. However post-UHV annealing after sputtering rather recovers the sample surface quality and restores the half-order spots though it maintains the deficiency of oxygen at the sample surface. Temperature dependence of half-order intensity was performed every time after passing the sample through Ar sputter and UHV anneal cycles. A gradual decrement in the Néel temperature was observed with oxygen deficiency in the sample. We measured  $T_N$  values as 465 K, 435 K, 410 K and 345 K of the sample after 1st, 2nd, 3rd and 4th sputter-anneal cycle, respectively. The significant amount of intensity reduction of the half-order spots as a result of increased sputter time (or increased oxygen deficiency) at RT is notable. Intensity of the half-orders almost vanishes under more sputtering of the sample and could not be detected at RT. Annealing of the sample in oxygen environment ( $7 \times 10^{-6}$  mbar) for 30 minutes help in recovering back the surface Ni to O stoichiometry as well as as the magnetic strength of the sample which is reflected in the increment of  $T_N$  value. This reversible variation of the  $T_N$  with Ni to O stoichiometry confirms the vacancy dependence of the antiferromagnetic ordering in the NiO film. As the oxygen vacancy density increases, more Ni-O-Ni bonds are destroyed leading to the reduction of the  $T_N$  as a result of the reduced extend of the antiferromagnetic wave-function overlap (in other words, reduced dimensionality of the antiferromagnetic overlaps).

### 8.3 Conclusion

Creation of oxygen vacancies and metallic nickel states at the NiO/Ag(001) film surface and its effect on the valence band and core level electronic structure have been studied. While the oxygen vacancies in NiO films can be produced by UHV annealing at high temperature as well as mild  $\text{Ar}^+$  sputtering; metallic  $\text{Ni}^0$  states are only produced in the film by severe sputtering process. Angle dependent photoemission studies provide an idea about the distribution of defect densities at various depths of the oxide film. The effect of UHV and oxygen annealing on the electronic structure of the film has also been reinvestigated.

Removal of oxygen atom affect the superexchange interaction between the up-spin and down-spin Ni atoms in the crystalline NiO film and thus decreasing the antiferromagnetic order and strength of the film which is reflected in the Néel temperature decrement. The temperature dependency of the LEED half-order intensity shows consistent decrement of  $T_N$  value with increased oxygen vacancy concentration at the NiO film surface.

The effect of stoichiometric variation (by introducing oxygen vacancies) on the antiferromagnetic order as well as electronic structure of NiO appears to really an interesting phenomena. However, our studies (with LEED and photoemission) explored new pathways for detailed microscopic investigation in future.

## Bibliography

- [1] J. Stöhr, H. C. Siegmann, *Magnetism From Fundamentals to Nanoscale Dynamics*, Springer, 2006.
- [2] L. Duò, M. Finazzi, and F. Ciccacci, *Magnetic Properties of Antiferromagnetic Oxide Materials*, WILEY-VCH Verlag GmbH Co. KGaA, Weinheim, 2010.
- [3] H. Krakauer, A. J. Freeman, and E. Wimmer, Phys. Rev. B, **28**, 610 (1983).
- [4] E. Wimmer, A. J. Freeman, and H. Krakauer, Phys. Rev. B, **30**, 3113 (1984).
- [5] S. Ohnishi, A. J. Freeman, and M. Weinert, Phys. Rev. B, **28**, 6741 (1983).
- [6] R. L. Fink, C. A. Ballentine, J. L. Erskine, and Jose A. Araya-Pochet, Phys. Rev. B, **41**, 10175 (1990).
- [7] R. Allenspach, M. Stampanoni, and A. Bischof, Phys. Rev. Lett., **65**, 3344 (1990).
- [8] L. M. Falicov, Daniel T. Pierce, S. D. Bader, R. Gronsky, K. B. Hathaway, H. J. Hopster, D. N. Lambeth, S. S. P. Parkin, G. Prinz, M. Salamon, I. K. Schuller and R. H. Victora, J. Mat. Res., **5**, 1299 (2011).
- [9] Z. Jin, T. Fukumura, M. Kawasaki, K. Ando, H. Saito, T. Sekiguchi, Y. Z. Yoo, M. Murakami, Y. Matsumoto, T. Hasegawa and H. Koinuma, App. Phys. Lett., **78**, 3824 (2001).

- [10] D. L. Mills, *J. Magn. Magn. Mat.*, **100**, 515 (1991).
- [11] M. Finazzi, L. D'ùo, and F. Ciccacci, *Surf. Sci. Rep.*, **64**, 139 (2009).
- [12] P. W. Anderson, *Phys. Rev.*, **79**, 350 (1950).
- [13] C. L. Fu, A. J. Freeman and T. Oguchi, *Phys. Rev. Lett.*, **54**, 2700 (1985).
- [14] O. Hjortstam, J. Trygg, J. M. Wills, B. Johansson, and O. Eriksson, *Phys. Rev. B*, **53**, 9204 (1996).
- [15] N. D. Mermin, and H. Wagner, *Phys. Rev. Lett.*, **17**, 1133 (1966).
- [16] A. Punnoose, H. Magnone, M. S. Seehra and J. Bonevich, *Phys. Rev. B*, **64**, 174420 (2001).
- [17] X. G. Zheng, C. N. Xu, K. Nishikubo, K. Nishiyama, W. Higemoto, W. J. Moon, E. Tanaka, and E. S. Otabe, *Phys. Rev. B*, **72**, 014464 (2005).
- [18] E. N. Abarra, K. Takano, F. Hellman, and A. E. Berkowitz, *Phys. Rev. Lett.*, **77**, 3451 (1996).
- [19] D. Alders, L. H. Tjeng, F. C. Voogt, T. Hibma, G. A. Sawatzky, C. T. Chen, J. Vogel, M. Sacchi, and S. Iacobucci, *Phys. Rev. B*, **57**, 11623 (1998).
- [20] S. Sako, K. Ohshima, M. Sakai, and S. Bandow, *Surf. Rev. Lett.*, **3**, 109 (1996).
- [21] S. Gangopadhyay, G. C. Hadjipanayis, C. M. Sorensen and K. J. Klabunde, *J. Appl. Phys.*, **73**, 6964 (1993).
- [22] D. A. Resnick, K. Gilmore, Y. U. Idzerda, M. T. Klem, M. Allen, T. Douglas, E. Arenholz, and M. Young, *J. Appl. Phys.*, **99**, 081501 (2006).
- [23] L. He, C. P. Chen, N. Wang, W. Zhou, and L. Guo, *J. Appl. Phys.*, **102**, 103911 (2007).
- [24] R. M. Wang, C. M. Liu, H. Z. Zhang, C. P. Chen, L. Guo, H. B. Xu, and S. H. Yang, *Appl. Phys. Lett.*, **85**, 2080 (2004).

- [25] E. L. Salabas, A. Rumpelcker, F. Kleitz, F. Radu, and F. Schuth, *Nano. Lett.*, **6**, 2977 (2006).
- [26] M. E. Fisher, and M. N. Barber, *Phys. Rev. Lett.*, **28**, 1516 (1972).
- [27] R. Zhang, and R. F. Willis, *Phys. Rev. Lett.*, **86**, 2665 (2001).
- [28] M. P. Seah and W. A. Dench, *Surface and Interface Analysis*, **1**, 2 (1979).
- [29] M. A. Van Hove, W. H. Weinberg and C. M. Chan, *Low-Energy Electron Diffraction Experiment, Theory and Surface Structure Determination*, Springer-Verlag Berlin Heidelberg (1986).
- [30] L. J. Clarke, *Surface Crystallography: an introduction to low energy electron diffraction*, John Wiley (1985).
- [31] A. Zangwill, *Physics at Surfaces* Cambridge University Press (1992).
- [32] Y. Liu, *Angle Resolved Photoemission Studies Of Two Dimensional Electron Systems*, Ph.D thesis (2010).
- [33] K. M. Schindler, M. Huth, W. Widdra, *Chemical Physics Letters* **532**, 116-118 (2012).
- [34] W. Palmberg, R. E. DeWames, L. A. Vredevoe, *Phys. Rev. Lett.* **21**, 682 (1968).
- [35] E. Tamura, S. Bliigel and R. Feder, *Solid State Communications*, **65**, 1255-1257 (1988).
- [36] C. G. Shull, W. A. Strauser and E. O. Wollan, *Phys. Rev.*, **83**, 333 (1951).
- [37] J. Singer, *Phys. Rev.*, **104**, 929 (1956).
- [38] Suman Mandal, Ph. D Thesis, University of Calcutta (2012).
- [39] S. Hüfner, *Photoelectron Spectroscopy: Principles and Application* Berlin: Springer; Third Edition (2003).
- [40] F. Reinert and S. Hüfner, *New Journal of Physics*, **7**, 97 (2005).
- [41] A. Damascelli, Z. Hussain and Z. X. Shen, *Rev. Mod. Phys.*, **75**, 473 (2003).

- [42] S. Hüfner, *Very High Resolution Photoelectron Spectroscopy*, Springer; First Edition (2007).
- [43] S. D. Kevan, *Angle Resolved Photoemission: Theory and Current Applications*, Elsevier Science, Amsterdam, 1992.
- [44] H. Hertz, *Ann. Phys.*, **31**, 132 (1887).
- [45] A. Einstein, *Ann. Phys.*, **31**, 132 (1905).
- [46] C. Nordling, E. Sokolowski, K. Siegbahn, *Phys. Rev.*, **105**, 1676 (1957).
- [47] K. Siegbahn, *Phil. Trans. R. Soc. A*, **268**, 33 (1970).
- [48] C. N. Berglund and W. E. Spicer, *Phys. Rev. A*, **136**, 1030 (1964).
- [49] T. C. Chiang, *Surface Science Reports*, **39**, 181 (2000).
- [50] S. Doniach and M. Sunjic, *J. Phys. C*, **3**, 285 (1970).
- [51] D. P. Woodruff and T. A. Delchar, *Modern Techniques of Surface Science*, Cambridge, Solid State Science Series, (1986).
- [52] S. K. Mahatha, K. S. R. Menon, *Curr. Sci.*, **98**, (2010) 759.
- [53] H. Luth, *Surfaces and Interfaces of Solid materials*, (Springer, Berlin, 1995).
- [54] H. Luth, *Solid Surfaces, Interfaces and Thin Films*, Springer, 4th edition (2001).
- [55] A. M. Ezpeleta, *Electronic Structure of Low Dimensional Systems Analyzed by Angle Resolved Photoemission Spectroscopy*, Ph.D Thesis, (2002).
- [56] G. Bunker, *Introduction to XAFS: a practical guide to x-ray absorption fine structure spectroscopy*, Cambridge University Press (2010).
- [57] J. Stöhr, *NEXAFS spectroscopy* (Springer Series in Surface Sciences).
- [58] E. Beaurepaire, H. Bulou, F. Scheurer, J. P. Kappler (Editors), *Magnetism: A Synchrotron Radiation Approach* (Springer Lecture Notes in Physics).

- [59] L. Düo, M. Finazzi, F. Ciccacci (Editors), *Magnetic Properties of Antiferromagnetic Oxide Materials: Surfaces, Interfaces and Thin Films*, (Wiley-VCS, 2010).
- [60] H. Hopster and H. P. Oepen (Editors), *Magnetic Microscopy and Nanostructures*, (Springer, 2005).
- [61] E. Bauer, M. Mundschan, W. Sweich and W. Teliëps, *Ultramicroscopy*, **31**, 49 (1989).
- [62] F. U. Hillebrecht, *J. Phys. : Cond. Matt.*, **13**, 11163 (2001).
- [63] T. Kinoshita, T. Wakita, H. L. Sun, T. Tohyama, A. Harasawa, H. Kiwata, F. U. Hillebrecht, K. Ono, T. Matshusima, M. Oshima, N. Ueno, Y. Saitoh and T. Okuda, *J. Phys. Soc. Jpn.*, **73**, 2932 (2004).
- [64] H. B. Møller, A. L. Trego and A. R. Mackintosh, *Solid State Commun.*, **3**, 137 (1965).
- [65] H. B. Møller and A. R. Mackintosh, *Phys. Rev. Lett.*, **15**, 623 (1965).
- [66] Y. Hamaguchi, and N. Kunitomi, *J. Phys. Soc. Jpn.*, **19**, 1849 (1964).
- [67] G. Allan, *Phys. Rev. B.* **19**, 4774 (1979).
- [68] S. Blügel, D. Pescia, and P. H. Dederichs, *Phys. Rev. B.*, **39**, 1392 (1989).
- [69] R. Wiesendanger, H. J. Guntherodt, G. Guntherodt, R. J. Gambino and R. Ruf, *Phys. Rev. Lett.*, **65**, 247 (1990).
- [70] U. Grandmann, *J. Mag. Magn. Mat.*, **100**, 481 (1991).
- [71] J. Noffke, L. Fritsche, *J. Phys. C: Sol. Stat. Phys.*, **14**, 89 (1981).
- [72] M. Wuttig, B. Feldmann, T. Flores, *Surf. Sci.*, **331**, 659 (1995).
- [73] A. J. Freeman, *J. Magn. Magn. Mat.*, **15-18**, 1070 (1980).
- [74] A. J. Freeman and C. L. Fu, *J. App. Phys.*, **61**, 3356 (1987).
- [75] C. L. Fu and A. J. Freeman, *Phys. Rev. B.*, **33**, 1755 (1986).

- [76] C. L. Wooten, J. Chen, G. A. Mulhollan, J. L. Erskine, J. T. Markert, Phys. Rev. B., **49**, 10023 (1994).
- [77] S. Blügel, M. Weinert, P. H. Dederichs, Phys. Rev. Lett., **60**, 1077 (1988).
- [78] S. Blügel, Phys. Rev. Lett., **68**, 851 (1992).
- [79] S. Blügel, B. Drittler, R. Zeller, P. H. Dederichs, App. Phys. A, **49**, 547 (1989).
- [80] L. E. Klebanoff, S. W. Robey, G. Liu and D. A. Shirley, Phys. Rev. B, **30**, 1048 (1984).
- [81] A. D. Johnson, J. A. C. Bland, C. Norris, H. Lauter, J. Phys. C: Sol. Stat. Phys. **21**, L899 (1988).
- [82] M. C. Hanf, C. Pirri, J. C. Peruchetti, D. Bolmont and G. Gewinner, Phys. Rev. B, **36**, 4487 (1987).
- [83] F. E. Wang, *Bonding Theory of Metals and Alloys*, Elsevier Inc. (2005).
- [84] D. A. Newstead, C. Norris, C. Binns, P. C. Stephenson, J. Phys. C: Sol. Stat. Phys, **20**, 6245 (1987).
- [85] J. E. Ortega and F. J. Himpsel, Phys. Rev. B., **47**, 16441 (1993).
- [86] M. E. Haugan, Q. Chen, M. Onellion and F. J. Himpsel, Phys. Rev. B., **49**, 14028 (1994).
- [87] C. Krembel, M. C. Hanf, J. C. Peruchetti, D. Bolmont, G. Gewinner, **44**, 8407 (1991).
- [88] M. C. Hanf, C. Krembel, D. Bolmont and G. Gewinner, **68**, 144419 (2003).
- [89] J. F. Lawler, R. G. P. van der Kraan, H. van Kempen, A. J. Quinn, J. Magn. Mag. Mat., **165**, 195 (1997).
- [90] A. J. Quinn, J. F. Lawler, R. Schad, H. van Kempen, Surf. Sci., **385**, 395 (1997).
- [91] P. Steadman, C. Norris, C. L. Nicklin, N. Jones, J. S. G. Taylor et. al. Phys. Rev. B, **64**, 245412 (2001).

- [92] D. Rouyer, C. Krembel, M.C. Hanf, D. Bolmont and G. Gewinner, Surf. Sci., **287/288**, 935 (1993).
- [93] C. Krembel, M. C. Hanf, J. C. Peruchetti, D. Bolmont, and G. Gewinner, J. Vac. Sci. Tech., **10**, 3325 (1992).
- [94] M.C. Hanf, C. Krembel and G. Gewinner, Surf. Sci., **519**, 1 (2002).
- [95] C. Krembel, M. C. Hanf, J. C. Peruchetti, D. Bolmont and G. Gewinner, Surf. Sci., **269**, 748 (1992).
- [96] E. Bauer, Z. Kristallogr. 110, **372** (1958).
- [97] M. C. Hanf, C. Pirri, J. C. Peruchetti, D. Bolmont and G. Gewinner, Surf. Sci., **39**, 1546 (1989).
- [98] D. Rouyer, C. Krembel, M. C. Hanf, D. Bolmont, G. Gewinner, Surf. Sci., **331**, (957) 1995.
- [99] P. Schieffer, D. Rouyer, C. Krembel, M. C. Hanf and G. Gewinner, Surf. Sci., **349**, 81 (1996).
- [100] M. C. Hanf, C. Pirri, J. C. Peruchetti, D. Bolmont, G. Gewinner, Phys. Rev. B., **39**, 1546 (1989).
- [101] M. C. Hanf, C. Pirri, J. C. Peruchetti, D. Bolmont and G. Gewinner, Phys. Rev. B., **36**, 4487 (1987).
- [102] M. C. Hanf, C. Pirri, J. C. Peruchetti, D. Bolmont and G. Gewinner, Phys. Rev. B., **39**, 3021 (1989).
- [103] M. C. Hanf, C. Pirri, J. C. Peruchetti, D. Bolmont and G. Gewinner, Phys. Rev. B., **36**, 4487 (1987).
- [104] P. W. Palmberg, R. E. DeWames, L. A. Vredevoe and T. Wolfram, J. App. Phys., **40**, 1158 (1969).

- [105] T. Wolfram, R. E. DeWames, W. F. Hall and P. W. Palmberg, *Sur. Sci.*, **28**, (1971) 45.
- [106] C. Krembel, M. C. Hanf, J. C. Peruchetti, D. Bolmont and G. Gewinner, *J. Magn. Magn. Mat.*, **119**, 115 (1993)
- [107] K. Namikawa, *J. Phys. Soc. Jap.*, **44**, 165 (1978).
- [108] K. Hayakawa, K. Namikawa and S. Miyake, *J. Phys. Soc. Jap.*, **31**, 1408 (1971).
- [109] K. S. R. Menon, S. Mandal, J. Das, T. O. Montes, M. A. Nino, *Phys. Rev. B*, **84**, 132402 (2011).
- [110] J. Das, A. K. Kundu, K. S. R. Menon, *Vacuum*, **112**, 5 (2015).
- [111] J. Das, S. Biswas, A. K. Kundu, S. Narasimhan and K. S. R. Menon, *Phys. Rev. B*, **91**, 125435 (2015).
- [112] M. A. Leroy, A. M. Bataille, F. Bertran, P. Le Fèvre, A. T. Ibrahimi and S. Andrieu, **88**, 205134 (2013).
- [113] A. B. Shick, S. Khmelevskiy, O. N. Mryasov, J. Wunderlich, and T. Jungwirth, *Phys. Rev. B*. **81**, 212409 (2010).
- [114] B. G. Park, J. Wunderlich, X. Martí, V. Holý, Y. Kurosaki, M. Yamada, H. Yamamoto, A. Nishide, J. Hayakawa, H. Takahashi, A. B. Shick and T. Jungwirth, *Nature Materials*. **10**, 347 (2011).
- [115] C. Krembel, M. C. Hanf, P. Wetzel, C. Pirri, J. C. Peruchetti, D. Bolmont and G. Gewinner, *Vacuum*, **41**, 460 (1990).
- [116] D. Rouyer, C. Krembel, M. C. Hanf, D. Bolmont and G. Gewinner, *Surf. Sci.*, **331**, 957 (1995).
- [117] C. Krembel, M. C. Hanf, J. C. Peruchetti, D. Bolmont, and G. Gewinner, **10**, 3325 (1992).

- [118] H. Erschbaumer, A. J. Freeman, C. L. Fu and R. Podlucky, *Surf. Sci.*, **243**, 317-322 (1991).
- [119] see <http://www.quantum-espresso.org> for Quantum- ESPRESSO package; P. Gianozzi et al., *J. Phys.: Condens. Matter* **21**, 395502 (2009).
- [120] *Density Functional Theory Based Strategies for Tailoring the Magnetic and Morphological Properties of Surfaces*, Ph.D Thesis, Sananda Biswas, Theoretical Sciences Unit, JNCASR, India. (2014).
- [121] D. Vanderbilt, *Phys. Rev. B*, **41**, 7892 (1990).
- [122] P. Perdew, K. Burke, and M. Ernzerhof, *Phys. Rev. Lett.*, **77**, 3865 (1996).
- [123] H. Monkhorst and J. Pack, *Phys. Rev. B*, **13**, 5188 (1976).
- [124] N. Marzari, D. Vanderbilt, A. De Vita, and M. C. Payne, *Phys. Rev. Lett.*, **82**, 3296 (1999).
- [125] F. Schiller, D. V. Vyalikh, V. D. P. Servedio and S. L. Molodtsov, *Phys. Rev. B*, **70**, 174444 (2004).
- [126] P. Habibi, C. Barreteau and A. Smogunov, *J. Phys. Cond. Mat.*, **25**, 14 (2013).
- [127] C. Kittel, *Introduction to solid state physics*, Wiley.
- [128] J. Hermanson, *Sol. Stat. Comm.*, **22**, 9 (1977).
- [129] D. Wang, A. J. Freeman and H. Krakauer, *Phys. Rev. B.*, **29**, 1665 (1984).
- [130] R. Richter, J. G. Gay and J. R. Smith, *J. Vac. Sci. Technol. A*, **3**, 1498 (1985).
- [131] S. Blügel, M. Weinert and P. H. Dederichs, *Phys. Rev. Lett.*, **60**, 1077 (1988).
- [132] C. Krembel, M. C. Hanf, J. C. Peruchetti, D. Bolmont and G. Gewinner, *Phys. Rev. B.*, **44**, 11472 (1991).
- [133] G. Allan, *Phys. Rev. B.*, **44**, 13641 (1991).
- [134] M. D. Mermin and H. Wagner, *Phys. Rev. Lett.* **17**, 1133 (1966).

- [135] M. Bander and D. L. Mills, Phys. Rev. B, **38**, 12015 (1988).
- [136] J. Kohlepp, H. J. Elmers, S. Cordes, and U. Gradmann, Phys. Rev. B. **45**, 12287 (1992).
- [137] H. J. Elmers, J. Hauschild, U. Gradmann, J. Magn. Magn. Mater. **140**, 1559 (1995).
- [138] C. H. Back, Ch. Wursch, A. Vaterlaus, U. Ramsperger, U. Maier, and D. Pescia, Nature, **378**, 597 (1995).
- [139] Z. Q. Qiu, J. Pearson, and S. D. Bader, Phys. Rev. B, **49**, 8797 (1994).
- [140] C. Rau, P. Mahavadi, and M. Lu, J. Appl. Phys., **73**, 6757 (1993).
- [141] P. W. Palmberg, R. E. De Wames, and L. A. Vredevoe, Phys. Rev. Lett., **21**, 682 (1968).
- [142] L. Onsager, Phys. Rev., **65**, 117 (1944).
- [143] C. N. Yang, Phys. Rev., **85**, 808 (1952).
- [144] S. Maekawa, T. Tohyama, S.E. Barnes, S. Ishihara, W. Koshibae, G. Khaliullin, Physics of Transition Metal Oxides, Springer, Berlin, 2004.
- [145] N. Tsuda, K. Nasu, A. Fujimori, K. Siratori, Electronic Conduction on Oxides, 2nd ed., Springer, Berlin, 2000.
- [146] N. F. Mott, Proc. Phys. Soc. Lond. Sect. A, **62**, 416 (1949).
- [147] S. Hufner, Adv. Phys. **43** (1994) 183. And references therein.
- [148] A. M. Balagurov, I. A. Bobrikov, J. Grabis, D. Jakovlevs, A Kuzmin, M. Maiorov, N. Mironova-Ulmane, IOP Conf. Series: Materials Science and Engineering, **49**, 012021 (2013).
- [149] H.J. Freund, H. Kuhlenbeck, V. Staemmler, Rep. Progr. Phys. **59** 283 (1996).
- [150] M. Blaumer, H. J. Freund, Prog. Surf. Sci., **61** 127 (1999).

- [151] H. D. Chopra, B. J. Hockey, P. J. Chen, W. F. Egelhoff Jr., M. Wuttig, S. Z. Hua, Phys. Rev. B, **55** 8390 (1997).
- [152] S. Hufner, Adv. Phys., **43**, 183 (1994).
- [153] H. J. Freund, Phys. Stat. Sol., (b) 192 407 (1995).
- [154] S.A. Chambers, Surf. Sci. Rep., **39** 105 (2000).
- [155] D. W. Goodman, J. Vac. Sci. Technol. A, **14**, 1526 (1996).
- [156] H. J. Freund, Angew. Chem., Int. Ed. Engl., **36**, 452 (1997).
- [157] D. A. Muller et al., Phys. Rev. Lett., **80**, 4741 (1998).
- [158] H. L. Meyerheim et al., Phys. Rev. Lett., **87**, 076102 (2001).
- [159] S. Schintke et al., Phys. Rev. Lett., **87**, 276801 (2001).
- [160] Y. T. Matuvich, T. J. Vink, and P. A. Z. van Emmichoven, Phys. Rev. Lett., **89**, 167601 (2002).
- [161] S. Altieri, L. H. Tjeng, and G. A. Sawatzky, Phys. Rev. B, **61**, 16948 (2000).
- [162] S. Altieri, L. H. Tjeng, and G. A. Sawatzky, Thin Solid Films, **400**, 9 (2001).
- [163] D. M. Duffy, J. H. Harding, and A. M. Stoneham, Acta Metall. Mater., **43**, 1559 (1995).
- [164] K.Marre, H. Neddermeyer, Surf.Sci., **287** 995 (1993).
- [165] K.Marre, H. Neddermeyer, A. Chasse, P. Reinnert, Surf. Sci., **357** 233 (1995).
- [166] T. Bertrams, H. Neddermeyer, J. Vac. Sci. Technol. B, **14**, 1141 (1996).
- [167] F. Muller, R. de Masi, P. Ser, D. Reinicke, M. Stadtfelt, and H. Hufner, Surf. Sci., **459**, 161 (2000).
- [168] T. Bertrams and H. Neddermeyer, J. Vac. Sci. Technol. B, **14**, 1141 (1996).

- [169] I. Sebastian, T. Bertrams, K. Meinel, and H. Neddermeyer, *Faraday Discuss.*, **114**, 129 (1999).
- [170] J. Wollschläger, D. Erdös, H. Goldbach, R. Hopken, and K. M. Schröder, *Thin Solid Films*, **400**, 1 (2001).
- [171] C. Giovanardi, A. di Bona, S. Altieri, P. Luches, M. Liberati, F. Rossi, and S. Valeri, *Thin Solid Films*, **428**, 195 (2003).
- [172] P. Luches, S. Altieri, C. Giovanardi, T. S. Moia, S. Valeri, F. Bruno, L. Floreano, A. Morgante, A. Santaniello, A. Verdini, R. Gotter, and T. Hibma, *Thin Solid Films*, **400**, 139 (2001).
- [173] C. Giovanardi, A. di Bona and S. Valeri, *Phys. Rev. B*, **69**, 075418 (2004).
- [174] S. D. Peacor, T. Hibma, *Sur. Sci.*, **301**, 11 (1994).
- [175] A. Rota, S. Altieri, and S. Valeri, *Phys. Rev. B*, **79**, 161401(R) (2009).
- [176] C. A. Ventrice, H. Geisler, A. W. K. Liu, M. B. Santos (Eds.), *Thin Films: Heteroepitaxial Systems*, World Scientific, Singapore, 1999, p.167.
- [177] S. A. Chambers, *Surf. Sci. Rep.*, **39** 105 (2000).
- [178] J. Schoiswohl, W. Zheng, S. Surnev, M. G. Ramsey, G. Granozzi, S. Agnoli, F. P. Netzer, *Sur. Sci.*, **600** 1099 (2006).
- [179] S. Casassa, A. M. Ferrari, M. Busso, and C. Pisani, *J. Phys. Chem. B*, **106**, 12978 (2006).
- [180] C. Giovanardi, A. di Bona, S. Altieri, P. Luches, M. Liberati, F. Rossi, S. Valeri, *Thin Solid Films*, **428**, 195 (2003).
- [181] C. Lamberti, E. Groppo, C. Prestipino, S. Casassa, A. M. Ferrari, and C. Pisani, C. Giovanardi, P. Luches, S. Valeri, F. Boscherini, **91**, 046101-1 (2003).
- [182] Z. X. Shen, R. S. List, D. S. Dessau, A. J. Arko, R. Barttlet, O. Jepsen, B. O. Wells and F. Parmigiani. *Sol. Stat. Comm.*, **79**, 623-628 (1991).

- [183] Z. X. Shen, C. K. Shih, O. Jepsen, W. E. Spicer, I. Lindau, and J. W. Allen. Phys. Rev. Lett., **64**, 2442 (1990).
- [184] Z. X. Shen, R. S. List, D. S. Dessau, B.Q. Wells, O. Jepsen, A. J. Arko, R. Barttlet, C. K. Shih, F. Parmigiani, J. C. Huang and P. A. P. Lindberg. Phys. Rev. B, **44**, 3604 (1991).
- [185] C. M. Cheng, C. C. Wang, H. T. Jeng, C. S. Hsue, B.
- [186] P. Müller, A. Saul, Surf. Sci. Rep., **54** (2004) 157.
- [187] M. Mavrikakis, B. Hammer, J.K. Norskov, Phy. Rev. Lett., **81**, 2819 (1998).
- [188] C. Castellarin-Cudia, S. Surnev, G. Schneider, R. Podlucky, M.G. Ramsey, F.P. Netzer, Surf. Sci., **554** L120 (2004).
- [189] Q. Guo, C. Xu, and D. W. Goodman, Langmuir, **14**, 1371 (1998).
- [190] S. Altieri, M. Finazzi, H. H. Hsieh, M. W. Haverkort, H.J. Lin, C. T. Chen, S. Frabboni, G. C. Gazzadi, A. Rota, S. Valeri, and L. H. Tjeng, Phys. Rev. B. **79**, 174431 (2009).
- [191] J. Stöhr, A. Scholl, T. J. Regan, S. Anders, J. Lüning, M. R. Scheinfein, H. A. Padmore, and R. L. White, Phys. Rev. Lett., **83**, 1862 (1999).
- [192] M. Schulze and R. Reissner, Surf. Sci., **482** 285 (2001).
- [193] M. Caffio, A. Atrei b, U. Bardi, G. Rovida, Surf. Sci., **588**, 135 (2005).
- [194] K. Amemiyaa and M. Sakamaki, App. Phys. Lett., **98**, 012501 (2011).
- [195] M. Btiumer, D. Cappus, H. Kuhlenbeck, H.J. Freund, G. Wilhelmi, A. Brodde and H. Neddermeyer, Surf. Sci., **253**, 116 (1991).
- [196] G. T. Tyuliev and K. L. Kostov, Phys. Rev. B., **60** , 2900 (1999).
- [197] J. Wollschlager, Thin Solid Film, **400**, 1 (2001).
- [198] J. Wollschlager, D. Erdos, K. M. Schroder, Surf. Sci., **402**, 272 (1998).

- [199] A. Fujimori, F. Minami, and S. Sugano, *Phys. Rev. B*, **29**, 5225 (1984).
- [200] G. A. Sawatzky and J. W. Allen, *Phys. Rev. Lett.*, **53**, 2339 (1984).
- [201] K. Maiti, Priya Mahadevan, and D. D. Sarma *Phys. Rev. B*, **59**, 12457 (1999).
- [202] S. Hübner, *Solid State Commun.*, **52**, 793 (1984).
- [203] M. A. van Veenendaal and G. A. Sawatzky, *Phys. Rev. Lett.*, **70**, 2459 (1993).
- [204] S. Uhlenbrock, C. Scharfschwerdtt, M. Neumannt, G. Illing and H. J. Freund, *J. Phys. Cond. Mat.*, **4**, 7973 (1992).
- [205] D. Alders, F. C. Voogt, T. Hibma and G. A. Sawatzky, *Phys. Rev. B.*, **54**, 7716 (1996).
- [206] M. R. Thuler, R. L. Benbow and Z. Hurych, *Phys. Rev. B*, **27**, 2082 (1983).
- [207] A. Fujimori and F. Minami, *Phys. Rev. B*, **30**, 957 (1984).
- [208] P. W. Anderson, in *Frontiers and Borderlines in Many Particle Physics, Proceedings of the International School of Physics, "Enrico Fermi", CIV*, (Edited by R.A. Broglia and J.R. Schriffer), North-Holland, Amsterdam (1988).
- [209] J. G. Bednorz and K. A. Mfiller, *Z. Phys. B*, **64**, 189 (1986).
- [210] S. Hübner, J. Osterwalder, T. Riesterer and F. Hulliger, *Sol. Stat. Comm.*, **52**, 793-796 (1984).
- [211] S. Hübner, P. Steiner, I. Sander, F. Reinert, H. Schmitt, M. Neumann and S. Witzel, *Sol. Stat. Comm.* **80**, 869-873 (1991).
- [212] S. Hübner, P. Steiner, I. Sander, M. Neumann, and S. Witzel, *Z. Phys. B. Condensed Matter* **83**, 185-192 (1991).
- [213] K. S. Kim, *Chem. Phys. Lett.*, **26**, 234 (1974).

- [214] M. Taguchi, M. Matsunami, Y. Ishida, R. Eguchi, A. Chainani, Y. Takata, M. Yabashi, K. Tamasaku, Y. Nishino, T. Ishikawa, Y. Senba, H. Ohashi, and S. Shin. *Phys. Rev. Lett.*, **100**, 206401 (2008).
- Y. Hsu, D. J. Huang, K. D. Tsuei, *Physica B*, **403**, 1539 (2008).
- [215] B. H. Brandow, *Adv. Phys.*, **26**, 651-808 (1977).
- [216] J. W. Allen, in *Narrow Band Phenomena Influence of Electrons with both Band and Localized Character*, Vol. 184 of NATO Advanced Study Institute, Series B: Physics, edited by J. C. Fuggle, G. A. Sawatzky, and J. W. Allen (Plenum, New York, 1988), p. 155.
- [217] J. Zaanen, G.A. Sawatzky and J.W. Allen. *J. Magn. Mag. Mat*, **54-57**, 607-611 (1986).
- [218] P. W. Anderson, *Phys. Rev.*, **115**, 2 (1959)
- [219] N. F. Mott, *Proc. R. Soc. London Ser. A*, **62**, 416 (1949).
- [220] J. Hubbard, *Proc. R. Soc. London Ser. A*, **276**, 238 (1963).
- [221] J. C. Slater, *Phys. Rev.*, **82**, 538 (1951)
- [222] K. Terakura, T. Oguchi, A. R. Williams, and J. Kubler, *Phys. Rev. B* **30**, 4734 (1984); T. Oguchi, K. Terakura, and A. R. Williams, *ibid.* **28**, 6443 (1983).
- [223] D. E. Eastman and J. L. Freeoff, *Phys. Rev. Lett.*, **34**, 395 (1975).
- [224] S. J. Oh, J. W. Allen, I. Lindau, and J. C. Mikkelsen, Jr., *Phys. Rev. B*, **26**, 4845 (1982).
- [225] M. R. Thuler, R. L. Benbow, and Z. Hurych, *Phys. Rev. B*, **27**, 2082 (1983).
- [226] M. R. Thuler, R. L. Benbow, and Z. Hurych, *Phys. Rev. B*, **26**, 699 (1982).
- [227] G. K. Wertheim, H. J. Guggenheim, and S. Hufner, *Phys. Rev. Lett.*, **30**, 1050 (1973); G. K. Wertheim and S. Hufner, *ibid.*, **28**, 1028 (1982).

- [228] A. Fujimori, N. Kimizuka, M. Taniguchi, and S. Suga, *Phys. Rev. B*, **36**, 6991 (1987).
- [229] G. van der laan, C. Westra, C. Haas, and G. A. Sawatzky, *Phys. Rev. B*, **23**, 4369 (1981).
- [230] A. Fujimori, N. Kimizuka, M. Taniguchi, and S. Suga, *Phys. Rev. B*, **36**, 6691 (1987).
- [231] S. Yang, S. Seong and J.S. Kim, *Journal of the Korean Physical Society*, **57**, 1312 (2010).
- [232] F. Cinquini, L. Giordano, and G. Pacchioni, *Phys. Rev. B*, **74**, 165403 (2006).
- [233] O. Tjernberg, S. Söderholm, G. Chiaia, R. Girard, and U. O. Karlsson, H. Nylén and I. Lindau, *Phys. Rev. B*, **54**, 10245 (1996).
- [234] B.T. Thole, G. Van der Laan, G.A. Sawatzky, *Phys. Rev. Lett.*, **55**, 2086 (1985).
- [235] G. Van der Laan, B.T. Thole, G.A. Sawatzky, G.B. Goedkoop, J.C. Fuggle, J.M. Esteve, R. Karnatak, J.P. Remeika, H.A. Dabkowska, *Phys. Rev. B*, **34**, 6529 (1986).
- [236] C. Kittel, *Rev. Mod. Phys.*, **21**, 541 (1949).
- [237] A. Hubert and R. Schäfer, *Magnetic domains: the analysis of magnetic microstructures* (Springer-Verlag, 1998).
- [238] J. S. Smart, S. Greenwald, *Phys. Rev.*, **82**, 113 (1951).
- [239] P. W. Anderson, *Phys. Rev.*, **79**, 350 (1950).
- [240] W. L. Roth, *Phys. Rev.*, **110**, 1333 (1958).
- [241] Y. Y. Li, *Phys. Rev.*, **100**, 627 (1955).
- [242] B. T. Thole, G. van der Laan, G.A. Sawatzky, *Phys. Rev. Lett.*, **55**, 2086 (1985).
- [243] P. Kuiper, B. G. Searle, P. Rudolf, L. H. Tjeng, C. T. Chen, *Phys. Rev. Lett.*, **70**, 1549 (1993).
- [244] D. Alders, L. H. Tjeng, F.C. Voogt, T. Hibma, G.A. Sawatzky, C.T. Chen, J. Vogel, M. Sacchi, S. Iacobucci, *Phys. Rev. B*, **57**, 11623 (1998).

- [245] S. Altieri, M. Finazzi, H.H. Hsieh, H. J. Lin, C.T. Chen, T. Hibma, S. Valeri, G.A. Sawatzky, *Phys. Rev. Lett.*, **91**, 137201 (2003).
- [246] E. Arenholz, G. van der Laan, R. V. Chopdekar, Y. Suzuki, *Phys. Rev. Lett.*, **98**, 197201 (2007).
- [247] H. Ohldag, G. van der Laan, E. Arenholz, *Phys. Rev. B*, **79**, 052403 (2009).
- [248] I. P. Krug, F. U. Hillebrecht, M. W. Haverkort, A. Tanaka, L. H. Tjeng, H. Gomonay, A. Fraile-Rodryguez, F. Nolting, S. Cramm, C. M. Schneider, *Phys. Rev. B*, **78**, 064427 (2008).
- [249] J. Lüning, F. Nolting, A. Scholl, H. Ohldag, J. W. Seo, J. Fompeyrine, J. P. Locquet, J. Stöhr, *Phys. Rev. B*, **67**, 214433 (2003).
- [250] S. Gota, M. Gautier-Soyer, M. Sacchi, *Phys. Rev. B*, **64**, 224407 (2001).
- [251] Y. Z. Wu, Z. Q. Qiu, Y. Zhao, A. T. Young, E. Arenholz, B. Sinkovic, *Phys. Rev. B*, **74**, 212402 (2006).
- [252] S.R. Krishnakumar, M. Liberati, C. Grazioli, M. Veronese, S. Turchini, P. Luches, S. Valeri, C. Carbone, *J. Magn. Magn. Mater.*, **310**, 8 (2007).
- [253] F. U. Hillebrecht, H. Ohldag, N. B. Weber, C. Bethke, U. Mick, M. Weiss, J. Bahrtdt, *Phys. Rev. Lett.*, **86**, 3419 (2001).
- [254] J. Stöhr, A. Scholl, T.J. Regan, S. Anders, J. Lüning, M.R. Scheinfein, H. A. Padmore, R. L. White, *Phys. Rev. Lett.*, **83**, 1862 (1999).
- [255] A. Scholl, J. Stöhr, J. Lüning, J.W. Seo, J. Fompeyrine, H. Siegwart, J. P. Locquet, F. Nolting, S. Anders, E.E. Fullerton, M. R. Scheinfein, H.A. Padmore, *Science*, **287**, 1014 (2000).
- [256] F. Nolting, A. Scholl, J. Stöhr, J. W. Seo, J. Fompeyrine, H. Siegwart, J. P. Locquet, S. Anders, J. Lüning, E. E. Fullerton, M. F. Toney, M. R. Scheinfein, H. A. Padmore, *Nature*, **405**, 767 (2000).

- [257] T. Yamada, *J. Phys. Soc. Jpn.*, **18**, 520 (1963).
- [258] W. L. Roth, *Phys. Rev.*, **111**, 772 (1958).
- [259] T. Kinoshita, T. Wakita, H. Sun, T. Tohyama, A. Harasawa, H. Kiwata, F. U. Hillebrecht, K. Ono, T. Matsushima, M. Oshima, N. Ueno and T. Okuda, *Journal of the Physical Society of Japan*, **73**, 2932, (2004).
- [260] H. Ohldag, N. B. Webera, C. Bethkea, F. U. Hillebrecht, *J. Elec. Spec. Rel. Phen.*, **114**, 765 (2001).
- [261] S. Mandal and K. S. R. Menon, *Phys. Rev. B*, **80**, 184408 (2009).
- [262] Y. Z. Wu, Y. Zhao, E. Arenholz, A. T. Young, B. Sinkovic, C. Won and Z. Q. Qiu, *Phys. Rev. B*, **78**, 064413 (2008).
- [263] D. Spanke, V. Solinus, D. Knabben, F. U. Hillebrecht, F. Ciccacci, L. Gregoratti and M. Marsi, *Phys. Rev. B*, **58**, 5201 (1998).
- [264] W. H. Meiklejohn and C. P. Bean, *Phys. Rev.*, **102**, 1413 (1956).
- [265] J. Nogués and I. K. Schuller, *J. Magn. Magn. Mater.*, **192**, 203 (1999).
- [266] H. Ohldag, G. van der Laan and E. Arenholz, *Phys. Rev. B*, **79**, 052403 (2009).
- [267] A. Scholl, M. Liberati, E. Arenholz, H. Ohldag and J. Stöhr, *Phys. Rev. Lett.*, **92**, 247201-1 (2004).
- [268] J. A. Borchers, M. J. Carey, R. W. Erwin, C. F. Majkrzak, and A. E. Berkowitz, *Phys. Rev. Lett.*, **70**, 1878 (1993); P. J. van der Zaag, Y. Ijiri, J. A. Borchers, L. F. Feiner, R. M. Wolf, J.M. Gaines, R. W. Erwin, and M. A. Verheijen, *ibid.* **84**, 6102 (2000).
- [269] J. C. Marmeggi and J. Baruchel, *J. Magn. Magn. Mater.*, **10**, 14 (1979).
- [270] S. Heinze, M. Bode, A. Kubetzka, O. Pietzsch, X. Nie, S. Blügel, and R. Wiesendanger, *Science*, **288**, 1805 (2000).

- [271] U. Kaiser, A. Schwarz, and R. Wiesendanger, *Nature (London)*, **446**, 522 (2007).
- [272] G. K. L. Marx, H. J. Elmers, and G. Schönhense, *Phys. Rev. Lett.*, **84**, 5888 (2000).
- [273] M. G. A. vanVeghel and P. A. Zeijlmans van Emmichoven, *J. Magn. Magn. Mater.*, **311**, 565 (2007).
- [274] P. G. Evans, E. D. Isaacs, G. Aeppli, Z. Cai, and B. Lai, *Science* **295**, 1042 (2002).
- [275] R. M. Tromp, J. B. Hannon, A. W. Ellis, W. Wan, A. Berghaus, and O. Schaff, *Ultramicroscopy*, **110**, 852 (2010).
- [276] Th. Schmidt et al., *Ultramicroscopy*, **110**, 1358 (2010).
- [277] A. Locatelli, T. O. Montes, M. A. Nino, and E. Bauer, *Ultramicroscopy*, **111**, 1447 (2011).
- [278] E. Bauer, *Rep. Prog. Phys.*, **57**, 895 (1994).
- [279] T. Wolfram, R. E. Dewames, W. F. Hall, and P. W. Palmberg, *Surf. Sci.*, **28**, 45 (1971).
- [280] A. Locatelli, L. Aballe, T. O. Montes, M. Kiskinova, and E. Bauer, *Surf. Interface Anal.*, **38**, 1554 (2006).
- [281] R. M. Tromp, M. Mankos, M. C. Reuter, A. W. Ellis and M. Copel, *Surface Review and Letters*, **5**, No. 6, 1189 (1998).
- [282] S. Mandal, K. S. R. Menon, Francesco Maccherozzi and Rachid Belkhou, *Phys. Rev. B*, **80**, 184408 (2009).
- [283] M. P. Seah, W. A. Dench, *Surf. Interf. Anal.*, **1**, 2 (1979).
- [284] K. Namikawa, *J. Phys. Soc. Japan*, **44**, 165 (1978).
- [285] J. C. Loudon, *Phys. Rev. Lett.*, **109**, 267204 (2012).
- [286] S. Altieri, M. Finazzi, H. H. Hsieh, M. W. Haverkort, H. J. Lin, C. T. Chen, S. Frabboni, G. C. Gazzadi, A. Rota, S. Valeri, and L. H. Tjeng, *Phys. Rev. B*, **79**, 174431 (2009).

- [287] F. Reinert, P. Steiner, S. Hiifner, H. Schmitt, J. Fink, M. Knupfer, P. Sand and E. Berte, *Z. Phys. B*, **97**, 83 (1995).
- [288] S. Altieri and L. H. Tjeng, *Phys. Rev. B*, **61** 13403 (2001).
- [289] J. van Elp, H. Eskes, P. Kuiper, and G. A. Sawatzky, *Phys. Rev. B*, **45** 1612 (1992).
- [290] C. Giovanardi, A. di Bona, and S. Valeri, *Phys. Rev. B*, **69**, 075418 (2004).
- [291] J. M. McKay and V. E. Henrich, *Phys. Rev. B*, **32**, 6764 (1985).
- [292] S. Kennou, M. Kamaratos and C. A. Papageorgopoulos, *Sur. Sci.*, **256**, 312-16 (1991).
- [293] R. Reissner, U. Radke, M. Schulze and E. Umbach, *Surf. Sci.*, **402**, 71-5 (1998).
- [294] S. Uhlenbrock, C. Scharfschwerdt, M. Neumann, G. Illing and H. J. Freund, *J. Phys. Cond. Mat.*, **4**, 7973 (1992).
- [295] M. A. van Veenendaal and G. A. Sawatzky, *Phys. Rev. Lett.*, **70**, 2459 (1993).
- [296] I. Preda, A. Gutiérrez, M. Abbate, F. Yubero, J. Méndez, L. Alvarez and L. Soriano, *Phys. Rev. B*, **77**, 075411 (2008).
- [297] L. Soriano, I. Preda, A. Gutiérrez, and S. Palacín, *Phys. Rev. B*, **75** 233417 (2007).
- [298] K. S. Kim and N. Winograd, *Sur. Sci.*, **43**, 625 (1974).
- [299] M. W. Obertsa and R. T. C. Smart. *J. Chem. Soc. Faraday Trans.*, **80**, 2957 (1984).
- [300] A. Baraldi, L. Gregoratti, G. Comelli, V.R. Dhanak, M. Kiskinova and R. Rosei, *App. Sur. Sci.*, **99**, 1 (1996).
- [301] S. Park, H. S. Ahn, C. K. Lee, H. Kim, H. Jin, H. S. Lee, S. Seo, J. Yu, and S. Han, *Phys. Rev. B*, **77**, 134103 (2008).
- [302] W. B. Zhang, N. Yu, W. Y. Yu, and B. Y. Tang, *The Eur. Phys. Jour. B*, **64**, 153 (2008).